

NANOELECTRONIC AND NANOMECHANICAL DEVICES FOR
LOW TEMPERATURE APPLICATIONS

MATTHEW SARSBY, MPHYS (HONS.)

A thesis submitted in fulfilment of the requirements of the degree of

Doctor of Philosophy

at Lancaster University

24th January 2017

DECLARATION

This thesis is my own work, and has not been submitted in substantially the same form for the award of a higher degree elsewhere. Any sections of the thesis which have been published, or submitted for a higher degree elsewhere, are clearly identified.

Lancaster, 24th January 2017

Matthew Sarsby

The use of “we”, unless otherwise noted, refers to the team of researchers including the author.

ABSTRACT

Cooling physical experiments to low temperatures removes thermal excitations to reveal quantum mechanical phenomena. The progression of nanotechnologies provides new and exciting research opportunities to probe nature at ever smaller length scales. The coupling of nanotechnologies and low temperature techniques has potential for scientific discoveries as well as real world applications. This work demonstrates techniques to further extend physical experimental research into the millikelvin-nanoscale domain.

The challenge of thermometry becomes an increasingly complex problem as the temperature of a physical system lowers. We describe the development and methods for a specially modified Coulomb blockade thermometer to achieve electron thermometry below 4 mK overcoming the challenge of electron thermalisation for on-chip devices.

Mechanically vibrating devices can directly probe bulk and surface fluid properties. We developed practical measurement techniques and analysis methods to demonstrate the use of nanomechanical resonators, which for the first time were used to probe both the normal and the superfluid phases of helium-4. The doubly clamped beams had a cross section of 100 nm by 100 nm and were tested in length variants between 15 μm to 50 μm , The flexural resonance between 1 MHz and 10 MHz in response to the helium temperature dependent properties showed an encouraging agreement with established theories, providing experimental verification on a new smaller length scale. The smallest beams achieved a mass sensitivity in liquid of 10 ag.

We also created and analysed a new method of sampling peak-like functions that is applicable to many physical systems to provide around

20% improvements over the existing methods under certain situations. This was verified in ultra low temperature applications as a drop-in addition to accompany existing techniques.

PUBLICATIONS

The following are published works including the author.

- Nanoelectronic thermometers optimised for sub-10 millikelvin operation [1]
- Nanoelectronic primary thermometry below 4mK [2]

*Each piece, or part, of the whole of nature is
always merely an approximation to the complete truth,
or the complete truth so far as we know it.
In fact, everything we know is only some kind of
approximation, because we know that we do not know
all the laws as yet.*

— Richard Feynman [3]

ACKNOWLEDGMENTS

Many thanks to all those who supported me whilst I worked.

Particular thanks go to the ULT group in Lancaster, and to the many members of the newly formed QTC group. Thanks to Alan, Ian, Jon, and Dima, who managed to cope with a magnitude of spelling errors. Thanks to Viktor, Rich, George, Roch, Sergey, and Mal in ULT for being there and providing insight and a great environment to work in.

A special thank you to LGR who supported me at home and providing the much needed encouragement during creation of the final pages of this thesis.

This research was supported by,

- U.K. EPSRC (EP/K01675X/1 and EP/L000016/1)
- European FP7 Programme MICROKELVIN (project number 228464)
- Academy of Finland (project #252598)
- Tekes project FinCryo (Grant No. 220/31/2010)
- The Royal Society

CONTRIBUTIONS

Experimental physics is not a solo endeavour. The three projects shown in this thesis involved a lot of people collaborating. The author of this thesis was involved in the low temperature measurements and experimental design, development and analysis, but not including clean room work: as nanofabrication and design of the CBT devices was done by Aivon and VTT, and nanofabrication and design of the NEMS devices were carried out by Sergey Kafanov.

ACRONYMS

ADC	Analogue to Digital Converter
CBT	Coulomb Blockade Thermometer
DAC	Digital to Analogue Converter
DUT	Device Under Test
MC	Mixing Chamber of a dilution refrigerator
MEMS	Microelectromechanical System
NA	Network Analyser
NEMS	Nanoelectromechanical System
NMR	Nano Mechanical Resonator
PCB	Printed Circuit Board
SEM	Scanning Electron Microscope
ULT	Ultra Low Temperature

CONTENTS

1	INTRODUCTION	1
2	CBT	3
2.1	Introduction	3
2.2	Overview and Theory	6
2.3	Design and Fabrication	13
2.4	Measurements	17
2.4.1	Electrical Connections and Acquiring the Differential Resistance	17
2.4.2	Primary Mode	20
2.4.3	Secondary Mode	22
2.4.4	Pseudo Secondary Mode	22
2.4.5	Width and Excitation Settings	26
2.4.6	Vibrating Wire Resonator and Other Thermometry	28
2.5	Experimental Detail	33
2.5.1	Sintering	38
2.5.2	Filtering and Noise	42
2.6	Early Measurements	45
2.6.1	Self-consistent Properties	45
2.6.2	Excitation Dependence	48
2.6.3	Temperature Measurement Comparisons	51
2.6.4	Cooling Time Constant	53
2.7	Immersed CBT Measurements	56
2.7.1	Isothermal Measurements of the immersed CBT	56
2.7.2	Cooling Time Constant - Comparison	59
2.7.3	Peak Tracking at Low Temperatures	60
2.7.4	Coldest Measurements	62
2.7.5	CBT Saturation	63

2.7.6	Thermal Simulation of CBT Islands	65
2.8	Discussion	69
2.9	Further Work	71
2.10	Conclusions	74
3	AN IMPROVED PEAK SAMPLING SCHEME	75
3.1	Introduction	75
3.2	Theory	77
3.2.1	Peak Functions	77
3.2.2	Implementation	78
3.3	Results	81
3.3.1	Linear Sampling Pattern	81
3.3.2	Location of Parameter Information in the Sample Space	82
3.3.3	Equally Spaced Measurements in Phase	84
3.3.4	Search for Improvements by Genetic Algorithms	85
3.3.5	Generalising a solution	87
3.3.6	Experimental Verification on Real World Systems	89
3.3.7	Testing Tolerance Against Poorly Estimated Peak Parameters	90
3.3.8	Application to Other Peak Shapes	92
3.4	Further Work	94
3.5	Conclusion	94
4	NANOMECHANICAL RESONATORS AS PROBES FOR QUANTUM FLUIDS	95
4.1	Introduction	95
4.2	Background	98
4.3	Beam Manufacturing	100
4.4	Theory	104
4.4.1	Resonance	104
4.4.2	Fundamental Frequency	108
4.4.3	Overtones	112

4.4.4	NEMS in Helium	113
4.5	Measurement Circuits and Analysis	120
4.5.1	Test Measurements Circuits	120
4.5.2	Resonance Measurement Circuits	123
4.5.3	Measurements from a Network Analyser	125
4.5.4	Estimation of Displacement and Velocity of the Beam From Power	128
4.5.5	Measurements of the Induced Voltage from Res- onance	130
4.5.6	Electrical Measurements at High Frequencies	133
4.5.7	Signal Phase Compensation	134
4.6	Experimental Detail	136
4.6.1	Early Experiments	136
4.6.2	Cryostat-II Purpose Built Probe	142
4.7	Preliminary Measurements	146
4.7.1	Measurements In Vacuum	146
4.7.2	Beam Failure Modes	152
4.7.3	Nanomechanical Beam Thermal Modelling and Simulation	153
4.8	Results	158
4.8.1	Measuring Resonance	159
4.8.2	Higher Harmonics	166
4.8.3	Power Response and Drive Sweeps	169
4.8.4	Pressure Dependency	173
4.8.5	Resonance Response to the Temperature De- pendent Properties of Liquid Helium-4	175
4.8.6	Measuring in the Superconducting State	180
4.9	Discussion	183
4.10	Further Work	186
4.11	Conclusions	189
5	CONCLUSIONS	191

A APPENDIX	195
A.1 Code Listings	196
BIBLIOGRAPHY	200

LIST OF FIGURES

Figure 2.2.1	Circuit Diagram of an Island	7
Figure 2.2.2	Junction Energy Diagram	9
Figure 2.2.3	Sketch I-V of a CBT	9
Figure 2.2.4	Conductance Drop with Temperature	10
Figure 2.3.1	CBT Chip Layout	15
Figure 2.4.1	Measurement Block Schematic	17
Figure 2.4.2	CBT Wiring Diagram	18
Figure 2.4.3	Differential Resistance Sketch	19
Figure 2.4.4	Polynomial Fitting Algorithm	25
Figure 2.4.5	Auto Width Choice	27
Figure 2.4.6	Sketch of a VWR	28
Figure 2.4.7	VWR Measurement Circuit	30
Figure 2.4.8	RuO ₂ Measurement Power	31
Figure 2.5.1	CBT outside the Mixing Chamber	34
Figure 2.5.2	CBT Immersion Schematic	36
Figure 2.5.3	CBT Immersion Cell Photo	37
Figure 2.5.4	Kapitza Resistance of a Sinter	38
Figure 2.5.5	CBT Holder with Sinter	41
Figure 2.5.6	Line Sinters	41
Figure 2.5.7	Thermal Path Model	43
Figure 2.5.8	CBT Package	44
Figure 2.6.1	Consistent Capacitance	46
Figure 2.6.2	Consistent Resistance	47
Figure 2.6.3	Excitation Dependence	49
Figure 2.6.4	Simulated Excitation Dependence	50
Figure 2.6.5	Temperature Measurement Comparisons	52
Figure 2.6.6	Thermometry Comparison	54

Figure 2.6.7	Long Term Cooling Trend	55
Figure 2.7.1	Conductivity Curve Sweeps	57
Figure 2.7.2	CBT Thermal Recovery After DC Heating . . .	58
Figure 2.7.3	Cooling Time Comparison	59
Figure 2.7.4	Centre Shift on Secondary Mode Tracking . . .	61
Figure 2.7.5	One Shot Cooling	63
Figure 2.7.6	CBT Trend to Saturation	64
Figure 2.7.7	Island Simulation Temperatures	67
Figure 2.7.8	Island Simulation Powers	68
Figure 3.2.1	The Five Parameters that Define a Peak	77
Figure 3.2.2	Comparison of Peak Shapes	78
Figure 3.3.1	Linear Spaced Sampling	81
Figure 3.3.2	Location of Information	83
Figure 3.3.3	Equal Phase Sampling Pattern	85
Figure 3.3.4	Progression of the Genetic Algorithm	87
Figure 3.3.5	The generation of the Mphasy Pattern	88
Figure 3.3.6	Comparison of the Proposed Sampling Pattern .	89
Figure 3.3.7	Experimental Verification on a ULT VWR . . .	90
Figure 3.3.8	Testing Non-Ideal Pattern Generation Parameters	91
Figure 3.3.9	Noise and Sampling Density Tests	92
Figure 3.3.10	Comparison of the Proposed Sampling Pattern .	92
Figure 4.3.1	SEM of a 15 μm Aluminium Beam	102
Figure 4.3.2	SEM of a Buckled Beam	103
Figure 4.4.1	Beam Deflection Diagram	104
Figure 4.4.2	Dynamic Range of a Resonator	108
Figure 4.4.3	Beam Area Moment Of Inertia	109
Figure 4.4.4	Predicted Frequencies	110
Figure 4.4.5	Irregularities of the Beam Shape	111
Figure 4.4.6	Beam Resonant Frequency Theory	113
Figure 4.4.7	Phase Diagram of Helium-4	114
Figure 4.4.8	Liquid Densities of Helium-4	115

Figure 4.4.9	Attached Mass on the Beams	117
Figure 4.5.1	DC Measurement Circuit	120
Figure 4.5.2	AC Measurement Circuit	122
Figure 4.5.3	Network Analyser Beam Checking Circuit	122
Figure 4.5.4	Resonance Measurement Circuit	124
Figure 4.5.5	The Scattering Matrix	125
Figure 4.5.6	Measuring Power From a Vector Network Analyser	126
Figure 4.5.7	Inferring Induced Voltage	131
Figure 4.6.1	Brass Cell Design	137
Figure 4.6.2	Dirty Bonding Method	138
Figure 4.6.3	Electrical Grounding Diagram	139
Figure 4.6.4	Resonance Measurement Circuit	141
Figure 4.6.5	Advanced Cryostat - Photograph	143
Figure 4.6.6	Advanced Cryostat - Sketch	144
Figure 4.7.1	Resonance Measurements in Vacuum	147
Figure 4.7.2	Additional Resonance Peaks	148
Figure 4.7.3	Off Axis Modes	149
Figure 4.7.4	4 K to 300 K Frequency Shift of Resonance	150
Figure 4.7.5	NEMS Failure Modes	152
Figure 4.7.6	Vacuum Thermal Model	155
Figure 4.7.7	Thermal simulation profile	156
Figure 4.8.1	15 μm Wide Sweep in Vacuum	160
Figure 4.8.2	Phase Corrected Data	161
Figure 4.8.3	Fitting to S_{21}	163
Figure 4.8.4	The power in the 15 μm long beam	164
Figure 4.8.5	Force, Velocity, and Displacement	165
Figure 4.8.6	50 μm Beam - a Wide Sweep in Vacuum	166
Figure 4.8.7	Comparison of Harmonics	167
Figure 4.8.8	50 μm Beam - Power Sweep	170
Figure 4.8.9	25 μm Beam - Power Sweep	171
Figure 4.8.10	Measuring peak-symmetry	172

Figure 4.8.11	Quality Factor Length Dependence in Gas . . .	173
Figure 4.8.12	Quality Factor Length Dependence Model Comparison	174
Figure 4.8.13	Corrected Resonance Sweep Data During Temperature Change - 25 μm Beam	176
Figure 4.8.14	Fitting Frequency to Temperature Dependence In Liquid - 50 μm Beam	177
Figure 4.8.15	Fitting Resonance Width to Temperature Dependence In Liquid - 50 μm Beam	178
Figure 4.8.16	Resonant Frequency Ratio Comparison	179
Figure 4.8.17	Width Change Comparison	180
Figure 4.8.18	Centre Frequency Change Comparison	181
Figure 4.8.19	Low Field Measurements	182
Figure 4.9.1	Sketch of the Attached Fluid Volume	183
Figure 4.9.2	Viscous Penetration Depth of a Beam	184
Figure A.0.1	Mixing Chamber VWR Calibration Curve . . .	198
Figure A.0.2	NEMS Manufacturing Process	199

LIST OF TABLES

Table 1	Coefficients for Harmonics	113
Table 2	Measured Overtone Frequencies	167
Table 3	Beam Tension	168
Table 4	Fitting Parameters in Liquid	177
Table 5	Summary of Temperature Dependence Fits . . .	179

Table 6	Effective Surface Area of the Beams	185
---------	---	-----

LISTINGS

Listing A.1	Peak Convolution Function	196
Listing A.2	Generalised Improved Sampling Pattern	197
Listing A.3	Equal Phase Sampling Pattern	198
Listing A.4	Linear Sampling Pattern	199

INTRODUCTION

This thesis covers the experimental work of two of the major undertakings and one small project, and is laid out in three parts.

The first part is work on a commercial Coulomb Blockade Thermometer, CBT, that we modified for use at low-millikelvin temperatures. We demonstrate the cooling of electrons in a nanoelectronic device to a record low temperature below 4 mK and measure the deviation away from the phonon temperature as the coupling between electrons and the cold source becomes weaker. During this we developed new techniques to measure temperature with CBTs as the challenges of noise, thermal coupling, and thermovoltages become greater.

The second part is a short interim to cover work on a different domain sampling pattern to improve the parameter estimation of peak-like curves. This provides insight into experimental data acquisition when sampling systems that have peak-like responses such as the resistance peak of a CBT or the resonance peak of a mechanical or electrical oscillating system. The improved sampling pattern is verified experimentally on a vibrating wire resonator in a demagnetisation stage of a microkelvin helium-3 sample. The standard measurements of a peak-like curve typically involve sampling in equal spaced increments across the peak encompassing some of the tail on both sides and the peak in the middle. We measure the accuracy on simulated data to show the correctness of the estimated parameters at different sampling widths using the even spacing technique. We used a genetic algorithm to search for an improved accuracy in measurement of the peak parameters in a variable space of sampling points. This discovered optimised sampling pattern is generalised to a measurement pattern

algorithm for general purpose use, and is shown to provide an improved accuracy in height and width by 30% for the same sampling width and number of sampling points.

The third and last part covers work on nano-scale mechanical oscillators to be used as probes to measure the dynamic properties of fluid helium-4 and potentially helium-3. The oscillators are aluminium doubly-clamped beams which are categorised as nano-electro-mechanical-systems, NEMS. The beams have a 100 nm by 100 nm cross section and lengths of tens of micro metres long, covering a frequency range of 1 MHz to 100 MHz. We characterise resonance behaviour of these beams in vacuum, different helium gas pressures at 4.2 K, and in liquid helium at different temperatures between 1.2 K and 4.2 K. We measure the change in resonance width and shift over a range of temperatures including temperatures above the superfluid transition. We can use a model of the expected changes in resonance described by the known fluid properties and some geometric parameters to describe most of the changes observed; however the model does not hold for short beams with higher frequency resonances. We expect acoustic damping is becoming a significant contributor to the measured effects, and work is on-going to build and test models to fully describe this.

DEMONSTRATION OF COOLING ELECTRONS IN A NANOSTRUCTURE TO BELOW 4 mK USING A COULOMB BLOCKADE THERMOMETER

INTRODUCTION

A Coulomb Blockade Thermometer is a device that measures the temperature of electrons using the physical phenomena of Coulomb blockading. A low temperature Coulomb Blockade Thermometer, CBT, was designed and manufactured in Finland by the VTT Technical Research Centre of Finland, and by Aivon (<http://aivon.fi/>). We worked in collaboration to test and develop thermalisation and experimental techniques for operation of CBTs in the millikelvin temperature regime.

It is very hard to cool the electrons in nanoelectronic devices in the low millikelvin regime. The electron temperature is usually higher than the phonon temperature of the sample, cooled by thermal contact to a dilution refrigerator. These ‘overheated’ electrons determine the device properties, so developing direct electron thermometry is of high importance to determine ways of improving this thermal contact. CBTs provide the opportunity for pseudo-primary low temperature thermometry in the millikelvin regime.

CBT were an invention of J.P Pekola [4, 5]. Modern CBTs provide primary low temperature thermometry in the millikelvin regime. If used appropriately, CBTs can be a replacement to the traditional calibrated resistor thermometry that is seen in commercial dry fridges.

We continue the work my colleagues previously made measuring a CBT in a cryogen free dilution refrigerator at temperature at 7 mK. At this operating temperature it appeared that the CBT has not yet saturated the available cooling capacity and should be possible to cool the device further. To test the limiting physics of the system we transitioned to a custom dilution refrigerator [6] with a much lower 2.6 mK base temperature and we developed a holder to suspend the CBT underneath the mixing chamber. While this method worked to lower the temperature of the electrons in the CBT we then went on to develop an experimental cell mounted inside the mixing chamber itself. This immersion experiment provides more direct cooling from the refrigerant, which resulted in much faster thermalisation times. The immersion into the refrigerant extended the practical temperature domain of the CBT into the low millikelvin temperature range.

Along with the CBT, there were other thermometry devices including a commercial RuO₂ calibrated resistor, used for comparison to official NIST temperature scales, a tuning fork, and at least one vibrating wire resonator, as the de facto helium temperature scale.

The current generation of commercial dilution refrigerators typically reach 5 to 10 mK [7][8, 9, 10], and custom academic built units have records of 1.75 mK [11]. Within this regime CBTs have the potential of primary thermometry with inherent magnetic field independence. In the expanding field of quantum information, the CBT (as well as a competing technology N-I-S junctions [12]) could provide local on-chip electron thermometry, as experimental work continues to work with lower temperature for improved charge sensitivity and increased coherence times [13, 14].

The first section of this part of the thesis covers the theory of CBTs, including the physical principle of operation and then discuss of some of the key equations for thermometry measurements. It also covers how the physical characteristics of specific CBTs are found from electrical

measurements. The measurements section covers the laboratory setup and the analysis and on-line software used for the acquisition of data. The CBT Design and Fabrication section covers some of the design choices made by our collaborators, that make this CBT particularly well suited to low temperature measurements. It also covers the cell design and the modifications we made for operation in helium.

The results section are split into the early work where the electrical properties of the CBT are measured and analyse the challenges of CBT operation at low temperatures. This section includes a comparison to other thermometers and a cooling time constant while attached underneath the mixing chamber. The second results section includes data from the CBT while it was immersed, measured and analysed using the techniques developed from the initial experimental run. This chapter finishes off with a discussion of our conclusions and suggestions of further work.

The work described in this chapter lead to a publication in Nature Communications [2].

OVERVIEW AND THEORY

A Coulomb blockade thermometer, measures the temperature of electrons using the phenomena of Coulomb blockading. Coulomb blockading is an increased resistance, or reduced conductance, of a pair of tunnel junctions at small bias voltages due to a build up of electrons and the energy required to charge a low capacitance island between the tunnel junctions. Measurements of this change in resistance yields information about the electron temperature in the CBT. If the electron temperature of the system is well coupled to the lattice temperature then the CBT can be used as a self-calibrating primary thermometer for low temperature applications.

Temperature measurements using a CBT can be acquired by analysing the electrical current vs. voltage, $I - V$, curve, in a manner that only uses natural physical constants and calculable prefactors. Hence CBTs are primary thermometers, and do not need calibration against an existing temperature scale.

The function of a CBT depends, exclusively, on coulomb blockading of tunnel junctions, and consequently is insensitive to magnetic fields [15].

A tunnel junction is a semiclassical device made of a thin insulating volume sandwiched between two electrodes, as shown in figure 2.2.1. A voltage bias across the device causes electrons to tunnel through the insulating barrier and cause a current flow with some effective resistance. For a CBT, the electrodes around the insulating barrier are normal-conducting, meaning the charge carriers are single electrons, if the electrodes are superconducting then pairs of electrons will tunnel as Cooper pairs. The CBT we use is made of aluminium which has a superconducting phase, but we use the device in a magnetic field to avoid it.

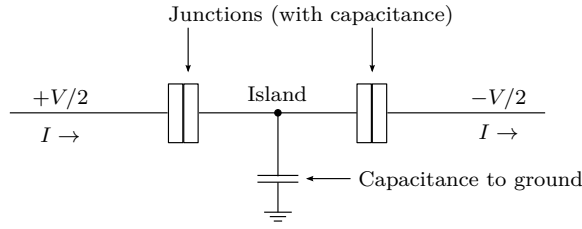


Figure 2.2.1: A sketch of an island made up between two junctions. There is capacitance of each junction and some capacitance to ground. A voltage V is split over two junctions and a current I flows. Electrons collect in the island due to the capacitance.

Classical physics prevents an electrical current flow through an insulating region, but there is a small non-trivial and non-vanishing probability for the electron's position to be the other side of the insulating volume due to its wavelike nature [16]. This means that there is some electron transport across the insulator [17], (as was first formulated in 1985-1986 by D. Averin and K. Likharev [18]). In the presence of a voltage bias, there is a net current across the barrier. The current is proportional to the amplitude of the bias, and at large biases the junctions appear to act like an ohmic resistor. The resistance is exponentially dependent on the barrier thickness, which is typically on the scale of nanometres in size. These junction also acts as a capacitor with the insulating gap as the dielectric.

Next we consider two junctions in series with an isolated conducting island between them, as shown in figure 2.2.1. This island has an overall capacitance, C , from both of the junctions and some intrinsic capacitance, typically to a ground plane. The discrete nature of electron tunnelling into this island causes a small voltage rise on the island by $U = e/C$ according to the elementary electron charge e . The rise of voltage on the island reduces the bias across the junction and this reduces the tunnelling of further electrons onto the island, increasing the resistance. When an extra electron joins the island, the potential rises by e/C , the next electron requires an extra e^2/C energy to join the island. The number of electrons that have this extra energy depends

on temperature, $k_B T$. Increasing the bias across the island provides extra energy, eV , to the electrons which helps tunnelling to the island. If the bias is larger than the charging energy then most electrons will be able to join the island and the temperature dependent blockading effect is negligible. The current suppression can be seen at low biases, when the energy of the bias eV is comparable to the Fermi surface energy $k_B T$, figure 2.2.2. We can see coulomb blockading effect on a differential resistance sweep, as a dip in conductivity centred at zero bias, seen in figures 2.2.3 and 2.2.4.

The Coulomb blockading effect can be described using energy considerations of the electron thermal energy, $k_B T$, and the electrostatic energy, E_c , required to charge the capacitance of the junction, C . The total charging energy is, $E_C = e^2/(2C)$, [19]. If E_c is larger than a few $k_B T$, then no electron will have enough energy to charge up the island, and the device will be fully Coulomb blockaded. If $E_c \ll k_B T$ the effect of an electron in the island will have almost no effect changing the bias over the junction and the device is insensitive to temperature. Devices work as Coulomb Blockade Thermometers when the charging energy is smaller than the thermal broadening at the Fermi surface, $k_B T > E_C$. CBTs are designed to operate in this regime because of the temperature dependence, where the temperature should dominate the electrical transport characteristics [4, 20].

The orthodox theory of electron transport neglects the shape of the islands, so it is a zero dimensional description. A second assumption is that both the tunnelling process and charge redistribution after tunnelling are instantaneous. The tunnelling time has been shown to be finite, about 1×10^{-14} s [21]. A third assumption is that the energy spectra in the islands and the connecting leads are continuous (non-discrete) [22].

Figure 2.2.3 shows a differential resistance $R = dV/dI$, to highlight the region of interest, which is the local slope of resistance at a bias.

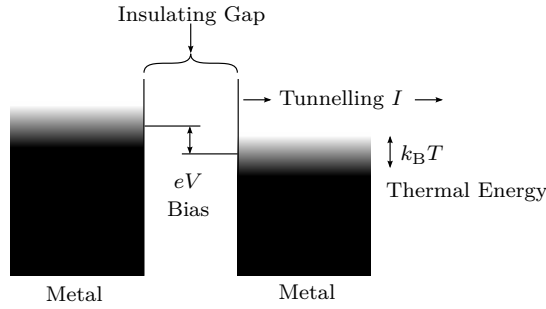


Figure 2.2.2: The energy diagram of a Normal-Insulating-Normal (NIN) junction. The applied bias causes a shift of eV between the Fermi energies on the two sides. The electron probability distribution on each side is thermally broadened by $k_B T$. When $eV \approx k_B T$, this provides a temperature dependent tunnelling rate, as at lower temperature there are less empty accessible states.

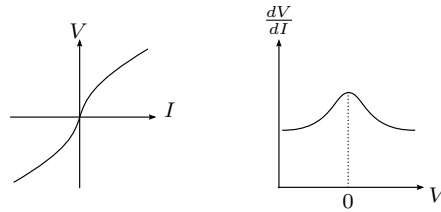


Figure 2.2.3: The $I - V$ characteristic curve of a CBT. In the region around 0 the gradient is higher than the surroundings. This is seen as a peak in resistance above some background.

The local resistance is a function of voltage or current, $R(V)$ and $R(I)$, rather than the usual total effective resistance $R = V/I$. When discussing CBTs it is common to describe the conductance, $G = 1/R = dI/dV$, rather than the resistance. Pekola's CBT equations [4] for thermometry use the differential conductance G , and it is common to use a normalised form of G to the background tunnelling conductance G_T , G/G_T , when publishing results for ease of comparison, figure 2.2.4 shows a typical published work.

A typical CBT design is to use a 2-dimensional array of parallel and series junctions [23, 15]. Junctions in series increases the width of the conduction dip, described in equation 2.2.1. This makes measurements at low temperatures, when the peak is narrowest, easier. The additional tunnel resistance for each junction increases the total resistance. The

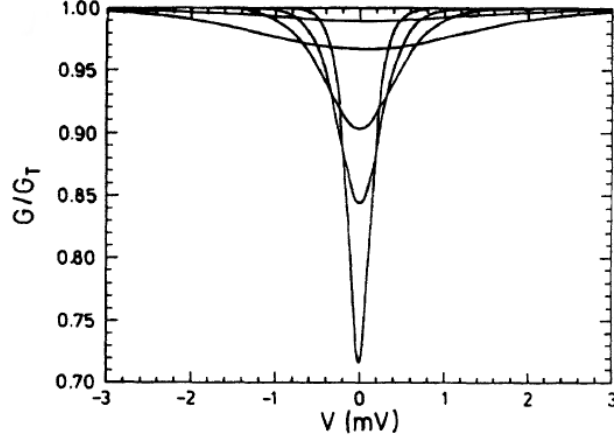


Figure 2.2.4: The conductance drop for a CBT at five different temperatures, 10, 3, 1, 0.6, and 0.3 K, reproduced from [4]. Data from colder measurements have narrower and deeper conductance dips. The CBT in [4] had $C_\Sigma = 3$ fF.

series of junctions are duplicated in parallel to lower the background resistance to a range that is easier to measure.

A lowest order approximation for the shape of the dip has been described [4, 24] for an array of N junctions. Assuming that the charging energy is much less than the thermal energy enables a Taylor expansion in terms of $(e^2/2C)/k_B T$. It is also assumed that resistance of each junction R_j is greater than the resistance quantum $h/2e^2 \approx 12.9$ k Ω , which is named the “weak tunnelling regime”. The Coulomb blockaded gap would have sharp transition at zero temperature $T = 0$, but is ‘smeared’ at higher temperatures to a width of

$$V_{1/2} = 5.439 N k_B T / 2. \quad (2.2.1)$$

The peak height is normalised to the background tunnel conductance G_T , and is described by

$$G(V)/G_T = 1 - \frac{E_C}{k_B T} \cdot g\left(\frac{eV}{N k_B T}\right). \quad (2.2.2)$$

The dip shape, g , is

$$g(x) = \frac{x \sinh(x) - 4 \sinh^2(x/2)}{8 \sinh^4(x/2)}, \quad (2.2.3)$$

with $x = eV/N k_B T$ Equation 2.2.2 uses the measurable properties of the device: the background conductance measured far away from the

blockaded region G_T , and the total effective capacitance, $C_\Sigma = \frac{NC}{2(N-1)}$, which is used to find the total charging energy of the system [24],

$$E_C \equiv \frac{N-1}{N} \cdot \frac{e^2}{C} = \frac{e^2}{2C_\Sigma}. \quad (2.2.4)$$

The approximations in equations 2.2.2, are improved with higher order terms, including modelling of non-uniformities in the array [23]. The additional terms do not affect the CBT as a primary thermometer. A non-ideal non-uniform distribution of tunnel resistances of the tunnel junctions means that equation 2.2.2 yields systematic error, but the influence of the inhomogeneity on temperature is weak, and typically results in a 1% or smaller error [23].

Measurements of the width of the dip can use the full width at half minimum $V_{1/2}$, equation 2.2.1, to obtain the temperature of the electrons in the system without calibration or numerical fitting.

Measurements of the CBT blockading width are called primary mode measurements, but it is possible to also measure the maximum blockading dip - the conductance at zero bias,

$$\frac{\Delta G}{G_T} = \frac{E_C}{6k_B T}. \quad (2.2.5)$$

However this approach requires E_C - a value dependent on the overall capacitance, and G_T - a value derived from the background conductance, to be known. Both of these can be found by a self-calibration process: by taking preliminary full $I - V$ measurements at a few different temperatures and fitting the curves to equation 2.2.2. Individual measurements of C_Σ and R_T should have no dependence on temperature, and once found can be used at any temperature. Measurements of the peak height $\frac{\Delta G}{G_T}$ are called secondary mode measurements.

The dip in the zero bias conductance G_0 has the analytic approximation [20], arising from equation 2.2.2 evaluated at $V = 0$.

$$G_0 \approx G_T \left(1 - 1/6u_N - 1/60u_N^2 + 1/630u_N^3 \right) \quad (2.2.6)$$

where u_N is a dimensionless inverse temperature,

$$u_N \equiv E_C/k_B T, \quad (2.2.7)$$

which comes from

$$u_N = 2 \frac{N-1}{N} \left(\frac{e^2}{2Ck_B T} \right), \quad (2.2.8)$$

and E_C from equation 2.2.4. Another term to describe the effect of blockading is $v_N = eV/NkT$, although we do not use it we require that $v_N \ll 1$. This is the formalisation of the requirement for Coulomb blockading.

The tunnelling conductance G_T or resistance R_T is the background asymptotic conductance or resistance at $I_{DC} \rightarrow \infty$. To observe Coulomb blockading, we have a practical need for $\Delta G > 0.01G_T$, so that the peak is resolvable from the background. The blockading width $V_{1/2}$, equation 2.2.1, scales with T and can become practically too wide. This limits the high temperature measurements, and is why the current generation of CBTs only work accurately up to 60 K [25, 26]. Coulomb blockading has managed to be seen at up to 300 K [27] in quantum dot nano-structures.

The low temperature measurements are limited by the ability to cool the electron gas in the region of the junctions. This can be because of the self-heating from the applied measurement causing Joule heating, and the limited thermal connection to a cold source. The electrons in the isolated islands between the two tunnel junctions cool primarily through electron-phonon coupling to phonons in the island, which in turn couple to the substrate and through the junction themselves [23]. Any electrical noise causes additional current to flow and additional Joule heating.

For the fastest and most responsive thermometry, secondary mode is preferred because it requires the fewest number of samples, potentially just one at $V = 0$, to acquire temperature [28]. Another method used by Bergsten [28] that uses sampling at a bias where the third derivative

is zero, $d^3I/dV^3 = 0$. This bias scales linearly with T . The sign in an error of d^3I/dV^3 when $d^3I/dV^3 \neq 0$ provides information about how to modify the bias to correct for the next sample if $d^3I/dV^3 \neq 0$. However this method is inappropriate for use at extremely low temperature because of the deliberate finite current through the device.

At low temperatures the full I - V data is fitted using a full single electron tunnelling model [29]. This fitting models the known CBT ohmic self-heating from the amplitude of the DC current, the electron-phonon cooling power, and a parasitic heat leak, by the heat flow into the island which should be zero in equilibrium,

$$\dot{Q} = \frac{V_{\text{DC}}^2}{R_T} - \Sigma\Omega (T_e^5 - T_p^5) + \dot{Q}_{\text{leak}}. \quad (2.2.9)$$

The electron temperature T_e is extracted from the model if we can also measure separately the phonon temperature T_p . This enables us to acquire the electron temperature even when the electron temperature begins to become decoupled from the phonon temperature. The term Σ describes the strength of the electron-phonon coupling and Ω , the coupling volume.

DESIGN AND FABRICATION

Following their success with previous tunnel junction fabrications, our collaborators in VTT, Finland, designed and fabricated the CBT used in our investigation [30].

Inside a CBT the electrons tunnel through the junctions between islands and because of the temperature dependent tunnelling effects, it is only the temperature of the electrons that is measured. The electrons are cooled by scattering off the phonons inside some thermalisation volume around the tunnel junctions [23]. The amount of coupling between the electrons and the phonons is given by,

$$\dot{Q}_{\text{ep}} = \Sigma\Omega (T_e^n - T_p^n). \quad (2.3.1)$$

The rate of scattering is dependent on the atomic structure of the material, characterised by Σ . If there is more material then there is also more opportunity for electrons to scatter, hence the volume, the Ω term, in 2.3.1. This is linearly proportional to a material constant Σ and the volume Ω , and an integer $n = m + 2$. m depends on the parameter ql where q is the wave vector of the phonons and l is the electron mean free path. In metals below 1 K, if $ql > 1$ then the phonon scattering is only from longitudinal phonons and $m = 3$, and $n = 5$. Alternatively if scattering with transverse phonons then $m = 2, m = 4$ and Σ is then proportional to $1/l$ [31]. The value for m changes for ordered and disordered metals. If there is scattering on boundaries and or impurities m can be 4. In our case we suspect that the metal is reasonably pure and highly ordered, and the size of the fins are large, $m = 3$ and so $n = 5$. [32], a fifth power has been observed in metals of similar purity [33]. The cooling power is proportional to the fifth power of the temperatures of the electron temperature T_e and the phonon temperature T_p . As temperatures drop, the cooling power available to the electrons drops very quickly and can cause T_e to be significantly overheated compared to T_p .

Devices designed to work well at low temperatures aim to maximise \dot{Q}_{ep} . This is achieved by attaching thermalisation volumes, the cooling fins, that are as large as possible, and chosen to be made from a material that has a high Σ . The configuration of the parallel and series array of junctions can also be chosen to improve low temperature performance. The width Coulomb Blockade can be increased with more series junctions, which makes practical measurements easier, at the cost of an increased end to end resistance. This high resistance can be reduced to improve Joule heating by implementing more parallel strings of junction, reducing the resistance.

Our collaborators in Finland, have designed a device shown in figure 2.3.1, that is designed with this in mind. It is of scientific and

commercial value to see if the device is limited by the electron-phonon coupling and to demonstrate that it is possible to thermally couple sufficiently well to the electrons to expand the available domain of experimental physics.

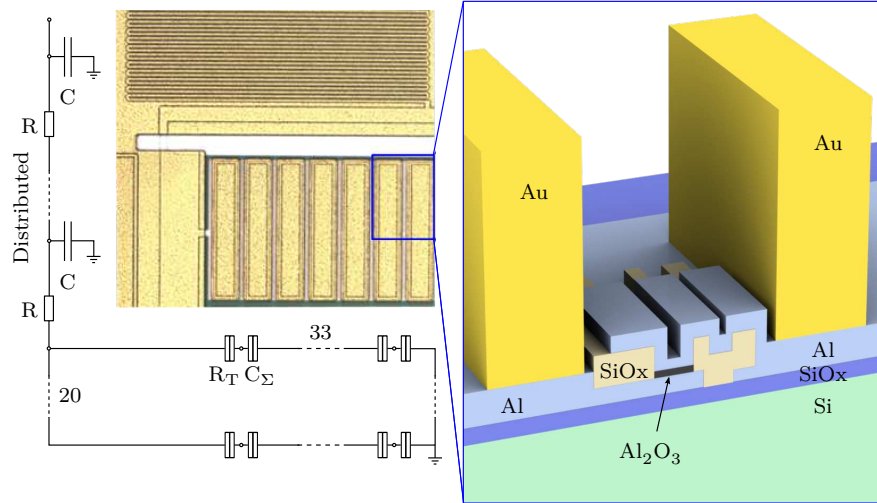


Figure 2.3.1: An optical micrograph taken by Aivon with VTT, top left, shows several islands and the cooling fins, the junctions are not visible underneath the fins. The equivalent electrical circuit diagram underneath the micrograph shows the on chip filtering and the array layout. The junctions are arranged in 20 parallel arrays of 33 series junctions each. The total device resistance is $40\text{ k}\Omega$. The right side shows a 3D rendering of islands and junctions. The layout of the Au cooling fins are attached on top of the Al islands. The junction material Al_2O_3 separates the islands. Figure redrawn from [2].

The CBT shown in figure 2.3.1 has a design optimised for sub 10 mK operation. This includes an on-chip distributed RC filter, and a large cooling fin volume ($\approx 5 \times 205 \times 40\ \mu\text{m}^3$). The large fin volume, Ω is to maximise the electron-phonon (EP) coupling, equation 2.3.1.

The aluminium islands are prevented from becoming superconducting by a small applied magnetic field above the critical field from a small permanent neodymium magnet mounted in the holder.

The fins are made from gold because of the large coefficient Σ . The electron phonon scattering rate for gold has been previously

measured [34] to be $\Sigma_{\text{Au}} = 2.4 \times 10^9 \text{ WK}^{-5} \text{ m}^{-3}$. For comparison copper has $\Sigma_{\text{Cu}} = 2.1(2) \times 10^9 \text{ WK}^{-5} \text{ m}^{-3}$ [31]. There is also some additional EP coupling from the aluminium volume before and after the junction, resulting in a sum of total coupling between the electrons and different volumes with different coupling coefficient, leading to some effective coupling $\Sigma_{\text{eff}} \Omega_{\text{eff}}$,

$$\dot{Q}_{\text{ep}} = \sum_{\text{volumes}} \Sigma_V \Omega_V (T_e^5 - T_p^5) \quad (2.3.2)$$

$$= \Sigma_{\text{eff}} \Omega_{\text{eff}} (T_e^5 - T_p^5). \quad (2.3.3)$$

The 3D rendered cross-sectional schematic shows the location of the Al_2O_3 tunnel junction between Al islands and that two large Au thermalisation blocks, ‘fins’, connect to each of the Al islands. The islands are about $45 \mu\text{m}$ across, and $300 \mu\text{m}$ long.

MEASUREMENTS

Electrical Connections and Acquiring the Differential Resistance

The CBT is electrically connected using four wires, in a Kelvin style arrangement: one twisted pair of leads carry the measurement current, and another twisted pair carry the voltage signal. The current is set by a voltage controlled current source inside an Aivon PA10 amplifier. This amplifier sums both an AC and DC voltage to create a current with an offset bias, I_{DC} , and excitation I_{AC} .

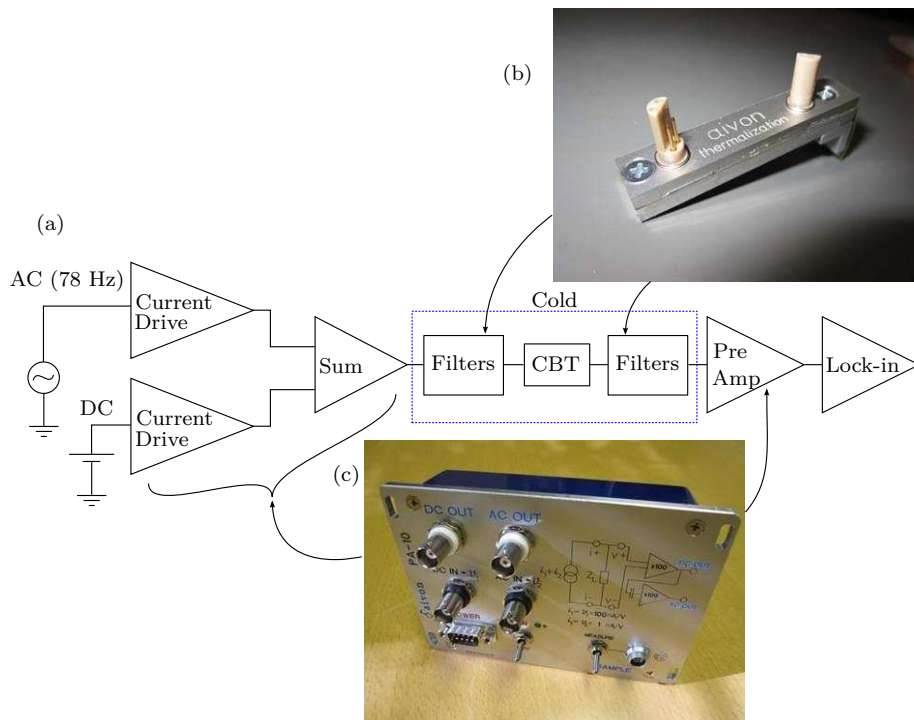


Figure 2.4.1: (a) A block diagram of the measurement of the CBT. Two signals, AC and DC are summed together, this is then used to drive current through the CBT. The measurements are made using a lock-in amplifier synchronised to the AC driving frequency. (b) The low temperature filtering is provided by Aivon as well as the summing and current drive electronics (c).

Figure 2.4.1 shows a measurement block diagram. The PA10 also includes a pre-amplifier that is used before connecting to a lock-in amplifier. The lock-in amplifier measures the V_{AC} at the driving

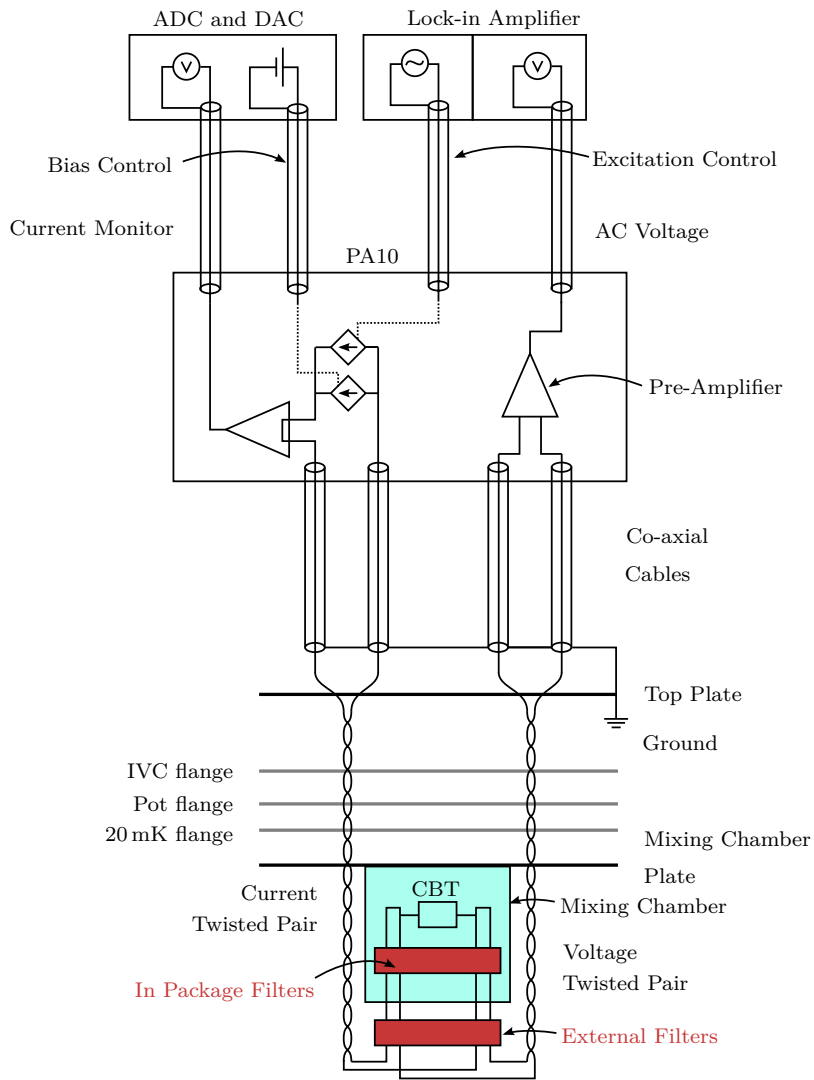


Figure 2.4.2: A wiring diagram showing the four point connection to the CBT using the PA10, Lockin Amplifier, filters, and a DAC/ADC.

frequency, typically between the 50 Hz mains electrical frequency and the 100 Hz overtone. This configuration is used to measure the differential resistance $R = V_{AC}/I_{AC}$ at some offset bias. The AC signal is generated using the lock-in internal oscillator which outputs an AC voltage, as we know the current drive amplifier gain in nA mV^{-1} we can convert the set voltage amplitude to know the AC current amplitude at the device. Figure 2.4.3 shows a sketch of a differential resistance measurement, measuring the resistance using a small excitation at a bias. The lock-in amplifiers used in the early work was a Stanford Research Systems Model SR830 DSP Lock-In Amplifier and then, for the later work we transitioned to using a Signal Recovery Model 7265 Dual Phase DSP Lock-in Amplifier. The change of equipment is because of the improved noise and precision of low amplitude AC voltage output from the Signal Recovery.

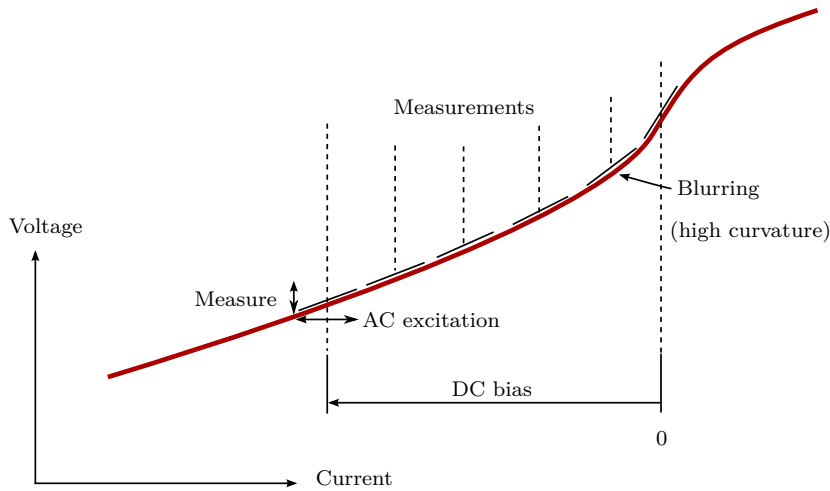


Figure 2.4.3: A sketch of a differential resistance curve being measured using a DC current component added to an AC excitation current. The differential resistance is calculated by $R = V_{\text{Lock-in}}/I_{AC}$. The depicted AC excitation range is shown expanded for clarity.

There are a few different approaches to measuring the temperature from the I_V curve of the CBT, these are called modes. Primary mode is a full measurement of the differential resistance curve using a span of I_{DC} that covers the full Coulomb blockade peak. Secondary mode is a single measurement of the maximum resistance at zero bias, and

there is a pseudo-secondary mode that uses small sweeps over the top of the peak to measure both the maximum resistance and, if there is any, track the current bias offset of the peak.

Primary Mode

The full shape of the differential resistance curve can be acquired by incrementally changing the bias current and measuring the differential resistance at that bias. At each step computer control is used to set a DAC to feed a DC current control voltage into the PA10 drive box. The AC voltage source for the current drive comes from a controllable sinusoidal output of the lock in amplifier. By using the lock-in amplifier internal oscillator as the source, the measured voltage signal is already synchronised. The PA10 enables measurements of V_{DC} , the DC component of voltage across the CBT. The V_{DC} is measured using an ADC along with the V_{AC} measured by the magnitude of the signal from the lock in amplifier.

Both the data of V_{DC} and $V_{Lock-in}/I_{AC}$ have noise. Noise of V_{DC} was reduced by averaging many samples. To reduce noise in $V_{Lock-in}$ we tried two methods. One method used a shorter time constant and taking a few samples and averaging in the computer, verses another method which uses a longer time constant on the lock-in amplifier with a single sample. This latter sampling method that entrusts the lock-in amplifier to provide the lowest noise, had better results. We wait 4 intervals of the chosen time constant to enable the measurement to settle.

The excitation current exists over a small, but finite, range of currents. This means that the resistance measured at a DC current is actually the average resistance over the range $I_{DC} \pm I_{AC}$. If I_{AC} is small then we can approximate to point-like samples. The effect can be accounted for during fitting, the fitting routine uses a polynomial

approximation of the curve sampled with a known excitation amplitude that is provided during the curve fitting routine.

The data set of I_{DC} and R is fitted using the gratis, libre, and open-source software py-CBT written by Aivon Oy [35]. This implements the conductance calculations [4], equations 2.2.2 and a single electron tunnelling model. During the collaboration with Aivon Oy, py-CBT was improved by its authors to include the electron-phonon thermal model, and the excitation smearing.

With py-CBT, we can measure the temperature from a single data set of differential conductances over the peak. This includes fitting equation 2.2.2 for both the free parameters R_T , and C_Σ , as well as a bias offset current that accounts for a bias shift from unbalanced thermo-voltages in the DC lines. To better self calibrate the CBTs physical characteristics, of R_T and C_Σ , py-CBT has a multi-fit routine which uses data from multiple different sweeps acquired at different isothermal temperatures to simultaneously optimise the parameters. The parameters from the multi-fits are then used for subsequent primary and secondary mode measurements of T_e . Finding these physical characteristics is called the self-calibration process.

For the low temperature primary mode measurements, R_T and C_Σ are not free parameters, as they are known. But the fitting routine needs to know the amplitude of the current excitation and the phonon temperature. We assume that the phonon temperature is the same as the mixing chamber temperature, which is provided by vibrating wire resonator.

With the CBT self-calibrated from multi-sweep fits we can use the CBT for secondary mode measurements.

Secondary Mode

Secondary mode measurements are when I_{DC} is set to zero and only the point of maximum Coulomb blockade peak is used to find the temperature. In principle a single measurement of the device is needed to acquire the electron temperature. As only one point is needed, these measurements are much quicker at yielding T_e than recording full bias sweeps which may require several tens of data points.

As this is quicker, secondary mode measurements reduce the duration of observation, and are a more suitable approach if, for example, the CBT is experiencing a change of temperature. If the CBT is changing temperature by a significant fraction during the time it takes to make one full primary mode bias sweep, the apparent sampled peak will be asymmetric, a result of a complicated mix of different peaks. In this case we are unable to use an isothermal phonon temperature approximation during curve fitting.

With R_T and C_Σ of the CBT known from self-calibration, we can derive the values of E_C , and G_T . In practice equation 2.2.6 is used to create a large look-up table that is used to map R to T with smooth interpolation. This enables the device to be used as a practical thermometer in real time as measurements are being acquired.

Pseudo Secondary Mode

Secondary mode measurements take one data point per measurement, this is at zero bias, and relies on the assumptions that the peak is centred and does not get affected by shifts in the effective device bias. This approximation can fail if there are thermo-electric effects, creating some DC offset between the top plate where equipment sets the current, to the bottom of the cryogenic stack, about 300 K cooler. A technical distinction to make is that the peak is centred at zero bias, so this

offset we are compensating against is an error from the inability of the room temperature equipment to precisely set a DC voltage at the device. This means that in order to know where zero bias is, or equivalently, what offset is needed to set zero, we need to have a method of finding the centre of the peak. This is not a problem with primary mode measurements, as the peak centre can be simply a free parameter during fitting. For true secondary mode operation we need to acquire this additional information from the device. One way is to take a small mini-sweep over the peak: just varying the DC bias by a small amount so that the data sweep has some small amount of curvature to it. The curvature has some centre that is the DC bias offset. For the lowest temperature measurements we need to keep the mini-sweep bias small as so to not introduce too much ohmic heating.

Each of these mini-sweeps is numerically fitted to find the new centre, and can be used to measure the peak height, this is the maximum of a smooth curve fitted to the sweep. This is not just the maximum value measured, which would introduce a strong selection bias. With knowledge about the bias offset, the next mini-sweep can be sampled covering a span to more appropriately cover the centre of the peak. The sequence of measure, fit, modify, makes up an online algorithm for tracking and measuring the electron temperature.

The trade-off between sampling a single point repeatedly, for more temperature measurements, and sampling the mini-sweep, for one temperature and centre measurement, seems to favour the mini-sweep. Each of the measurements, m , that make up one of the mini-sweeps has the same noise as the equivalent secondary mode measurement. When the numerical fitting is done, the height from the fitting has approximately $1/m$ less noise, similar to averaging many single points, but with the addition of measuring the centre as well.

To fit these mini-sweeps we could use the full peak shape, equation 2.2.2, but this would be ill fitted and poorly defined due to the lack of

measurements at the tails. This could lead to poor physical estimations. A fitting with equation 2.2.3 ($g(x)$) would have the correct shape but without the physical constants for the device included. As the results of fitting only use the two parameters, for the centre and the height, this would be reasonable approximation.

However for use in automation, there is a better and more robust method. Numerical fitting of an arbitrary function is often implemented through some iterative minimisation algorithm. These have an unknown completion time, and to prevent the Halting Problem [36] the algorithms often implement a `max_iterations` or equivalent “Sentinel value” to stop fitting if there is some problem [37]. As the mini-sweeps are very close to the top, they only have one curve in the data that covers the top of the peak, and not three curvatures from the top and the two wings. Fitting a single curvature with a simpler quadratic polynomial is possible. Polynomial fitting methods typically follow a Gaussian Elimination as part of polynomial regression [38], which has guaranteed completion in $O(mn^2)$ (a worst case of mn^2 iterations) for polynomial order n , and m data points. This guaranteed completion in a much faster time is very useful for online measurement algorithms. Using the results of a quadratic fitting of the differential resistance $R \rightarrow y$, and $I_{DC} \rightarrow x$. The function $y = ax^2 + bx + c$, has the centre at $x_c = -b/2a$, and a maximum value of

$$y_{\max} = y|_{x=x_c} = \frac{-b^2}{4a} + c. \quad (2.4.1)$$

To add additional robustness, we also need to acknowledge situations where the mini-sweep data is not sufficiently covering the peak, and in if poorly initialised, may be measuring a region of the peak where the peak curvature is positive. Figure 2.4.4 shows this situation in red.

We can handle the poorly initialised situation as well as include some arbitrary limits, ΔX_{\max} , on how far the algorithm is allowed to modify the current guess of the centre, x_c^{current} from the result of the fit x_c^{fit} .

$$x_c^{\text{next}} = x_c^{\text{current}} - \text{sign}(a) \max(\min(x_c^{\text{fit}} - x_c^{\text{current}}, \Delta X_{\max}) - \Delta X_{\max})$$

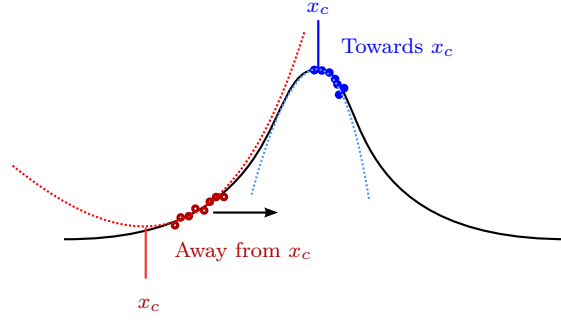


Figure 2.4.4: After fitting, if the data was close to the peak, then the leading quadratic term, a is negative, and results for peak maximum and peak centre could be used. Future data should be taken closer to or around x_c . However in the case where $a > 0$, y_{\max} is not representative, and future data should be taken further away from x_c .

(2.4.2)

This method is an implementation of a hill-climbing algorithm [39].

Using the polynomial fitting and the hill-climbing algorithm doesn't have to mean that we are only relying on the polynomial fits to measure the peak height. Use of a full numerical fit using equation 2.2.3 post-acquisition is still preferable, and used, for physical correctness, but the difference is negligible.

Problems with this method may come up if the mini-sweeps measurement span is too broad and covers the 'wings' of the Coulomb blockade peak. This second curvature is not accountable for by a second order polynomial but, as the result is still symmetric, the centre x_c is still in the correct place. The method still tracks and acquires data over the correct centring of DC biases. This is also why the full data set is saved, and different fits are tested in post.

Fitting the mini-sweeps post acquisition, we use the $g(v)$ equation (equation 2.2.3) re-parameterised with a free parameter for the centre. This retains a physically correct shape,

$$y(x) = 6h \frac{x' \sinh(x') - 4 \sinh^2(x'/2)}{8 \sinh^4(x'/2)} + c, \quad (2.4.3)$$

where

$$x' = 2 \times 2.71958 \times (x - o)/w. \quad (2.4.4)$$

The value of h is the height of the peak from the background c , o is the voltage offset, and w is the Full-Width-at-Half-Maximum, FWHM. This differs from equation 2.2.3 by the prefactor of 6 because

$$\lim_{x \rightarrow 0} \frac{x \sinh(x) - 4 \sinh^2(x/2)}{8 \sinh^4(x/2)} = 1/6. \quad (2.4.5)$$

The factor of 2.71958 changes the width to be parameterised by the FWHM. The only goal of secondary mode is to acquire G_0 , fitting 2.4.3 we can get $G_0 = 1/(h + c)$.

A Taylor series expansion of $g(x)$ at zero further explains why using a quadratic fitting is successful as a first approximation to the peak because,

$$g(x) \approx \frac{1}{6} + \frac{x^2}{60} + \frac{x^4}{1008} + \frac{x^6}{21600} + \frac{x^8}{532224} + \dots \quad (2.4.6)$$

is dominated by the x^2 term, and the higher order terms have rapidly increasing denominators.

Width and Excitation Settings

Operating the CBT in the pseudo-secondary mode with tracking takes sufficient care of the DC bias settings. To accomplish a full unattended operation the choice of excitation amplitude, the lock-in time constant (to compensate for lower excitation amplitudes), and the span of the mini-sweep needs to be also controlled algorithm. These three extra settings need to have knowledge of T from G_0 , and at the time of our measurements, this was not finalised. However, future work could include these for automation. If T is known from the last sweep, then the next measurement span should be

$$V_{\text{span}} = K \cdot 5.5NkBT/2, \quad (2.4.7)$$

with some factor K that determines the fraction of the peak that to be scanned. This is a a scaling of the equation for $V_{1/2}$, equation 2.2.1. The introduction of K is user specified chosen factor, typically small, for example 0.2, that used to represent only the top of the peak. k needs to be large enough so there is some small measurable curvature left that would be enough for the online fitting to correctly acquire the peak centre, an example shown in figure 2.4.5. One could also scale the span of measurements by setting a target ratio of the measurement noise to visible curvature.

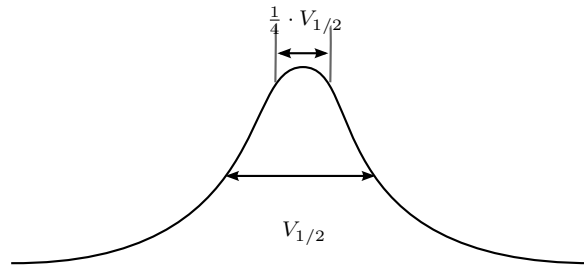


Figure 2.4.5: Picking a small fraction of the peak width automatically by some fraction of $V_{1/2}$ using the temperature of the device and equation 2.2.1.

The excitation required during measurement and the required averaging time could also be be approximated numerically.

Software was written to automate the data acquisition using each of the modes above. There are a few extra best-practices that were followed during data acquisition. The current bias can be ‘parked’ at zero when not acquiring data, this removes an unnecessary source of heat flowing into the device. Changes of the bias current should not make large step-like jumps, as this causes high frequency transients to travel to the device, so instead the bias should be ramped between changes.

Vibrating Wire Resonator and Other Thermometry

A Vibrating Wire Resonator, VWR, can be any section of free-to-move wire that oscillates when excited by current in the presence of a magnetic field. The motion of the wire directly probes the medium around the wire. VWR devices have been used to measure the viscosity of helium-3 [40, 41], and are well suited to sensitive measurements of the saturated dilute phase helium in mixing chambers [42, 43].

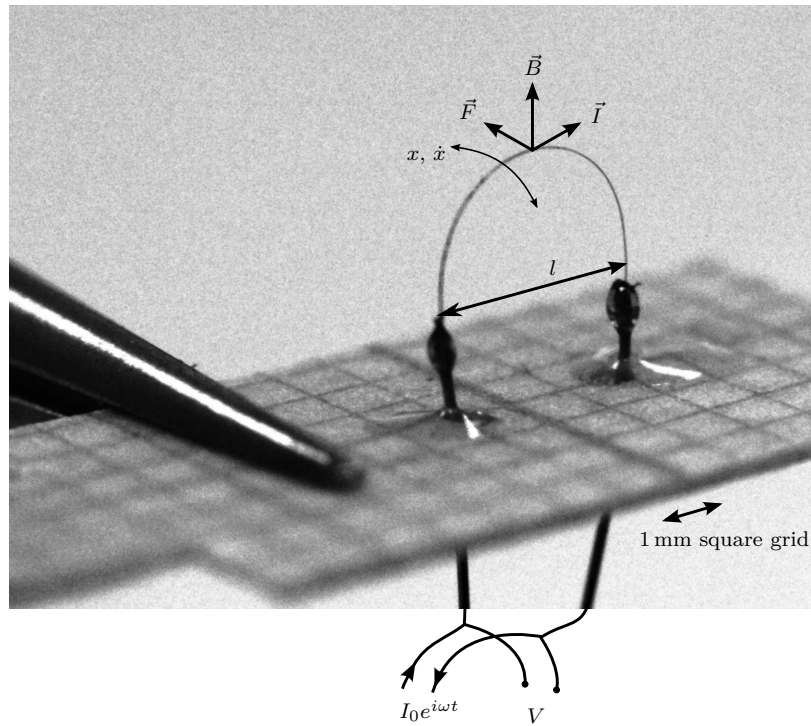


Figure 2.4.6: A macro photograph of a half-loop vibrating wire resonator built at Lancaster [44], equivalent fabrication and design as the VWR in the mixing chamber. Current in the wire produces a force perpendicular to the current and the magnetic field. Induced voltage is measured across the device.

The VWR that was used alongside the CBT, is a semicircular loop of superconducting tantalum wire, with the ends of the loop fixed to a base plate using a two part epoxy resin Stycast-1266 [45]. A similar VWR is shown in figure 2.4.6. When current is applied, the wire moves creating a voltage across the ends. Current is driven using a signal generator through a current drive resistor and an audio transformer

for isolation. The induced voltage is measured with a lock-in amplifier synchronised to the driving frequency. Measurements of induced voltage over a range of frequencies has a modified¹ Lorentz shape [46]. The width of resonance is affected by the viscosity of the medium around the wire. Figure 2.4.7 shows the measurement circuit and electrical connection.

The temperature in the mixing chamber of the dilution refrigerator is measured by a vibrating wire resonator that is probing the well known viscosity of the saturated dilute phase of helium-3 in helium-4 [42, 47].

The calculation for the resonance width is a solution based on Stoke’s hydrodynamic theory [40]. The resonance width is given by [48],

$$\Delta f_2 = f_0 \frac{\rho}{\rho_{\text{wire}}} k' \left(1 - 1.14 \frac{\rho}{\rho_{\text{wire}}} k \right). \quad (2.4.8)$$

The equations were written into specialised VWR software [49], which generates resonant width and frequency shift as a function of temperature for a wire with different sizes and density. The width to temperature conversion is then generalised with a fourth order polynomial in log-log space for smooth interpolation. The generated curve that maps the resonance width to temperature is included in the appendix, figure A.0.1.

The measurements of temperature from the VWR are automated by a computer controlling the signal generator and the lock-in amplifier. We sweep a frequency range that covers the resonance of the VWR and measure the response, and on-line curve fitting fits the expected response and selects an appropriate frequency range for the next measurements. The amplitude of the current is selected to target a set resonance height, usually 10 μV .

To compare the temperature of the mixing chamber measured using the VWR to an externally calibrated temperature scale we use a commercial thermometry resistor. This is a ruthenium oxide, RuO_2 , cal-

¹ A Lorentz peak describes the amplitude of the position, however the voltage is proportional to the velocity.

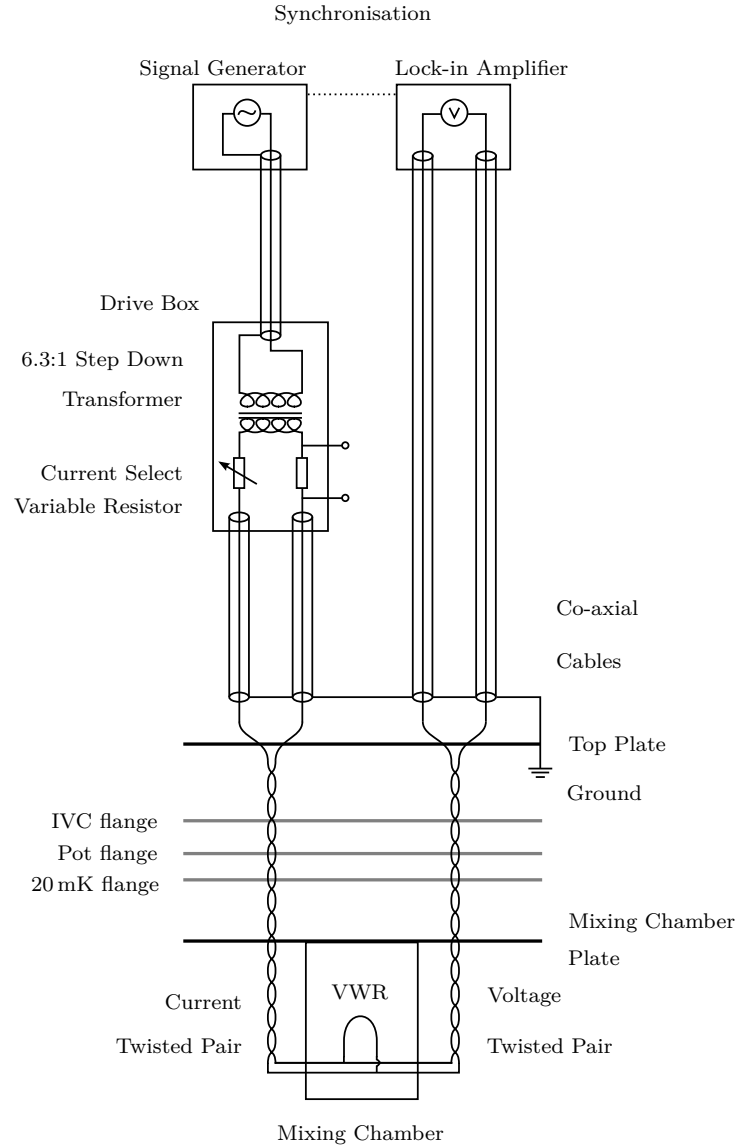


Figure 2.4.7: The electrical connections for measuring the vibrating wire resonator. The Current Select variable resistor is a choice of $100\ \Omega$, $1\ \text{k}\Omega$, $100\ \text{k}\Omega$, $1\ \text{M}\Omega$. A fixed inline $100\ \Omega$ resistor can be probed to check the current. Coaxial cables shield the connections outside the fridge, and twisted pairs reduce electromagnetic interference and cross talk.

ibrated resistor, model RX-102B [50]. This resistor has a temperature calibration between 30 K to 20 mK, and behaves monotonically above 10 mK. This is measured with a 4-point connection to a Lakeshore model 370 AC resistance bridge. The measurement power in the RuO₂ resistor was checked for self heating effects and we are operating far from the self heating limit. This was tested by incrementally increasing the measurement power until self heating is seen. The results are included in the figure 2.4.8.

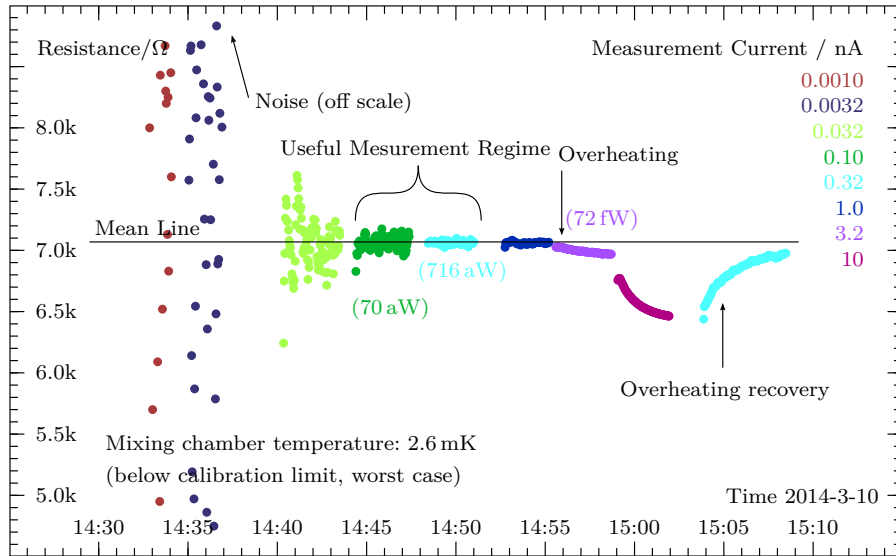


Figure 2.4.8: The RuO₂ calibrated resistor is measured with different measurement currents, while as cold as possible. This is the worst case scenario and any self-heating seen here would only be reduced at higher temperatures. While possible to measure with even lower power, the noise increase is too large to be useful. Each colour here represents an order of magnitude more power from 7.1 zW (10^{-21}) to 710 fW.

A tuning fork in the mixing chamber probes the fluid alongside the VWR. The resonance width of the tuning fork changes with temperature and we can use the temperature scale from the vibrating wire resonator to calibrate the tuning fork as a secondary thermometer [51]. When the magnetic field changes, we can still use the capacitively driven, magnetic field independent, tuning fork. This tuning fork was

only used in the first experimental run, when the CBT was mounted outside the mixing chamber.

EXPERIMENTAL DETAIL

Previous experimental work has been performed in a commercial BluFors dry cryo-free dilution refrigerator, BF-LD250 [8], which has a base temperature of 7 mK. In the work reported here we use one of our custom dilution refrigerators [6] with a base operational temperature of about 2.5 mK to extend the tested range of the device and to challenge the thermalisation capabilities of the CBT and the additional components that are used to measure it. Dilution refrigerators use pure helium-3 dissolving across a phase boundary into a saturated helium-3 and helium-4 mixture, this process absorbs entropy from the surroundings. For general details on ULT techniques and dilution refrigerators in particular, see reference [52].

The first work on the 2.5 mK refrigerator mounted the CBT suspended underneath the mixing chamber alongside an Aivon filter and thermalisation box, the mounting is shown in figure 2.5.1. Next to the CBT is a RuO₂ resistor. Further down the cold finger are some SPEERs resistors. The temperature in the mixing chamber was measured using a tuning fork, and two vibrating wire resonator (VWR) thermometers. The primary VWR is higher up in the saturated dilute phase of helium as it exits the mixing chamber. The secondary VWR was mounted on the cone at the base of the mixing chamber. Each VWR has its own independent solenoid providing a small magnetic field to each wire. This experimental run was useful to see the CBT's thermalisation time (section 2.6.4) and to check the measurement excitation dependence and the device self consistency (sections 2.6.2 and 2.6.1).

The CBT has its own small permanent neodymium rare earth magnet that provides enough magnetic field to prevent the aluminium in the CBT from becoming superconducting. The magnet is mounted into a matching recess in the CBT case below the chip. GE varnish [53] and vacuum-grease were used to help thermalise the magnet to the case.

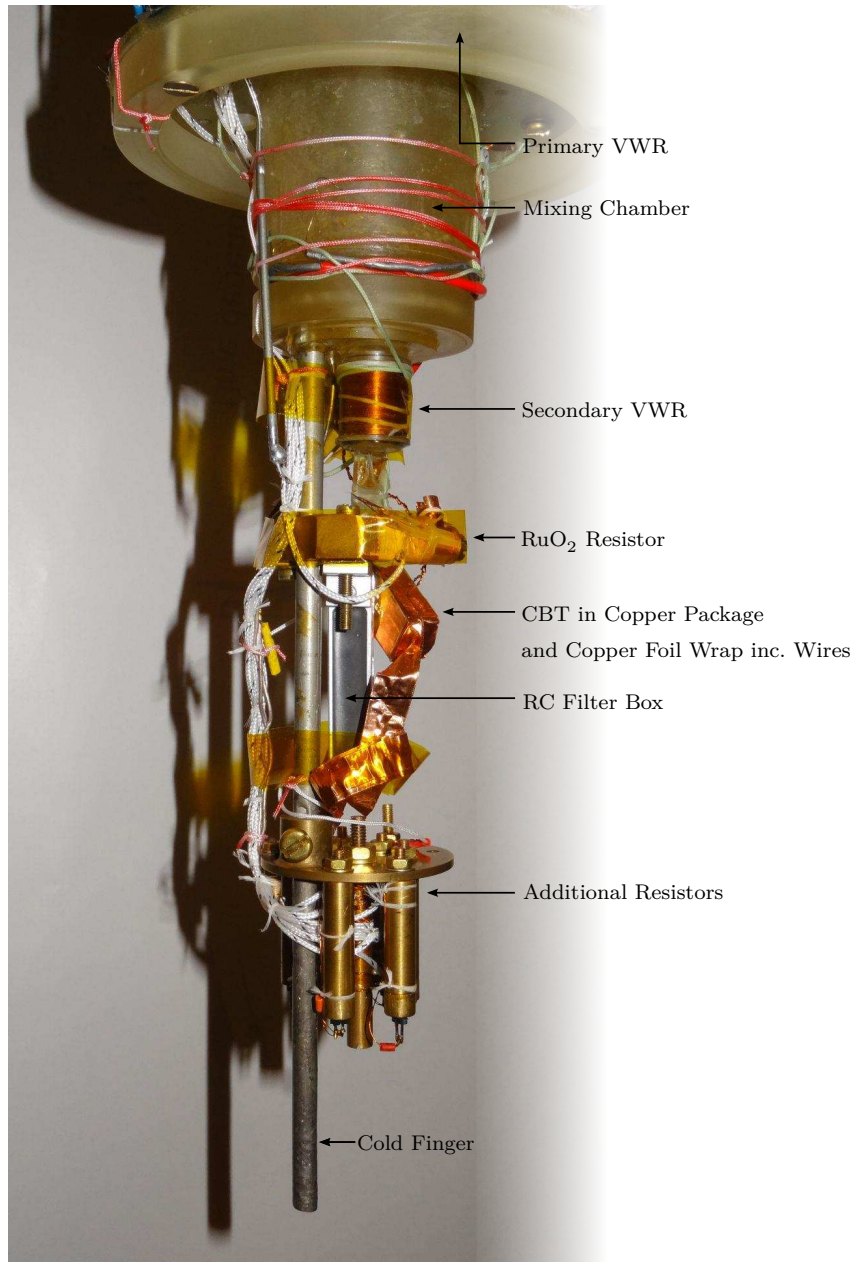


Figure 2.5.1: The CBT is mounted outside the mixing chamber. A cold finger cooled by a silver sinter pad immersed in the fluid in the mixing chamber extends from a detachable plastic cone. The CBT and the RC filters are bolted to the cold finger, using pressure to make thermal contact to the cold finger. The addition of copper tape is providing additional shielding to the CBT and the four wires between the filters and the CBT case.

The first experimental run showed a very long thermalisation time for the electrons in the device, with T_e taking more than 70 hours to come to equilibrium, as will be discussed in section 2.6.4. So in a best effort approach we designed and built an experimental cell to be immersed into the liquid refrigerant inside the mixing chamber. This would bring the device much closer to the cold source. Figure 2.5.2 shows a schematic of the CBT inside the mixing chamber, the same filters that were used before are mounted just outside, and we use the same RuO₂ resistor to measure the filter temperatures.

While the CBT is immersed inside the fluid we can use low temperature sintering techniques to improve the coupling of the device to the liquid temperature. We create individual sinters for each of the four measurement lines of the CBT, and one for electrical ground. These sinters are a comparatively huge volume, many orders of magnitude bigger than what is possible with nanofabrication techniques, to get electron phonon coupling to cool the electrons in the lines. Each of the five sintered lines - the four for measurement and one ground - are silver powder sinter on annealed silver sheets and silver lines that feed through the base of the mixing chamber to additionally provide cooling and connect to the Aivon filter/thermalisation box. Figure 2.5.3 shows a photograph showing the mixing chamber immersion cell.

Electrical shielding is provided in part by the inner vacuum can, and two radiation shields. The outer metallic dewar surrounding the refrigeration system acts as a Faraday cage. The twisted wires used inside the dilution refrigerator are part of a loom and are surrounded on both sides by grounded wires to further aid shielding. The room containing the measurement electronics and the dilution refrigerator is shielded to reduce electromagnetic radiation. Shielded coaxial cables are used to connect equipment.

The CBT is sensitive to electrical noise, which deposits heat into the islands and has a warming effect. As well as warming, any noise adds

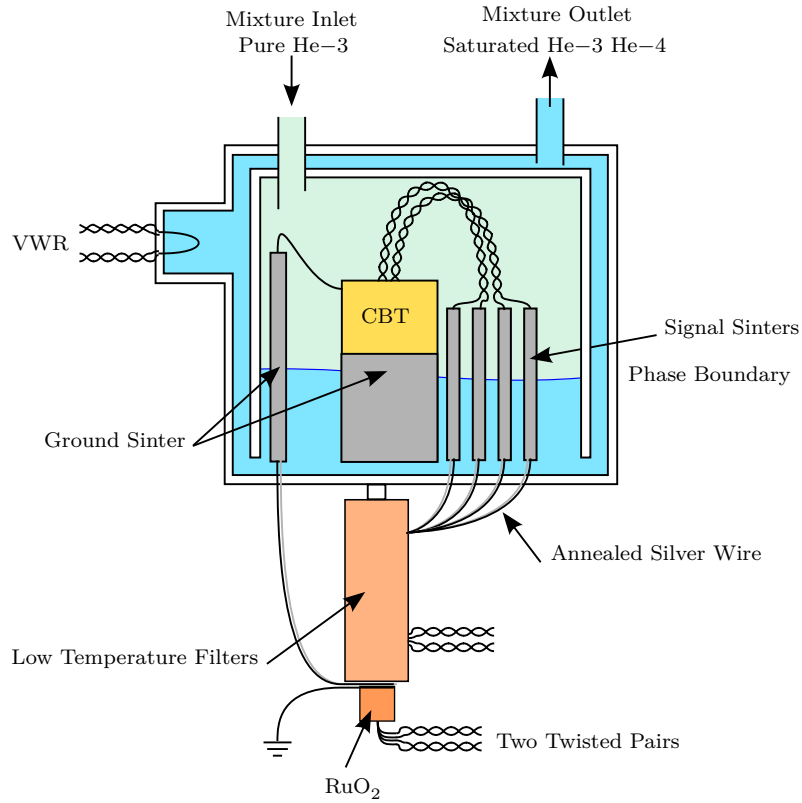


Figure 2.5.2: The CBT with a sintered holder immersed in the mixing chamber of a dilution refrigerator. The sinters are placed vertically at a height so that the phase boundary, the source of cooling, is in contact with the sinter. The electrical lines are all sintered and immersed in the cold liquid helium. The sinter have annealed silver lines that thermally connect to the low temperature RC filters, and to the RuO₂ calibrated resistor. Twisted pairs are used to reduce loop area to reduce magnetic field coupling. The signal lines are also thermalised further up at the 20 mK and at several places up to 4.2 K. In this diagram the components are not to scale.

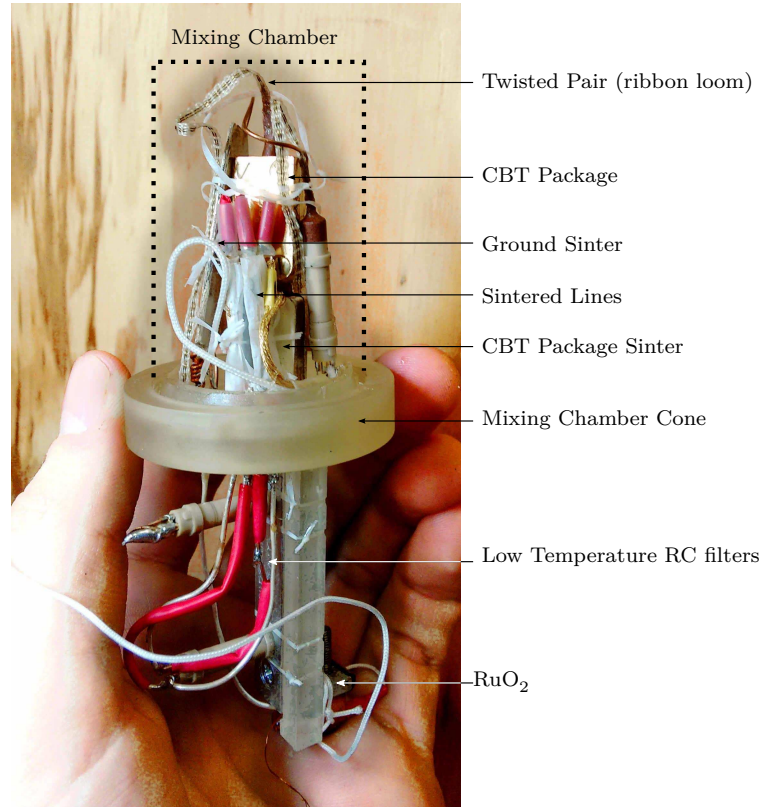


Figure 2.5.3: Mounting the CBT package onto a custom mixing chamber cone.

The sinters are wrapped in filter paper to provide electrical isolation while still being porous to the refrigerant. The silver wires to the low temperature filters have heat shrink on alternating lines, but are stiff enough (a 1.2 mm OD) to not move, this prevents electrical acoustic coupling. Loop area is reduced by using wiring loom and matched twisted pairs. Electrical ground is the large uncovered sinter at the back, a ground wire is wrapped around the CBT package and held in with screwed pressure. The RuO_2 is outside the mixing chambers, cooled by the ground sinter line, and the filter sinter lines.

to the effective I_{AC} . The noise can broaden the measured CBT peak even when the current due to noise is so small that it doesn't cause any significant heating. This is in the same way a large I_{AC} can broaden the measured CBT peak even when the CBT is cold.

Reduction of electrical noise, and filtering has noticeable effects. We were careful to remove un-needed ground loops, and added additional ground paths to reduce ground impedance where needed.

Sintering

The case of the immersed CBT is sintered to improve thermalisation while inside the helium-3 – helium-4 mixture. The thermal path from the device to the cold source is limited by the boundary resistance between the metal and the refrigerant. This is overcome using a physical structure known as a sinter, created from silver powder. The sinter is a large ensemble of grains of powdered metal that are then compressed under pressure, 20 kN cm^{-2} to 30 kN cm^{-2} , and heat, usually 180°C to 200°C , to form a porous sponge-like material with an extensive surface area. The large surface area overcomes the unavoidably weak coupling between metal and liquid.

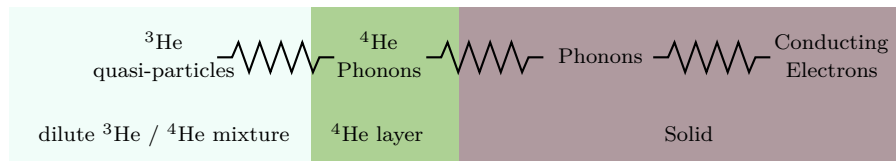


Figure 2.5.4: The Thermal path between cold helium mixture to the metal of the sinters. Image redrawn from [54].

In the mixing chamber, there is a thin monolayer of helium-4 that plates out over all surfaces because of a lower zero-point energy. This means the thermal path is from the mixture, to the monolayer, then to the metal. Inside the metal the thermal transport is dominated by the electrons, the thermal path is shown in figure 2.5.4.

Thermal transport between the liquid refrigerant and the solid of the metal is dominated by phonons passing from one material to the other. The acoustic mismatch of the phonon velocities in the two materials causes phonons at a high incident angle to be reflected, rather than transmitted. The macroscopic view of the boundary thermal resistance is described by the Kapitza resistance [54, 55] R_k ,

$$R_k = \frac{\Delta T}{\dot{Q}} = \frac{c}{AT^3} \quad (2.5.1)$$

which relates the heat flow, \dot{Q} , and the temperature difference, ΔT , to the area a and a natural material constant c . The prediction of T^{-3} comes from Khalatnikov’s acoustic mismatch theory. At low temperatures experiments shows a much better thermalisation than T^{-3} with some reporting T^{-2} , and even T^{-1} . These are attributed to some new different vibration modes, the “soft-phonon” modes from the finite grain size of material, and a magnetic channel [56, 57].

Independent of the actual dependence, we can use still aim to maximise \dot{Q} ,

$$\dot{Q} = \frac{\Delta T AT^3}{c} = \frac{\Delta T}{R_k}, \quad (2.5.2)$$

by having a very large area, and a large material constant. The material is silver, because of the better thermal transport. This model does not take into account of the transport across the sinter, there is a practical upper limit to how large sinters should be, where thermal transport across the sinter becomes limiting, and volume limitations inside of a mixing chamber would reduce flow and could add viscous heating.

Sinters fabricated with silver nano-particles can have the surface area of a football field, as measured with the Brunauer–Emmett–Teller, BET, method [58, 59]. A rule of thumb suggests that sinters should have a mass-density of 50% of the pure material, which can be achieved with modifications to the pressure applied during the fabrication process.

The thickness of the sinter also matters. We aimed to get the thickness of sinter to approximately match the wavelength of the

phonons in the liquid [60, 61]. Although the silver has holes on the nano scale, with huge porosity, sinter performance is also dependent on macroscopic size of the sinter that shows a limiting factor in sinter performance.

It is thought that the dominant means to cool the electrons in the device is by the electrical connections and through the substrate. Hence each of the electrical connections are sintered, as well as the copper CBT holding package, as this is in intimate thermal contact with the substrate. For this reason, we worked with Aivon to acquire a empty CBT package without the CBT chip already installed. This empty holder was modified to use a sinter, and returned to Aivon to get the CBT installed. We designed a method to silver sinter onto the CBT case directly, as this is some of the closest bulk material to the chip, The improved cooling on the package improves thermal contact to the in-case filters, the on-chip filters, and cools the CBT through the chip substrate Si and SiOx.

The holder had a sheet of silver welded to the original mounting point. This silver sheet acts to hold together the sinter and to provide a better thermal path across the sinter. This should improve the thermal conductivity from the farthest parts of the sinter to the holder, shown in the top half of figure 2.5.5. In total about 4 grams of silver nanoparticles, of 99.99% (4N) purity, and 50 nm average particle size, were used to make the sinter.

The four electrical lines that measure the CBT are routed through silver sinter pads that have a large surface area in a flat rectangle geometry. This large face area and volume is to help the cooling. Each individual line sinter has 0.5 g of sinter on annealed silver lines, shown figure 2.5.6.

The CBT holder is made of low-oxygen copper and covered with gold plating. The plating was removed to eliminate an extra Kapitza

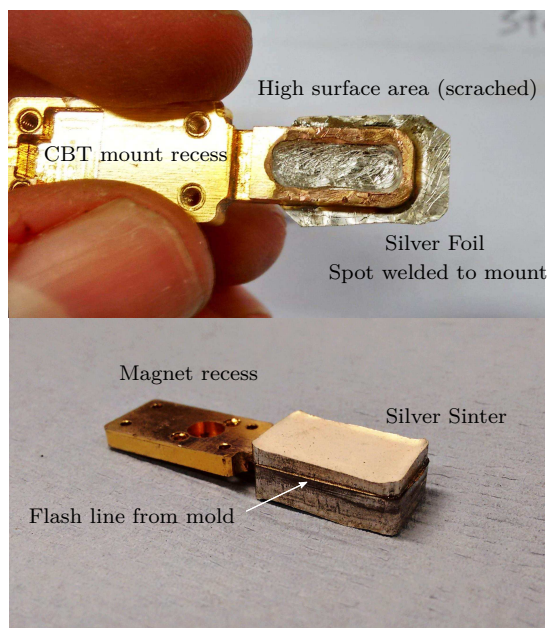


Figure 2.5.5: The CBT holder is modified to accept a block of sinter. The original mounting method was to bolt it to the mixing chamber plate using the hole (top picture) and would rely on pressure to get thermal contact. A patch of annealed silver sheet is spot-welded onto the original mounting point to improve the coupling to the copper of the holder and improve thermalisation across the width of the sinter. The copper is scratched to a rough finish, giving the sinter a stronger hold on the copper.



Figure 2.5.6: The line sinters made from compressed silver nanoparticles. Lines are made from annealed silver wire, to an RRR over 1000.

resistance, and surface roughness is added to improve sinter adhesion and sinter-copper area.

An improvement would be to add additional sinter on the package just underneath where the CBT is held. This shortens the physical thermalisation path across the length of the holder.

The benefits of using the sintering and locating the CBT inside the mixing chamber should increase the ability to thermalise the electrons in the islands, however the thermal path from the cold source to the electrons is complex with multiple heat paths. Figure 2.5.7 shows and some of the thermal connections between the cold source and the CBT islands.

Filtering and Noise

Reducing the electrical noise that reaches the CBT is important as it forms a source of very local heating at the junctions, and can broaden the peak by effectively increasing I_{AC} . All fluctuations in current at the CBT can cause ohmic heating, higher frequency noise can pass capacitively through the device.

A series of low pass filters are inline with the electrical leads to remove noise. These work as part of a multi stage filter. There are three low temperature filters before the CBT. The external filter/thermalisation box is first. This has a cut-off frequency of about 300 kHz. Inside the chip holder there is another filter, visible in figure 2.5.8. Having the filters physically located closer to the chip reduces area and wire length for noise to be introduced after them. Finally there is the distributed filter on chip, shown in figure 2.3.1 above, this is made of a meandering electrode between two grounded metal films, insulated with a dielectric of SiO_x (250 nm). The on chip filter is characterised with $R \approx 500 \Omega$ and $C \approx 10 \text{ pF}$. It has a cut-off frequency of 40 MHz. The filters have a low inline resistance to reduce Joule heating, which is especially

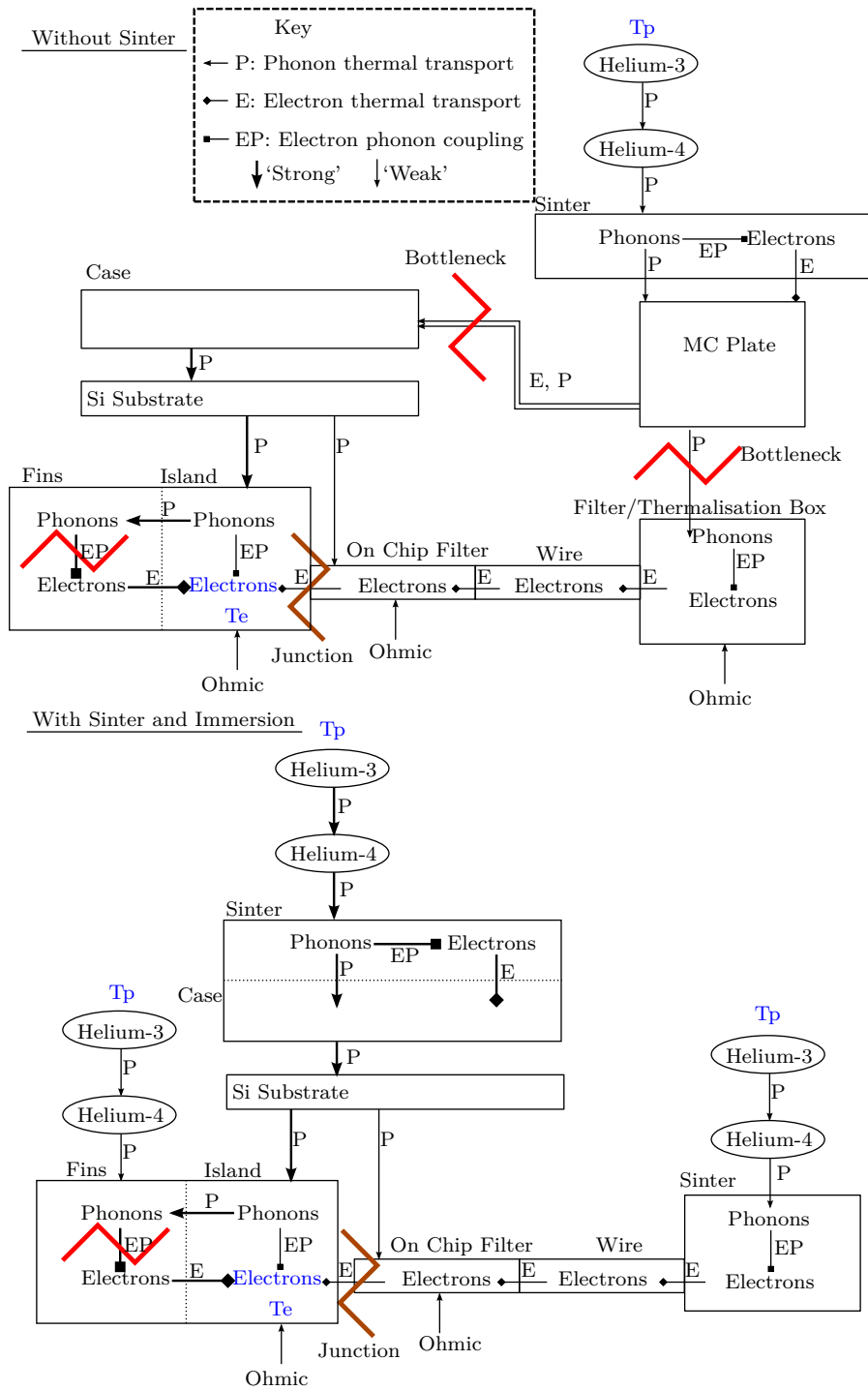


Figure 2.5.7: The expected dominant thermal paths from the cold source to the electrons in the islands.

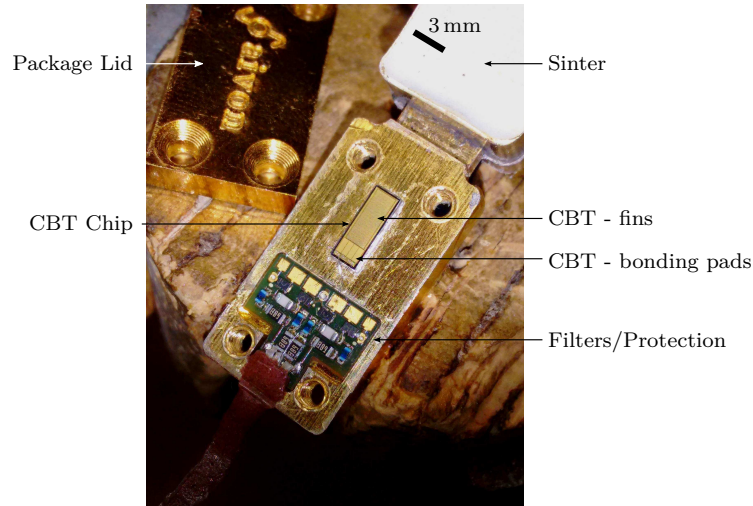


Figure 2.5.8: The CBT chip mounted in the sintered package. The chip is attached to the copper body through the back via electrodag conductive adhesive. The bonding pads go to some protection diodes and more filters. This package is designed by Aivon-Finland as a commercial product. The package lid closes over the wiring to form an electrical shield for the exposed bonding wires and filters.

important near the junctions of the device. The on chip filters provide a final stage of filtering right next to the device, which has been shown to help CBT temperature measurements [62]. On top of the chip and inside the chip holder a small amount of filtering epoxy is added. The epoxy is a magnetically loaded dissipative dielectric, and is commercially available under the trade name Eccosorb [63]. This can provide additional shielding and filtering above 5 MHz [64]. The EcoSorb works similarly to silver-epoxy, and copper-epoxy filters which have been used before to aid cooling of CBTs [65].

We do not use electrical models of the filters as the cut-off frequencies are very high compared to the AC excitation frequency, so we can assume all the current we apply goes through the device, and only a trivial amount of current is bypassing the chip through the filters.

EARLY MEASUREMENTS WITH THE CBT MOUNTED BELOW
THE MIXING CHAMBER

The results in this section are from an experimental run when the CBT is mounted below the mixing chamber, thermalised through silver lines and the filter-box as seen in figure 2.5.1. We look at how the physical characteristics of the device are self consistent and discover additional challenges with thermalisation time and excitation amplitude when measuring at low temperatures.

Self-consistent Properties

We check that the physical characteristics of the device island capacitance C_Σ and the tunnel junction resistance R_T remain constant over the range of temperatures measured, and that the measured electron temperature agrees with both the VWR thermometry and the RuO₂ thermometry. Any unaccounted for change in the physical parameters would suggest that the Coulomb blockade model used to describe the data would be insufficient and that there are other confounding physical processes.

The temperature of the mixing chamber is slowly increased from the base temperature by applying an increasing heat directly into the mixing chamber, keeping to a pseudo-isothermal approximation with each measurement. The change in one measurement is less than the uncertainty in temperature from the VWR, around 0.1 mK at 3 mK which scales to around 2 mK at 50 mK. We acquire data from the CBT between 5 mK and 100 mK. We also changed the amplitude of the I_{AC} excitation component of the applied current, as we suspected that I_{AC} effect the heating and potential broadening of the Coulomb blockade. We acquired data in primary mode, varying the bias to acquire data over the whole Coulomb blockade feature of the $dI/dV, V$ curve.

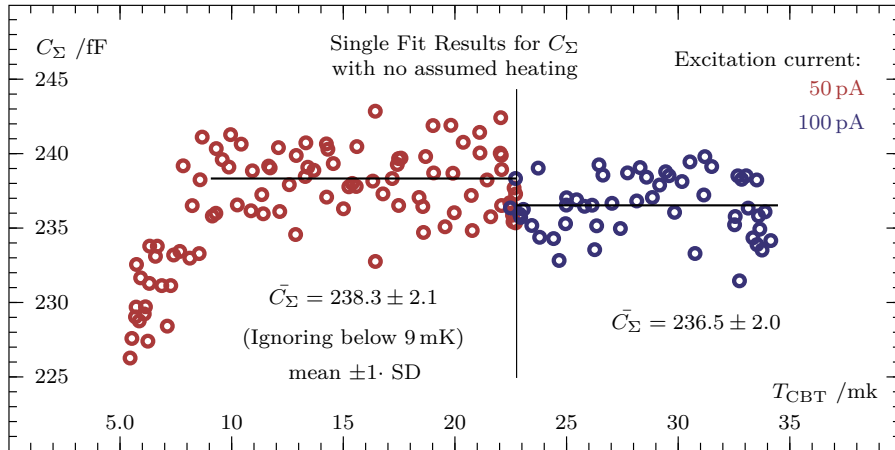


Figure 2.6.1: Using individual fittings for each data set the capacitance is nearly constant. There is a statistically significant, albeit small, change in the measured capacitance when changing the measuring current. The values quoted are the mean \pm one standard deviation.

Each data set of a completed bias sweep is analysed individually and is fitted to the equation 2.2.2 with the free parameters of R_T , C_Σ and T_e and a bias offset. We look at C_Σ and R_T separately, each a function of temperature.

Figure 2.6.1 shows the fitting parameter C_Σ of the total capacitance of the CBT. The step seen at about 22 mK is from a change in excitation. Thermal contraction, while able to change capacitance of devices, is incompatible with the changes in figure 2.6.1. It would be a continuous change, and is negligible below 60 K [66], an order of magnitude above our operating temperatures.

At low temperatures there is a trend away from a constant capacitance. This could be the measurement model of the CBT failing. It is not expected that the CBT to perfectly follow the mixing chamber temperature as the temperature reaches the low milli-kelvin range. However with overheated electrons, we would still expect the capacitance to remain constant. The low temperature analysis techniques are improved using a thermal model, taking into account

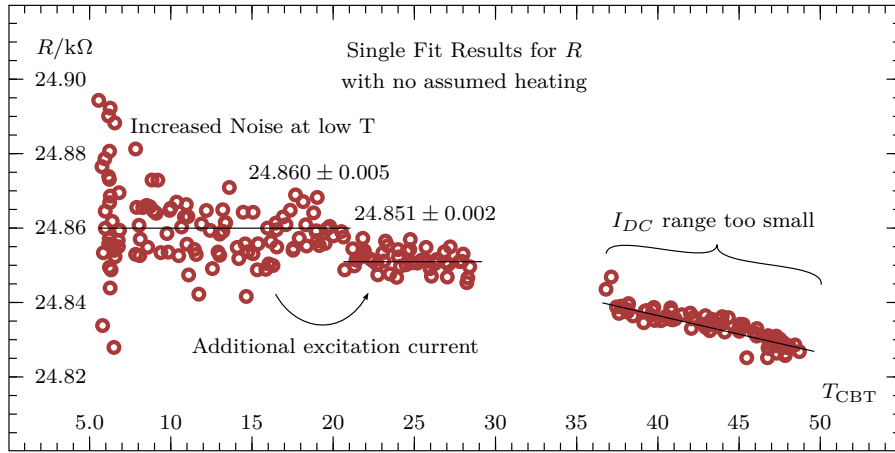


Figure 2.6.2: Fitting the physical parameter R_T for each junction from individual primary mode measurements.

that at low temperatures T_e is not equal to T_p and the excitation spread averaging over the sampling domain.

Looking at the tunnel resistances in figure 2.6.2 shows the same step at 22 mK and much more noise as T is low. The overall change in R is relatively small.

The apparent slope of the resistances above 36 mK is another measurement artefact. The span of I_{DC} remained constant and becomes too small compared to the width. The fit to the peak relies significantly on determination of the background, if the sweep is too narrow to get the background, then a poor fit results.

The asymptotic background resistance at high biases away from any Coulomb blockading is directly related to the parameter R_T and the number of junctions in series and parallel, $R = R_T \cdot n_{\text{series}}/n_{\text{parallel}}$. for example a typical value from figure 2.6.2 would suggest $24.86 \text{ k}\Omega \times 33/20 = 41.02 \text{ k}\Omega$ which agrees with the backgrounds seen in figure 2.6.3.

These measurement excitation changes are significant so we look at them in more detail.

Excitation Dependence

While the mixing chamber is at a stable base temperature of about 2.6 mK, we measure the differential resistance curves using different AC excitation amplitudes, and observe the effects on the peak. Figure 2.6.3 shows data from three different excitations. These range from an amplitude that is too large for the CBT at this temperature, 500 pA, down to an excitation that should be small enough to correctly resolve the peak, 5 pA. The large excitation has the effect of rounding off the top of the peak. If this amplitude of excitation would be used in a primary mode thermometry measurement, the results would be a reduced change in resistance, and would lead to incorrect temperatures. Additionally the curves measured with higher excitations are likely to have a higher electron temperature due to the additional ohmic heating from this higher current.

The offset in the DC bias position in figure 2.6.3 is a DC measurement artefact, and is the same for each measurement. The offset is presumably thermoelectric in origin.

Smearing of the peak due to a large excitation and overheating due to additional heating both have a similar effect, reducing the peak height, and a widening of the FWHM. We created a simulation to help explain partially why the excitation amplitude is causing such changes in the data, and to what extent, figure 2.6.4. The simulated data uses the $g(V)$ peak function, and is smeared according to an average of samples acquired around each point separated and weighted by a sinusoidal pattern. The largest amplitude excitation, 500 pA, does have a shape change due to the measurement excitation averaging over a significantly curved region, but the other two do not. The smearing effect alone is not enough to fully describe the discrepancy, so the discrepancy is likely due to a combination of this effect with the additional heating due to the measurement current.

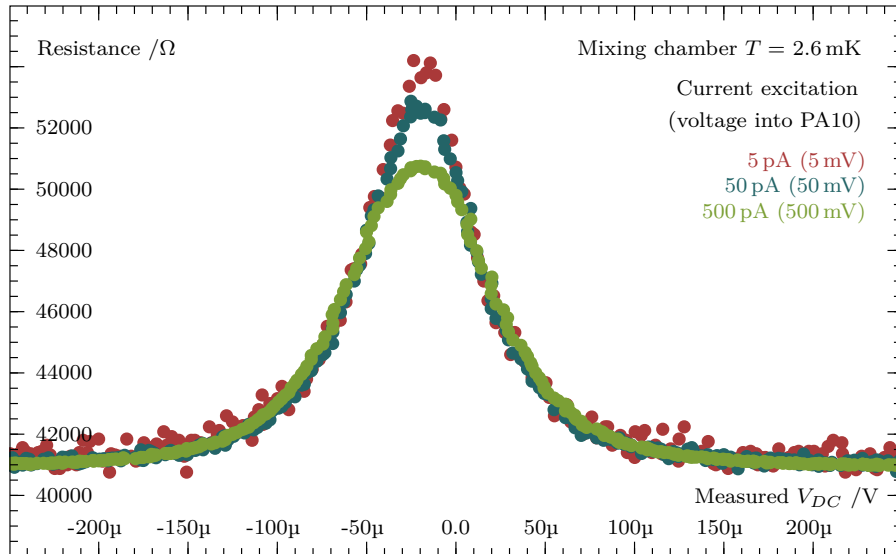


Figure 2.6.3: All three curves are acquired at the dilution refrigerator base operation temperature of 2.6(1) mK. Data acquired using the highest 500 pA excitation shows a much lower peak and is slightly wider at the FWHM. Using a lower excitation of 5 pA, is approaching the limit of the equipment, and shows a much taller peak. The noise increases significantly as the excitation drops. The 5 pA data, drawn in green, required 6 hours to measure, whereas the 500 pA data, drawn in green, was completed in 5 minutes. The peak is symmetric around a small offset current in all cases.

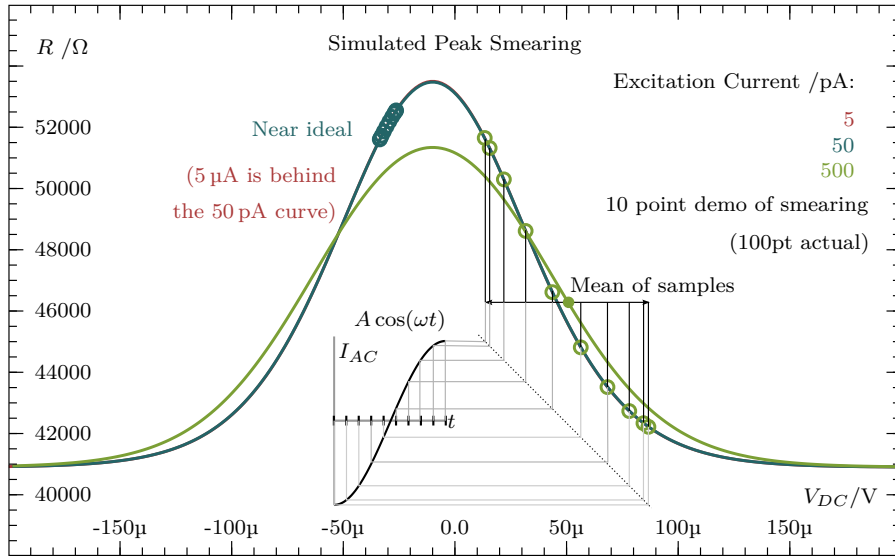


Figure 2.6.4: A simulation to match the curves in figure 2.6.3. Excitations are approximately to scale. Smearing is not enough to describe the difference between the 5 pA and the 50 pA, but does shows how the data with 500 pA excitation is shaped.

Our code for the demonstration of this smearing effect is included in appendix listing A.1. The implementation of fitting with a known smearing, as used in pyCBT, was written by its authors and is based on a polynomial approximation to excitation based averaging. We then fit using the improved fitting routines. The addition of the measurement base smearing does not add a free parameter to the measurement model or CBT model, as I_{AC} is known by choice at the time of acquisition.

The smaller excitation comes at the cost of additional noise in the measured resistance. The absolute noise from the lock-in amplifier has not changed, however now the noise is fractionally much larger compared to the signal, to result in more noise in R .

Setting the excitation amplitude is something that needs to change with different temperatures. Higher temperatures require a larger excitation to resolve the peak above the noise, as the peak is much smaller at higher temperatures. While lower temperatures require the excitation to be reduced so that it does not broaden the peak, and importantly to cause less ohmic heating. This means that the low

temperature measurements require more time to measure, as there is still noise, and with much less excitation the only resolution is to wait longer to average out this noise.

Temperature Measurement Comparisons

We analysed the CBT thermometry compared to the de facto VWR thermometry and the calibrated RuO₂ resistor. We swept the temperature of the mixing chamber slowly, to keep pseudo-isothermal conditions for any one measurement, in both directions as we measure the temperature from all devices. Each device is measured at a device appropriate rate. Figure 2.6.5 shows the temperature of the VWR (T_{VWR}) and RuO₂ (T_{RuO_2}) compared against the electron temperature in the CBT, T_{CBT} .

The different thermometers are measured individually at a rate suited to each device. To plot a comparison between each device we interpolate temperature data using time. The method used to produce figure 2.6.5 used binning of the faster thermometry data to the time aperture of the CBT measurement, which is the slowest. In a bin a linear fit is used to the temperature data during the CBT sweep and using the centre value chosen. This approach has minor technical merits as there is a small but measurable drift in temperature over the time aperture, but a mean-binning method would be as good as the difference between the interpolation methods is still dominated by random noise. Over the temperature range shown, the binning reduces noise, but the error bars are not plotted as the noise can be easily seen.

While using the RuO₂ standard as a fixed point at a temperature reasonably far away from the calibration limit of 20 mK, we made minor correction to the assumed wire thickness of the VWR, as this is the only parameter available to be adjusted. A change of the assumed wire diameter from 125 μm to 132.5 μm was made. which could be either

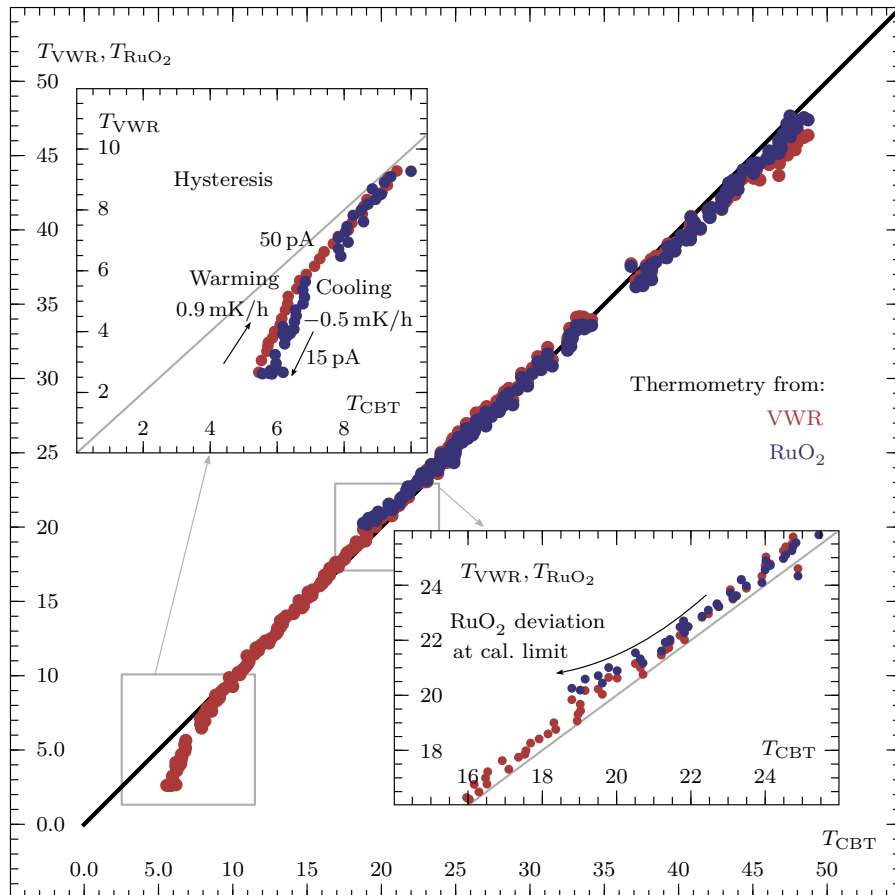


Figure 2.6.5: The temperature measured by the mixing chamber compared to the CBT and the RuO₂, for the CBT mounted in vacuum outside the mixing chamber. A 1:1 line is drawn to aid comparisons. All temperatures have units of mK.

a thin coating of oil or manufacturing tolerances of $\pm 10\%$ [67]. This thermometry curve is used and continues to agree with the CBT below the limit of the RuO₂.

The CBT agrees well with the other thermometers until it approaches sub 10 mK. But we can also note that it is not the same during cooling and during warming, subplot figure 2.6.5. It seems that after spending more time at the lower temperature it cools further, indicating that it is not fully thermalised, and the rate of temperature change of $0.5(1) \text{ mK h}^{-1}$ is too much. We look into the cooling time constant of the device to understand the thermalisation performance at low temperatures.

Cooling Time Constant

We lowered the temperature of mixing chamber from above 12 mK, towards the base operating temperature of approximately 2.6 mK. This state was maintained for several days. Figure 2.6.6 shows each of the thermometer's raw data measurements over time, in each case an increasing resistance or width means a lower temperature.

The CBT was operating in pseudo-secondary mode, only measuring differential resistance over the centre of the peak. The vibrating wire resonant width, which directly measures the helium temperature in the mixing chamber, responded very quickly with the mixing chamber reaching equilibrium in approximately 0.5(1) days of the heater being switched off. The RuO₂ saturated at some unknown temperature, after changing resistance non-monotonically and saturating outside its calibrated regime. The peak resistance of the CBT, inversely related to the temperature, continued to cool asymptotically approaching a value of $57 \text{ k}\Omega$.

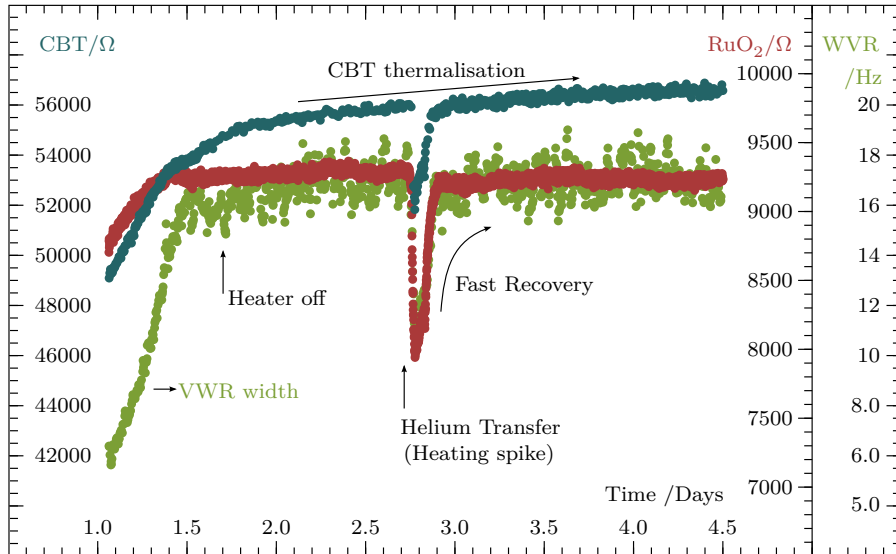


Figure 2.6.6: As the mixing chamber of the dilution refrigerator reaches its base temperature. The raw data from each thermometer (not yet converted to temperature) shows how each enters equilibrium. Each of the CBT data points is from pseudo-secondary sweeps. ± 2 pA DC range, 31 data points, waiting three times a five second time constant. The excitation was 5 mV.

We look to analyse further how the CBT thermalised by assuming a trend towards 57 k Ω and transforming the data to be $-1 \times (R_{\text{CBT}} - 57 \text{ k}\Omega)$. This is shown in figure 2.6.7 plotted with a logarithmic y-axes.

While waiting for the device to thermalise, the dilution refrigerator required cryogenic fluid transfers to continue operation. This involves adding liquid helium-4 to the bath, and liquid nitrogen to the dewar. The transfer creates a physical vibration and motion and temporarily increases the temperature. The transfer warmed the mixing chamber up above 3.5 mK, and this is seen on all the devices. A thermal recovery of the CBT after this shock was substantially quicker and did not reset the long term cooling trend. This means that the source of heat slowly coming out of the CBT, causing the long time constant, is almost disconnected from the system.

A suspect of heating is the small neodymium magnet mounted in the CBT case that keeps the aluminium non-superconducting, the complex structure of Nd₂Fe₁₄B alloy [68] could retain a lot of heat that is

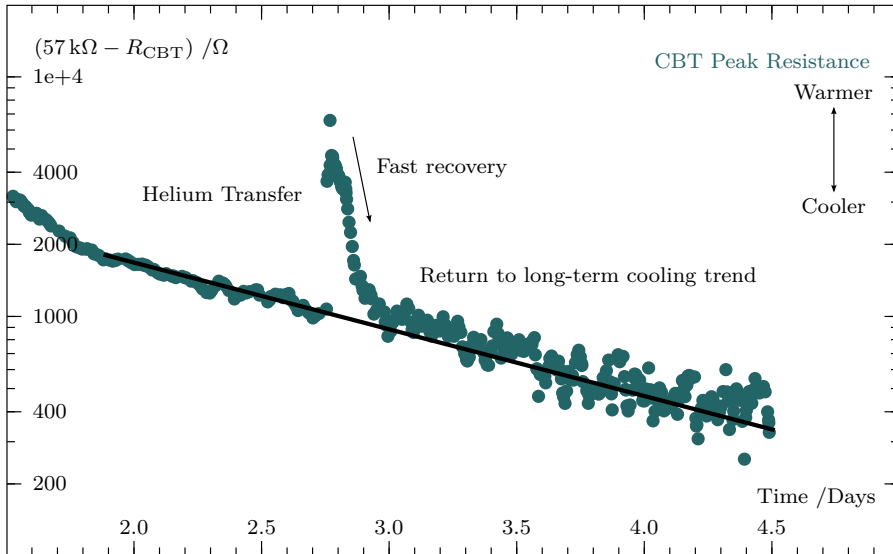


Figure 2.6.7: The CBT seems to follow an exponential convergence with a long time constant of many days. A helium transfer during the experimental run briefly heats up the CBT but the CBT recovers quickly back onto the original long time constant trend.

released slowly, and that heat source would be in close proximity to the substrate of the CBT.

We fit the equilibrium to an exponential decay, $(57 \text{ k}\Omega - R_{\text{CBT}})/\Omega = Ae^{Bt}$, which measures, $R = 6818.6e^{-0.645t}$. This equates to a time constant of $\tau = 1.55$ days, or a half-thermalisation time of $t_{1/2} = 1.07$ days, or one decade in 3.56 days.

This is far too long for commercial applications. Long cooling times directly incur financial costs associated with general operation of dilution refrigerators and the time of the operator and personal involved. A faster turn-around time is needed for practical uses of CBT in the sub 10 mK regime. It also suggests that this methodology is not sufficient to deploy similar devices into the low millikelvin regime and ultimately sub 1 mK regime which is one of the long-term aims of this work.

MEASUREMENTS WITH THE CBT INSIDE THE MIXING CHAMBER

In an attempt to cool a device to a lower temperature, and to approach the refrigerator limit, we needed to improve the thermal contact between the electrons inside the CBT and the phase boundary of the dilution refrigerator. Our method involved immersing the device directly in the cold liquid of the mixing chamber as outlined earlier in section 2.5 figures 2.5.2, and 2.5.3. A different CBT device of the same design is mounted in a case which is covered in sintered silver with the measurement wires individually cooled by their own individual sinter pad.

The Coulomb blockade analysis software pyCBT was improved by its authors to include a thermal model with separate electron and phonon temperature, and to account for averaging from the amplitude of the excitation current.

Isothermal Measurements of the immersed CBT

The improved experimental process and analysis is used when acquiring data. Figure 2.7.1 show four full primary mode measurements of the dip on conduction due to Coulomb blockading. The three warmest curves are analysed simultaneously to measure R_T and C_Σ as a self calibration. The coldest measured conduction curve used these known physical parameters and uses the mixing chamber temperature from the VWR as the phonon temperature T_p . The coldest electron temperature during a bias sweep is as zero bias, when there is no additional ohmic heating.

The 3.86 mK conductivity curve in figure 2.7.1 is performed ‘inside out’. The self heating from a DC bias offset raises the temperature of the device, and subsequent re-cooling takes some significant amount

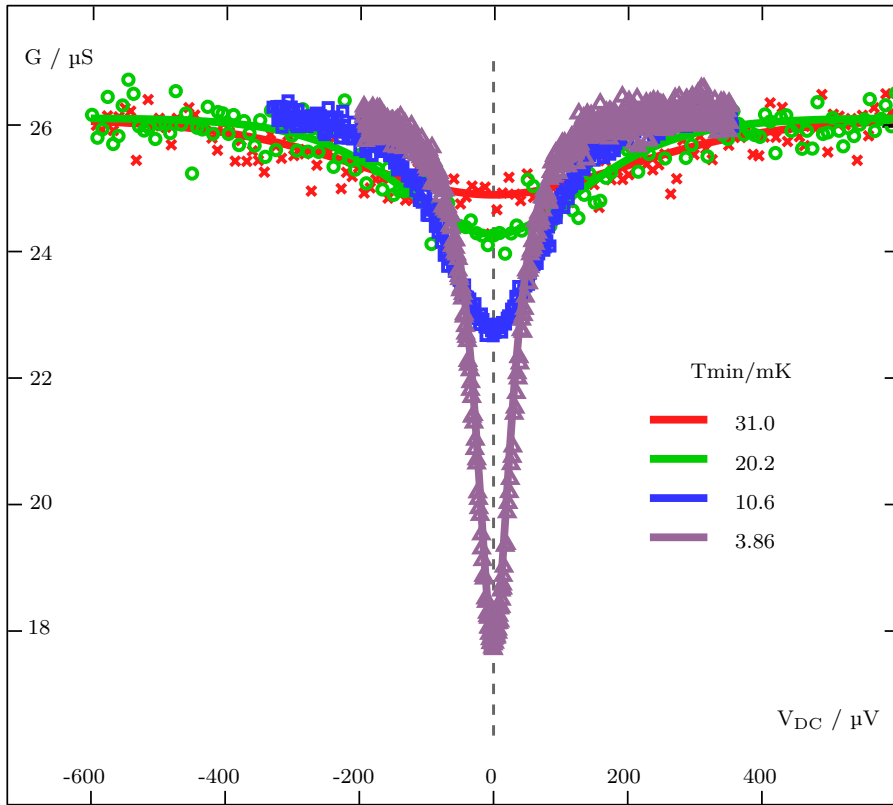


Figure 2.7.1: Conductivity in microsiemens of the immersed CBT acquired at temperature stable isotherms.

of time on the order of about a 5 minutes. The time to warm up the device using a DC bias occurs much quicker, faster than we were able to record. The asymmetry of thermalisation time can be described by the asymmetry in the thermal paths in each situation. Ohmic heating adds heat directly to the electrons during scattering events, while to remove heat from electrons requires electron-phonon coupling to the fin volume and then a combination of phonon carriers and electron carriers.

The acquisition of data for the coldest curve is separated into two halves, each half sweeping outwards from near zero bias with a little overlap² so that the device uses the quicker thermalisation per point to become isothermal. This is an improvement between waiting 5 minutes per data point to one. At the end of measuring the first half, the DC bias is substantial and the device is warmer. So between the halves the device is allowed to cool by using the pseudo-secondary mode. We

² This is so we can check alignment and be assured the peak centre has not changed

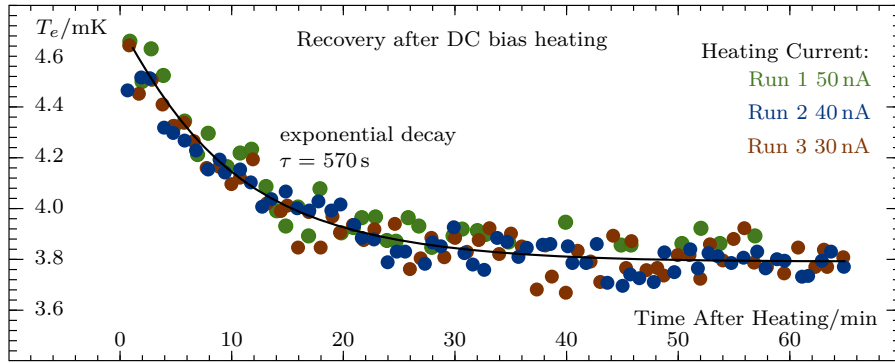


Figure 2.7.2: The thermal recovery of the immersed CBT after it has been heated by an applied DC bias current. An exponential decay shows a 570 s time constant towards a saturation temperature of 3.8 mK. The scatter in CBT temperature shows that the uncertainty of one measurement is around 0.2 mK.

track the cooling progress until the temperature has stopped changing to within the noise.

We tested the effects of DC heating by applying a DC bias far away from the centre, about 20–60 nA, for different lengths of time, 1–20 minutes, then observing the recovery. Figure 2.7.2, shows three examples of thermal recovery after heating. The device takes only a few minutes, $\tau = 570$ s, to recover from these heating events, and seems to be insensitive to the duration or amount of bias. This rapid recovery can be ascribed to the heating saturating whatever mass it is warming and a cooling channel becomes adequate to remove this level of heat. The cooling channel might be the electron-phonon coupling, which has a strong temperature dependence, suddenly switching ‘on’ and removing the heat. The DC current heating recovery suggests the measuring time constant needed for primary mode measurements: if the bias starts large and becomes smaller the we need to allow enough time for the electrons to thermally recover.

Cooling Time Constant - Comparison

The improvements to thermalisation of the CBT should reduce the time needed for the device to reach equilibrium with the mixing chamber. We compare the results of thermalisation of the immersed CBT to the non-immersed CBT shown in figure 2.6.7.

The cooling of the devices are shown in figure 2.7.3, these are aligned in time to match when both the measured electron temperature are equal: the data sets both start with the mixing chamber warmed above 10 mK and then cooled as fast as possible.

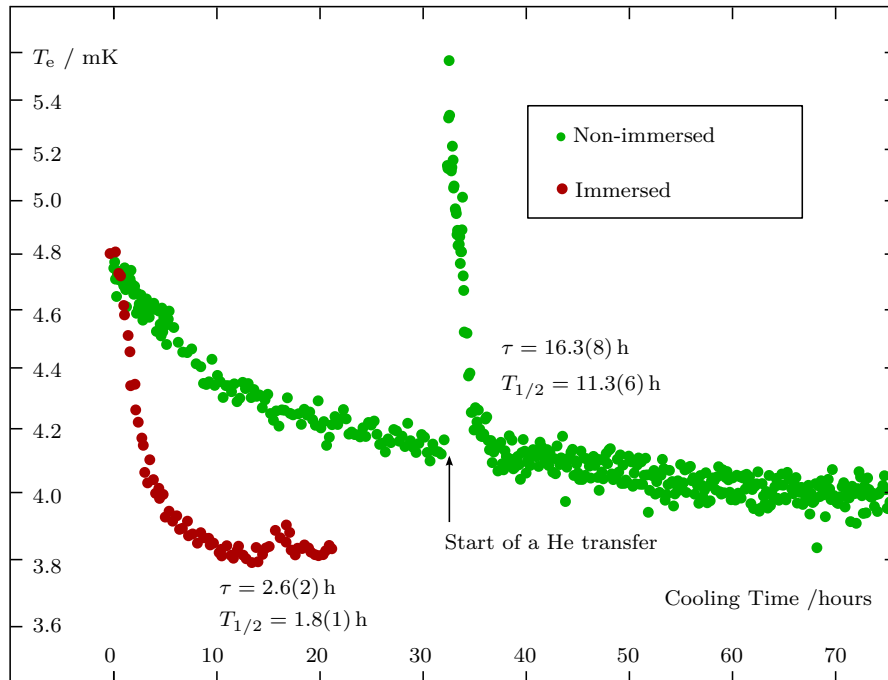


Figure 2.7.3: Cooling the CBT to reach equilibrium with the mixing chamber.

One case where the CBT is mounted below the mixing chamber, and when the CBT is immersed in refrigerant inside the mixing chamber. The temperature of the mixing chamber reaches a base operating temperature of 2.6(1) mK for the non-immersed CBT and 2.7(1) mK in the immersed case.

The equilibrium time for both data sets is measured by fitting to an exponential decay with offset, $T_e = Ae^{-t/\tau} + c$. Data around the heating event is ignored during fitting. The improvement in thermalisation

is 6.3(5) times faster with the immersed CBT than the traditionally mounted, non immersed, CBT.

Both data sets appear to approach a common saturation temperature of 3.8 mK. The data for the non-immersed CBT is from section 2.6.4.

It is clear that the immersed CBT reached the equilibrium base temperature much quicker than the non-immersed CBT. However, it is unclear whether this is due to the better thermal anchoring of the measurement leads or the case of the device holder.

Peak Tracking at Low Temperatures

The pseudo-secondary mode method was developed to overcome a problem of measurements taken using the centre point secondary mode. The centre of the Coulomb blockade peak was not completely stationary, causing single point measurements that are thought to be on-peak at zero bias to be lower than expected.

It is required to use a self-centring method to pick the measurement region. This was achieved by acquisition of several data points over a small range of biases around the peak centre. Using a quadratic fit provides enough feedback for the next over-peak sweep; more detail is included in section 2.4.4. The width of the bias span needs to be small in relation to the width of the peak. This was chosen manually for the temperatures we worked with, but could be automatic if the mapping from peak resistance to temperature is known at the data acquisition time.

The application of a non-trivial DC bias, compensates for an offset in the Coulomb blockading peak centre, potentially due to thermoelectric effects on the DC lines. The required offset bias appears to drift with the changing temperature of the mixing chamber. It may be that a repeatable temperature dependence is not possible, or rate dependent. A steady drift in the helium level changing the temperature distribution

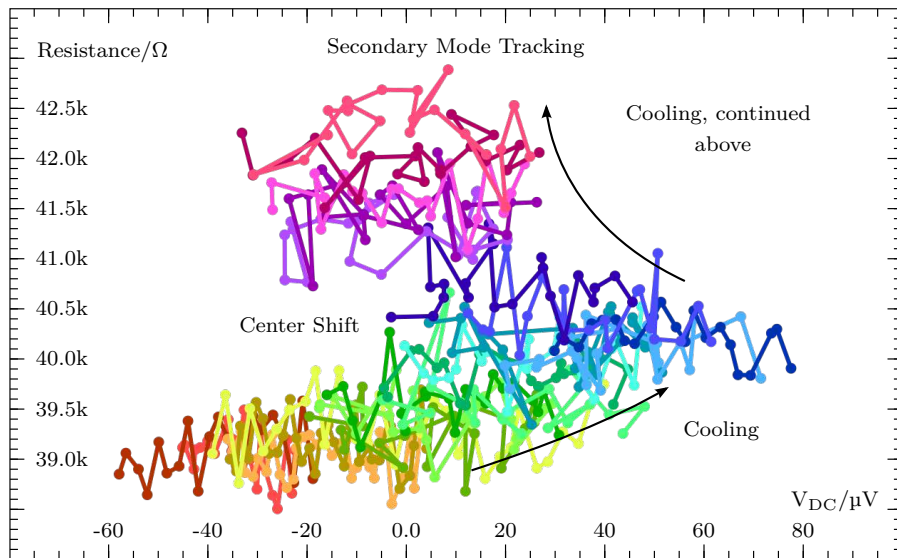


Figure 2.7.4: The shifts in the peak centre using a centre tracking method with the CBT is cooling. A series of mini bias sweeps just over the centre of the peak and performing an on-line analysis to find the centre and perform the next sweep with setting to be more centred over the peak. The curves also show an indication of the differential resistance noise. The colour used on the plot is only to distinguish between individual curves.

higher up in the cryostat is much more likely as thermal EMFs are negligible at ULT temperatures.

Figure 2.7.4 shows some of the differential resistance data acquired during the cooling of the device. The shift appears to cover a substantial fraction of the Coulomb blockade peak width. The figure may exaggerate the peak shifting because of the finite time for one measurement to take place. As the device cools, the last measurement acquired at the end of a sweep, the CBT is cooler, with a higher resistance, which mimics a peak with a different centre. The mini-sweeps are acquired using a bias that is changing from negative-to-positive, This agrees with a centre shift towards the positive biases. It appears that the time dependence seems to be causing a larger problem with the centre tracking. This is a choice between being able to measure a single bias, which may not be the peak, and being able to track the centre. The tracking however does recover from the rapid temperature change to acquire data around a new centre bias that is different from the starting centre bias.

Coldest Measurements

To fully use the available cooling power of the ULT dilution refrigerator, we perform a one-shot operation to briefly lower the mixing chamber temperature. This temporally stops the continuous flow of circulating helium-3 which in turn lowers the heat load on the mixing chamber, resulting in a lower temperature. The temporary cooling stops as the existing supply of helium-3 in the heat exchanges is exhausted and the flow of helium-3 atoms, \dot{n} , across the phase boundary drops.

The one-shot operation changes the temperature quickly, the CBT inside the mixing chamber being measured in pseudo-secondary mode changes temperature along with the mixing chamber.

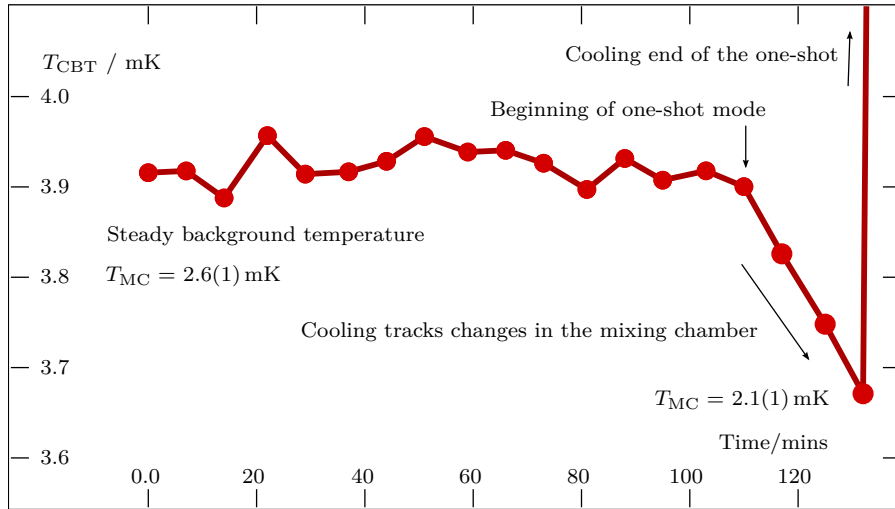


Figure 2.7.5: To measure the lowest temperature of the immersed CBT we put the dilution refrigerator in to a one-shot cycle. This reduces the temperature of the mixing chamber for a brief time. We measure the CBT in secondary mode and measure the lowest temperature, below 3.7 mK. We can also estimate the noise from the steady background temperature to be ± 0.05 mK which can be extrapolated to the lower temperature measurements.

Figure 2.7.5 shows CBT during the one-shot and includes the coldest measured electron temperature using the CBT. The figure shows the limited rate of measurements. In the low temperature limit, we need to acquire enough points for the tracking to work and each data point needs a long time constant. This restricts the sweep time to a minimum of about 7 min per measurement. It is clear that the CBT continues to cool with the mixing chamber. This means that we have not yet reached the lowest possible temperature achievable with this device.

CBT Saturation

The electron temperature inside the CBT is coupled to the phonon temperature of the helium-3 via a combination of thermal links. The final coupling is between the electrons in the cooling fins and islands,

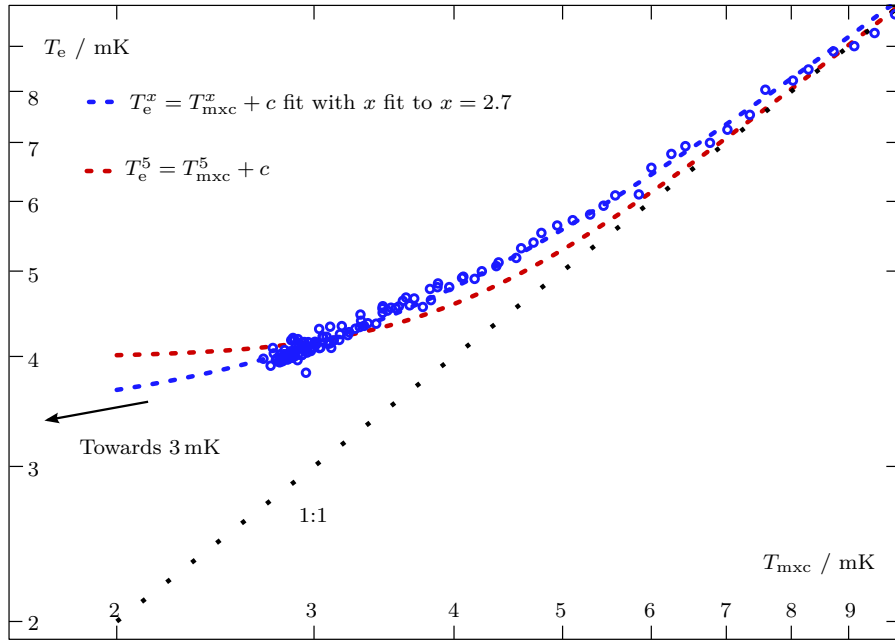


Figure 2.7.6: As the mixing chamber temperature, T_{mxc} , is lowered, the CBT electron temperature, T_e , is no longer in thermal equilibrium. The temperature is slowly lowered to 2.7 mK over 12 h as we take secondary mode data. The fits show two different curves, one of the expected T^5 behaviour, and one with a free parameter for the power.

to the phonons. The electron-phonon coupling has a T^5 behaviour, described in equation 2.3.1, which is likely to be the limiting process.

Figure 2.7.6 shows T_e from the CBT vs T_{mxc} of the mixing chamber measured by a VWR. As the CBT electron temperature falls, the CBT electron temperature no longer follows the mixing chamber temperature. This is the saturation of the cooling channel, and is known as the saturation of the device.

It does not follow the T^5 trend expected if the device was limited by the electron-phonon scattering physics. The best fit shows a $T^{2.7}$ dependence. The best fit shows an eventual saturation temperature approaching 3 mK.

Above 7 mK the device can be used to measure the bulk temperature from the electron temperature.

Thermal Simulation of CBT Islands

To try and understand the unexpected power law dependence seen in figure 2.7.6, we consider the validity of the assumption that all the CBT islands are at the same temperature. We use a simulation to see if the thermalisation of the islands through conduction between elements, and the coupling between the electron to the phonons, can cause some significant change of the island temperatures down the length of the series of islands. This could be used to explain any discrepancies between experimental data and theory.

We construct a 1D thermal simulation of an array of islands. We model heat conduction between islands according to the Wiedemann Franz law, and electron phonon coupling in the presence of a constant heat load into each island. The simulation balances the energy flow of heat into an island and the energy flowing out via EP coupling to an infinite heat capacity phonon bath and WF conduction to neighbouring islands.

Each element, e , receives a constant heat leak, $\dot{Q}_{\text{leak}}dt$, to it per simulation step with duration dt . The heat leak into each element is $\dot{Q}_{\text{leak}} = 50 \times 10^{-18} \text{ W}$, this typical with what is used as part of the thermal model, equation 2.2.9.

Then each element conducts heat between itself and its neighbours according to a Wiedemann Franz conductivity. The heat flow to the left side neighbour is

$$\dot{Q}_{\text{conduction}} = \frac{L\Delta T_{\text{left}}\bar{T}_{\text{left}}}{R}. \quad (2.7.1)$$

R is the tunnelling resistance between islands, and is known from measurement to be $R = 24.4 \text{ k}\Omega$ (figure 2.6.2). Between elements the conductivity is proportional to the average temperature, \bar{T} , of the element and it's neighbour, and the temperature difference ΔT , only true if $\Delta T \ll T$. L is the Wiedemann–Franz constant, $L =$

$2.44 \times 10^{-8} \text{ W}\Omega/\text{K}^2$, Equation 2.7.1 is also used for the right side neighbouring simulation elements.

The electron phonon coupling interaction is modelled by $\dot{Q}_{\text{EP}} = (T_e^5 - T_{\text{bath}}^5)\Sigma\Omega$ for the island volume of the electron bath, $\Omega = 40 \times 10^{-15} \text{ m}^3$ and the coupling constant $\Sigma = 2 \times 10^9 \text{ Wm}^{-3}\text{K}^{-5}$.

Each element has a change in temperature due to the energy $\sum \dot{Q}dt$ deposited during the simulation step dt , the electronic heat capacity of the islands, C_e , and the mass of the islands, M_e :

$$dT = \sum \dot{Q} \cdot dt / C_e M_e. \quad (2.7.2)$$

The island temperature is updated $T + dT \rightarrow T$. For convenience we set $M_e = C_e$ to unity and arbitrarily modify dT to stabilise the simulation as we are not concerned with convergence time, just the steady state.

The boundary conditions on the first and last element are set to the temperature to be the phonon temperature, $T_p = 2.6 \text{ mK}$, this mimics well thermalised electrons in the electrical connections.

The simulation runs until there is no temperature change larger than $0.1 \mu\text{K}$ per step and the simulated islands have reached a steady state. Figure 2.7.7 shows the temperature of each island and the deviation away from the maximum temperature.

There is a large jump in temperature between the outermost islands and the centre islands, due to the good isolation between islands, L is weak, and chosen requirement for the well thermalised leads. Across most of the islands the temperature is constant, and the average island temperature $3.75(1) \text{ mK}$ (ignoring the first and last) is very close to the experimentally observed temperature, figure 2.7.5. There is sensitivity of the choice of \dot{Q}_{leak} , which could impose uncertainties of a factor of two.

The deviation plot inset into figure 2.7.7 shows the difference between each island temperature and the maximum island temperature, of $0.0037517877960736 \text{ K}$ - this level of precision is required for the deviation calculation. The flat base after the outer 9 islands is an

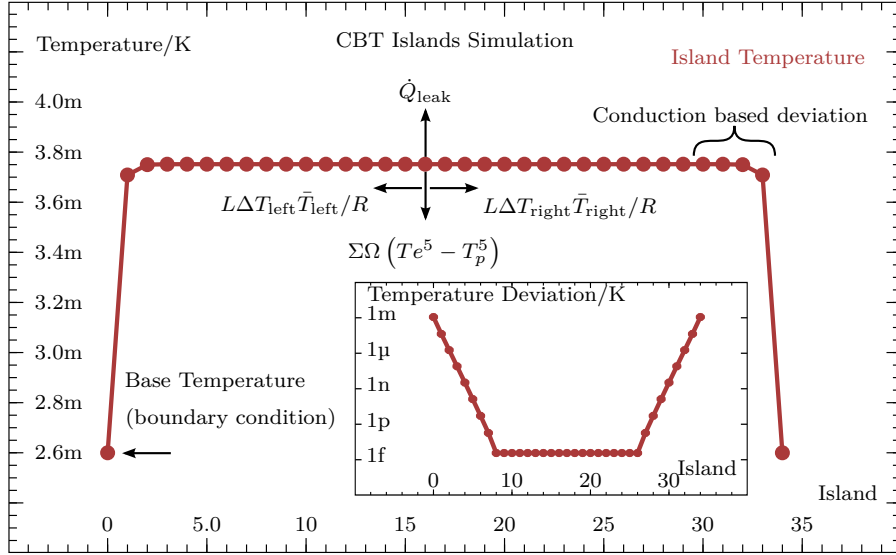


Figure 2.7.7: The temperature of each island along a 1D array of islands. A constant heat load increases the temperature, and conduction and EP coupling provide cooling.

artificial limitation of double precision floating point numbers with only 15 significant figures. The largest deviation of island temperatures are at the edges, 1 mK for the first and last islands. It is the third and pre-penultimate elements which show a temperature difference of 1 μ K, after which the temperature differences might be considered inconsequentially small.

The simple model has the island phonon bath with an implicit infinite heat capacity. The energy flow into it from \dot{Q}_{leak} would warm it up otherwise which is not accounted for. So there is an implicit strong thermal conduction between the islands to the substrate and the cold source, giving an effectively infinite heat capacity.

Figure 2.7.8 shows the power into each element. This shows that the constant heat leak is counteracted by the electron phonon coupling in the fins, and not by conduction down the array. Conduction does have a small influence at the few edge elements.

A near uniform temperature distribution implies that we do not need to model each of the islands separately. There is not enough thermal conduction between islands to become a dominant source of cooling,

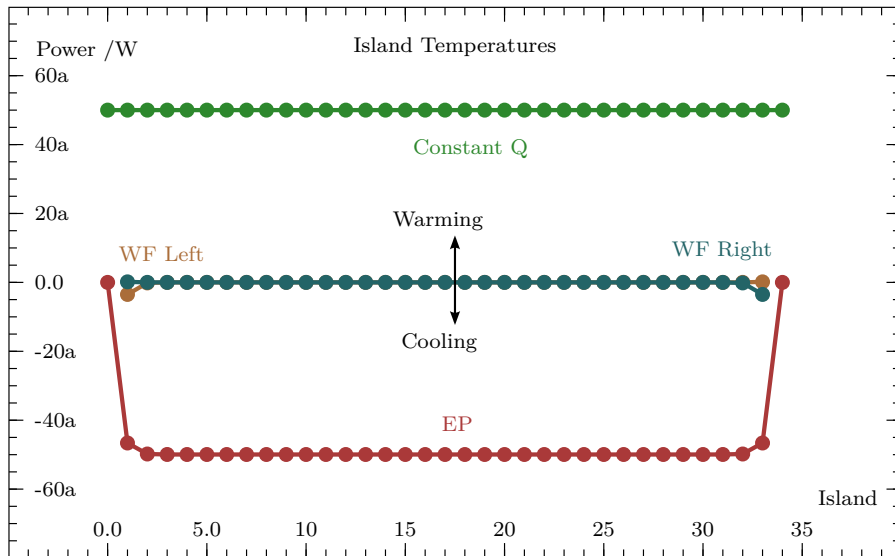


Figure 2.7.8: The component powers that change an island temperature.

Conduction only has a minor contribution at the beginning and end of the row of islands. Equilibrium is reached as the sum of the powers for all islands is zero.

and each of the islands can be considered to be thermally independent. An improved thermal conduction between islands would cause a more significant temperature gradient. The temperature of the islands is dominated by the electron phonon coupling, $Q_{EP} \gg Q_{\text{conduction}}$.

The temperature distribution of the islands implies what really matters for low temperature is the cooling of the fins, to the substrate or to the liquid directly, and that the leads are not that important, causing only edge effects. However cooling of the leads is needed so that the electron temperature of the edge few islands is close to matching the temperature of the electrons in the centre islands. This could explain the ‘hot magnet’ effect, from page 55.

For a 2D array of islands, as in the actual device, each set of series islands will be coupled via the substrate to the neighbouring parallel series of islands. If the Joule heating was excessive enough so that the assumed infinite heat capacity of the substrate is incorrect then the centrally located islands on the chip would be at a higher temperature than the islands located nearer the edges of the chip.

DISCUSSION

We managed to measure an electron temperature lower than 4 mK using a combination of silver sinters in dilution refrigerator at 2.6 mK. For this we needed to use a thermal model of the CBT and use an assumed phonon temperature of the CBT cooling fins. The thermal model also needs to include the effect of ohmic heating from the applied bias during a bias sweep. This means that there is a measured electron temperature per point on a coulomb blockading conductivity dip, with the lowest temperature measured at zero bias.

We have demonstrated the CBT as a primary thermometry, there was no free calibration parameter to adjust measurements. We measure the breakdown to non- T^5 saturation behaviour at low temperatures indicating the device is not electron-phonon coupling limited. This is useful information for the ongoing development of CBTs, suggesting that maybe the fin-volume is not limiting, but thermalisation of the fins could be limiting. Experimental work on the electron-phonon coupling in thin films below 1 K [69] has seen a T^3 behaviour, rather than a T^4 for ‘dirty’ metals. This is not far away from our measured $T^{2.7}$. We don’t know if the EP coupling temperature dependence has itself changed or that the T^3 is from another thermal coupling link or a combination. It could be any of the thermal links shown in the idealised thermal path model, figure 2.5.7.

The island simulation showed that the electrons are dominantly cooled by the EP coupling in the islands and not by conduction through the barrier, which at low temperature is too severely limited by the Wiedemann Franz thermal conduction. The boundary conditions in that simulation were set to the base phonon temperature assuming that the leads to the CBT are very well thermalised. According to the simple simulated model, the electrons in the central islands are very well thermally isolated from the temperature of the electrons

in the leads. So any temperature difference in the leads will cause a diminishing temperature gradient over only the first few islands until the equilibrium temperature. The potentially large temperature difference from the leads to the outer islands will change the differential conductivity curve. For islands of different temperature we can suppose some combination of the curves in figure 2.7.1 according to the individual island temperature; for example $2/33$ of the 33 mK for the outer islands, and increasing fractions of the colder curves for the central islands. It would be impractical to have electron thermometry before and after the CBT electron thermometry so we need to, by experimental design, become confident that the incoming leads are well thermalised.

Full bias sweeps of the CBT can cause too much ohmic heating that directly and quickly warms up the electrons in the islands. This has an effect that reduces the resistance peak height and broadens the peak width. At low temperatures using secondary mode reduces the heat load into the CBT. The excitation for low temperature measured was discovered to be required below 5 pA.

The recovery from DC current heating of the immersed CBT has a five minute time constant. This was tested by measuring at a point far away from the peak for 15 minutes, and then returning to secondary mode. This is much faster than the long 1-2 day time constant displayed by non-immersed CBT. This implies that the material being heated by ohmic heating is different from the mass with the long time constant. DC heating directly warms the electrons in the fins and the islands.

We suggest that the sources of long time constant heating are a combination of the small permanent magnet, and the Eccosorb shielding/filtering. If used in applications where there is a field larger than B_c for aluminium (about 50 mT) then the rare-earth magnet could be omitted. Removal of the Eccosorb above the chip may however

be counterproductive, because of the shielding and filtering benefits it provides.

We find that the maximum rate of temperature measurement at the lowest temperatures is around 1 point every 10 minutes, even using the fast pseudo-secondary mode.

The improvements by submersion of the CBT in the refrigerant, cooling the CBT package with sinters, and having the electrical connections each thermalised to the refrigerant did significantly improve the thermalisation time.

FURTHER WORK

Our work has demonstrated that it is possible to cool the electrons in a nano-scale device to below 10 mK, and as low as 3.7 mK. Further work needs to be carried out to fully understand the limits of cooling nano-scale devices into the low millikelvin and onto the high microkelvin regime. This would require a different refrigerator, an adiabatic nuclear demagnetisation refrigerator would be ideal. We would need to make modifications to the device mounting scheme. Work is already under way in Lancaster to mount these types of devices onto a nuclear refrigerator. I will now discuss possible modifications and improvements to the techniques described in this thesis.

One significant area that could be developed would be the full automation of the sweep procedure. Full automation of all of the bias sweep parameters that were operator chosen and controlled during our experiments could be automated away. We needed to change the measurement excitation amplitude as the temperature changes. For higher temperature the peak has a much smaller height and G/G_0 is smaller, the noise in the measured differential resistance is fractionally larger compared to the peak and so a larger excitation can give better results without having to increase measurement time or the

number of samples. For low temperatures the inverse is true, the excitation needs to be low, not because we don't need to see the smaller change in resistance because G/G_0 is larger, but because the excitation leads to heating and broadening of the peak. The lower temperature measurements need to be acquired with more averaging and a longer time constant, that too could be an automatic choice.

As the temperature changes, the other main feature of the Coulomb blockade, the width, changes linearly with T . The choice of the range of biases, how wide to sweep the bias to fully cover the peak and enough of the background, needs to change. Failure to correctly change the measurement bias range could lead to poor numerical fitting.

Once an approximate temperature of the CBT is established, all the choices for excitation amplitude, lock-in time constant, DC bias range, can be estimated. The fully automatic choices, and knowledge free operation, would be very useful in a commercial application. When operating the device in secondary mode, the choice of the excitation amplitude and time constant should also be changed to reflect how best to measure the device.

There is potential to use a faster method of measuring the CBT temperature based on the third derivative of the $I - V$ curve, the d^3I/dV^3 , curvature [28]. Using this technique the curve is sampled at a bias I_{DC} such that $d^3I/dV^3 = 0$. This works if the peak is centred around 0, but any bias offset can be corrected for by measuring at both $+I_{DC}$ and $-I_{DC}$ and averaging $|I_{DC}|$. When taking measurements of d^3I/dV^3 any non-zero result gives direct information on how to take the next data point to minimise error. This is more direct than the current hill-climbing optimisation in pseudo-secondary mode. The constantly applied current needed for I_{DC} causes heating, so this method it is inappropriate for use at low temperatures, however this could become useful at higher temperatures where electron-phonon thermalisation is not limiting.

In addition, the thermal model could be further developed to include separate CBT island temperatures. To avoid over-parameterisation the improved model may need to include a Wiedemann-Franz conductivity between islands, similar to the simulation, to define the inter-island temperature differences.

The sinters could be improved using recent advances in sinter topology, using built in flow channels for fluid refrigerant, that removes the self-thermal-shielding effects of the sinter[70]. In this work the authors used nylon lines embedded in the sinter powder that can be chemically dissolved away after the sinter is fabricated.

Thermally induced DC offsets can causes problems with tracking the offset bias of the peak during cooling. When approaching our limit of T_e , these thermal DC offsets are non-trivial compared to the peak width. For low temperature work, the width could be designed to be wider by increasing the number of junction in series (n in equation 2.2.1). This comes at the expense of a larger series resistance but could be overcome by fabricating additional parallel channels. However, the additional fabrication of more junctions increases the size of the device, which means more challenging fabrication and additional cost.

Finally, it may be possible to directly couple the exposed gold islands on the chip to the surrounding cold liquid. The CBT case is not vacuum sealed and there is liquid helium-4 covering all surfaces of the chip. The very close cold helium could be good for thermalisation of the fins of the CBT, and with modification of the CBT design could be changed to have a larger surface area to be sinter-like directly on chip. The CBT case has a narrow volume of metal between where the bolt-hole, and where the sinter was attached, and the main body of the holder. This could be a thermal bottleneck preventing cooling of the chip substrate. The narrow section can be seen in figure 2.5.8.

CONCLUSIONS

We demonstrated cooling a CBT to below 3.7 mK using immersion cooling of the device and of the electrical connections. We used direct cooling of the electrical leads with sintered pads in a mixing chamber, and a more direct thermal anchoring of the CBT. A careful process of screening and multi stage filtering of signals of the leads of the leads reduces noise, and heating into the CBT. We developed and used a thermal model to help explain the electron temperature decoupling from the phonon temperature inside the device.

We suggest that a CBT is a useful tool to characterise noise in low temperature experiments. The sensitivity to electrical noise provides useful diagnostics of the apparatus, inside and outside of the dilution refrigerator. If used in place of a future experiment the CBT could provide experimental electron thermometry and diagnostics before swapping out for another device which may not be as sensitive. If possible, it would be better to fabricate a CBT on the same chip as the experiment. In this case, the CBT would provide both electrical diagnostics and direct thermometry.

This work gives incite into how to approach cooling as we approach 1 mK and lower. This research is beginning the development to measure on-chip devices into the sub mK regime which is of interest to new research.

AN IMPROVED PEAK SAMPLING SCHEME

INTRODUCTION

This section describes a method for improving the acquisition of data from physical systems with peak like behaviours to improve the accuracy of the post-acquisition curve fitting parameters. This maximises the information that is extracted by only modifying the sampling method. We test changing the span of samples over the peak, and experiment with different sampling densities to focus on more information dense regions of the peak.

Measurements of peak-like functions are used to extract information about a system. The two other sections in this thesis are both examples of devices with peak like measurements that provide thermometry. This section focuses on the Lorentz peak that is used to describe the velocity as a function of the driving frequency of oscillating systems. These are often used in low temperature physics as oscillating devices are used to probe the properties of cryogenic fluids. Coulomb blockade thermometers operate very differently, but still have a characteristic peak of differential resistance as a function of a DC bias.

The standard method of sampling is to decide on a span of the available sampling domain that is centred around the feature to be measured. The individual samples are at locations that are evenly distributed between the start and stop points, this describes a uniform density of sampling. Experimental intuition encourages the choice of the span to be sufficiently wide so that all of the curves of the peak full peak are measured, but not too wide as to measure too much

background and dilute the samples that are on the peak itself. The choice of where measurements are sampled around the peak may not always be optimal in order to get the best acquired data that can then be used for a numerical curve fitting. One part of this chapter explores in detail the trade-off in choices of the sampling span. We will show that the parameterised peak information is not spread out evenly in the sampling domain, and show improvements are possible by making a sensible decision about where to sample. We also use an algorithm to estimate the location or density of the parameterised information in the sample space.

We only concern ourselves with acquiring data in a in the form of a complete sweep of samples that are then used as a whole for numerical fitting. There are also systems of sampling that use a series of individual samples for a higher rate of data acquisition, but these are considered out of scope, as they use a different acquisition algorithm.

Using an optimised form of a uniform sampling density still may not be the best. If we explore non-uniform sampling distributions we can try to focus more samples around regions of higher information. In these situation there can be more points measured around the centre of the peak, or at the edges in order to focus in on some aspect of the curve. This section goes on to describe the results of simulated tests of alternative sampling patterns that can provide more accurate measurements of the peak. We used a genetic algorithm to search for an improved pattern of samples that can provide even better peak information and improve the quality of parameter estimation. The generated sampling pattern that resulted from the genetic algorithm was generalised to be used with any number of sampling points and was verified experimentally to be an improvement by implementing the new pattern to measure vibrating wire resonators in a ULT cryostat.

THEORY

Peak Functions

The peak functions that we are looking to measure better all have five parameters. There are three for the peak and two for a linear background. These are shown in figure 3.2.1.

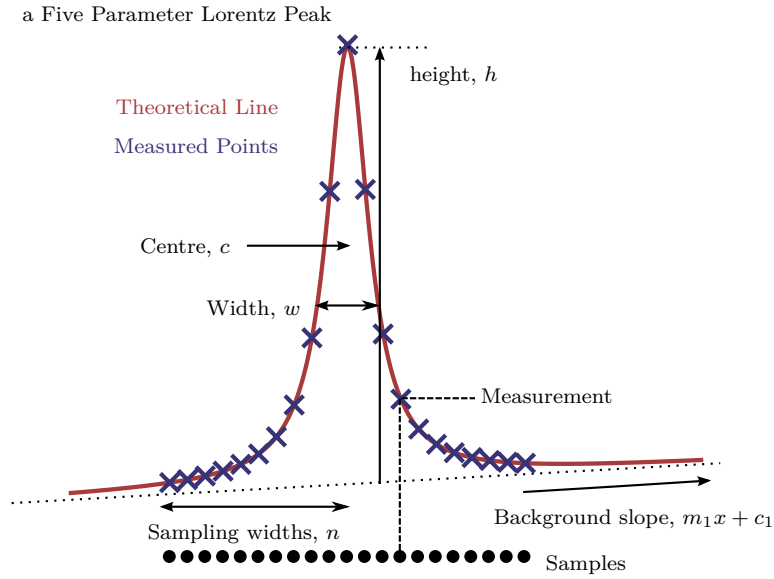


Figure 3.2.1: The five parameters that define a peak. 21 points are samples on the peak spread evenly from $c - nw$ to $c + nw$.

We focus on the Lorentz peak that is used for velocity response of vibrating objects. The functional form of this peak typically has a domain of f , but we are using x for consistency when describing other peaks. The Lorentz peak is

$$V_x(x) = \frac{hw^2}{w^2 + (x - c^2/x)^2} + m_1x + c_1 \tag{3.2.1}$$

where w is the full width at half maximum (FWHM), c is the centre of the peak, h is the height from the baseline to the peak, and $m_1x + c_1$ is a linear background. The oscillation response also has a function for the out-of-phase component. We use this later to describe the pattern of

measurements that are equally spaced in the phase. This out-of-phase response, also known as the quadrature is

$$V_y(x) = \frac{-hw(x^2 - c^2)}{w^2 + (x - c^2/x)^2} + m_2x + c_2. \quad (3.2.2)$$

The background of V_y is also linear, but with uncorrelated parameters called m_2 and c_2 .

Two other peak shapes we will test are a peak based on the sinh function, and a Gaussian peak. The Sinh peak that describes a Coulomb Blockade can be written as

$$S(x) = 6h \frac{x' \sinh(x') - 4 \sinh(x'/2)^2}{8 \sinh(x'/2)^4} + m_1x + c_1 \quad (3.2.3)$$

where $x' = 2 \times 2.71958 \times (x - c)/w$. A Gaussian peak that is parameterised by the FWHM is approximately

$$G(x) \approx h \exp\left(\frac{-1(x - w/2.35482)^2}{2(w/2.35482)^2}\right) + m_1x + c_1. \quad (3.2.4)$$

The slightly different peak shape from these three functions are shown in figure 3.2.2.

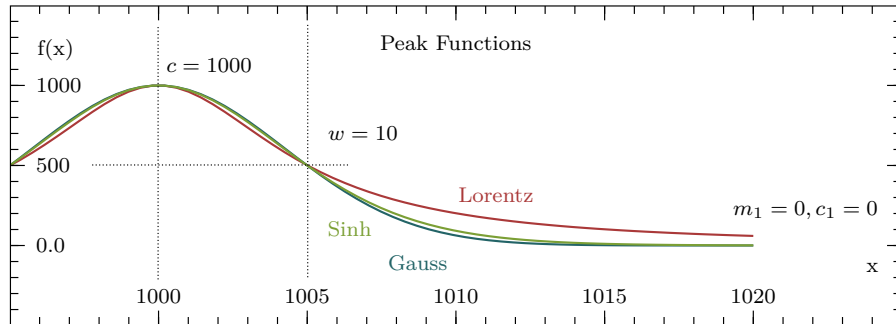


Figure 3.2.2: A comparison of the three peak shapes. Each of the functions are parameterised by the same FWHM and height. The Lorentz peak has much wider tails. The Gaussian peak is the sharpest.

Implementation

We define the peak parameters to be used for the simulation and then simulate the measurements on the peaks by generating an array of sampling points \mathbf{x} according to a sampling pattern. The linear sampling

pattern has evenly-spaced points in a span around the peak. The result of the peak function sampled over \mathbf{x} is added to noise to acquire simulated measurements \mathbf{m} i.e. $\mathbf{m} = V_x(\mathbf{x}) + \text{noise}$. The simulated measurements are then numerically fitted to find the measured peak parameters. The measured peak parameter will not be the same as the provided peak parameters due the inclusion of noise. The comparison between these two sets of parameters gives information about sampling can provide the peak parameter estimation under the influence of noise.

The process of measuring and fitting is repeated to build a collection of fitted parameters, p_i . This is compared to the known true parameters P when all the test are completed to find an estimation of the error.

$$E = \frac{\sqrt{\frac{1}{n_t} \sum_i (p_i - P)^2}}{P}. \quad (3.2.5)$$

We normalise to account for the number of tests, n_t , and the value of true peak parameters. This error is informative of how well the parameters are being measured under the current sampling pattern. When we change the sampling pattern we can see how well each parameter is estimated.

A property of the Lorentz peak that is used to characterise resonators is the “height times width over drive” value. This uses the product of the peak width w and the height h . We create an additional pseudo peak parameter, wh , that is evaluated as after the curve fitting to include this. The error on wh is evaluated the same way as equation 3.2.5 and is called the ‘score’. The score is used as a meter for the sampling pattern quality. Improving the score also accounts for any cross-correlation between the width and the height.

The complete experimental system of code including the numerical curve fitting was implemented twice using two different curve fitting methods. A JavaScript implementation used a modified version of `fminsearch` from Jonas Almeida [71] which in turn is based of the Nelder-Mead simplex method [72]. A later re-implementation in Python

used the SciPy [73] implementation of The Levenberg-Marquardt algorithm [74]. The two implementations showed no significant difference.

Each time the fitting algorithm is used the fitting parameters are initialised to the true parameters, as this helps to start minimisation quicker. Deviation of the fitting parameters occurs only from the added noise.

RESULTS

Linear Sampling Pattern

The simplest and most common sampling pattern uses a linear spacing between the first and last points. For a peak function this pattern is centred around the peak centre and with a chosen span. Very small spans will only cover the top of the peak and very wide spans will measure lots of the background around the peak with only a few point to cover the peak itself. We test a choice of the size of the sampling span based on the width of the peak. The peak This sampling span, n , is based on the natural width outwards from the centre, so that a span of $n = 2$ will be between $c - 2w$ to $c + 2w$.

We used a simulation of measurements with different sampling patterns whilst varying the span. The error in the peak parameter estimation, equation 3.2.5 is shown in figure 3.3.1.

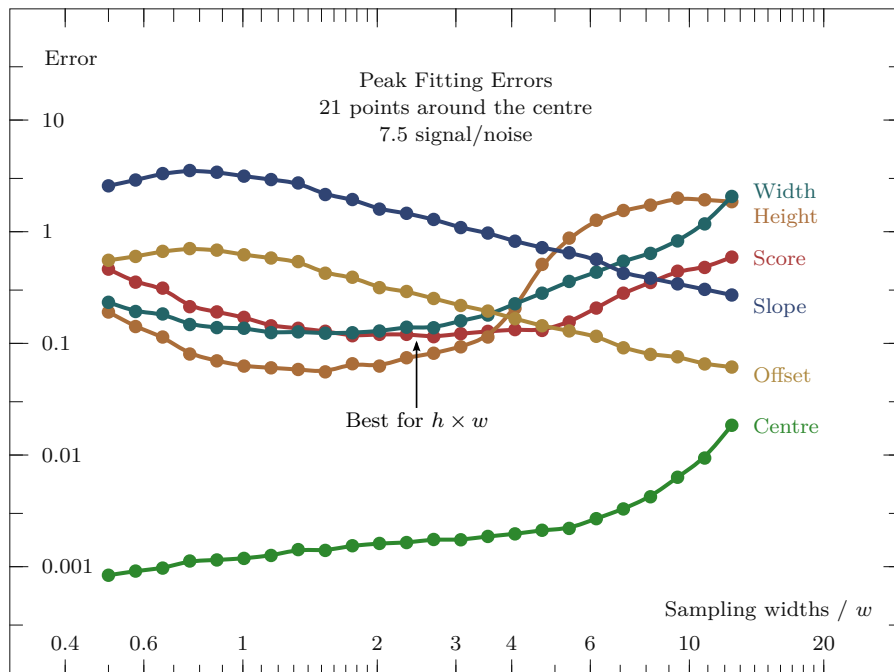


Figure 3.3.1: The averaged error of each parameter as the width of a linear spaced sampling changes. The best window for the lowest error on $h \times w$ is at $c \pm 2w$. Using 21 points, and a signal to noise ratio of 7.5.

Figure 3.3.1 shows that the error in estimation of any one parameter can change by nearly an order of magnitude depending on the chosen sampling span. This shows that the centre becomes poorly defined as span increases while inversely the linear background parameters benefit with a wider span. This is intuitive to understand as errors reduce with repeat measurements, particularly around where a parameter has the most influence would better define that parameter. The width has a ‘u’ shape trend suggesting that the best span to use is between 1.5 and 2. The score has a minimum around 2.

The results in figure 3.3.1 show what is commonly known, measuring too narrow, under one width away in each direction, loses information about the background and slope, and consequently the peak height, and measuring too wide reduces the number of points over the peak, increasing fitting error of the centre, width, and height. There is a ‘sweet spot’ of about 2–3 times the width of the peak that is a trade off between too narrow and too wide.

The same sampling pattern but used with more sampled points will reduce the errors, as would reducing the size of the simulated noise. These are kept constant so that only the influence of the span effects the errors. The bend seen on the centre error line on figure 3.3.1 around 6 spans is likely to be because one of the 21 sampling point moving off the peak.

Location of Parameter Information in the Sample Space

We extend our method of peak parameter error estimation to extract the location of the parameters information. This is achieved by initially providing a collection of linearly spaced sample points over the peak to provide context, then adding a highly weighted point on the curve with zero noise. This provides the curve fitting algorithm with an effective known point on the curve. A known point on the curve at a particular

sampling position over the peak will reduce the parameter errors because of the information available at that point. Sweeping the known point across the curve maps out the extraction of information from the peak. Figure 3.3.2 shows the reduction in each peak parameters error, normalised, and separated for visual clarity.

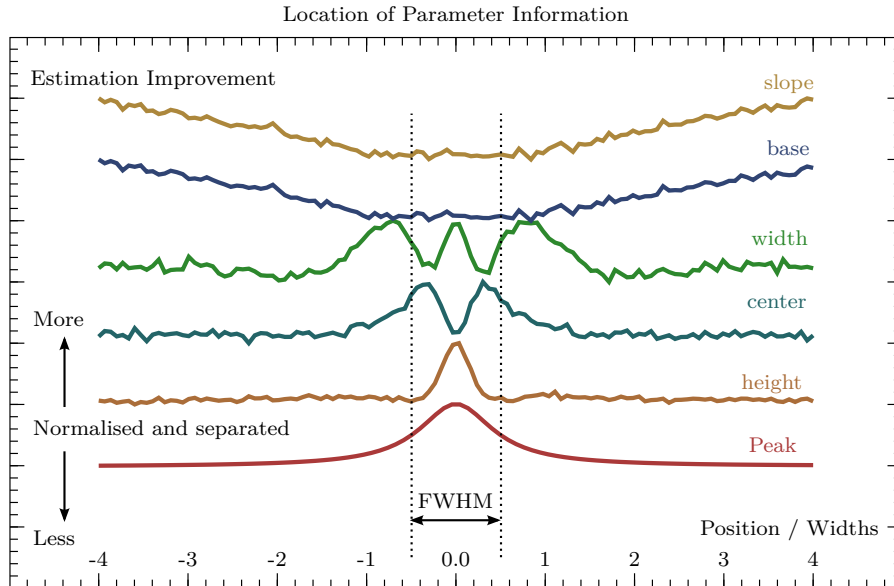


Figure 3.3.2: The approximate location of information of each parameter that defines a peak. The vertical axis for each curve is normalised and offset. The 51 evenly spaced context points covered 4 widths either side of the peak with the parameters $h = 1000, w = 10, c = 1000, c_1 = 100, m_1 = 0.1$. The known point adds an additional 100 data points at a specific position on the peak. The measurement errors on each of the peak parameters are averaged over 1000 tests.

Figure 3.3.2 shows the improvement of particular parameters. Measurements of the heights are improved only in the region of ± 0.3 widths from the centre. The measurement of the centre is improved mostly with samples within ± 1 but not at within ± 0.1 probably due to the vanishing gradient. The width is most improved by samples made at around ± 0.7 widths, and at centre, but surprisingly not improved by samples at about ± 0.3 width of the peak. The peak parameters are generally improved within ± 2 widths of the centre, in this sampling

range the background has the lowest improvements in measurement from the additional samples. Outside of ± 2 widths the background information starts improving linearly.

There seems to be no parameter that is particularly improved at ± 0.5 widths, the FWHM point, of the peak.

Equally Spaced Measurements in Phase

The evenly spaced sampling pattern is not the only available. Our initial ideas for improvement using a non-uniform sampling density is to produce a pattern that is equally spaced around the complex phase of the Lorentz peak. The phase can be swept knowing the width of the peak, w , and the centre, c . A sample point is at

$$x_i = \frac{w}{2} \times \tan\left(\frac{\theta_i \pi}{2}\right) + c \quad (3.3.1)$$

where $\theta = \{-\theta_{\max}, \dots, +\theta_{\max}\}$. Each θ is equally spaced between $\pm\theta_{\max}$.

The parameter θ_{\max} , is a value that is close to, but not equal to, 1 and is used to define finite endpoints. The values of $\theta = \pm 1$ will generate samples at $\pm \text{inf}$ which for many systems is physically impossible. The approach to infinity is asymptotic as θ_{\max} approaches 1, and so typical useful values will be 0.95, 0.99, or 0.995. We solve for θ_{\max} in terms of a number of measurement widths, n ,

$$\theta_{\max} = \frac{2}{\pi} \tan^{-1}(2n) \quad (3.3.2)$$

so that we can form comparisons between a pattern generated by the equal phase method and a linearly spaced sampling pattern.

A hodograph shows V_x vs V_y , and draws out a circular shape as the frequency moves around the phase. The demonstration peak has a non-zero gradient in the background, this causes the beginning and end points to curl away and not form a closed loop.

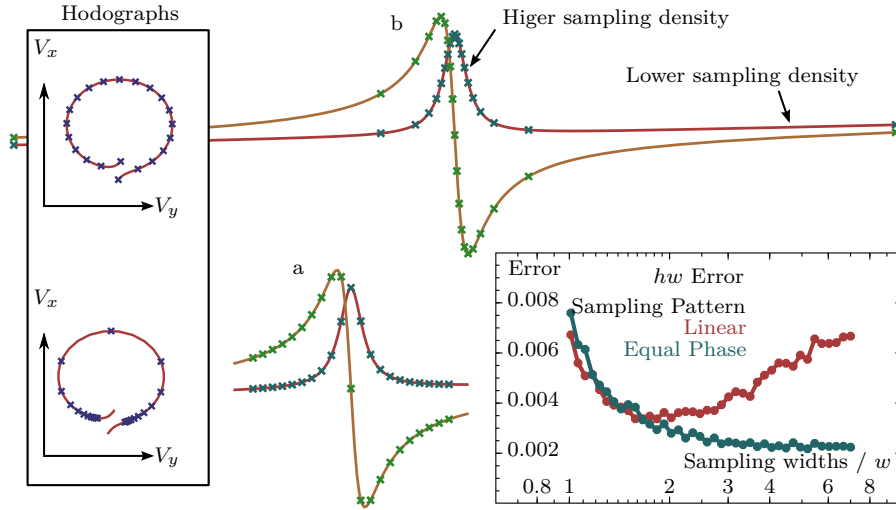


Figure 3.3.3: The two peaks show an equal phase pattern between $\theta = \pm 0.98$, and linearly spaced pattern $n = \pm 2.5$ widths. They are drawn on hodographs, and with the score error when measured with either the widths or θ_{\max} .

We test the scores based on the equal-phase pattern against scores using a linear spaced pattern, figure 3.3.3. This shows that the phase based measurement points can be an improvement by about 20%, but the benefit is only when sweeping with very large θ_{\max} , this can be many tens of widths away from the peak, a feat that is not practical in practical scenarios. We think the largest weakness of the phase based method at low θ_{\max} is because of the lack of measurements near the background, away from the peak, the bottom of the hodograph, where the two parameters for the background are defined.

Search for Improvements by Genetic Algorithms

There is no apparent direct improvement that can produce smaller parameter errors. The choice of sampling pattern is an unconstrained optimisation problem; we can not test all possible patterns. So we use a general purpose genetic algorithm [75] to search for improved sampling locations. The genetic algorithm mimics the biological process of evolution to iterate a better pattern. Each individual generated

in a simulated population has DNA-equivalent that is a sampling pattern. In every iteration all sampling patterns are tested and the best patterns are used to produce new similar patterns and poorly performing patterns are discarded.

The choice to use a genetic algorithm over some of the alternatives like simulated thermal annealing [76, 77], or an f-min search (a divide-and-conquer approach) is arbitrary, either could work. Genetic algorithms have been used for complex optimisation problems with no clear strategy [78, 79].

We build the algorithm with the postulates: the pattern is symmetric around the peak centre, there is one sample at the centre. Each individual is scored on the reciprocal of the error in wh , so that less error yields a better score. We initialise the algorithm using a pattern from the equal phase method. The genome we use is an array of numbers of widths, these numbers range around 0.2 to 4, and are then converted to frequency when the individual is tested. We use a moderate population size of 50. The re-population after a generation uses a semi-best:random method using a random linear interpolation of a genome. We add an extra linear combination mutation step to encourage more random testing [80, 81]. The genomes are kept sorted to reduce problems with central convergence; averaging any two genomes will tend a middle value. These algorithm choices are the result of experimentation to achieve convergence to a solution in a reasonable amount of time.

Figure 3.3.4 shows the progression of the algorithm and one of the best solutions. The genetic algorithm improves against the previous best system by appearing to take only five bunches of data; two bunches at either side of the peak near the baseline, two bunches around the FWHM points, and a few points near the top.

The best pattern in the pool is also the best of the noisy distribution of scores. To avoid measurement bias in figure seen in 3.3.4 we re-test the best in pool before plotting.

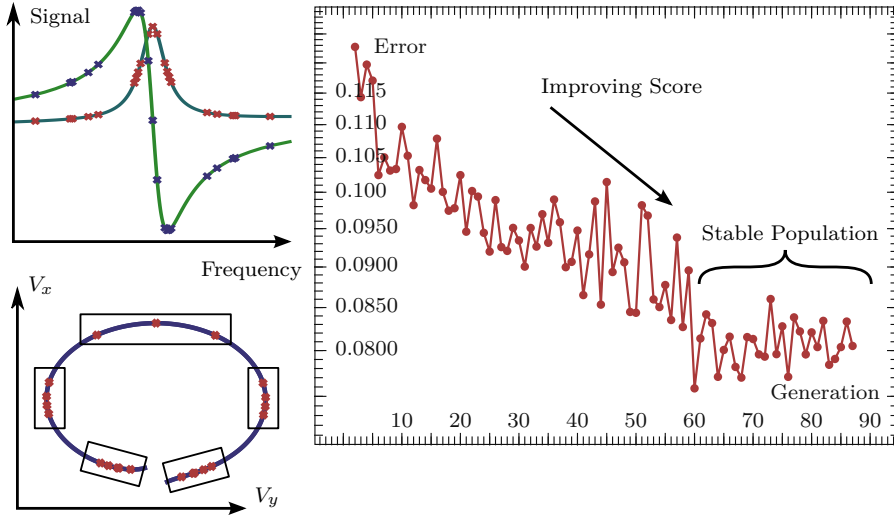


Figure 3.3.4: The score of the best individual each generation is plotted as the system iterates. This shows the progression of population as the pattern is improved. One of the final individuals is drawn showing an evolved bunching pattern.

Generalising a solution

To make the result from the genetic algorithm more general so that it can be applied with any number of points we need to create a function that generates a sampling pattern that mimics the result of the evolved distribution. There are many ways to do this, but we show only one.

We start by observing bunching at both sides near the base and at the width points, and a small bunch close to the top. Starting from a characterised phase base distribution $t = \{-1 \dots 1\}$: we decide to apply three transforms before converting to frequency space.

1. Apply a bunching towards the limits -1 and 1 , these are to improve the bunching near the tails of the peak, and shrink the phase range by some chosen scaling factor. A factor of t_{\max} is a choice defined later, and is solved by numerical methods.

$$t' = t_{\max} \left(t + \frac{\sin(\pi t)}{\pi} \right) \quad (3.3.3)$$

The factor of $\frac{1}{\pi}$ ensures that the gradient of t' is always positive or zero, this means that frequencies are always increasing. π is the solution to k in

$$\frac{\partial}{\partial t} \left(t + \frac{\sin(\pi t)}{k} \right) \Big|_{t=-1,1} = 0 \tag{3.3.4}$$

- Apply bunching near each focus of: the tails, the two \pm width, and the centre.

$$t'' = t' - \frac{\sin(4\pi t')}{4\pi} \tag{3.3.5}$$

This is gradient limited in a similar manner to equation 3.3.3.

This measurement pattern that mimics the evolved pattern is called Mphasy, and the steps are shown graphically in figure 3.3.5. Code listing are available in the appendix listing A.2.

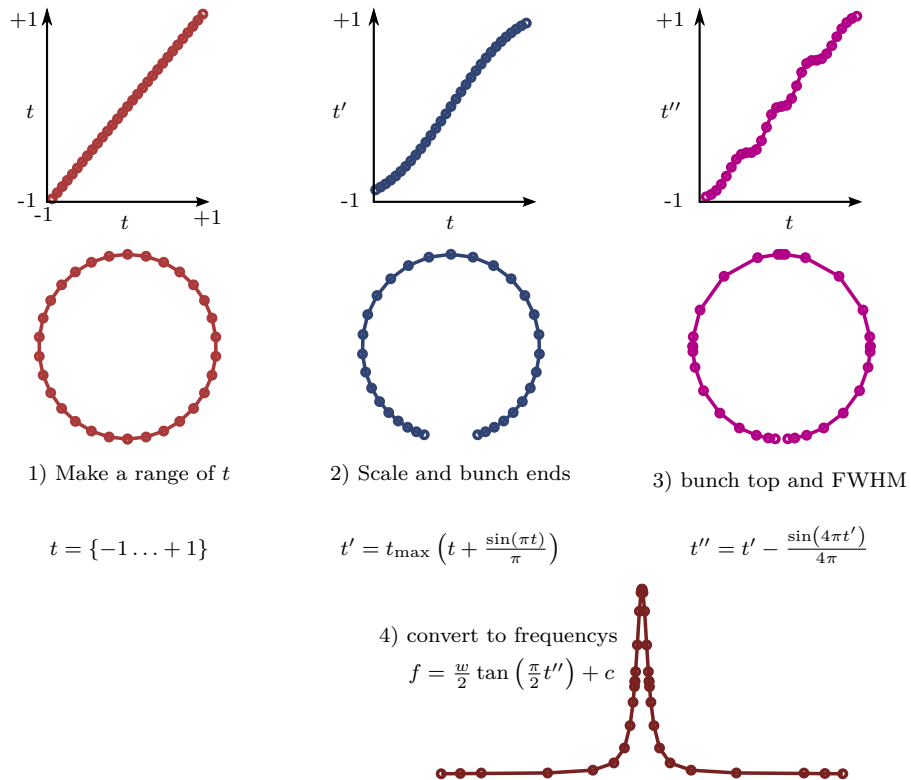


Figure 3.3.5: The generation of the Mphasy Pattern

The pattern has a free parameter, the t_{\max} scaling factor applied in step 1, this factor represents how wide the pattern will be. The factor after the two later transforms is no longer representative of θ_{\max} given in equal-space phase method, and equation 3.3.2 doesn't apply.

A direct analytically solution mapping widths to t_{\max} scaling is not possible, so we use a direct numerical method to solve this.

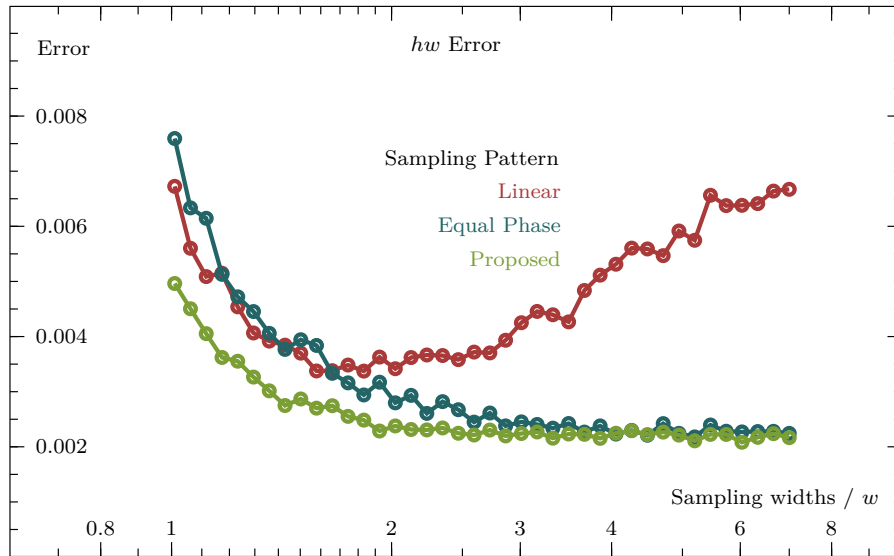


Figure 3.3.6: Comparing the new pattern to the equal in phase pattern and the linear pattern. The peak measured was sampled with 21 points and a 7.5 signal/noise.

Figure 3.3.6 shows that the Mphasy measurement pattern is an improvement on the equal phase pattern. The Mphasy pattern and the equal phase pattern trend to the same result when using a wide span, but at lowest error for the linear pattern is always higher than the Mphasy pattern. In practical terms, using Mphasy we get the improvement of measuring with equal phase while not having to sample as wide.

Experimental Verification on Real World Systems

We tested the new pattern using a vibrating wire resonator that was in use in a Lancaster University Dilution Refrigerator during the pre-cool stage and the beginning of an adiabatic demagnetisation process. The new sampling pattern was implemented in LabView and integrated into the existing measurement software.

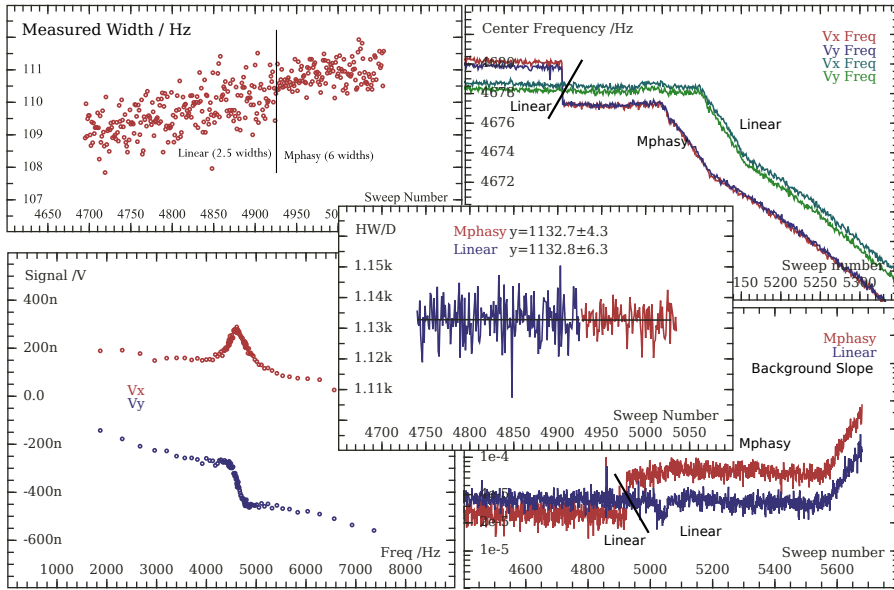


Figure 3.3.7: A collection of tests on the Mphasy measurement pattern compared to the linear spaced pattern on a real experimental vibrating wire resonator.

Figure 3.3.7 shows that using the proposed pattern gives a distribution of measurements with much less noise. In the top-left we can see the noise of the measured width is reduced. Top-right shows the tracking of the centre frequency has improved, and the V_x and V_y fitted curves now show the same fitted frequency. In the centre graph we see that the noise on the height \times width is reduced by about 33%.

The deviation away from an agreed value of frequency in the case of the linear spacing pattern is because of oscillator ring down and ring up, there is a lag between the setting of the generator driving frequency and the object oscillating steadily. This is partially mitigated in the new method as the step size between frequencies is smaller near the peak where the change in signal is largest.

Testing Tolerance Against Poorly Estimated Peak Parameters

If the inputs to the sampling pattern generator are not accurate then the benefits from the new pattern can be reduced. We test the proposed pattern against the linear pattern when the pattern generation used a

different centre and a different width to what the actual peak function used. In the regime where the peak is shifted by less than $0.5w$, Mphasy has a lower parameter error. When the width is mis-estimated, Mphasy is almost always better. The linear patterns at 2.8 and 5 widths, while individually tested, is correctly represented as a shift in width scaling factor. The symmetric shape of the 2.8 widths linear line is additional evidence that a linear width pattern around 2.8 is ideal if the width is well known.

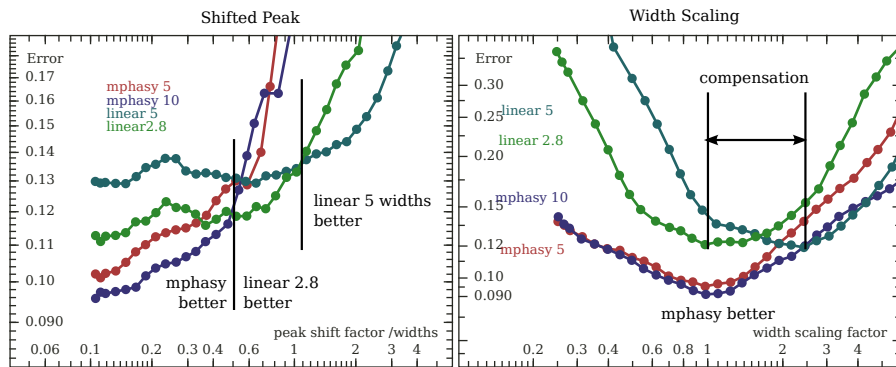


Figure 3.3.8: Testing the new sampling pattern against non-ideal pattern generation parameters. Each test uses 7.5 signal/noise and 21 points. The number after pattern indicated the span of sampling in multiples of the width.

If the peak isn't well known or is changing very quickly, greater than 0.5 widths between repeated measurements, a uniform density sampling pattern is better.

Benefits from the proposed pattern will scale as the number of measurement points increases. With an increased number of measurement points the effect of noise is reduced and the fitting error will decrease. Similarly if the noise is smaller the line shape will approach ideal and the fitting measurement error will drop.

Figure 3.3.9 shows the effect of the number of measurement points and the signal to noise ratio. The left graph can be interpreted as being able to get improved data for the same number of points, or you can get the same fitting quality by acquiring less data points, saving time.

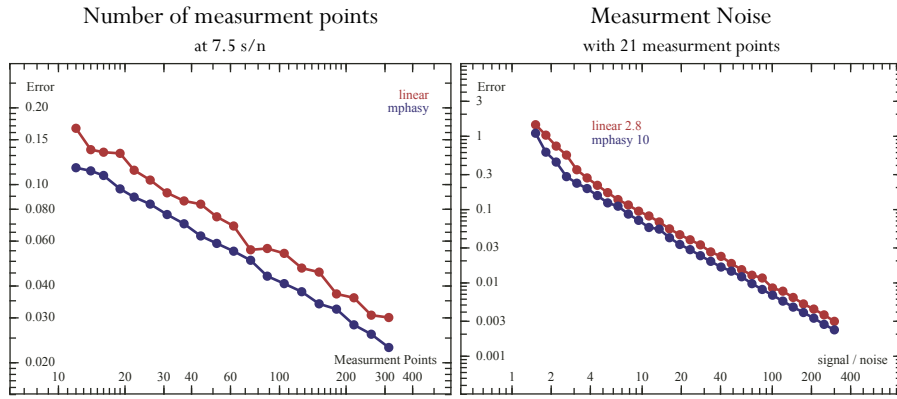


Figure 3.3.9: As the noise increases the improvement by using Mphasy stays near a constant ratio. By increasing the number of sampling points, the improvement ratio is constant.

Application to Other Peak Shapes

We can naively try the Mphasy pattern on other peak functions and test for improvements too. Because we designed the sampling patterns to use the width of the peak we need to use re-scaled version of the typical peak functions. The peaks of a Gaussian and Sinh are shown alongside the Lorentz in figure 3.3.10 as the improvement that the new pattern provides over a linear sampling pattern.

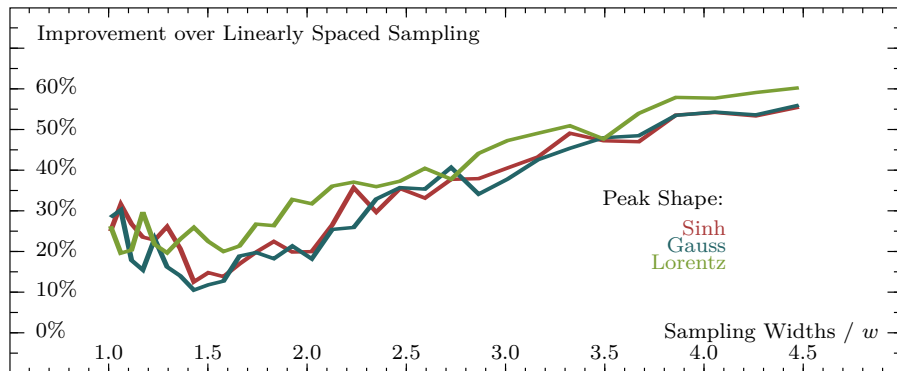


Figure 3.3.10: Using the proposed pattern compared to a linear pattern of the same span.

The largest improvements of the new pattern is when sampling the peak over a very wide span. When the optimum uniform density sampling span is chosen, around 2, then the improvement of the proposed pattern is near 30%. The improvements shown on the Gauss

and Sinh peaks are not as great as the improvement when used on the Lorentz peak. This is expected as the pattern was designed and optimised for the Lorentz peak but are nevertheless still apparent.

FURTHER WORK

The Mphasy pattern suggested here is only one of many ways to improve the measurement pattern. Other methods could implement potentially simpler or improved patterns. We focused on only one aspect of the peak measurement, additional development with a other focuses could find alternative optimisations. A shim function between the Mphasy pattern and new and different peak like functions could be used to account for the different definitions of width.

CONCLUSION

Using a linear spaced sampling pattern over a peak has the lowest measurement errors if the span of the sampling pattern starts approximately two peak widths below and ends two peak widths above the centre.

The linear pattern is not the best for measuring a peak, a more selective pattern that focuses more samples in five groups, the FWHM points on both sides, the top, and two regions that are the furthest away allowed, shows improvements of 30% or more. This sampling pattern is an improvement only if the centre location are initially estimated to within one FWHM of the true centre. As such the improved pattern is useful for repeated measurements on the same curve in peak tracking or monitoring application.

There are additional benefits using the new pattern on real world oscillating systems because of reduction in ringing caused of reduced sampling step size df near the peak.

Our sampling pattern is a useful method to be included alongside traditional methods when measuring peak like signals.

NANOMECHANICAL RESONATORS AS PROBES FOR QUANTUM FLUIDS

INTRODUCTION

This section documents work on the pioneering use of nanomechanical beams as probes for low temperature fluids. We operate the beams in liquid helium-4 between 1.2 K to 4.2 K, and test the feasibility of their use in micro-kelvin helium-3. Nanomechanical beams are in a category of devices called NEMS, Nano-Electro-Mechanical Systems, these are devices with a length scale less than 1 μm . NEMS are promising devices due to the small unit length mass to surface area ratio and they expand the available sensitivity range of probes and available techniques in Ultra Low Temperature, ULT, applications.

We use doubly clamped beams that have a square shape cross section of 100 nm by 100 nm and lengths in the range of 15 μm to 50 μm . This corresponds to mechanical resonant frequencies from 1.5 MHz to 8.4 MHz. The beams are electromagnetically driven and measured by a sweep of the drive frequency through resonance using a commercial vector network analyser.

Nanomechanical vibrating wire resonators have been previously used in a helium gas at 4.2 K, but did not succeed in measuring resonance while immersed in liquid [82] because of assumed technical difficulties. We present data of recently fabricated nanomechanical beams, and show the temperature dependence of liquid helium effecting the resonant characteristics. We operate the beams in vacuum, gaseous helium, and liquid helium at temperatures between 1 K and 4.2 K, and

compare the results of the change in mechanical resonance response to established hydrodynamic theories. There is potential for divergence from the two fluid hydrodynamic model by Blaauwgeers and Blazkova, that could be due to the acoustic effects becoming significant.

This work is very preliminary in the field of NEMS in quantum fluids, and should work well as a handbook for the handling and use of NEMS in a ULT experimental laboratory.

The first section introduces nanomechanical beams in more detail from the perspective of measuring the properties of liquid and gaseous helium. It goes on to explain the beam in more detail and briefly covers the fabrication process.

The second section outlines a brief theory of mechanical resonance as applied to doubly clamped beams, the electromotive motion, and how this creates measurable signals. The details of the various measurement circuits are described and analysed; this includes the simple test circuits, for beam integrity, as well as the resonance measurement circuits. This theory section includes information on helium-4 and the properties of a superfluid that are of scientific interest to this work.

The thermal properties of the beam are evaluated in a simulation to build an understanding of the device durability to electrostatic discharge and thermalisation along the beam.

The third section details the laboratory equipment, and the experimental cell designs used. Two different cryostats were used as we moved beyond basic feasibility and onto temperature dependence measurements. The preliminary experimental work took place in a 1.3 K glass cryostat using a small cell with a fixed magnetic field and limited thermometry and pressure control. The second purpose-built cryostat has more involved design. An external magnet provides a variable magnetic field, and the device is situated in a controllable helium-4 pot in a vacuum can for improved shielding, extended temperature range, and control.

The results sections are split according to the cryostats. The early tests show the ability to establish a signal from resonance and looked to observe if the resonance is mechanical. Several problems using NEMS beams in a ULT lab are addressed as progress is made to make nanomechanical beams a practical device. The beams are then used in the more advanced helium-4 cryostat and we measure the resonance and the resonance overtones of beams of different lengths. We test the behaviour of the device in gas at various pressures and the device response in fluid as the temperature changes. We draw comparisons between the response of different lengths and match it to a model of mass-displacement and viscosity.

BACKGROUND

Nanomechanical resonators join the other mechanical devices already used in the field of probes for experimental low temperature physics. Mechanically vibrating resonators are well suited to work in fluids in the milli-kelvin and even micro-kelvin regime as they directly measure the response of the fluid to motion and produce almost no heat leak into the experimental volume. This is due to devices typically being either superconducting or being only electrically reactive. The best experimental oscillating devices have a low ‘intrinsic width’: the resonance width at zero pressure and temperature, and have a large quality factor.

One of the applications of vibrating wire resonators, VWR, is to detect turbulence in superfluids [83]. VWR are used in many low temperature experiments, as thermometry in helium-3 [84, 85], creating vortices [86], measuring turbulence decays [87, 88], and measuring vortex line densities [89].

Many vibrating devices have been used to probe liquid helium including microspheres [90], wires [91], and grids [92]. Grids are particularly good at generating excitations in fluids. A recent development is to use piezoelectric quartz tuning forks [93, 94, 95]. Originally tuning forks were used for timing in electronic circuits, however tuning forks are being applied in other scientific fields such as scanning probe microscopy [96]. Due to the relatively small size and convenience compared to wire resonators, tuning fork arrays are being used detectors of quasi-particles in the fluid [97, 98]. The aims of this work is to understand one of the remaining challenges of classical physics - turbulence [99]. This application of detector arrays is of particular interest during development, because NEMS can be fabricated as arrays and could probe quantum fluid phenomena on a smaller physical length scale.

A category of devices called Microelectromechanical Systems, MEMS, are already being used to probe fluids [100]. MEMS for measuring helium can detect the viscosity of microkelvin helium-3 [101], with structures designed as combs [102]. Other MEMS devices are goal-post shaped cantilevers [103] which can be used with capacitive tuning [104] for frequency selection or are vibrating wire like [105]. MEMS have been used for measuring fluid flow, although they are dominated by surface effects [106]. MEMS have shown that it is currently possible to measure the fluid on increasingly small length scales, with NEMS as the next logical progression of sensors.

NEMS have been able to be fabricated since 1996 [107], but are only now being developed as fluid probes. This has been limited by the lack of a high fabrication yield, and high throughput fabrication, particularly in industrial settings [108]. Traditionally NEMS have been used as ultra-sensitive mass detectors involved in sensor applications in such diverse fields as explosives detection, drug discovery, and food diagnostics [109, 110].

The benefits of both MEMS and NEMS based technology is that they enable custom designed structures that are capable of probing at designed length scales chosen because of different transport properties. This could be of use in quantum fluids for detecting topological structures such as quantum vortexes.

The field of NEMS as probes hope to see the benefits of construction of arrays already seen in MEMS sensors for other systems [111].

Nano electro mechanical beam oscillators have been used in gaseous helium by Andreas Kraus et al [82]. This work did not achieve measurements in liquid, and were limited to showing gas dependency as results showed the signal almost completely disappears as the helium pressure increases. The devices used in our work have the benefit of being longer - 15 μm compared to 1 μm - and thinner - 100 nm to 200 nm, and are constructed with aluminium which results in a much

lighter linear mass density which improve suitability for measuring in liquid. Other work with nanomechanical oscillators [112] has measured singularly clamped resonators in three gases, He, N₂, and Ar, but not in liquid. Some non-wire based NEMS are a nano-scale mechanical cavity resonator and have used nanofluidic channels to probe liquid helium [113].

Nanomechanical resonators that have a large length compared to the thickness or width, are also called ‘nanotubes’ and ‘nanowires’, these are of interest in experimental physics because of their high sensitivity [114]. These devices can operate linearly [115], however a strong nonlinear response imposes a limit on the useful linear dynamic range [116], which limits the applications [117]. As nano scale beams are fabricated smaller the quality factor, Q , drops [118]. Experimentally, Q scales roughly as the inverse of the surface to volume ratio and is found to be in the range $10^3 - 10^4$ [119] in vacuum between 4 K to 40 K.

BEAM MANUFACTURING

The nanomechanical beam used for this work were fabricated by a colleague Sergey Kafanov in a clean room environment based on the previously established methods [120]. A brief outline of the fabrication process is as follows. Each chip starts off as a Si wafer with two layers of spun-on resist, a high contrast resist layer followed by a low contrast layer. The resists form a positive mask. An electron-beam lithography machine is used to draw the pattern of the beam and the transmission lines onto the resist. Once developed, the regions exposed to the electron beam are removed by plasma ashing, this leaves a void through the mask for the aluminium to be deposited onto. The top, low contrast, resist forms an aperture that aluminium will be deposited through into a larger void formed by the thicker rough mask. Aluminium was deposited over the wafer using an evaporator until a

height of 100 nm is built up. Acetone was then used to remove the mask, which leaves only the pattern of the unsuspended beam on the wafer substrate.

An O_2 and SF_6 100 W plasma at 180 mTorr is used to etch away the silicon substrate, this process removes the material surrounding the aluminium eventually undercutting enough to leave the beam suspended. The plasma is low power and high pressure to increase the isotropy of etching which improves the undercutting. A detailed recipe including timing and settings can be found in the appendix, figure [A.0.2](#).

The beams we used were designed to have a square profile of 100 nm by 100 nm, and can be produced with any length in the range of from 5 μm to 100 μm long, although the typical fabricated lengths were 15 nm, 25 nm, and 50 nm. One of the 15 μm long beams is shown in figure [4.3.1](#). These are among the slimmest aluminium beams compared to similar structures found in literature [[121](#)].

The choice of material, aluminium, is due to the low mass density and for its potential to be superconducting at low temperatures. The potential to be superconducting occurs if the magnetic field is below about 30 mT, and the temperature below about 1 K [[122](#)]. A lower mass density of aluminium increases mass sensitivity as it reduces the linear mass density of the beam. The aluminium beams with a 100 nm by 100 nm cross section have a linear mass density of $2.5 \times 10^{-11} \text{ kg m}^{-1}$ which is much lower than the silicon beams used in [[82](#)] of $3 \times 10^{-10} \text{ kg m}^{-1}$. Having a lower mass density increases the fraction of helium mass that comprises the total effective mass of the beam. The granular structure of the aluminium from the deposition process and the small cross sectional area can suppress the superconducting state. We expect the superconducting critical field and critical temperature B_c and T_c to scale together. An investigation

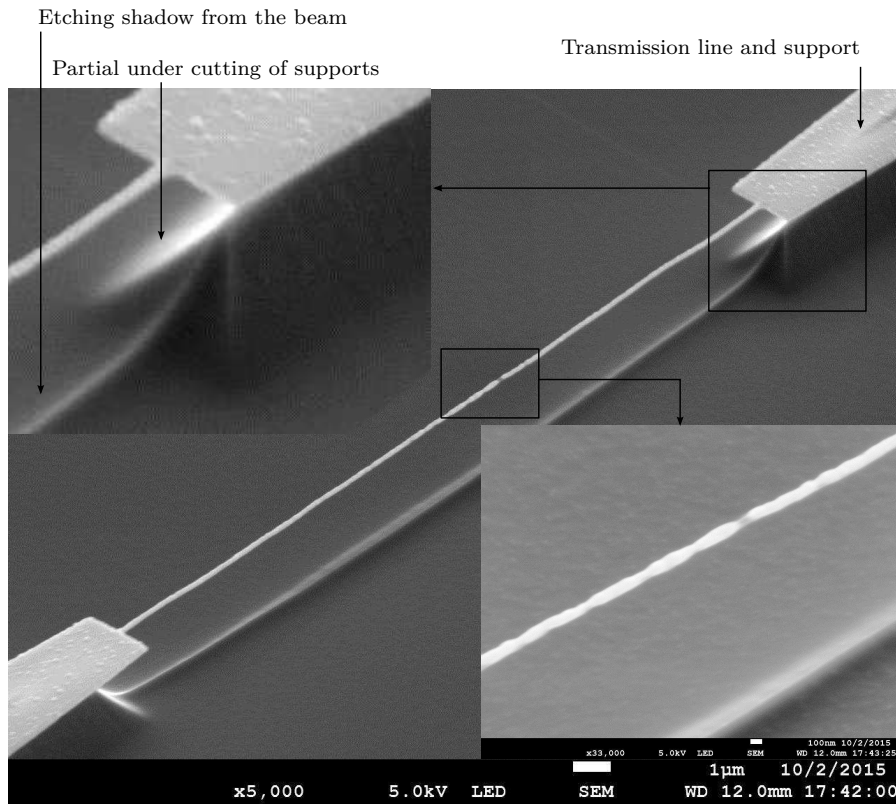


Figure 4.3.1: A scanning electron microscope image of a 15 μm long aluminium nanomechanical beam. An etching shadow is visible underneath the beam as a result of the plasma etching process. The plasma isotropy that causes undercutting of the beam also causes undercutting to the supports, this is seen as overhangs. The beam is suspended a few micrometres above the SiO_2 substrate. The insert shows the width changing down the length of the structure, this is due to imperfections of the aluminium deposition process.

of critical temperature for superconductivity of aluminium nanowires suggests a value well below the bulk value [123].

The devices will not be stress free after fabrication. The temperature of the aluminium during deposition is warmer than at room temperature, implying that at room temperature the beams will be in tension. The beam shown in figure 4.3.1 can be seen to be just curved as if slightly buckled, this seems to be caused by the etching process that removes the silicon for suspension. The beam is slightly longer than the support spacing. The exact shape of the beam changes for each individual beam, so that even sister devices will have slightly different tension and length characteristics. The device shown in figure 4.3.2 has a more extreme buckling. The extent of buckling can displace the beam by a distance equivalent to the separation between the beam and the substrate. This is a cause of concern as the beam should be probing bulk fluid, and motion in the vicinity of a surface could cause the beam to be probing partially clamped fluid in a complex manner.

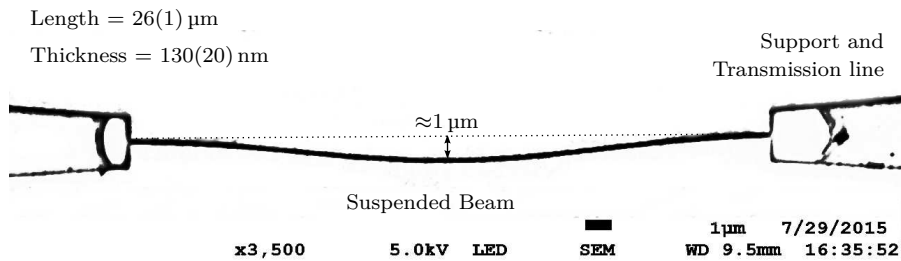


Figure 4.3.2: A digitally contrast enhanced image from a scanning electron microscope. One of the 15 μm long nanomechanical beams. The buckling from centre reaches a distance of 1 μm away from the centre-line. The effective length of the beam is slightly longer as the beam is stretched during the plasma etching. Measurements taken from the image have large uncertainties.

THEORY

This section will cover the theory of resonance of mechanical devices and describes the expected resonance shape for displacement and induced voltage as a function of frequency. The fundamental resonant frequency of the beam in vacuum can be predicted using existing models of massive doubly clamped beams, and we can use models that take into account additional tension from resonance and pre-existing tension. This section outlines some of the attempts to describe the overtone behaviour of the beam. Then, lastly, there is an introduction to helium and the superfluid behaviours that can be measured.

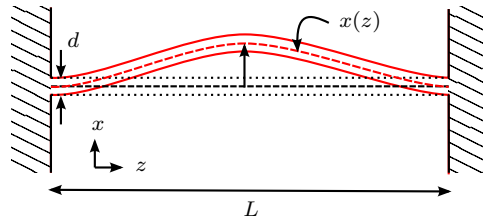
Resonance

Figure 4.4.1: The deflection of a beam because of the magnetomotive force.

Diagram re-created from [116].

In general resonating objects can be described by differential equations. There is a good introduction to resonance by Feynmann [99] that covers a derivation of the equation of motion starting with a summation of forces from mass m , restoring force k , and damping c

$$m\ddot{x} + c\dot{x} + kx = F \quad (4.4.1)$$

where $\dot{x} = \frac{d}{dt}x$ and $\ddot{x} = \frac{d^2}{dt^2}x$. The frequency dependent displacement ratio to the driving force is a function and angular frequency, $x = \mathcal{R}(\omega)F$ given by

$$\mathcal{R} = \frac{1}{m(\omega_0^2 - \omega^2 + i\gamma\omega)}. \quad (4.4.2)$$

The derivation for the measurable properties of a beam is a specific case of resonator and follows a similar derivation as used when describing the motion of a half-loop vibrating wire resonator [46]. The beam is modelled approximately as an infinite long cylinder in a magnetic field with a mass per unit length $\mu = m/L$. This approximation is good as the aspect ratio of thickness to length is large.

The beams are excited and detected using the magnetomotive scheme [124]. The beam experiences a Lorentz force exerted by a driving current $I = I_0 e^{i\omega t}$ in a magnetic field, producing a motion perpendicular to both the magnetic field and the current. The driving force is equal at every point on the beam. A restoring force is dependent on the beam displacement x away from the resting position $x = 0$. This force is proportional to an effective spring constant, k : $F = -kx$. The motion at resonance has the relation $\omega_0 = \sqrt{k/\mu}$, so that a force per unit length acting on the beam is $\mu\omega_0^2 x$.

The equation of motion per unit length is described as the sum of forces equal to the driving force,

$$\mu\ddot{x} + \mu\lambda\dot{x} + \mu\omega_0^2 x = BI_0 e^{i\omega t}. \quad (4.4.3)$$

The term with λ is used to describe a velocity dependent damping force. If the beam is immersed in liquid this would partially relate to the viscosity of the fluid. The complex nature of $\lambda \rightarrow \lambda_2 + i\lambda_1$ can be used to describe both the in-phase dissipative component, and an out-of-phase non-dissipative component that is associated with the inertia of fluid backflow [46].

Equation 4.4.3 can be solved for a steady state solution ($\dot{x} = \dot{x}_0 e^{i\omega t}$) to give

$$\dot{x}_0 = C \frac{I_0 B}{\mu} \left(\frac{i\omega}{\omega_0^2 - \omega^2 - \omega\lambda_1 + i\omega\lambda_2} \right). \quad (4.4.4)$$

This introduces a constant C that is used to describe the maximum spacial displacement. The term ω_0 is the resonant frequency in the

presence of zero damping, $\lambda_1 = 0$. The maximum velocity with damping is at the effective resonance frequency ω'_0 , which is when $\omega_0^2 - \omega^2 - \omega\lambda_1 = 0$. The solution to the quadratic $w_0^2 - w_0'^2 - w_0'\lambda_1 = 0$ is

$$w'_0 = \frac{1}{2} \left(\sqrt{4\omega_0^2 + \lambda_1^2} - \lambda_1 \right). \quad (4.4.5)$$

The width of resonance is the difference between the frequencies which have half the maximum amplitude, ω_{half} , and called the full width at half maximum, FWHM. This is found by the difference between the positive two solutions to the quartic equation $(\omega_0^2 - \omega_{\text{half}}^2 - \omega_{\text{half}}\lambda_1)^2 - \omega_{\text{half}}^2\lambda_2^2 = 0$ which is

$$\omega_{\text{half}}^+ = \frac{1}{2} \left(\sqrt{4\omega_0^2 + \lambda_1^2 - 2\lambda_1\lambda_2 + \lambda_2^2} - \lambda_1 + \lambda_2 \right) \quad (4.4.6)$$

$$\omega_{\text{half}}^- = \frac{1}{2} \left(\sqrt{4\omega_0^2 + \lambda_1^2 + 2\lambda_1\lambda_2 + \lambda_2^2} - \lambda_1 - \lambda_2 \right) \quad (4.4.7)$$

$$\Delta f = \frac{\omega_{\text{half}}^+ - \omega_{\text{half}}^-}{2\pi}. \quad (4.4.8)$$

Using the full form of the frequency response curve on experimental data is not possible if we allow both ω_0 and λ_1 to be free parameters. We can simplify the damping term, λ , and set for any one curve $\lambda_1 = 0$ and then use the form

$$\dot{x}_0 = A \left(\frac{i\omega}{\omega_0^2 - \omega^2 + i\omega\lambda_2} \right) \quad (4.4.9)$$

which gives a width of $\Delta f = \lambda_2/2\pi$ at resonant frequency of $f_0 = \omega_0/2\pi$ and a maximum velocity of A/λ_2 .

The beam moving due to a magnetic field also induces a voltage across the beam proportional to \dot{x} . We use equation 4.4.9 to fit the induced voltage response of the beam absorbing geometric factors and field strength into A .

We can further modify the equation 4.4.9 to be parameterised with the width and height as fitting parameters. Experimental data can be fitted to a Lorentz peak of the real component, V_x , and the complex components V_y using

$$V_x(f) = \frac{A\Delta f^2}{\Delta f^2 + \left(f - \frac{f_0^2}{f} \right)^2}, \quad (4.4.10)$$

and

$$V_y(f) = \frac{\frac{-1}{f} A \Delta f (f^2 - f_0^2)}{\Delta f^2 + \left(f - \frac{f_0^2}{f}\right)^2}. \quad (4.4.11)$$

These are equivalent to

$$V_x(f) = \frac{A \Delta f^2 \cdot f^2}{\Delta f^2 f^2 + (f^2 - f_0^2)^2} \quad (4.4.12)$$

and

$$V_y(f) = \frac{-A \Delta f \cdot f (f^2 - f_0^2)}{f^2 \Delta f^2 + (f^2 - f_0^2)^2}. \quad (4.4.13)$$

The second form is preferred if computational fitting time is important, as there is one less division at the cost of pre-computing f^2 .

Some derivations [94] make the assumption that the resonant quality factor is large and that the damping is small, $\lambda_1, \lambda_2 \ll \omega$, however we can not make these.

Any power that is absorbed into the beam during resonance will have a frequency dependence of $P(f) \propto |V(f)|^2$. The proportionality constant can be absorbed into the height free parameter, A , and then the power absorbed has a shape of

$$P(f) = V_x(f)^2 + V_y(f)^2. \quad (4.4.14)$$

with a maximum power absorbed on resonance of $P_{\max} = A^2$.

The Lorentzian line shape of resonance is only valid if the beam is oscillating in a linear way. Physical resonant objects respond linearly at low amplitudes and velocities. However at large amplitudes there may be damping from a non-linear term, c ,

$$\ddot{x} = -\beta \dot{x} - kx(1 + cx^2) + A \sin(\omega t). \quad (4.4.15)$$

This can cause the tip of the peak to ‘bend’ towards higher or lower frequencies, causing an asymmetric and un-centred frequency response. If the frequency at high amplitudes increases, this is known as spring hardening or k -hardening. It physically means that as the amplitude of displacement increases the spring constant of the oscillator, like

a harder spring. Similarly there is also k -softening where the spring constant effectively drops at high amplitudes. This non-linear oscillator is called a Duffing oscillator [125]. An oscillator changes from linear to non-linear, Lorentzian to Duffing, gradually. The peak becomes increasingly non-symmetric with increasing power and eventually reaches a critical amplitude, at which the response has a discontinuous jump or is multi-valued, shown in figure 4.4.2. This appears at an amplitude called the critical amplitude a_c . The nonlinearities can occur because of the way the beam is clamped to the support material, or be due to an electrostatic attraction to a nearby electrode, or from the geometry if the displacement exceeds the thickness of the beam [126].

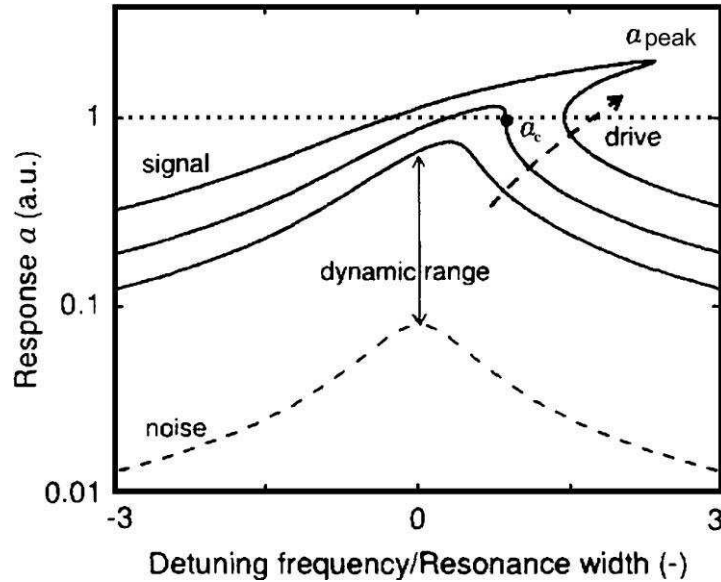


Figure 4.4.2: The dynamic range of an oscillator response is the linear region between the noise floor and the onset to non-linearity. Extracted from [116].

Fundamental Frequency

The expected resonant frequency $\omega_0 = 2\pi f_0$ of nanomechanical beams will depend on the length of the beam, l , and the two other beam dimensions, depth d , and thickness t , as well as the material properties including the density ρ and Young's modulus, E . We can look up book

values for the Young's Modulus for aluminium $E = 69 \text{ GPa}$, and the mass density of aluminium $\approx 2700 \text{ kg m}^{-3}$.

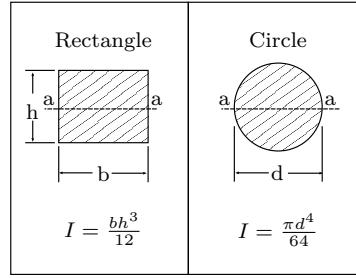


Figure 4.4.3: The moment of inertia for vibrating beam [127].

A property called the area moment of inertia, I , limits the motion of the beam and depends on the cross sectional area of the device. The value for I is a geometrical property of an object with respect to an arbitrary axis. Figure 4.4.3 shows the result for a square and a circular profile moving about an axis from the centre, marked a-a in the diagram.

However, the exact shape of the cross section is unknown, as a result of the manufacturing which causes some rounding of the edges, visible in figure 4.3.1. The etching process will not create a straight sided walls, creating a rounded rhombus, or ‘egg’ shaped cross section. We can estimate limits of the area moment of inertia by assuming that the depth and width of the beam are equal, $d = b = h$ in figure 4.4.3, so that the maximum the area moment of inertia is the square profile which has

$$I_{\max} = \frac{d^4}{12}. \quad (4.4.16)$$

We can use the circular profile as a prediction for the lower limit of I ,

$$I_{\min} = \frac{\pi d^4}{64} \approx 0.59 I_{\max}. \quad (4.4.17)$$

We can look at some of the earliest fabricated nanomechanical beams made of Si in 1996 [107]. This suggest that the resonant frequency of beams whilst not under tension is

$$\omega_0 = 2\pi C_0 \sqrt{\frac{E}{\rho}} \frac{w}{l^2} = \left(\frac{4.73}{l}\right)^2 \sqrt{\frac{EI}{\rho A}} \quad (4.4.18)$$

where w is the width of the beam in the direction of the motion, and l is the length of the beam. This relation has described experimental beams of frequencies up to 380 MHz [118].

Further analysis of the resonance of beams includes the effect of tension [116]. The motion of the beam includes a sum of residual tension T_0 , and the bending-induced tension. The equation describing the motion of the beam can not be solved exactly, but has been approximated by the Galerkin discretization procedure [125] to arrive at the resonance frequency

$$\omega_0 = \frac{4\pi^2}{L^2} \sqrt{\frac{EI}{3\rho A} \left(1 + \frac{L^2 T_0}{4\pi^2 EI}\right)}. \quad (4.4.19)$$

An approximation of the error on ω_0 in equation 4.4.19 suggests the actual expected frequency is lower.

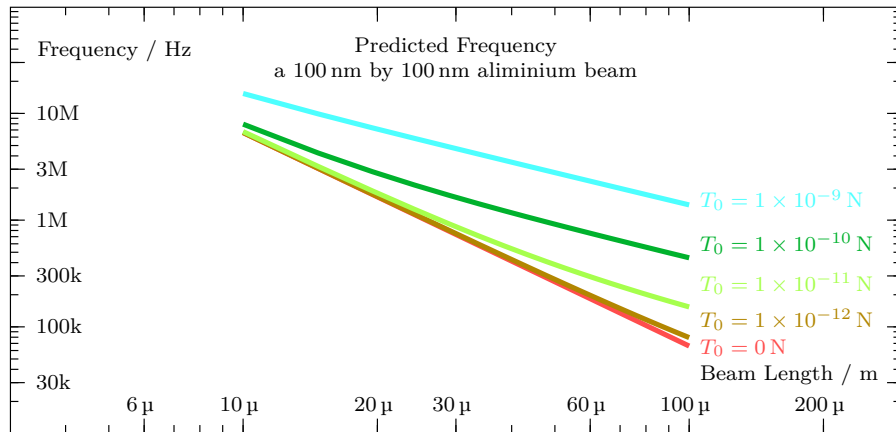


Figure 4.4.4: The predicted resonant frequencies using equation 4.4.19 with a range of tensions.

We can use a predictable thermal differential contraction between the aluminium and the silicon substrate to predict one contribution to the tension, T_0 . As the relative length of the beam changes ΔL , the tension is $T_0 = EA(\Delta L/L)$. The length contraction is relative between the two materials, $\Delta L/L = \left(\frac{\Delta L}{L}\right)_{\text{Al}} - \left(\frac{\Delta L}{L}\right)_{\text{Si}}$. As the device cools down the aluminium beam shrinks more than the silicon substrate, increasing the tension along the beam, which increases ω_0 . We can use the thermal contraction between room temperature, 300 K, to the measurement temperatures of approximately 4 K. The value of $(\Delta L/L)_{\text{Al}}$ is between

0.0038 and 0.0041 depending on the aluminium purity [128], and for silicon $(\Delta L/L)_{\text{Si}} = 0.000242$ [129], which is comparably negligible. This gives a thermal tension of $T_0 = EA(0.0038) = 3.0(3)$ nN. This model needs to be expanded even further to enable some intrinsic beam tension, T_i , which exists at room temperature, $T_0 = EA(\Delta L/L)_{\text{Al}} + T_i$.

The usefulness of prediction of resonant frequency is limited further by the sizeable uncertainty of the area moment of inertia, and the unknown tension in the beam after fabrication. Without knowing either the boundary conditions, exact geometry, or the precise cross section, estimates of f_0 have a wide span of frequencies. The string-like model of equation 4.4.19 describes straight beam and the resonance induced tension from the Young's modulus. As our beams are often not entirely straight, shown in figure 4.4.5, and have additional beam length that is longer than the support distance, just like a coiled spring, the effective Hooke's constant is reduced over simply the bulk Young's modulus value that equation 4.4.19 would imply. This effects the tension from thermal differential contraction and the resonance induced tension.

A possible remedy would be to SEM image each individual device to acquire the exact 3D geometry and then use finite element analysis to model the resonance frequency.

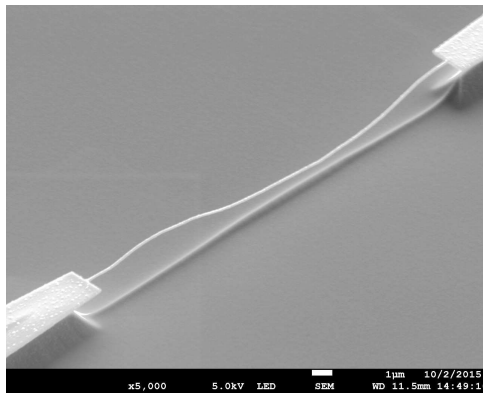


Figure 4.4.5: An SEM image of a 15 μm beam showing the irregularities of the beam's shape. Due to the extra length of the beam between the supports, the resonance induced tension and the tension from differential thermal contraction, will not scale with an unknown fraction of the Young's modulus of bulk aluminium.

Overtones

The prediction of the overtones are not included in the equation 4.4.19 [116], so we compare other existing models.

We look at different models to try and predict the harmonic and overtone behaviours of the beam. A simple model is to use a sonometer,

$$f_0 = \frac{n}{2l} \sqrt{\frac{T}{\mu}}. \quad (4.4.20)$$

The mass per unit length μ and the length l are well known, but the tension T is unknown. This predicts that each harmonic number n scales the frequency of the resonator, $f_{n=2} = 2f_{n=1}$. This scaling is also the same if the beam has very low tension.

We look up the formula for the frequency for common systems and find that for a so-called ‘massive beam’, a beam with continuous distributed mass, that is suspended between two points [130, 127]. The resulting equation depends on the boundary conditions. The likely boundary conditions is the fixed-fixed case, as shown in figure 4.4.6. The fixed-fixed boundary condition sets the gradient of amplitude to zero at the edges. The massive beam system suggest a resonant frequency of

$$f_0 = 2\pi \cdot A \sqrt{\frac{EI}{\mu \ell^4}} \quad (4.4.21)$$

where E is Young’s modulus, and I is the area moment of inertia. The coefficient A is shown in table 1, from pre-calculated solutions to the equations of motion with different boundary conditions [130, 127].

The scaling of the harmonic frequency increase much faster with these systems than the sonometer. We can use the ratio of the observed harmonics to understand which system is the nanomechanical beam behaving like.

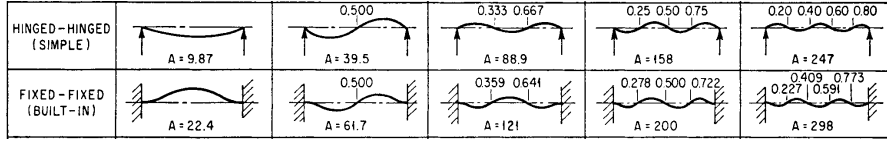


Figure 4.4.6: The resonant frequency of a massive beam suspended between two fixed points [127]. Each of the overtones are at slightly different ratios of the fundamental frequency. The value of A for each mode is a calculated coefficient used for predicting the resonant frequency, equation 4.4.21.

Table 1: Table of Coefficients for equation 4.4.21, predicting the Resonant Frequency [130], extended by calculations in [127], table 7.3. The Hinged-Hinged values scale above 5 as $\approx (\pi n)^2$, and the Fixed-Fixed values scale as $\approx ((2n + 1)/2)^2$.

Mode:		1	2	3	4	5
Hinged-Hinged	A	9.87	39.5	88.9	158	247
	A/A_1	1	4.002	9.007	16.00	25.03
Fixed-Fixed	A	22.4	61.7	121	200	298
	A/A_1	1	2.754	5.401	8.929	13.30

NEMS in Helium

The interest of the nanomechanical beams is to probe the behaviour of quantum fluids. A quantum fluid has quantum mechanical effects that are observable at the macroscopic level. These quantum fluids are realised in superfluids, superconductors, and some ultra cold gases. Helium is interesting because of its superfluid states.

Helium has two stable isotopes, helium-4 and helium-3. All experimental results described in this NEMS part of the thesis was done in helium-4. Of the two, helium-4 is much more common, with approximately 1 000 000 He^4 atoms for every He^3 atom [131]. Helium-4 has an atomic mass of 4.0026u from two neutrons and two protons. The two electrons that balance the charges of the protons are in the

$1s^2$ electron shell [132]. Because of the complete outer shell, helium is chemically inert.

Helium-4 has two neutrons in the nucleus, with each having a half integer spin, giving the whole atom a net integer spin. This means that helium-4 is a composite boson that obeys Bose-Einstein statistics [133]. At low enough temperatures the helium will undergo a Bose-Einstein condensation and many of the helium atoms will have macroscopic occupation the ground state energy level, becoming indistinguishable [134, 135, 136].

The discovery of this phase of the fluid [137, 138] showed that helium-4 has no viscosity below a transition temperature of 2.17 K at saturated the vapour pressure.

The phase diagram of helium, sketched in figure 4.4.7, shows no triple point and splits the liquid state by a λ -line. Below the λ -line is the superfluid state, called HeII [139].

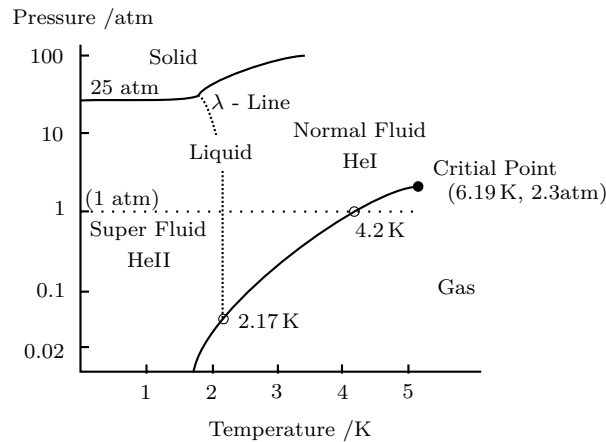


Figure 4.4.7: A sketch of the pressure-temperature phase diagram for helium-4. Based on an image from [133].

The phase diagram of helium can provide thermometry of the liquid by having a system on the saturated vapour pressure line, between gas and liquid. This line is single-valued which enables a measurement of the pressure above a vessel of helium that is being pumped towards vacuum, to on the saturated vapour pressure line, and have a known temperature. Assuming that there is no significant flow impedance

between the pump and a pressure gauge, then the ITS-90 temperature scale can be used [140].

Once in a superfluid state, the fluid has non-classical phenomena such as irrotationality, quantum turbulence [141], and thermal counterflow [142] that are still being studied [143]. The vortices in quantum turbulence can be spontaneously created above a critical velocity [144] and have quantised circulation.

The superfluid can be described with a phenomenological model of a normal fluid as a gas of excitation over the ground state superfluid [141]. The two fluid model logically separates the fluid into two interpenetrating and non-interacting components called the normal viscous fluid component n , and the superfluid component s with zero viscosity and zero entropy. The density of each changes over temperature $\rho = \rho(T)$ where $\rho_n + \rho_s = \rho$. Total density is conserved with each component moving separately to form a momentum current density $\vec{j} = \rho_n \vec{v} + \rho_s \vec{v}_s$. As the temperature decreases, there is less normal fluid component and more of the superfluid component, until at zero temperature when $\rho_n/\rho = 0$. The fraction of normal fluid at 1.5 K is 10%, and the fluid is considered pure superfluid below 1 K [145]. The densities are shown across a range of temperature in figure 4.4.8.

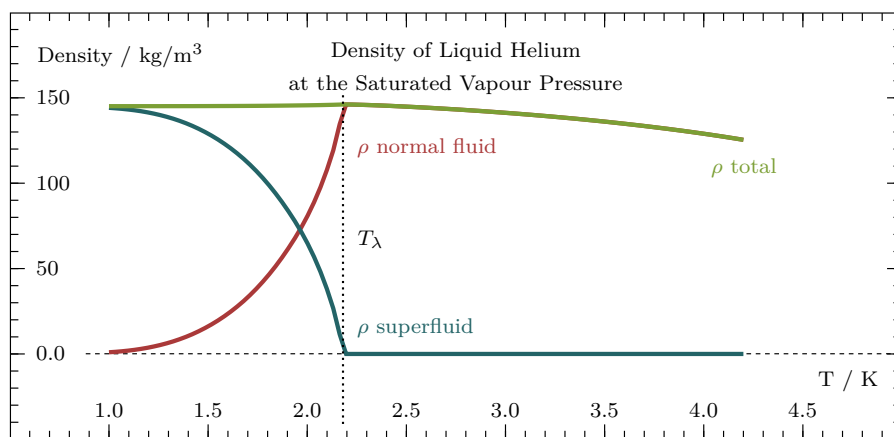


Figure 4.4.8: The densities of liquid helium-4 at the saturated vapour pressure.

This shows superfluid density appearing below T_λ , and the normal fluid density dropping conserving total density. These curves are produced from the spline fits documented in [145].

*Frequency Shift and Width Changes due to the Temperature Dependent
Liquid Helium Properties*

We use a theory from Blaauwgeers et al [51] that uses the two fluid model to describe how the centre frequency and resonant width changes using the hydrodynamic effects of the fluid effective mass and the Stokes' drag. This method has been used to describe wires and tuning forks [146].

Their theory uses three free parameters for the geometry of the oscillator, β , B , and C , as well as the fluid properties. The terms β and B describe the mass enhancement of the beam while in liquid. β describes the mass of helium that is displaced by the volume, V , of the beam, while B describes the mass of the attached fluid in a volume extruded a distance of the viscous penetration depth, δ , around the beams' surface, S , this is sketched in figure 4.4.9. The additional mass is

$$m^* = \beta\rho V + B\rho_n S\delta. \quad (4.4.22)$$

The displaced volume term uses the full density of the fluid ρ while the attached mass only uses the normal fluid fraction, as by definition the superfluid component can not be attached. The fluid properties are functions of temperature that have been measured for liquid helium and are known and provided by parametric curves from Donnelly and Barenghi 1998 [145].

The change of the resonance frequency in liquid, f_i away from vacuum resonance, f_0 , is derived by relating the same oscillator, with same spring constant k , but with two different masses, m and $m + m^*$. In vacuum, $\omega_0 = \sqrt{k/m}$, and in liquid, $\omega_i = \sqrt{k/(m + m^*)}$, which are related through k to get $(f_0/f_i)^2 = (m + m^*)/m$. This simplifies to

$$\left(\frac{f_0}{f_i}\right)^2 = 1 + \beta\frac{\rho(t)}{\rho_{\text{obj}}} + B\frac{S\delta\rho_{\text{nf}}}{V\rho_{\text{obj}}}. \quad (4.4.23)$$

V is the volume of the beam and is calculated by the length, width, and thickness ($V = lwt$), similarly S is the surface area of the beam,

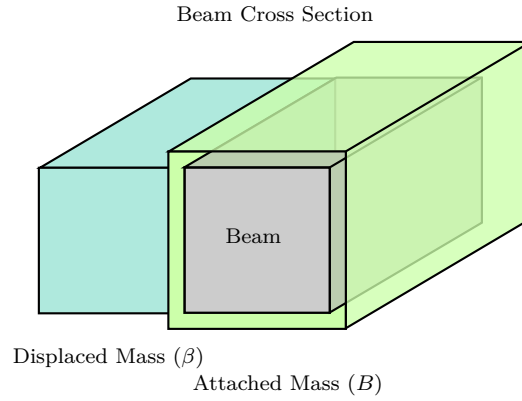


Figure 4.4.9: A sketch showing a section of beam and a volume around the beam representing the attached mass, and a volume beside the beam showing the displaced mass. The displaced mass scales with the volume of the beam and a coefficient β , and the attached mass scales with the surface area of the beam and a coefficient B .

estimate as $S \approx 2l(w + t)$. The term ρ_{obj} is the density of the beam, of aluminium, 2700 kg m^{-3}).

The viscosity of helium-4 as a function of temperature, $\eta(t)$, is related to the viscous penetration depth, δ , by

$$\delta = \sqrt{\frac{2\eta}{\rho\omega}}. \quad (4.4.24)$$

The resonant width is an application of Stoke's drag by the liquid, this is

$$\Delta f = C \frac{S}{2\rho_{\text{obj}}V} \cdot \sqrt{\frac{\rho_{\text{nf}}(t)\eta(t)f_i}{\pi}} \left(\frac{f_i}{f_0}\right)^2. \quad (4.4.25)$$

When using the equations 4.4.25 and 4.4.23 for fitting experimental data, the free fitting parameters are β , B , and C . β and B are found using equation 4.4.23, and C is found by fitting 4.4.25.

The physical meaning of C depends on geometry of the oscillator, a value of $C = 2$ implies an infinitely long cylinder oscillating perpendicular to its axis, while $C = 3/2$ would be an oscillating sphere. The terms β and B also have pre-calculated values, for a sphere, $(\beta \ B) = \left(\frac{1}{2} \ \frac{3}{4}\right)$. For an elliptical cylinder described by perpendicular radius r_{\perp} and parallel radius r_{\parallel} with regards to the axis of motion then

$\beta = r_{\perp}/r_{\parallel}$. For a rectangular beam with parallel and perpendicular sides, a_{\perp} and a_{\parallel} , then $\beta = \frac{\pi a_{\perp}}{4 a_{\parallel}}$. So with our beams we can expect $\beta \approx B \approx 1$. These expected values are derived from substantial numerical computation [147].

Gas Sensitivity

We modify the equation for damping in liquid using the ideal kinetic gas equations. We build a model to which describe the gas in terms of the mean free path, and root-mean-squared velocity and describe the expected width, Δf , behaviour in gaseous helium. To modify equation 4.4.25 to be applicable in gas, the liquid dependent terms of $\rho_n(t)$ and $\eta(t)$ are replaced with the gas density and gas viscosity,

$$\rho = \frac{Pm}{k_{\text{B}}T}, \quad (4.4.26)$$

and,

$$\eta = \frac{1}{3}\langle v \rangle \langle \lambda \rangle \rho, \quad (4.4.27)$$

where m is the mass of a helium-4 atom $m = 6.64 \times 10^{-27}$ kg, $\langle v \rangle$ is the RMS velocity of a helium atom in the gas, and $\langle \lambda \rangle$ is the mean free path. The mean free path of an ideal gas is

$$\langle \lambda \rangle = \frac{1}{\sqrt{2}\sigma n} = \frac{k_{\text{B}}T}{\sqrt{2}\pi d^2 P} \quad (4.4.28)$$

where σ is the collision area between two atoms $\sigma = 4\pi d^2$, d is the diameter of a helium atom $d = 140 \times 10^{-12}$ m from the van der Waals radius, and the RMS velocity is $\langle v \rangle = \sqrt{\frac{3k_{\text{B}}T}{m}}$.

The viscosity of gas with the $\langle v \rangle$, $\langle \lambda \rangle$, and ρ terms expanded is

$$\eta = \frac{1}{\pi d^2} \sqrt{\frac{k_{\text{B}}Tm}{6}} \quad (4.4.29)$$

which is used in equation 4.4.25 so that

$$\Delta f = \frac{CSm}{2\pi\rho Vd} \cdot \sqrt{\frac{Pf_i}{\sqrt{6}k_{\text{B}}Tm}}. \quad (4.4.30)$$

This gives a quality factor, $Q = \Delta f/f_i$, of

$$Q = \frac{2\pi\rho Vd}{CSm} \cdot \sqrt{\frac{f_i\sqrt{6}k_{\text{B}}Tm}{P}}. \quad (4.4.31)$$

The value of C in equation 4.4.31 is the same as C in equation 4.4.25 and should be consistent across two different experiments: the temperature dependence in liquid, and the pressure dependence in gas.

Equation 4.4.31 shows a $Q \propto 1/\sqrt{P}$ dependence when described by damping of an ideal gas. However at very low pressures there is the Couette-flow model and Christian's Model for Rarefied Air Damping, which both suggest $Q \propto 1/P$ [148]. These are low pressure theories, that assume gas molecules collide with the device, but not each other, then the number of collision increases linearly with P . The paper [149] has shows a $Q \propto 1/P$ pressure-Q model that work with a MEMS beam, 200 μm long and 40 μm wide.

Previous theoretical work has also shown that at high pressures the quality factor should be $Q \propto P^{-1/2}$, a results of the Navier-Stokes equations [150, 112].

MEASUREMENT CIRCUITS AND ANALYSIS

This section covers the experimental circuits for measuring the resonance of the beam, as well as several test circuits. The test circuits measure the continuity and the finite resistance of the beam, using DC, AC and a vector network analyser. This section describes the analysis of extracting the properties of the beam, like the maximum displacement and velocity during resonance. The problems of working with high frequency signals are addressed and we describe how we can extract induced voltages in spite of a frequency dependent phase shift.

Test Measurements Circuits

Measurements of nanomechanical beams need to be careful to apply low powers to the beam, as the very small beams act like very sensitive fuses. The beam needs a very low measurement current of the order of nano-amps, as well as requiring static safe methods to attach the beam to the measurement circuits.

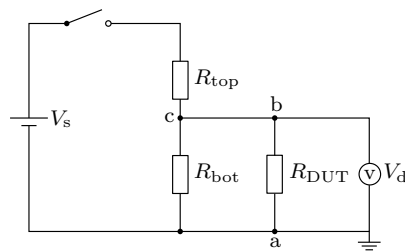
DC measurements

Figure 4.5.1: A DC measurement circuit used to find the DUT resistance using very low excitation currents. The circuit was constructed using coaxial lines to reduce electrical noise and was grounded only through the nano-voltmeter.

Figure 4.5.1 was used to measure the DC resistance of a beam, called the Device Under Test, DUT. Before the beam was attached, it was

necessary to attach electrical shorts that were connected to ground on both sides of the beam. We were careful to protect against an inrush current from the parasitic capacitance between points c and a, which is why we had chosen $R_{\text{bot}} = 1 \text{ M}\Omega$ to bleed down any trapped charge to ground. The choice of $1 \text{ M}\Omega$ was too large, a correct choice would be 200Ω , which is approximately the same magnitude as the beam resistance. The bottom resistor, R_{bot} , sets up a current divider that reduces sensitivity if too low, and reduces protection if it is too high.

To measure the resistance, we needed a low noise nanovoltmeter from point (b) to ground. Practically we also needed to remove a background voltage, V_{bg} , that is measured when the switch is open. The background voltage is subtracted from the on voltage, V_{on} , measured when the switch was closed to find the true divided voltage $V_{\text{d}} = V_{\text{on}} - V_{\text{bg}}$ and measure the device resistance

$$R_{\text{DUT}} = \frac{1}{\frac{V_{\text{s}} - V_{\text{d}}}{V_{\text{d}} R_{\text{top}}} - \frac{1}{R_{\text{bot}}}}. \quad (4.5.1)$$

We built this measurement circuit to run from a cr2032 battery for low noise (compared to usual transformer \rightarrow rectification \rightarrow filtering \rightarrow linear regulator \rightarrow filtering route) and for simplicity. The circuit is grounded only through the nanovoltmeter. The DC test circuit was built in a 300 nA and 100 nA variants by changing R_{top} . The resistance measurements are calibrated before use using known resistances, and the circuit achieves a 5Ω resolution at 100Ω . The DC circuit poor performance was superseded by the AC resistance measurement methods.

AC Resistance Measurements

We improved upon the accuracy of the resistance measurements using a differential amplifier and a signal generator as part of an AC circuit. Using a lock-in amplifier and a few external components we measured R_{DUT} with greater precision and lower currents than the DC method previously. The alternating current removes the need for background

voltage compensation and we can neglect the effect of large thermal-voltages from the Peltier-Seebeck or Thomson effects [151].

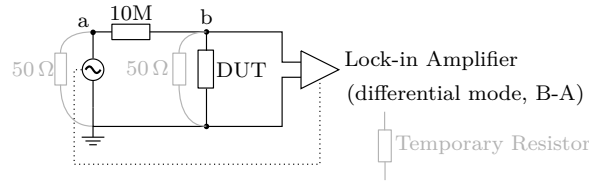


Figure 4.5.2: An AC circuit for measuring the beam’s resistance using very low amplitude excitation currents.

The lock-in amplifier (a Stanford Instruments SR830) has an oscillator output with a voltage range between 2 mV to 1 V. To attach the beam, we first attached 50 Ω pull down resistors between points a to ground and b across the device to ground. We kept the generator amplitude on to prevent any start up spikes, but at the lowest amplitude and then removed the pull down resistors in the order: first from point b and then from point a, to offer the most protection from static. Another benefit of the AC circuit is the ease of ramping the generator voltage to check the linearity of the ohmic response. It is easy to check currents from 1 nA to 5 nA in 1 nA steps to observe the ohmic response of the beam. We choose a low frequency of 83 Hz to avoid the mains, and the mains overtones, while still being low enough for reactance effects to be negligible.

Vector Network Analyser Beam Checking Circuit

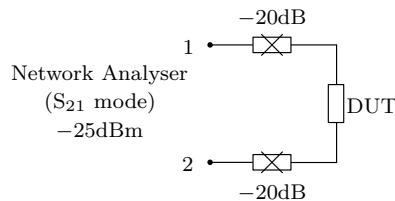


Figure 4.5.3: Using a network analyser to quickly test if the beam is intact and has electrical continuity. Attaching two -20 dB attenuators on both sides of the DUT ensures safe handling as it provides a low impedance current path around the device.

The quickest safe test of electrical continuity of the beam is to use a network analyser, abbreviated NA, in the configuration shown in figure 4.5.3. Using -25dBm of applied power, we determine that the beam has continuity if we measure a transmission of about -47 dB , or continuity is broken if we observe about -70 dB (this is the noise floor of an open circuit at this measurement power). The frequency range of the NA was set as low as possible to about 1 MHz in order to check for a flat frequency response. Some failures of the beam were very small fractures and these act like a capacitor in series, producing a drop of transmission only at low frequencies.

The test with symmetric attenuators on a NA is favoured due to the protection offered to the beam while still having ease of interpretation of the result. It was necessary to test the beams after mounting on the PCB as many were broken on the wafer. Then to test again after the cell is closed up and the magnets are attached, and when the cell is mounted on the probe. The chance of failure has been so high that quickly testing the state of the beam was essential to improve turnaround time.

Resonance Measurement Circuits

There are many ways to apply current and measure the induced voltage. The usual generator and lock-in methods used for vibrating wire resonators and tuning forks have additional complications at the high frequencies $> 1\text{ MHz}$. These can be overcome by using a high-frequency lock-in amplifier, but do not fix issues with signal reflection from mismatched transmission line impedance. A network analyser creates and measures the transmission and reflection of power through an electrical network and can be used to measure the transmission characteristics of the beam. The vector network analyser includes correction and calibration routines to account for high frequency signals.

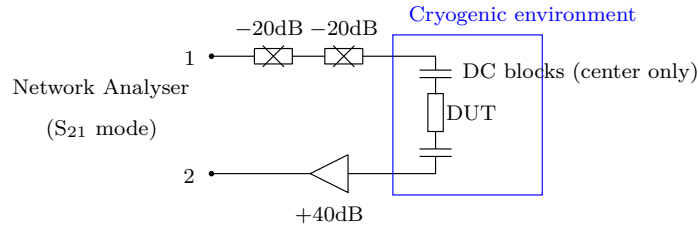


Figure 4.5.4: One of the resonance measuring circuits using a vector network analyser. Passive external attenuators reduced the vector network analyser’s output power. Optional DC blocks were used to protect the beam from stray DC currents. The vector network analyser measured the forwards transmission S_{21} .

A simple model of a vector network analyser is that a voltage is applied over the output resistor at a chosen frequency and the voltage over the measuring resistor is recorded with magnitude and phase related to the output voltage, in a manner similar to a generator and synchronised lock-in amplifier. The device expects the measurement line to be $50\ \Omega$ matched, but that is not guaranteed in our case. The beam will be driven by the current through it, but this is unknown from the output. Similarly we are not directly measuring the voltage across the beam, but the result of loss of power in the sensing resistor. The full measurement matrix from the NA does take into account reflection, so we can relate the loss of power in S_{21} to power absorbed into the beam and transmission lines. There is a constant background from the transmission lines (tested to be less than 0.5 dB at 300 K), and from the reflection between the $50\ \Omega$ of the lines and the mis-matched impedance of the beam, and there will be some power absorbed into the beam in the way of heat through ohmic losses. These effects should be near constant over frequency, so that any dip seen in S_{21} should be from resonances.

There will be standing waves down the total length of the transmission line, which is about 3 m long, that will appear every 100 MHz - well above the expected mechanical resonance of the beam. The cavity of the beam would have a frequency of terahertz, and any photons in

the measurement cell will have an electrical resonance about 0.3 GHz to 30 GHz. None of these should be a problem. We still check up to 100 MHz for features seen in the transmission with and without the beam to be sure that the dip in the power is actually correlated with the mechanical resonance of the beam.

Measurements from a Network Analyser

One way to get useful results from a network analyser is to apply post acquisition analysis to convert from the transmission fraction S_{21} to the power absorbed by the beam, taking in to account a pre-amplifier, with gain G and output attenuator A .

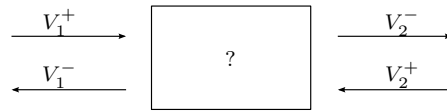


Figure 4.5.5: The Scattering Matrix on an unknown ‘black box’.

The data that is measured from the NA that is saved on disk is the complex number representing the transmission from port 1 to port 2, called S_{21} . This is just one component of the larger scattering matrix [152] used to describe black box RF devices, shown in figure 4.5.5. The device can reflect some power back towards the source, this reflection is measured as S_{11} . The inverse reflection and inverse transmission, S_{22} and S_{12} are also measurable. These four measurements form a two-port scattering matrix

$$\begin{pmatrix} V_1^- \\ V_2^- \end{pmatrix} = \begin{pmatrix} S_{11} & S_{12} \\ S_{21} & S_{22} \end{pmatrix} \begin{pmatrix} V_1^+ \\ V_2^+ \end{pmatrix}. \tag{4.5.2}$$

In any RF system, the amount of power reflected and the amount of power transmitted must be equal to the input power. This is written using reflection ratios and transmission ratios as $\mathbb{R} + \mathbb{T} = 1$. In the event that absorption, \mathbb{A} , is also a possible power loss mechanism, as

is the case for an in-line resistor, then the power conservation relation becomes $\mathbb{R} + \mathbb{A} + \mathbb{T} = 1$. Writing this in terms of the S-parameters is,

$$\mathbb{A} = 1 - S_{21} - S_{11}. \tag{4.5.3}$$

A dip in \mathbb{A} would be the power absorbed into the oscillator for resonance. The reflection S_{11} should be constant, so we only need to measure any change in S_{21} to see a change in absorption related to the power required for the oscillation.

The value we measure is transmission,

$$S_{21} = \frac{V_2^-}{V_1^+}. \tag{4.5.4}$$

This is the ratio of voltages as measured at the ports of the NA. S_{21} is a complex number, encoding both the magnitude of the transmission, and the phase, $S_{21} = V_x + iV_y$.

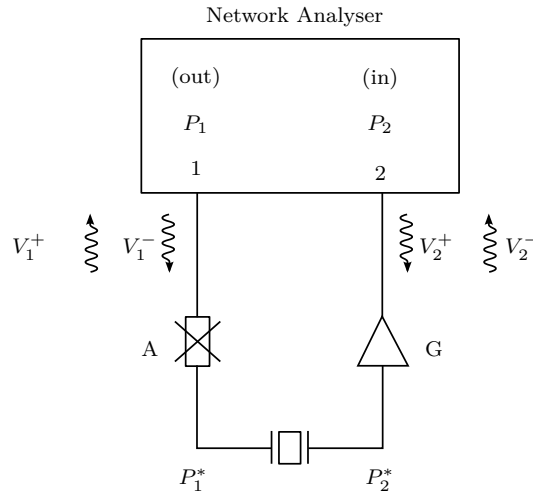


Figure 4.5.6: Measuring the power absorbed by the beam, from a NA using a known gain and attenuation.

This S matrix parameter is for the whole system outside of the NA. However we know that there is a fixed attenuation and gain between the measuring ports and across the beam, shown in figure 4.5.6. We use modification to S_{21} to measure as if the probes were across only the device, between points P_1^* and P_2^* .

We convert the output and measured voltages to power, using $P = V^2/R$, with R as a common $50\ \Omega$ on both ports the transmission is

$$|S_{21}|^2 = \frac{P_2}{P_1}. \quad (4.5.5)$$

The power before the amplifier which is described with a gain \mathcal{G} of some scaling factor, 10 000 for 40 dB, is

$$P_2 = P_2^* \mathcal{G}. \quad (4.5.6)$$

Similarly the power after the attenuation described by a factor \mathcal{A} , 1/10 000 for -40 dB, is

$$P_1 = P_1^* / \mathcal{A}. \quad (4.5.7)$$

These definitions are substituted into equation 4.5.5, to get

$$|S_{21}|^2 = \frac{P_2^* \mathcal{G} \mathcal{A}}{P_1^*}. \quad (4.5.8)$$

The measurement matrix across just the device from P_1^* to P_2^* is

$$|S_{21}^*|^2 = \frac{P_2^*}{P_1^*}. \quad (4.5.9)$$

This can be described with $|S_{21}|^2$ using 4.5.8,

$$|S_{21}^*|^2 = \frac{|S_{21}|^2}{\mathcal{G} \mathcal{A}}. \quad (4.5.10)$$

The transmitted power P_2^* rearranged from 4.5.9 is

$$P_2^* = |S_{21}^*|^2 P_1^*. \quad (4.5.11)$$

Substituting P_1^* from 4.5.7 yields

$$P_2^* = |S_{21}^*|^2 P_1 \mathcal{A}, \quad (4.5.12)$$

and then substituting $|S_{21}^*|^2$ from 4.5.10 yields

$$P_2^* = \frac{|S_{21}|^2}{\mathcal{G} \mathcal{A}} P_1 \mathcal{A} = \frac{|S_{21}|^2 P_1}{\mathcal{G}}, \quad (4.5.13)$$

which for convenience can be called P_b .

The NA, gain, and attenuators all use logarithmic units of power dBm and logarithmetic ratios of dB. It is convenient to use dB and dBm together so we equivalently write equation 4.5.13 as

$$P_b[\text{dBm}] = 10 \log_{10} |S_{21}|^2 - \mathcal{G}[\text{dB}] + P_1[\text{dBm}]. \quad (4.5.14)$$

The power P_b is the total power in the beam, which we simply model as some background power from ohmic losses, and the power involved in driving the resonator,

$$P_b = P_{\text{background}} + P_{\text{resonance}}. \quad (4.5.15)$$

The background, $P_{\text{background}}$ in the frequency space around the resonant frequency should be a experimentally measured linear function, this is a small frequency range approximation. The power of the resonance is

$$P_{\text{resonance}} = P_b - P_{\text{background}}. \quad (4.5.16)$$

Estimation of Displacement and Velocity of the Beam From Power

A nanomechanical beam, just like other macroscopic objects can be pushed into a driven oscillation by applying a driving current through the device while in the presence of a magnetic field, the current produces a force which can build up to oscillation. The movement of the beam in a magnetic field produces a voltage across the beam. In a four-wire measurement, a known driving current can be sourced from a generator and the induced voltage measured by a lock-in amplifier synchronised to the generator. The force on the beam can be estimated from the current, and the induced voltage indicates the beam's velocity. Network analyser methods typically describe electrical networks with the S matrix parameters and power, however, using a vector network analyser can measure the phase of the signal enabling us to extract the complex voltages induced by resonance.

Measurements of loss of power in transmission will have a shape based of the square of the Lorentz peak curve and will show the quality

factor of the beam oscillations. The quality factor is the ratio of the resonant frequency to the full-width-at-half-maximum of the voltage Lorentz peak,

$$Q = \frac{f_0}{\Delta f}. \quad (4.5.17)$$

The quality factor is also the approximate number of oscillations for the device to ring down, and is described by two energy parameters, E_s the energy stored in the oscillator, and E_d the energy lost in the oscillator per cycle.

$$Q = 2\pi \frac{E_s}{E_d}. \quad (4.5.18)$$

The energy lost per cycle is related to what is measured when performing transmission measurements. The measured transmission power loss is exactly what is being absorbed and lost by the oscillator while the beam is in a steady state. We are ignoring the energy requirements to ring-up the beam. The energy loss absorbed into the beam for resonance $P_{\text{resonance}}$ yields E_d ,

$$E_d = P_{\text{resonance}}/f. \quad (4.5.19)$$

The energy in the beam can be modelled with a simple harmonic oscillator, where the energy constantly shifts between kinetic and potential energy,

$$E_s = \frac{1}{2}mv^2 = \frac{1}{2}kx^2 \quad (4.5.20)$$

where $m = \rho_{\text{Al}}V$ and $k = Eht^3/2$. The meaning of k is some effective spring constant for the transverse motion of the beam, as the motion of the beam, is not the same as the spring constant for a mass-on-spring. The mass m of the beam can be found from predictable dimensions and the mass density of aluminium.

The physical meaning of both x and v on the right hand side of equation 4.5.20 can be consistent with either the RMS value or the peak value, but the choice also needs be consistent with E_d and

measurements of the power. The NA uses RMS for power, so we can choose to scale power by $\sqrt{2}$ to get a peak power absorbed/dissipated measurement. The average value for velocity and displacement, would gain the same factor of $\sqrt{2}$ to measure the peak values. This factor is only assuming a hinged-hinged oscillator, seen in figure 4.4.6, but if the oscillator has fixed-fixed boundary conditions, then the amplification factor would be ≈ 2 . This only comes from the average beam displacement compared to the maximum displacement.

Substituting E_d (equation 4.5.19) and $\frac{1}{2}mv^2$ as E_s , and Q (equation 4.5.17) into 4.5.18 yields

$$\frac{1}{\Delta f} = \frac{\pi mv^2}{P_{\text{resonance}}}, \quad (4.5.21)$$

which can be re-arranged to approximate the beam velocity v in known or measurable terms

$$v \approx \sqrt{\frac{P_{\text{resonance}}}{\Delta f \pi m}}. \quad (4.5.22)$$

Finding the force on the beam is then simply found from $P = Fv$,

$$F = \frac{P_{\text{resonance}}}{v} \approx \sqrt{P \Delta f \pi m}. \quad (4.5.23)$$

The displacement can be found by substitution of $\frac{1}{2}kx^2$ as E_s , instead of $\frac{1}{2}mv^2$.

$$\frac{1}{\Delta f} \approx \frac{\pi kx^2}{P_{\text{resonance}}}, \quad (4.5.24)$$

here k is substituted from the resonant frequency equation $\omega_0 = \sqrt{\frac{k}{m}}$, as $k = (2\pi f_0)^2 m$, so that

$$x \approx \frac{1}{2\pi f_0} \sqrt{\frac{P}{\pi m \Delta f}}. \quad (4.5.25)$$

These equations for v and x are consistent with $v = 2\pi f x$

Measurements of the Induced Voltage from Resonance

Another approach to acquiring the physical measurement of the velocity and the displacement can come from trying to directly infer the induced voltage across the beam from S_{21} .

At any frequency the induced voltage from resonance can be described as a function of current I and as a frequency dependent scaling factor γ , so $V_r = \gamma I$. This is because the induced voltage is proportional to the velocity of the beam, $V_r \propto \dot{x}$, and the velocity (equation 4.4.4) scales with the length and field which for any one measurement are fixed. For a linear resonator $\gamma = \gamma(f)$ is a Lorentz peak. We re-draw the measurement circuit to include the induced voltage and the effective extra resistance that this causes, as in figure 4.5.7.

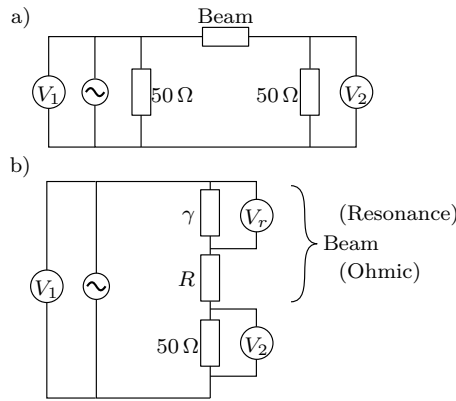


Figure 4.5.7: a) A sketch of the beam measured in series with a transmission line. This can be redrawn as b). The beam is logically modelled as the sum of an ohmic component and a resonance component.

We know V_1 by choice, and can get V_2 from transmission measurements of S_{21} . To find V_r is we apply Kirchoff's voltage conservation

$$\sum_{\text{loop}} V = V_1 - V_r - IR - V_2 = 0. \tag{4.5.26}$$

The current I is ideally assumed from the measurement of V_2 over $50\ \Omega$, and we can express the induced voltage as

$$V_r = V_1 - V_2 - R \frac{V_2}{50}. \tag{4.5.27}$$

We can now express how a change measured in V_2 would mean a change of V_r ,

$$\frac{dV_r}{dV_2} = -1 - R/50 = -(1 + R/50). \tag{4.5.28}$$

This means that any change seen in V_2 because of resonance will be the negative of the induced voltage, and shrunk by a factor of $1 + R/50$. We write this as,

$$\Delta V_2 \frac{dV_r}{dV_2} = \Delta V_r, \quad (4.5.29)$$

or simply with $Y = -(1 + R/50)$

$$\Delta V_2 Y = \Delta V_r, \quad (4.5.30)$$

where Y is used in this discussion to mean the scaling factor. It is useful to note $Y < 0$ always, and in the event that $R \rightarrow 0$ in a superconducting beam, then $Y \rightarrow -1$.

To include the additional complications of a pre-amplifier with a voltage gain \mathcal{G}_v before V_2 and attenuators after the output V_1 .

This follows a similar argument as that found in section 4.5.3. We measure a value for transmission, S_{21} , with a dip because of resonance which has a depth of ΔS_{21} . The gain \mathcal{G}_v and attenuation \mathcal{A}_v used here are a voltage gain and not a power gain, as previously discussed. We get the maximum resonance voltage,

$$V_r = \Delta S_{21} V_1 Y / \mathcal{G}_v, \quad (4.5.31)$$

and the measurement current,

$$I_r = \frac{S_{21} V_1}{50 \mathcal{G}_v}. \quad (4.5.32)$$

We infer the power of the resonance dip,

$$P_r = \frac{\Delta S_{21} S_{21} V_1^2 Y}{50 \mathcal{G}_v^2}. \quad (4.5.33)$$

This P_r should produce similar results to equation 4.5.16, which uses a direct conversion to power, then background subtraction. This method uses an effective background in S_{21} space then converting to power.

Equation 4.5.30 shows that the shape of the complex V_2 and S_{21} will have the inverted shape of the resonance voltage. We can fit data of $-S_{21}$ to the complex Lorentzian and measure the centre frequency and

resonance width without having to convert to power. The conversion from S_{21} to power is not a linear function, so will have some cross terms between $S_{21}^{\text{background}}$ and $S_{21}^{\text{resonance}}$. We can't use $S_{21}^{\text{resonance}}$ alone to acquire the beam velocity and displacement.

If we have measurement of V_r , then it is trivial to acquire the velocity and displacement using Faraday's Law,

$$\dot{x} \propto \frac{V_r}{Bl}, \quad x \propto \frac{V_r}{Bl2\pi f}. \quad (4.5.34)$$

These work only as an order of magnitude estimator, until the resonance shape is known, the length will become an effective length by scaling by a factor of order unity.

Electrical Measurements at High Frequencies

The resonant frequency of the device will be available in the range of hundreds of kilohertz up to tens of megahertz, electronic measurement and excitation circuitry will need to be able to operate across this frequency range. The low megahertz range can begin to be considered 'high frequency', which means that many of the low frequency circuit analysis is insufficient. This is when the signal wavelength λ is some non-trivial fraction of the electrical line length l :

$$\frac{c}{f} = \lambda \approx l \quad (4.5.35)$$

For example in a 10 m long line, at a frequency of 10 MHz the signal will be $2\pi/3$ radians out of phase by the time it takes to get back to the measurement electronics.

At low frequencies current travels along wires easily, meaning that there is efficient power transmission. A measurement of current and voltage do not change depending where it is measured as a position down the length of the wire, but this is untrue for when considering high frequency signals. There is a length dependence and the wire needs to have a matching impedance for efficient power transmission. The

high frequency lines are called transmission lines, which will often be quoted with a characteristic impedance, Z_0 , that is commonly $50\ \Omega$. If parts of the transmission line do not have the same impedance, there will be reflections at the boundary, and power will be reflected back towards the source. The reflection coefficient, Γ depends on the load impedance Z_L , $\Gamma = \frac{Z_L - Z_0}{Z_L + Z_0}$. Power is most efficiently transferred when the load is equal to the line impedance, $Z_L = Z_0 \rightarrow \Gamma = 0$. This means that circuits were built to operate with high frequency signals had components like attenuators and amplifiers that were impedance matched. The standard of $50\ \Omega$ is common, most of the impedance matching was already taken care of by default, but enabling a $50\ \Omega$ mode on some equipment was necessary. The experimental measurement lines were also needed to made from high frequency rated coaxial cables to reduce noise and to prevent radiation of signal. The construction of the lines used as few component sections as possible - to reduce reflections between the connections.

The nanomechanical beams were not designed with the resistance as a defining parameter, so it was unlikely to be impedance matched. The nanomechanical beam have a ohmic resistance typically between $100\ \Omega$ and $250\ \Omega$. Therefore we expected there to be a reflection of the signal between the transmission line where the beam starts and ends.

Signal Phase Compensation

When frequencies are high, the signal at the receiver will be out of phase with the output signal. The changing voltage in the wire takes a finite time to propagate the length of the wiring. Performing a wide frequency sweep will reveal a sinusoidal trend of the real and imaginary components of the signal, due to the resulting phase change.

The way the signal phase changes is predictable as a function of frequency. We can measure and fit the background using series of

measurements over a wide range of frequencies to the complex model of sinusoids with a fixed phase,

$$S_{21}^{\text{background}} = A \cos(\Omega f) - A \sin(\Omega f)i = Ae^{i\Omega f}. \quad (4.5.36)$$

The value A is a free parameter for the amplitude, and Ω is a free parameter to fit the frequency of the phase change. We fit the real and imaginary parts together simultaneously to reduce error. The value of Ω once acquired needs only to be measured once to be applicable for future measurements with the same apparatus.

EXPERIMENTAL DETAIL

This section describes the experimental setup used in the laboratory for measurements of the beam. The initial feasibility of the measurements is tested in a glass cryostat using a cell immersed into a pumpable helium bath capable of cooling to 1.5(2) K. We later improved on this by using a newly built, more advanced, cryostat with a vacuum can and the experimental volume inside a shielded helium pot. The newer cryostat has a lower base temperature of 1.1 K and a controllable magnetic field up to 5 T.

Early Experiments

Initial work to measure the nanomechanical beams at 4 K used a small brass cell that was immersed in a small 3 litre helium glass cryostat. The brass cell is used as a structure to hold permanent magnets and as a chamber to contain vacuum, or helium gas, or liquid helium-4.

Cell design

The beam needs to have a pair of RF electrical connections, in a superfluid tight chamber and in the presence of a magnetic field. We choose to apply a 0.5 T field from two neodymium magnets. The magnitude of the field was tested with a gauss meter at room temperature. The brass cell shown in figure 4.6.1. The cell has an indium seal connecting the two brass halves: in the lower half there are two SMA feedthroughs soldered into the brass, and a top that forms a lid. A 1 mm, dual purpose vacuum pumping line and filling line connects the sample volume to the top of the probe and to the gas handling system. The chip is held in place in a custom made PCB that fits around the feedthrough pins and rotates into place.

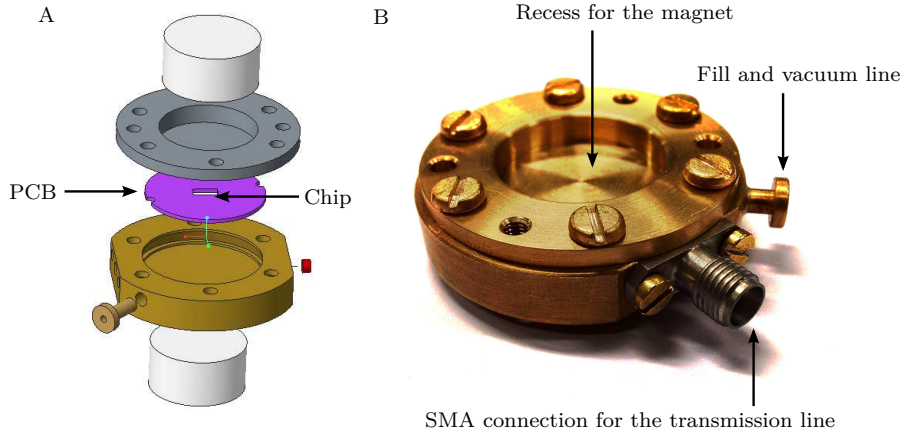


Figure 4.6.1: The cell designed to hold the nanomechanical beam. A: 3D model of the cell. B: a photograph of the brass body after manufacturing and the ceramic feedthroughs with stainless steel thread assembled. The permanent magnets are not attached in the photograph. The PCB is made with FR4 copper circuit board. The centre of the PCB is milled out to open up space for the chip to sit flush with the level of the copper traces.

The copper traces of the PCB in the cell are designed as $50\ \Omega$ transmission lines to improve transmission. The chip is held in place in a recess cut into the middle of the PCB and tacked down with vacuum grease. At 2 K to 4 K the thermal properties of the grease will not be an issue.

We used an adhesive-based bonding method instead of clean-room bonding to attach the PCB signal lines to the electrical lines on the chip. Using bonding in a clean room caused a very slow turn-around time between tests. The adhesive bonding method uses electrically conductive electrodag. Fine tweezers were used to place a drop of liquid electrodag from the chip to the copper transmission line. Care was needed to remove copper oxide that formed on the PCB traces as this is not otherwise broken or punctured with the electrodag. The chip bonding method is shown in figure 4.6.2.

The ground plane on the chip is bonded to the ground plane of the PCB using the same adhesion technique. The adhesion based bonding

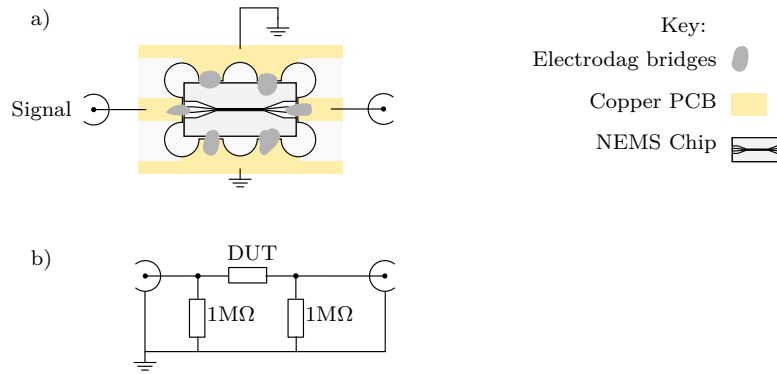


Figure 4.6.2: Using blobs of Electrodag as bridges to connect the signal lines of the PCB to the signal lines of the chip. One blob is used for each of the lines, and four more blobs are used to connect the PCB ground to the substrate. This is modelled in b) as some nominal high resistance to ground on each side of the DUT.

is not as selective as traditional wire based wedge or ball bonding, often the electrodag will run down the side of the chip contacting the substrate. The native silicon oxides have $\approx 1 \text{ M}\Omega$ per square, so any spill over from the electrodag over the edge of the bonding pad is not an issue. In fact this high impedance of the silicon oxide further protects the chip in the holder by enabling a gentle path for static charge to dissipate. This will prevent the electrical connections to the beam from electrically floating. The silicon oxide electrical conductivity lowers drastically at low temperatures and will isolate the signal path.

Ground points and Nanomechanical Beam Handling

Nanomechanical beams are fragile, and the production of them incurs significant time and cost. They require careful handling and consideration when working with. This involves redesigns and modifications of apparatus and equipment that comes into contact with the devices.

The probe is mounted in glass cryostat on a metal frame with the gas handling and pump control valves. We remove all the grounding from the cryostat and pumping system that are either to mains ground or to the water pipe ground (as they were different), and use nylon plastic earth breaks to separate the frame from the electrical noise from the

pumps. Thick-walled flexible rubber tubes were used when attaching temporary pumps or leak detectors. The electrical ground is carefully controlled, figure 4.6.3 shows the implemented layout.

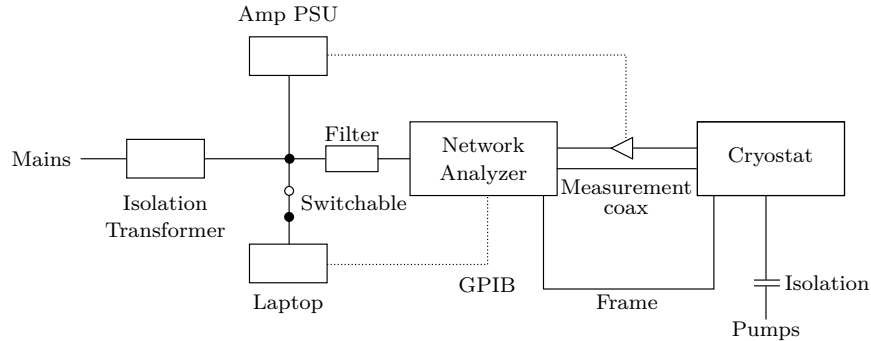


Figure 4.6.3: The implemented electrical grounding diagram used to prevent the presence of ground loops. We used two star points: one at the vector network analyser, and after the isolation transformer.

We attach only one ground path from the cryostat to the front of the vector network analyser. We choose the vector network analyser as the ground star point, so that any spikes from mains ground will effect the ground of the cryostat and the measurements of the signal line equally and with minimal effect. The path from ground to the transmission line needs to be considered as transient voltage spikes can get coupled asymmetrically across the beam causing it to melt.

While the nanomechanical beam is not being measured it can be stored in a safer way. The vector network analyser is disconnected at the SMA feedthroughs at the top of the probe and two $50\ \Omega$ ($-20\ \text{dB}$) attenuators are attached across the both sides of the beam. This connects one side of the beam to the other, each with the same impedance to ground.

The beam should also not be left in vacuum, a surrounding gas medium will enable the beam to cool much better than just relying on conductivity of the aluminium.

An abundance of rotary vane pumps around the lab cause a large measurable electromagnetic pulse from the motors during switching on and off. While the beam is safely stored it is more resilient to these

pulses. However, while it is being measured there is more potential for the beam to break. The measurement circuit has a low impedance via the attenuators from ground to one side of the beam, while the other side of the beam is well shielded. An asymmetric coupling from ground to the device creates a voltage across the beam. We discovered that cycling operational power on any pump within about 5 meters could induce enough voltage to melt the beam.

We add an isolation transformer, aka a ‘site-safety’ transformer, and a mains filter before the NA to reduce noise into the ground. The power supply from the +40 dB amplifier and the control computer come from the same distribution board to further reduce the ground loop area.

Practical Notes

Loading the strong neodymium rare earth magnets onto the experimental cell while the beam is mounted can cause a large and fast change in magnetic field. This will induce a current that is too strong for the beam. One way to improve the beam’s survival is to counter-intuitively remove all shorts from the signal lines. This removes electrical loops that enable current, isolating the beam. To load a pair of magnets adds additional complications; the second magnet will jump to the first causing large \dot{B} and a mechanical ‘clap’ that can break the beam. We found using a large iron block, i.e. from a lathe chuck or a vice, to magnetically hold the second magnet is good enough so that the cell can be lowered on towards it and make contact without a jump. The magnet will preferentially be attached to the ferromagnetic iron and the cell with the first loaded magnet can be presented to the second magnet at an arbitrarily slow speed. The loaded magnets can be slid off sideways off the iron. The mechanical clap of magnetic tools jumping to the magnets on the cell can also break the beam.

Pumping System

We assembled a gas handling system to extend the capability of the existing cryostat.

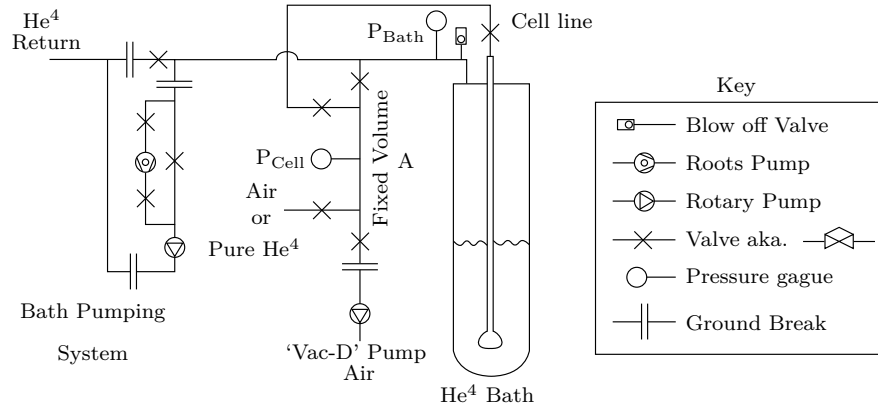


Figure 4.6.4: The cryostat pumping system and gas handling. Not included are the dewar vacuum systems for the inner spaces.

To enable us to vary the pressure in the cell we include a ‘gobbet’, volume A, with a pressure gauge. We can isolate the cell volume, then put a controlled amount of gas into the control volume and then release it into the cell. We can observe the cell pressure using the gauge on the control volume. We use the boil off of the bath as the source of pure helium-4.

To condense liquid into the cell, we open the cell volume to the bath volume. Cryopumping brings in gas from the boil off of the bath into the cell, filling with liquid as it condenses. The level in the cell (and the cell fill line) should be the same as the bath helium level. While condensing we periodically close off the cell/bath short and check that the cell pressure drops. If during a check the cell pressure doesn’t drop, then the cell is full.

When cooling and pumping on the bath volume we can isolate the cell again and watch the cell pressure drop according to the saturated vapour pressure curves. This means we are confident there is liquid in

the cell, and that as the cell pressure matches the bath pressure they are in good thermal equilibrium.

Cryostat-II Purpose Built Probe

Once the beam is verified to be measurable, the limitations of a glass cryostat hampered the careful acquisition of a temperature dependent response in liquid. The temperature control of the glass cryostat is too rough and the temperature stability is limited. The modification of a more advanced cryostat involved the building of a vacuum can and a separate inner helium chamber, called a pot, to be used with a larger metal dewar and superconducting solenoid electromagnet.

Figure 4.6.5 is a photograph of the experimental probe. The flanges show the inner vacuum can, IVC, and the pot can. The experimental volume is inside of the pot volume on a metal finger that extends into the field maximum of the superconducting electromagnet.

The experimental volume for the beam includes a half loop vibrating wire resonator, VWR, a commercial calibrated thermometry resistor, a RuO_2 , and a heater resistor. A sketch of the component parts is shown in figure 4.6.6.

The metal casing of the helium and nitrogen baths provide additional shielding for the experiment. The vacuum can and the pot can are also good electromagnetic shields, the wire running down the support column provide a long and narrow wave guide reducing EMI from the room.

Similar care was used on the new cryostat to electrically separate the gas handling and pumping system from the cryostat. The grounding diagram is effectively the same as figure 4.6.3. The additional electrics for the VWR are AC-coupled and the measurement of the resistors did not appear to affect the grounding. The magnet power supply is

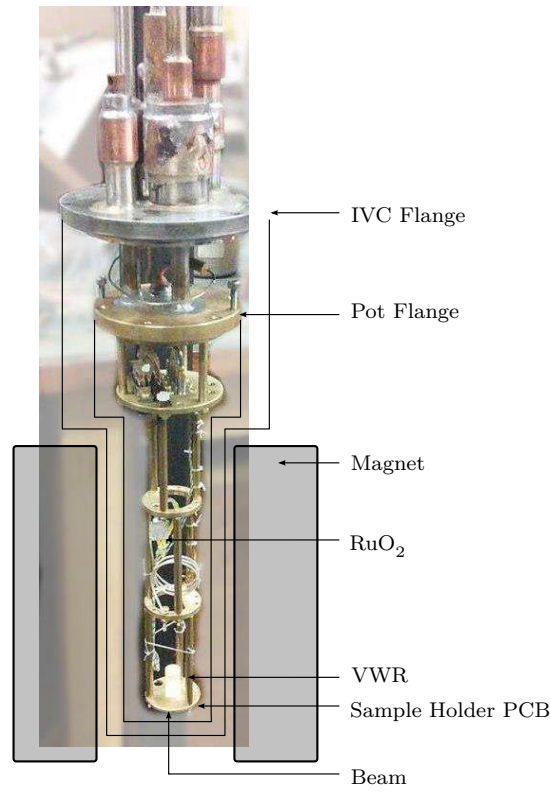


Figure 4.6.5: The probe for holding the beam. The outline for the pot and the IVC are drawn on. Both cans have a diameter reduction step to accommodate the small bore of the superconducting magnet. Each can is vacuum sealed with indium. The RF line connections are SMA on the first plate in the pot, and then half-indent SMP below. The final connections are semi-flexible coaxials to enable attaching the sample holder PCB which is downwards facing at the end of the mounting finger. The thermometry resistor, vibrating wire resonator, and additional heater resistor are attached with twisted pairs, to a micro-D connector.

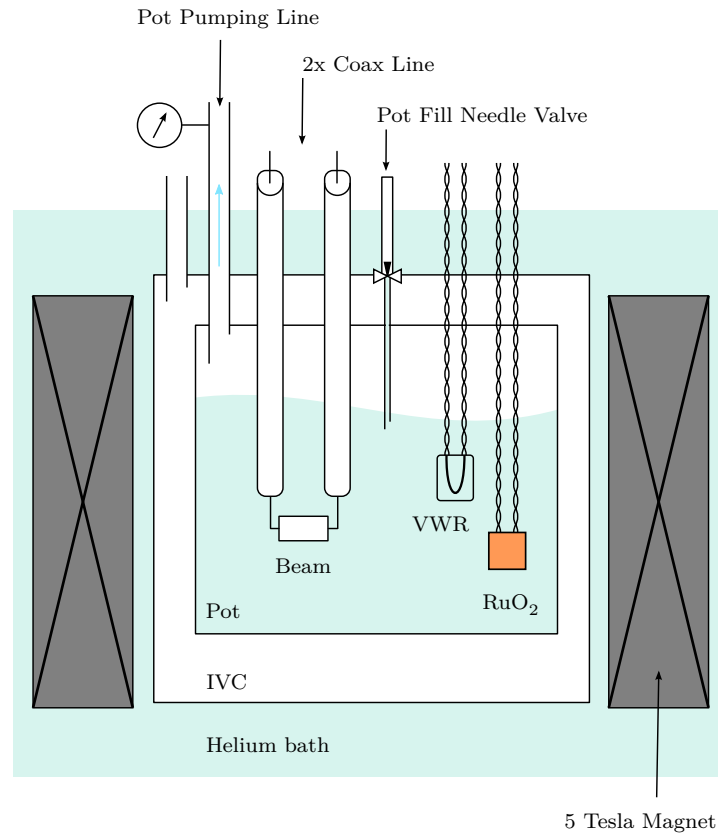


Figure 4.6.6: A sketch of the apparatus used to measure the beam in liquid.

The VWR and a thermometer resistor are submerged in liquid in a pot. The pot has controllable pumping and we can measure the saturated vapour pressure wire a gauge. The beam is connected by high-frequency coaxial cable fed through from the bath and the vacuum can. The VWR and RuO_2 resistor are measured with a four-point connection using twisted pairs. The device is located in the middle of the field produced from the superconducting magnet.

floating, and the magnet is persisted in typical use. Once persisted the current leads are removed.

The accompanying gas handling is more advanced than figure 4.6.4. Each of the cryostat volumes can be attached to the vacuum line, the helium return line, and a pure helium source for condensing in or adding exchange gas, as well as the associated safety valves. This enabled flexible operation methods. The only pressure gauge was a linear gauge between 0.1 mbar and 1.5 bar located close to the top of the pot pumping line to reduce the effects of the line impedance affecting pressure and saturated vapour pressure measurements. To keep the beam clean, the pot and the vacuum can volumes are evacuated to below 1×10^{-4} mbar using a turbo and rotary two stage pump [153]. The low starting pressure should remove all gasses that would condense onto the beam and prevent the beam becoming dirty from frozen gasses.

PRELIMINARY MEASUREMENTS

These experiments were the initial work to test basic feasibility and laboratory handling of nanomechanical beams. The successful measurements of resonance using existing equipment demonstrated the potential for further measurements. The preliminary nature of this initial experiment justifies the unrefined setup, favouring brevity and agile exploration over an investment in reusable hardware.

A nanomechanical beam is mounted inside a small brass experimental cell, shown in figure 4.6.1, and is cooled to liquid helium temperatures in a glass cryostat, as shown in figure 4.6.4.

Measurements In Vacuum

We measure the fundamental mechanical resonance mode of a 25 μm beam at 300 K in a pressure less than 1 mbar as measured by gauge P_{Cell} , from figure 4.6.4. The beam was connected to a vector network analyser as in circuit shown in figure 4.5.4. The transmission, S_{21} , from the vector network analyser is converted to power absorbed in the beam according to equation 4.5.14 and the background signal is removed to acquire the resonance beam power, as in equation 4.5.16.

Figure 4.7.1 shows the resonance response of the beam as the vector network analyser sweeps through frequencies. The peak shape is fitted to the expected power shape, 4.4.14. The numerical fittings describe the peak quite roughly, and are not perfect near the tails of the peak. The improvement of quality factor of the cold device is expected, and can be attributed to cryo-pumping on the cell increasing the quality of the vacuum, removing damping. The remaining width is intrinsic width of the oscillator which is also temperature dependent and decreases with temperature. The increased frequency of resonance is likely to be due to the differential thermal contraction of the aluminium of the

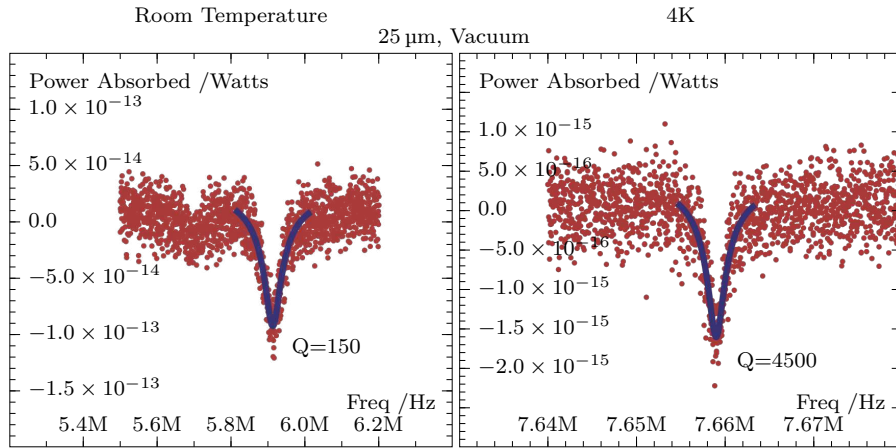


Figure 4.7.1: Measurements of Resonance of a 25 μm long beam in vacuum at 300 K before cooling, and with the same beam at 4.2 K. The quality factor of resonance increases from 150 to about 4500.

beam compared to the silicon of the substrate. The additional tension increases the resonant frequency, discussed previously in section 4.4.2 and equation 4.4.19.

A different 25 μm long nanomechanical beam was measured a second time, after a thermal cycle. It appears that on a second cooldown new resonance frequencies appear. The additional peaks are measured by a wide range frequency sweep while the sample is in vacuum at 4.2 K. Each of the peaks are individually then measured with increasing amounts of power to observe the linear and non-linear response. Figure 4.7.2 shows each of the power sweeps next to the resonance on a wide frequency sweep.

The fundamental frequency 4.7.2.a is nearly the same as the initial cooldown. However the additional peaks are not harmonic overtones of the fundamental. A few of the higher frequency resonances could be described through the rough trapezoidal profile of the beam. This could create easy oscillating modes that are normal to the angled facets, as sketched out in figure 4.7.3. At higher frequency modes can be explained by frozen gasses accumulating on the beam originating from a small amount of air in the cell before cooldown. The additional mass

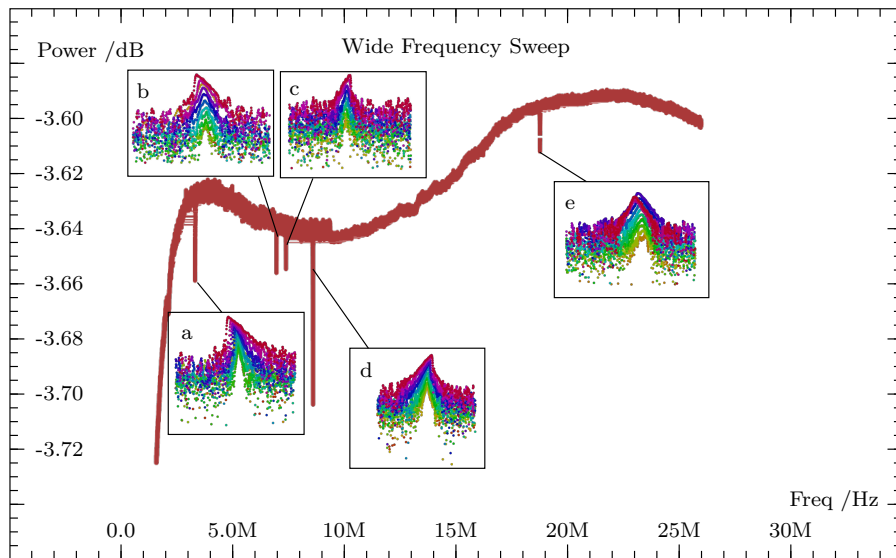


Figure 4.7.2: Additional resonant peaks appeared in the frequency response of the device after thermal cycling. The fundamental frequency appears to be the same, but there are other significant sized peaks, b-e, that appear. The non-linear response of these additional peaks varies between k -hardening, an increasing the resonant frequency, and k -softening, a reduction in the resonant frequency.

focused around a point would act as a nodal point for a higher frequency resonance, as sketched in figure 4.7.3.b.

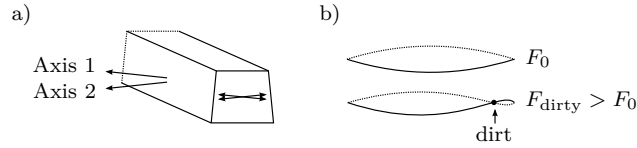


Figure 4.7.3: a) an idea to describe the higher frequency pair of resonant modes above the fundamental. These could be from oscillations slightly off axis out of the main oscillation plane, or b) the presence of some frozen-on dirt that acts as a nodal point, enabling asymmetric modes of the beam. Thinner regions of the beam, in a similar way to dirt could act as a hinge, also creating higher frequency modes.

The non-linear behaviour is inconsistent between resonances. Peaks a,b, and e show non-linear softening unlike peaks c, and d which shows non-linear hardening. The non-linear softening is unexpected and suggests a non-simple resonance mode. The pattern between hardening and softening nature of successive modes does not seem to follow a pattern with frequency.

The same device is measured repeatedly as the sample's temperature slowly increases as the cryogenic system is allowed to passively warm up. The frequency of the resonances are monitored by a wide frequency sweep, shown in figure 4.7.4. We were unable to acquire the quality factor of each resonance because of insufficient frequency resolution. The background of S_{21} changes as the beam warms up and the aluminium resistance increases. This increase in resistance visually separates one frequency sweep from the previous and roughly is used to separate the sweeps by temperature and time as the sample warms up.

Peaks a-d in figure 4.7.4 change to have a lower frequency as the temperature rises. This is described by the differential thermal contraction of the aluminium on the silicon, lowering the tension on the beam, just as with the fundamental frequency.

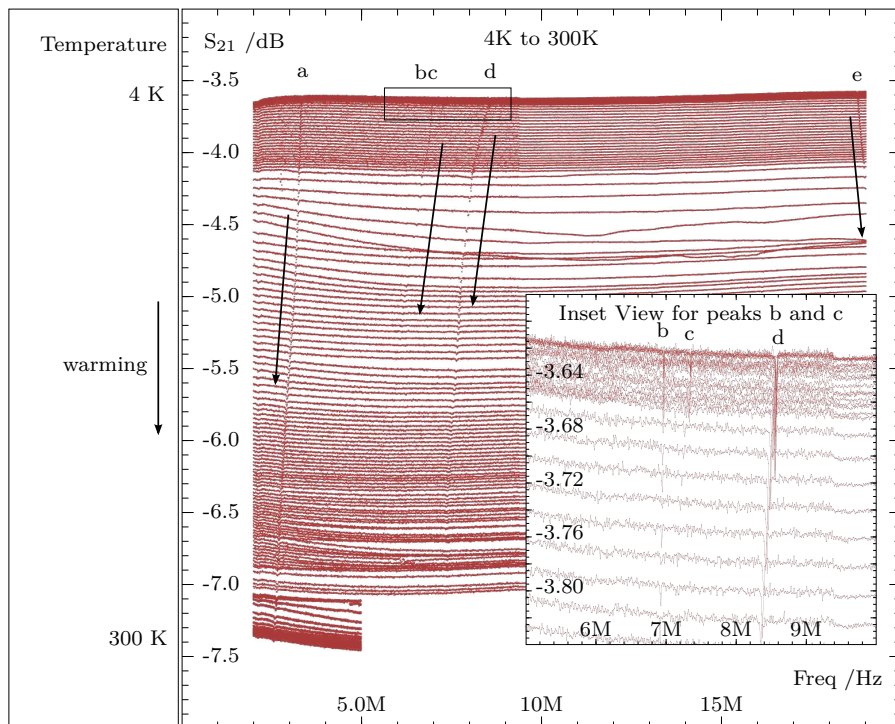


Figure 4.7.4: 4 K to 300 K Frequency Shift of Resonance. The peaks from figure 4.7.2, changing with temperature during a warming up of the cryostat. The temperature is only known at the start and at the end. Each sweep is 5 min apart.

Peaks b and c seem to disappear quite quickly as temperature increases. Peak d lowers in frequency at a rate much more quickly than the fundamental initially, but then disappears at higher temperatures. This could be that the larger amplitude of the d resonance, shown in figure 4.7.2 caused some additional tension in the beam that disappears quicker as thermal expansion reduces tension on the beam.

These peaks are inconsistent between runs of the same device, the higher frequency peaks appear and disappear as the device is thermally cycled. Between runs with different beams the fundamental frequency was not consistent, even between daughter chips of the same wafer. It is likely that the final beam shape after the plasma etching leaves the beams with a slightly different profile, length and tension.

Peak 4.7.4.e shifts frequency upwards as temperature increases. This upwards frequency shift isn't explainable by the tension in the beam increasing, as we know that by thermal expansion the tension is dropping. So instead the shift is explained by the effective mass decreasing. This can not be the metallic mass of the beam, but must be some dirt, frozen gasses, attached to the beam that are subliming or evaporating. This evidence that the beam is dirty could explain all the problems with additional peaks. Each of the dirt deposition sites down the length of the beam can act as a nodal point for higher frequency resonances. Another attempt to describe the change in fundamental frequency of the device was some form of annealing, or thermally induced stressing of the beam. The hope with thermal annealing is that it can be repeated by thermally cycling until it has reached a final annealed state.

We clean the beam by heating it up enough until the higher frequencies disappear and the fundamental frequency has stopped shifting. That can be done without change to the measurement circuit. Using the vector network analyser, we measure the span of resonances and incrementally increasing the driving power, much higher than the

usual measuring powers. As the power becomes significant the beam will heat up and boil or melt away attached impurities, the increasing power can keep going until the fundamental frequency no longer shifts with increasing power, and indicator that there is nothing left to boil away. There are significant risks of melting the beam with technique.

As we know the beam is dirty we forgo analysis of the harmonics.

Using this experimental setup for measuring the resonance of the beam with changing helium pressure at 4.2 K was successful, however the effects of temperature change in liquid were inconclusive. These are not included here as the latter experiments using the improved apparatus far superseded the collected results.

Beam Failure Modes

We learnt during the process of the preliminary work about the very fragile nature of nanomechanical beams. Beams can break during handling, during measurements, and by being incorrectly stored whilst around the lab. We used a scanning electron microscope to view some of the beams after different faults to observe the different failure modes.

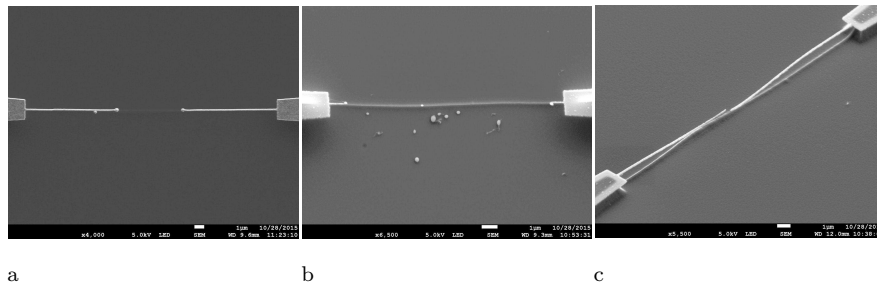


Figure 4.7.5: Three beams that have broken, viewed in a SEM. Each beam shown was originally in 25 μm long.

Figure 4.7.5 shows three different devices that have failed. The beam in figure 4.7.5.a shows the effect of too much current. The beam has melted in the middle, and the resulting molten beads of aluminium have, through surface tension formed balls on the ends of the remaining sections of the beam. As soon as the beam melts it breaks the electrical

circuit preventing ongoing current to flow, stopping the beam melting any further. But unlike figure 4.7.5.b it did not have enough energy to destroy the whole beam. The remains of the beam shown in figure 4.7.5.b we can assume are from a static discharge through the device. Drops from briefly molten aluminium can be seen scattered, a few μm from where the beam once was. There was a sufficient current through the beam that caused the whole beam to heat up to such a degree that it melted the whole.

We can approximate the energy required to fully melt the beam. The $25\ \mu\text{m}$ long beam has a mass of $675\ \text{fg}$ and has a specific heat capacity of $397\ \text{kJ kg}^{-1}$ [154]. The aluminium would have reached just above the melting temperature, about $934\ \text{K}$, which takes about $380\ \text{pJ}$, just to heat up from room temperature, then another $200\ \text{pJ}$ to melt about 70% of the beam. We estimate the time of static discharge from an RC discharge circuit. The transmission lines may have $C \approx 200\ \text{pF}$, and $R \approx 200\ \Omega$ from the beam, implies a discharge time of order $40\ \text{ns}$. This means a voltage contact only about $10\ \text{mV}$ is needed to cause 4.7.5.b.

Finally, figure 4.7.5.c shows the beam apparently snapping in the middle. We are unaware if this is from a driven oscillation while measuring, or the effect of a large - externally induced - mechanical shock. It might be coincidental that the beam just happened to be weakest at that point, as the cross section area of the beam is quite uneven.

Nanomechanical Beam Thermal Modelling and Simulation

The fragile nature of the beams prompted exploration by numerical simulation of the electrical current tolerances that we can expect. Any current through the beam produces Joule heating, the small volumes of the beams mean even a small amount of heat could rapidly raise the temperature. In vacuum, heat conduction along the beam's length could

be the dominant thermalisation method. In gas or liquid, conduction to the surrounding material would remove heat adequately. In a 2 K helium superfluid, the thermal counterflow [133] would be a fantastic thermal connection and the beam would be nearly unbreakable from measurement currents. However in the case of a vacuum the beam is the most sensitive to joule heating. The beam will typically be in vacuum during preparation stages of the experiment. Even plugging in mechanical pumps and other electrical equipment could destroy the beam.

We use the model of a cold bath at the beam's ends, this approximation should be sufficient as the material on the supports and transmission lines are orders of magnitude larger than the beam. The models are dependent on the electrical resistance of the beam for the Joule heating. To estimate the resistance of the beam, we use the bulk resistivity of aluminium, $\rho_{\text{Al}} = 2.65 \Omega \text{m}$ at room temperature and predict $R = \rho L/A$. For a $15 \mu\text{m}$ beam with a cross section of 100nm by 100nm square profile the predicted resistance is 39.8Ω . This bulk equation applied at the nano-scale on granular aluminium may not be representative of the physical device. A high resistance at the grain boundaries, will look like a regular beam in the SEM but will have a very large impedance.

We know from room temperature measurements of actual beams that the beam resistance is about $50(10) \Omega$ for a $15 \mu\text{m}$ beam, and $150(20) \Omega$ for the longer $50 \mu\text{m}$ beams. This shows a good agreement, with the differences attributable to either the aluminium composition raising the effective ρ , or the etching process removing additional material and lowering the area A . As the beams cool down the resistance drops, this is seen in figure 4.7.4 as the background changes. This is used to estimate a Residual-Resistivity Ratio, $\text{RRR} = R_{T=300}/R_{T=4.2} \approx 2$. This is very low and suggests a grainy aluminium. The aluminium beam sample stayed normal throughout the whole measurement, which is

expected as pure aluminium in bulk is a superconductor below 1.2 K in zero magnetic field [122].

The self cooling power of the beam, is the ability to remove heat by conduction, κ , this is given by, $\dot{Q} = \kappa A \Delta T$. For aluminium κ is between 5 and 30 $\text{Wm}^{-1}\text{K}^{-1}$ and is dependent on the purity and the RRR of the sample [155, 156]. The conductivity agrees with the Wiedemann-Franz law [157, 158] which states that $\kappa = LT/\rho$ with $L = 2.44 \times 10^{-8} \text{W}\Omega\text{K}^{-2}$. The thermal conduction for the model and simulation should be estimated for the worst case scenario, which is the lowest cooling power from an impure aluminium sample.

The temperature of a beam in vacuum in this model is cooled by thermal baths on each end. We match the Joule heating with a heat down a channel, shown in figure 4.7.6. The maximum temperature of the beam is in the centre, furthest from the thermal baths, and follows the form

$$T_{\text{max}} = T_{\text{bath}} + \frac{I^2 R L}{8 A \kappa}, \tag{4.7.1}$$

where I is the measurement current and R is a fixed beam resistance, and A is the cross sectional area. κ is assumed to be constant.

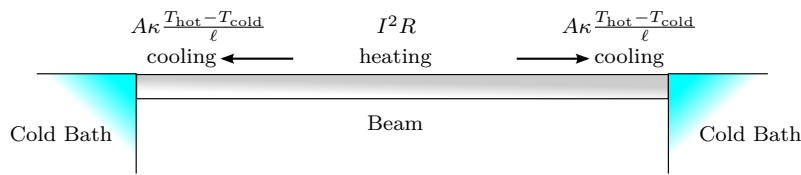


Figure 4.7.6: The thermal model of the beam in vacuum. Using contact with the beam supports as the only cooling mechanism.

A simulation of the beam using a 1 dimensional finite element analysis used the contact with an infinite thermal bath at each end to set boundary conditions, and per-element heat is produced according to Joule heating. Heat flow from each element to its neighbours is according to the conductivity and the temperature gradient. The model reaches equilibrium, and we can observe the temperature profile down

the length of the beam. The simulation is reasonably independent of the number of finite elements above a small number. We use 61 elements with a time step of 2 ns.

The Wiedemann–Franz based conductivity can provide a more realistic non-linear simulation of the conductivity. Using a temperature dependent conductivity suggests a lower maximum temperature. Figure 4.7.7 shows the temperature across the length of the beam using a fixed and non-fixed conductivity.

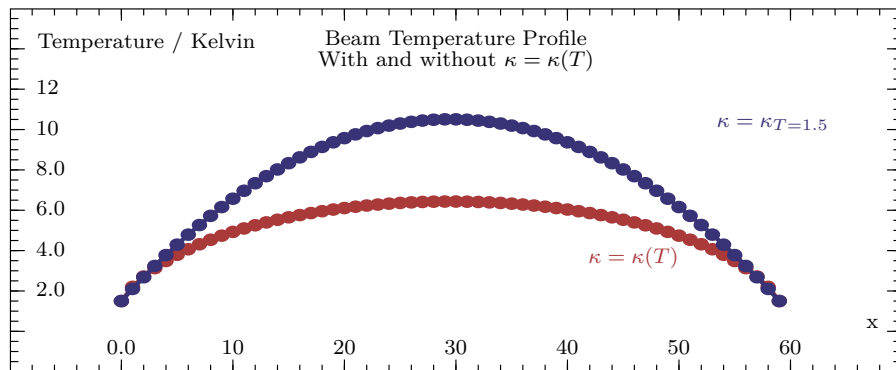


Figure 4.7.7: The temperature profile down the length of the beam, showing it is hottest in the middle. 30 μ A of current heats the simulated 60 finite elements that are shown across the x axis.

The simulation using a fixed conductivity at 1.5 K, $\kappa = \kappa_{T=1.5}$ shows a temperature profile that fits a quadratic curve, however the variable model shows as the maximum temperature decreases the varying thermal conductivity and the beam has more cooling power in the centre. This results in a flatter top with steeper sides temperature profile down the length of the beam.

The simulation shows that while the beam is cold, there is enough self cooling power to protect the beam from overheating until some significant currents, ones of microamps, which is enough to warm the beam to a few kelvins. The low resistance of the beam means that we need to protect it from any voltages in the range of tens of microvolts. Even small levels of static electricity can easily overwhelm the beam. The temperature profile of the beam indicates that it is the warmest in

the middle of the beam, which would be the first section of the beam to reach the melting point of 933 K, which agrees with both intuition and the images in figure 4.7.5. A rearrangement of equation 4.7.1 predicts a maximum current to reach the melting point as around $100\ \mu\text{A}$, which is a significant current, but only needs to be applied very briefly to cause failure.

RESULTS

This section describes the results from nanomechanical beam using a more advanced cryostat as described in figure 4.6.4. This experimental setup enabled a much more detailed investigating of the effects of the helium gas pressure effects on the resonator and the helium liquid temperature dependent effects.

The discussion of results begins with a walkthrough of the analysis of a single data set and demonstrates the corrections and fitting procedure.

We then show the analysis of the measured overtones frequencies of a 50 μm long beam. We analyse the beams resonant response to increasing the measuring power and establish the dynamic range and linear regime of the beams.

We measure the response of the beam in helium gas at 4.2 K and compare that to power law model and the gas damping of a kinetic gas model. The last results subsection describes the beams response to helium liquid at different temperature using three beams of different length.

Measuring Resonance

In this subsection we show the analysis methods and necessary corrections used to see a response shape that is close to ideal. The corrected data is used to measure the centre frequency and width of a single response curve. From a single curve we extract estimates of the peak velocity, force, and displacement.

We measured the resonance of the beam as a feature on the transmission through the beam as a function of frequency. Measurement are taken using the circuit setup shown in figure 4.5.4 but without the use of DC breaks.

Raw measurements of S_{21} have the peak shape shown in both the real and imaginary part of the signal. The S_{21} data can be fitted directly to a Lorentz induced voltage, but this is not very good as the background has a large offset and curvature due to the signal phase changing.

We acquire transmission, S_{21} , over a wide sweep of frequencies of a 15 μm long beam in vacuum to measure the background signal. This approach removes the need for the peak fittings to include a free parameter the background curvature.

We first use a wide sweep in vacuum to measure the signal phase change. The phase change is described in section 4.5.7. Data from a 15 μm long beam is shown in figure 4.8.1.

From the measured background, we extract the phase change frequency $\Omega = 1.793 \times 10^{-7} \text{Hz}^{-1}$. Using Ω we reconstruct how the signal would have looked without a propagation delay To un-rotate the data we apply a rotation matrix on a vector $(\text{Re}(S) \text{Im}(S))$. The amount of rotation at a frequency f is $\theta = \Omega f$,

$$\begin{aligned}
 S_{\text{rot}} = & \cos(\theta)\text{Re}(S) - \sin(\theta)\text{Im}(s) + \\
 & (\sin(\theta)\text{Re}(S) + \cos(\theta)\text{Im}(s)) i.
 \end{aligned}
 \tag{4.8.1}$$

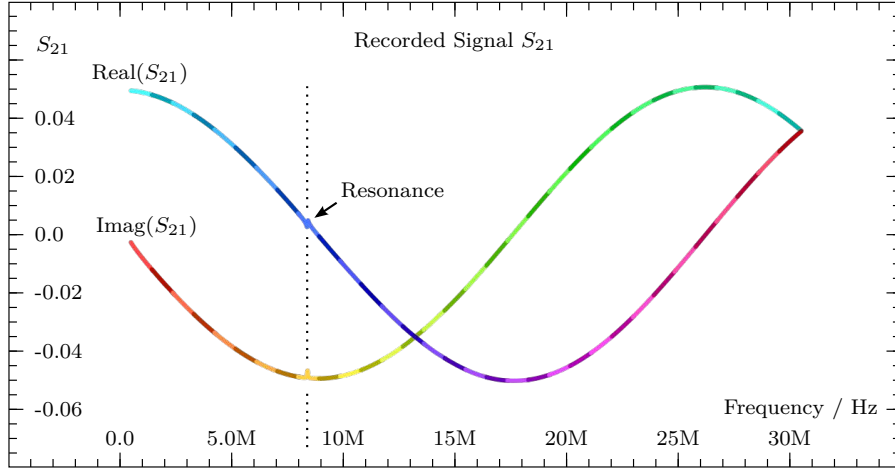


Figure 4.8.1: A 15 μm long beam measured in vacuum over a wide span of frequencies. The complex values of S_{21} changing with frequency. This data is used to establish a known background curvature. The effect of the resonant peaks on the fit is trivial as they account for a tiny fraction of the overall data set.

We use this phase change frequency, Ω , and the speed of light c to estimate and check the transmission line length,

$$l = \frac{c\Omega}{2\pi} \approx 8.5\text{m}, \quad (4.8.2)$$

which is physically reasonable.

All data using this experimental setup, using the same lines, the same attenuation, and the same amplifier use the measured value of Ω . However if the experimental setup changes then Ω would need to be re-measured.

An important difference between this frequency dependent rotation and simple rotation of the phase of the oscillator is that this rotation has a different rotation angle per data point as a function of frequency. The oscillator itself could still have a non-zero oscillation phase but that is accounted for separately.

The rotation correction removes curvature of the background and also brings the real and imaginary parts of the resonance response closer to what is expected. The effect of rotation correction correcting the background of resonance is shown in figure 4.8.2. This shows the first harmonic of the wide sweep vacuum data before and after rotation.

The mix of the oscillator's phase and the background phase are removed. A constant flat background is now only in the real component, this is the ohmic response of the beam, The imaginary component has a background near zero. The result is however still 'upside down' from the induced resonant voltage. The data shown in figure 4.8.2 is in vacuum, when the resonance is sharpest, the same resonance in liquid is much wider, where the curvature would be more difficult to extract.

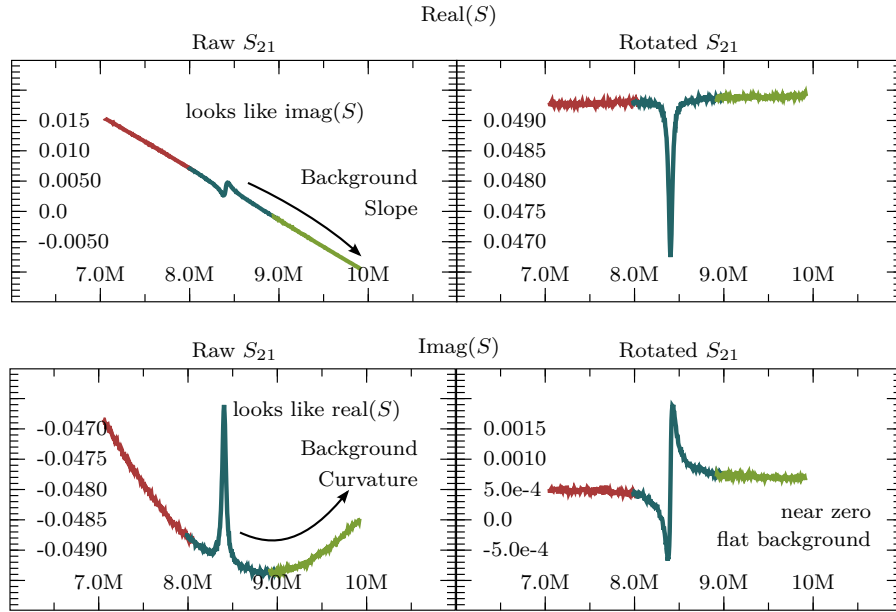


Figure 4.8.2: The measured background removed from the data removes a slight background curvature in the data. This shows the complex components of the oscillator are rotated back into the expected forms. A 15 μm long beam in vacuum, showing the fundamental resonance frequency .

The phase corrected data is still in S_{21} units. The resonance voltage is related to the transmission by equation 4.5.31 described in detail in section 4.5.5. Equation 4.5.31 relates the voltage $V_r = \Delta S_{21} V_1 Y / G$, where Y is always negative. Because of this we choose to simply flip S_{21} by -1 and apply a fitting of the voltage, absorbing the parameters V_1 , Y , and G , into the amplitude, A of the resonance peak. The complex voltage resonance peak is fitted by

$$V_{\text{peak}}(\omega) = \frac{A\omega i}{\omega_0^2 - \omega^2 + \lambda_2 \omega i}. \quad (4.8.3)$$

This function of the resonance is described in section 4.4.1. This is expressed in terms of the resonant angular frequency ω_0 , and the angular frequency ω . λ_2 relates to the damping on the wires, and affects the width of the peak. A λ_1 term could be included, but this is removed from the model because it is assumed to be small, and with one peak, it is un-separable from ω_0 leading to a non-finite covariance matrix, and no estimation of fitting errors. We use the model's free parameters to acquire more familiar terms, the resonance frequency $f_0 = \omega_0/2\pi$, and width $\Delta f = \lambda_2/2\pi$. The height of the peak at f_0 is $A_0 = A/\lambda_2$.

The model for V is extended to include a complex linear background, $V_{\text{bg}} = (af + b) + (cf + d)i$. This is to account for the large background that the in-phase component sees from the ohmic response of the beam, as well as any small frequency dependent effect on the signal. Small errors in the background phase correction are partially correct with this, but does not enable any extra curvature to be added or compensated for.

There is another free parameter, φ , was added to the resonance model to describe the resonance phase. This is a different phase from the background phase: it is a phase to rotate the peak to un-mix the complex components. We modify V_{peak} by the rotation matrix, \mathbf{R}_φ , by an angle φ to be,

$$V'_{\text{peak}} = \mathbf{R}_\varphi (V_{\text{peak}}) + V_{\text{bg}}. \quad (4.8.4)$$

All these together form an 8 parameter model, three for the peak, two pairs for the linear background, and one for the resonance phase. We fit the phase rotated corrected experimental data of S_{rot} to the model V'_{peak} . An alternative method to fit a Lorentz curve is described in [159]. To evaluate the effectiveness of the additions to the resonance model we compare the experimental data faster it is transformed to have the effects of $\Omega, \mathbf{R}_\theta$ and V_{bg} removed to show only the resonance shape V_{peak} . Figure 4.8.3 shows the resonance of the same 15 μm beam, while immersed in liquid helium at 1.2K. The figure shown suggests that

there is no extra background curvature and that we are successfully accounting for the nature of system.

We would have liked to remove the free parameter φ but the dotted line in figure 4.8.3 shows that the rotation is about the origin and is not negligible.

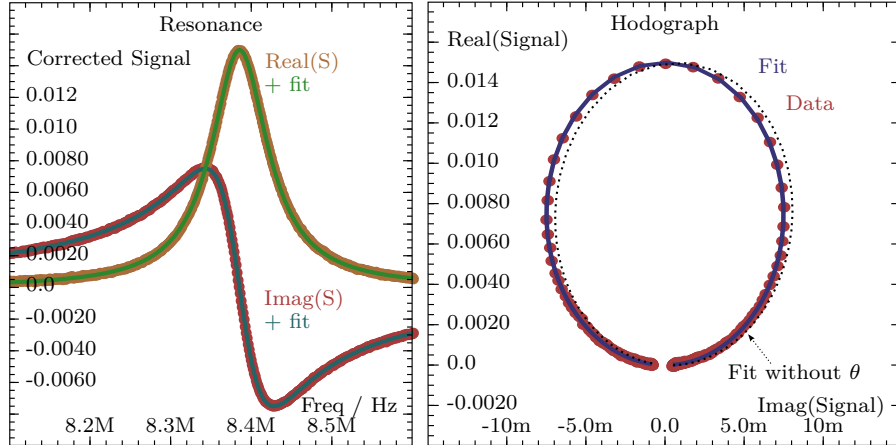


Figure 4.8.3: Fitting the S_{21} data after frequency dependent phase rotation to the model. A $15\ \mu\text{m}$ long beam in liquid at just over 1 K.

To acquire the force, velocity, and displacement of the beam during resonance we can use either of two methods:

- Fit the complex S_{21} data and the implied current, then measure the resistance of the beam while cold, to acquire Y , and use equations 4.5.31 - 4.5.34 to apply Faraday's Law. This would work if there was no reflection, and is used for low frequency signals. This method also involves a known beam resistance R and assumes a displacement profile.
- Fit the power absorbed by the beam. Start by fitting the complex S_{21} to find ω_0 , λ_2 , θ . Then convert S_{21} to power using equation 4.5.14 and use a fitting of power shaped curve, equation 4.4.14 with ω_0 , λ_2 , θ fixed, subtracted from a linear background. The resonance power can be used in energy conservation equations, 4.5.22, 4.5.23, and 4.5.25 to find the physical motion.

Fitting the power uses ω_0 , λ_2 , and θ measured by fitting S_{21} , or that step can be skipped and fit the power with all the free parameters. However we are unnecessary throwing away the phase information when we convert from the complex S_{21} measurements to power, $S_{21} \rightarrow P$ is lossy.

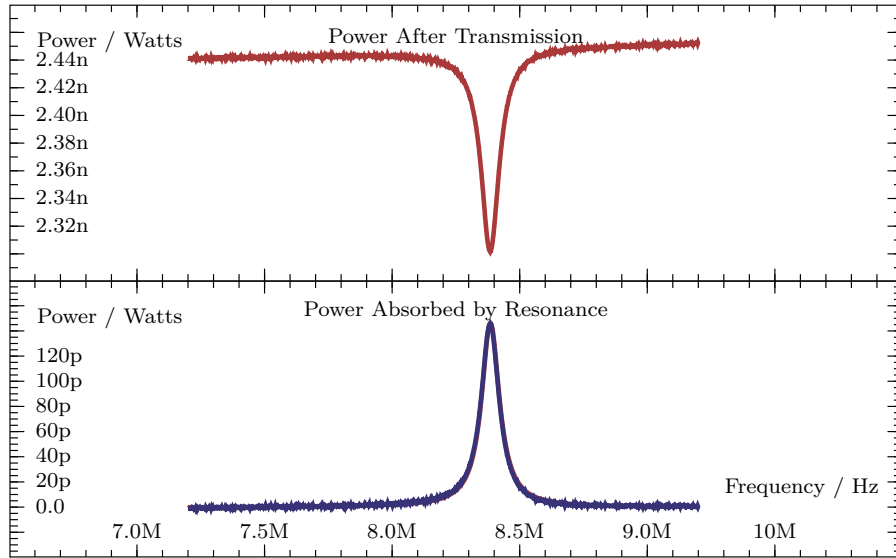


Figure 4.8.4: The power in the 15 μm long beam. The power after transmission accounting for the circuit gain and attenuation. This is converted to the power absorbed during the resonance of the beam by fitting the power model with a sloped background.

Figure 4.8.4 shows the transmission power and the power absorbed by resonance of the beam. The maximum power on resonance is used to find the velocity, displacement and the driving force. The equation 4.5.22, 4.5.23 are only true on resonance but are extrapolated to the rest of the measured powers over the frequency range. Each of the curves for velocity, displacement, and force have a similar line shape: \sqrt{P} , \sqrt{P}/f , and \sqrt{P} respectively and are drawn on figure 4.8.5. The force acting on the beam is actually independent of frequency so only $F = F_{\text{max}}$ at $f = f_0$.

Figure 4.8.5 shows the displacement maximum is 22.8 nm, this is very large compared to the beam thickness of 100 nm. The corresponding velocity also is very large to match. This data set was chosen to

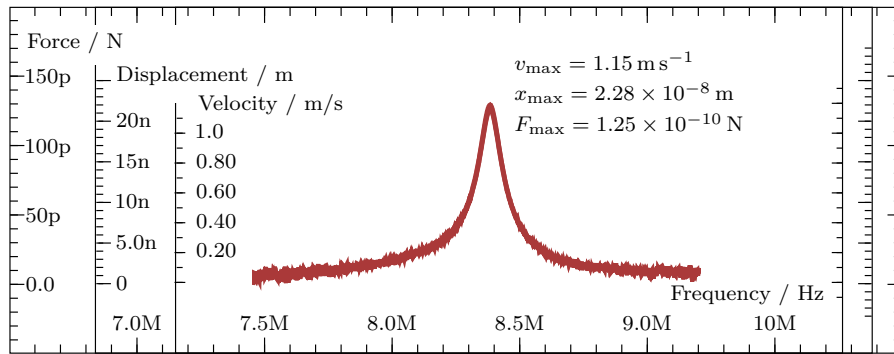


Figure 4.8.5: The force, velocity and displacement during resonance of a $15 \mu\text{m}$ long beam in liquid at 1.1 K . The -50dBm driving power is very high in this example.

clearly show the need for the corrections shown in figure 4.8.3, but the applied power of -50dBm is among the largest tested. A more typical applied power is -90dBm with typical velocities around 5 mm s^{-1} and displacements around 2 nm .

Higher Harmonics

Here we analyse the overtones of the beam. The transmission data is acquired by a wide sweep of the driving frequency while each sample is in vacuum at 4.2 K.

Figure 4.8.6 shows the visible overtones of a 50 μm long beam. The vacuum frequency is around 1.19 MHz, with the odd- n overtones at 3.82, 7.17, and 11.48 MHz. The quality factor for each harmonic is about 1500 and is independent of frequency. Table 2 compares each overtone as a ratio to the fundamental frequency. It seems that the beam has a frequency scale unlike the hinged-hinged beam or the fixed-fixed beam from table 1. The ratio of the frequencies suggest that the beam is acting more like a wire, rather than a clamped solid beam, as the ratios approximately follow n rather than n^2 for a Hinged-Hinged or $\approx ((2n + 1)/2)^2$ for a fixed-fixed behaviour.

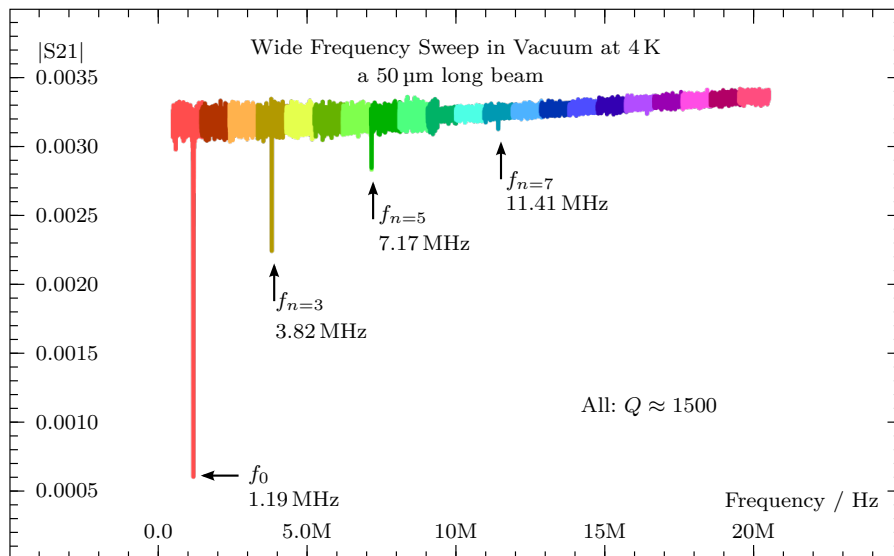


Figure 4.8.6: A collection of frequency sweeps covering a large range of frequencies. We can see 3 or 4 overtones. The step in noise at around 10 MHz is due to an internal filter as part of the operation of the vector network analyser.

Figure 4.8.7 shows similarly performed wide frequency sweeps for two other beams, a 15 μm and a 25 μm long beam. The 15 μm beam has

Table 2: 50 μm beam overtones in vacuum at 4.2 K

Harmonic	1	3	5	9
Frequency/MHz	1.19	3.82	7.17	11.41
Ratio $f_n/f_{n=1}$	1	3.21	6.03	9.61

additional higher frequency harmonics that we do not think are simply the beam's harmonic overtone, and look similar to the resonances found when the beam is dirty, as in figure 4.7.2. The data for the 15 μm and 25 μm samples are taken with much higher measurement power. The $n = 3$ harmonic of the 25 μm sample is visible at 13.6 MHz, a factor of 2.95 over the fundamental frequency of 4.6 MHz. This is similar to the 50 μm sample.

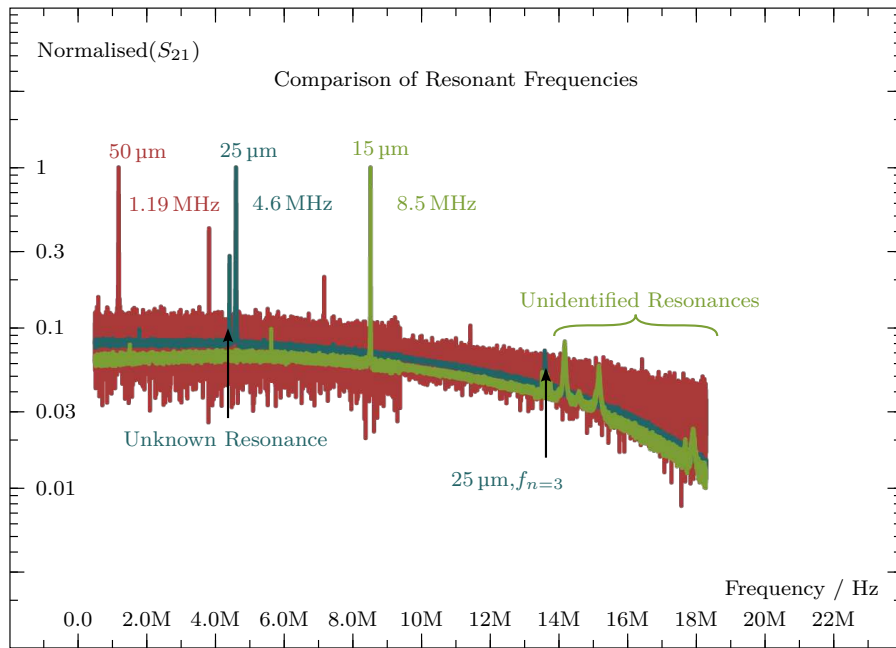


Figure 4.8.7: Combining wide sweep data from three different length nanomechanical beams, a 15 μm , a 25 μm and a 50 μm that was also shown in figure 4.8.6. All shown data sets were acquired at 4 K in vacuum at the beginning of an experimental run. The S_{21} data is normalised to be between range $0 \rightarrow 1$ so that a comparison can be seen.

We can use the information of the resonance frequency to estimate the tension on the beam using equation 4.4.19. The tabulated data,

table 3, shows that longer beams have less tension. The tension from thermal contraction 3 nN is negligible. This means that the beams, while deformed, are in considerable tension after fabrication. The tension appears to scale with the length, so longer beams have less tension. This can be attributed to longer beams having more geometric irregularities and a lesser effective spring constant. We can use a linear extrapolation to estimate the tension of a theoretical zero length beam to find $T_{L=0} = 1.8(2) \times 10^{-6}$ N. If we assume that the geometric irregularities scale with the length of the beam, then the zero length tension is the what the tension would be of a perfect beam. Using this we can estimate the 15 μm , 25 μm and 50 μm beams experience a tension of 73%, 59%, and 16% respectively of the ideal tension.

Table 3: The modeled tension on the beam using equation 4.4.19.

Beam Length	Resonance Frequency	Tension
15 μm	8.4 MHz	1.3×10^{-6} N
25 μm	4.6 MHz	1.1×10^{-6} N
50 μm	1.19 MHz	2.9×10^{-7} N

Power Response and Drive Sweeps

We measured the beam using different measurement powers, which are set by the output power of the vector network analyser and accounting for the external attenuators in the measurement circuit. The different powers caused differing electrical current to flow through the beam and cause the beam to be driven at different velocities and displacements. The relation between the force applied on the beam and the velocity of the beam is called the power response, and is useful to understand the dynamic range of the device. We describe a linear region of operation, which is used in subsequent measurements as known acceptable measurement power, and we measure a transition to non-linear operation where the beam has a Duffing-like or other non-linear behaviour. We compare the drive sweep in vacuum with a drive sweep in liquid.

Measuring the power response involves sampling the resonance of the beam over a range of different powers. From the raw complex S_{21} data we convert to power using equation 4.5.14. We find an average background across the range of applied powers, in S_{21} space, and use that as a common background loss. This approach of a shared background removes the error from background fittings of individual sweeps.

Figure 4.8.8 shows the power absorbed by the beam due to resonance over a range of applied powers. The range of powers is used to cover and demonstrate the linear regime, where the peak shape is Lorentzian, and as the applied power increases the peak becomes non-linear and shifts to higher frequencies. This shift is because the effective spring constant is increasing, called k-hardening. As the power increases the beam behaves non-linearly and shows a Duffing-like behaviour, characterised by the shark-fin shape at the top of the resonance. At the high powers we can see additional resonance peaks appearing, potentially from off-

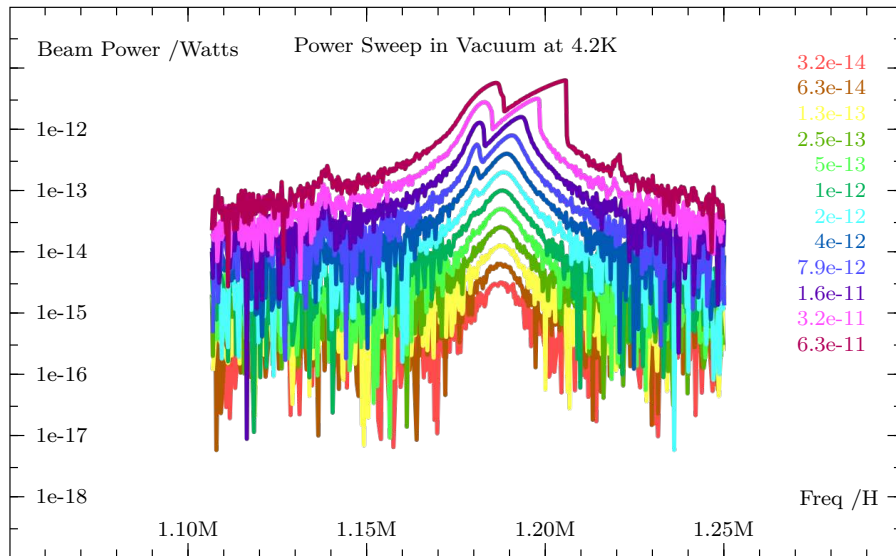


Figure 4.8.8: A power sweep of a $50 \mu\text{m}$ long beam in vacuum at 4.2 K. The applied powers are shown in the legend in watts. The data shows a $\frac{1}{5}$ subsample of the acquire curves.

axis resonance (shown in figure 4.7.3.a). This is due to the non-linear motion of the beam exciting off axis modes. In other experiments [160] the excitation of off-axis modes can be used and controlled if in the presence of an externally applied electric field, this has been used on nanomechanical resonators as two level systems in order to tune the degenerate modes. These degenerate modes may be what we are seeing, but for use as probes in liquid helium the addition of off-axis modes near the primary resonance is unwanted behaviour. We use the information about the dynamic range in linear regime to pick a measurement velocity to use during liquid measurements as we do not want to complicate the future analysis with handling and modelling the nonlinearities.

While the power response of the beam scales proportionally with the applied power, this is the linear regime of the beam. We use numerical curve fitting to measure the maximum power in the beam so that we can relate the applied power to the resonance power.

We use the peak power absorbed and the width to create estimates of the velocity (from equation 4.5.22) of the beam and the force on the

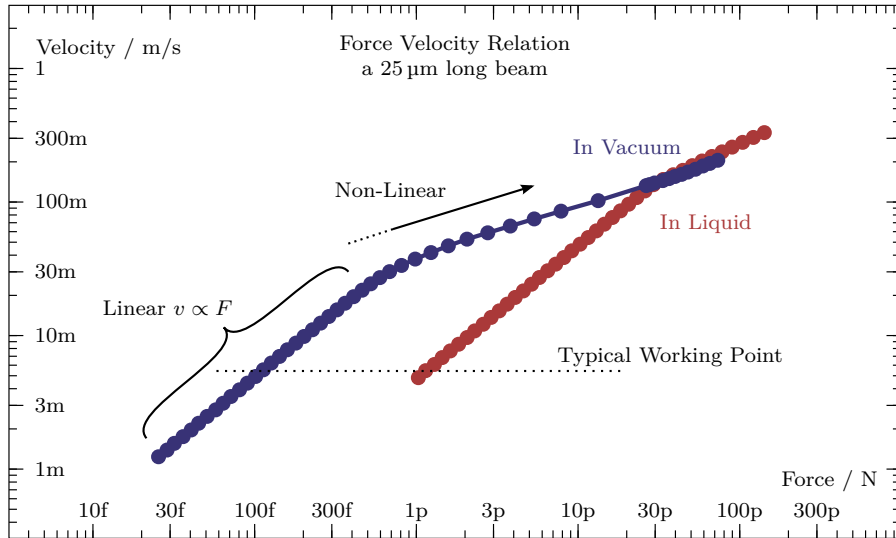


Figure 4.8.9: The results of a power sweep of a 25 μm long beam in vacuum at 4.2 K and in liquid at 1.2 K.

beam (from equation 4.5.23). A graph with logarithmic axes in figure 4.8.9 shows the transition from a linear to a nonlinear response.

Figure 4.8.9 shows that the velocity of the beam does scale with force.

We quantify an estimate of the non-linearity of the response in figure 4.8.8 by using the asymmetry of the peak. We split the peak into two parts around a pivot frequency which has the maximum amplitude. Each half is mirrored over the pivot point to create a pair of new synthetic symmetric peaks. This is demonstrated in figure 4.8.10. We then fit a Lorentz peak to each half individually, and call l the width of the peak from the left half, and r the width of the peak from the right half. If the beam is operating linearly, the peak is symmetric so $l = r$, but as it becomes more non-linear one side will appear to have a much smaller width. This difference, $l - r$, is normalised and provides a non-linearity parameter,

$$p = \left(\frac{l - r}{l + r} \right)^2. \quad (4.8.5)$$

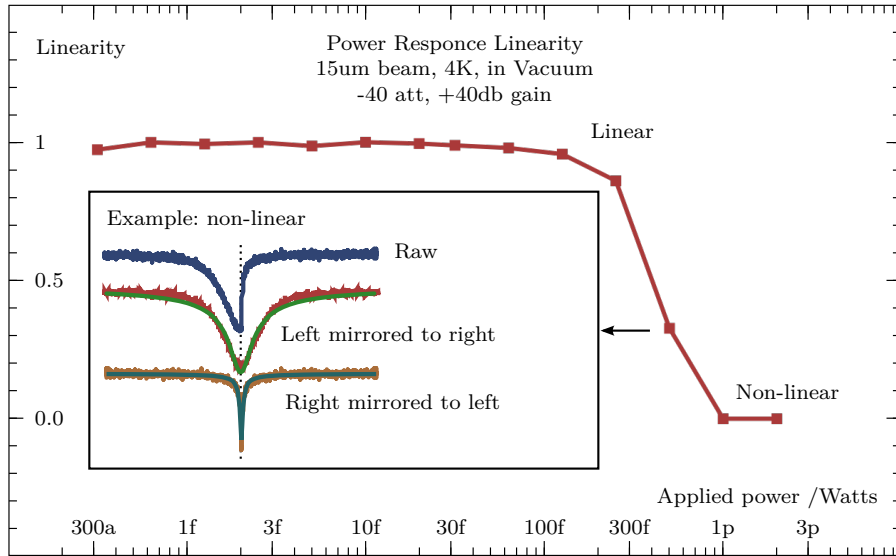


Figure 4.8.10: We estimate the linearity of a resonance peak by using symmetry peak. linearity is calculated according to equation 4.8.6. The transition is smooth starting around 100 fW, and become fully non-linear after 1 pW of measurement power.

As the beam becomes increasingly non-linear, l or r will approach zero, which will leave p trending to 1. This creates a 0 to 1 scale which is converted to linearity by $q = 1 - p$.

$$q = 1 - \left(\frac{l - r}{l + r} \right)^2 \tag{4.8.6}$$

Using this linearity estimator we estimate that the 15 μm long beam is performing linearly until about -100dBm , i. e. $1 \times 10^{-13}\text{ W}$ of applied power.

Pressure Dependency

A few samples of beams are measured at 4.2 K at different pressures of helium. This is achieved by control of a needle valve to the pot volume enabling pure helium to flow in from the bath. The change of pressure is applied very slowly to keep the gas temperature in thermal equilibrium with the bath temperature of 4.2 K. The pressure is measured using a gauge on the pot line just above the top-plate. Figure 4.8.11 shows the quality factor of resonance of a selection of devices over a range of pressures. This shows that the quality factor drops as gas pressure increases. Each of our devices has a similar response.

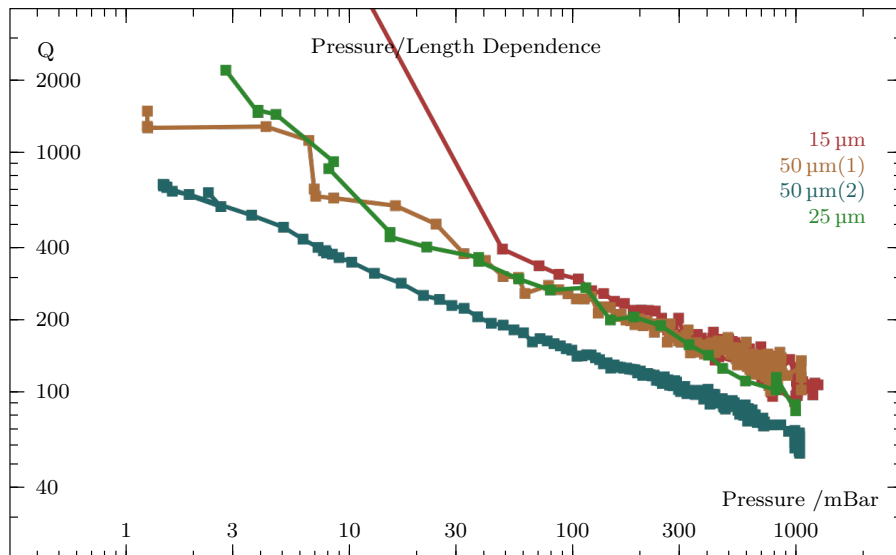


Figure 4.8.11: The quality factor of the beam changing with varying helium gas pressure. The dependency appears independent of the length of the beam.

Figure 4.8.12 shows one of our data sets and a numerical fit of the quality factor to the pressure according to a power law, $Q = kP^n$, for free parameters k and n . Also shown is data extracted from images in Kraus et al's paper [82]. Kraus et al used shorter, 1 μm, and thicker, 200 nm, beams, and presented data of the S_{21} transmission over resonance, which we have fitted to the power absorbed model, to extract the width, centre, and quality factor.

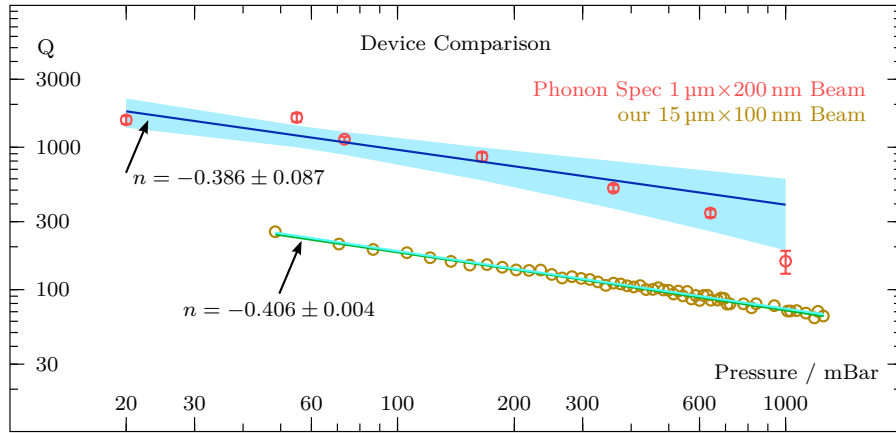


Figure 4.8.12: Fitting the Quality factor with a power law dependence. A model $Q = kP^n$ is fitted to each data series, and an 80% confidence interval shown.

Both our data and Kraus et al [82] show that a power law of $n \approx -0.4$. Fitting our data to the kinetic gas model for damping, equation 4.4.31, which has $Q \propto 1/\sqrt{P}$ and one free parameter, we find that $C = 1.8(2)$ has good agreement with one free parameter that is close to what is expected.

The authors of [149] propose a pressure-Q model that work for a MEMS beam, 200 μm long and 40 μm wide, but it seems that the behaviour of our devices and Kraus et al can not be explained by this model.

*Resonance Response to the Temperature Dependent Properties of
Liquid Helium-4*

We immersed nanomechanical beam in liquid helium-4 inside the pot volume. We use the same three devices as used for figure 4.8.7 and figures 4.8.8–4.8.3. We are assured the beam is immersed because a VWR positioned above the sample has a step change in width from approximately 0.5 Hz to 3 Hz.

The liquid temperature was changed using evaporative cooling. The temperature was measured with both a calibrated RuO₂ resistor inside the pot using a Lakeshore AC resistance bridge on a 4-points connection, which agrees with measurements by the helium-4 saturated vapour pressure at room temperature just above the cryostat on the pumping line.

To analyse each of the resonances we use the simultaneous complex fitting in S_{21} space to equation 4.4.9, as shown in figure 4.8.3 after a propagation phase correction. Once all of the curves for each temperature are fitted we have a collection of widths, central resonant frequencies, that change, and a collection of backgrounds that are consistent. Figure 4.8.13 shows only the changing resonance features of the data after curve fitting. This is only a small sampling of the data acquired during cooling of a 25 μm long beam, but does show the characteristic narrowing width change and increasing shift of resonance to higher frequencies as the fluid is cooled.

As expected in superfluid, the resonant frequency, f_i , increases as the temperature lowers, from the reduced density of the normal fluid component. And the width of the peak also reduces as the temperature goes down as the superfluid is less lossy. During the measurements the Q factor changes from 5 to 24.

Figure 4.8.14 shows the resonance centre frequency of the 50 μm long beam. The centre frequency is compared to the Blaauwgeers et

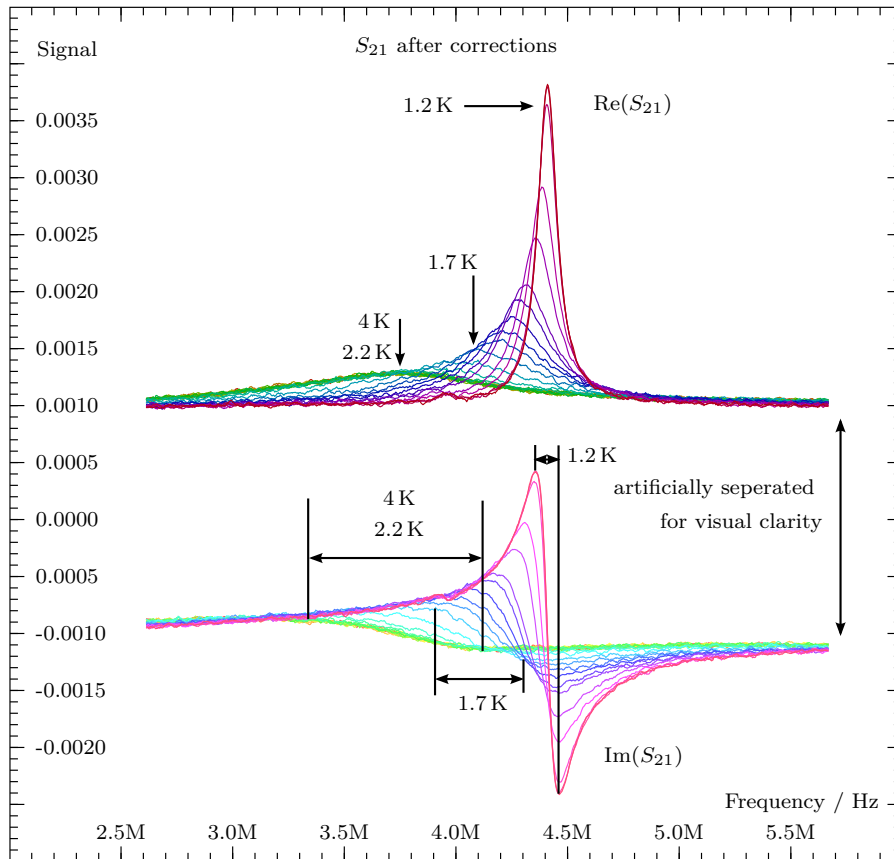


Figure 4.8.13: The corrected signal data of a 25 μm long beam that is immersed in liquid during a temperature change from 1.2 K to 4 K. This data has been smoothed for visual clarity in this plot, but not during fitting.

al model [51], fitting the centre frequency from equation 4.4.23 using the summarised helium properties in Donnelly et al [145]. The fitting parameters for the centre frequency are shown in table 4.

The fit for the centre frequency seems to be good across the whole range of temperatures tested. The confidence band that is drawn represents the likelihood that the true line from the model lies within that region. The vacuum frequency is also allowed to be a free parameter such that the low temperature data is able to be adjusted slightly. This is justifiable if we assume that the previously measured vacuum frequency was measuring a beam that is slightly different from the beam being measured during the temperature sweep, with differences attributed to tiny amounts of dirt attaching to the beam

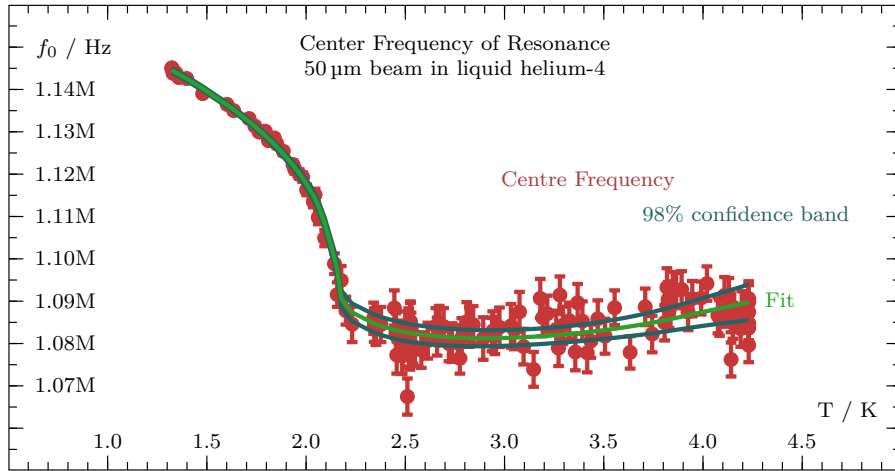


Figure 4.8.14: Fitting the resonance frequency as a function of temperature.

The error bars on individual data points come from the individual response curves, the confidence bands is generated from the covariance matrix and the derivatives evaluated per point on the curve.

from the helium filling process. The measured vacuum frequency of 1.187 MHz changes to 1.174 MHz, a shift of $-0.013 \text{ MHz} \approx -1\%$. The sign of the shift implies extra mass. This is consistent with ≈ 2 monolayers of solid helium-4 attached to the beam.

Table 4: Fit parameters for resonance frequency and width shown in figures 4.8.14 and 4.8.15.

Parameter	mean \pm sigma
β	0.56 ± 0.32
B	0.8706 ± 0.023
$f_{\text{vac}} / \text{Hz}$	$1.174 \times 10^6 \pm 9.8 \times 10^3$
C	1.792 ± 0.021
$\Delta f_{\text{intrinsic}} / \text{Hz}$	$2.37 \times 10^4 \pm 5.9 \times 10^2$

The width of the resonance for the same $50 \mu\text{m}$ data set is shown in figure 4.8.15. The fit of the resonance width uses equation 4.4.25. There is noise in the functional form of the fitting of the width because it uses the measured value of the centre frequency, . We have added an extra

constant to the fitting of the width, an intrinsic width $\Delta f_{\text{intrinsic}}$, so that the total width is, $\Delta f_2 = \Delta f_{\text{intrinsic}} + \Delta f_{\text{fluid}}$. The intrinsic width should be the width of the resonance in vacuum. The model has trouble fitting the flat response of the high temperature data, consistently fitting too narrow, and does not match the curvature of the low temperature data.

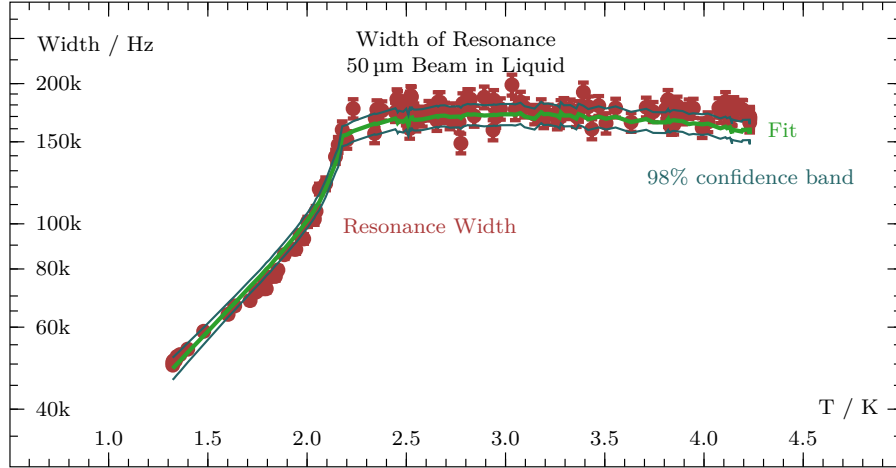


Figure 4.8.15: The resonance width of a 50 μm long beam immersed in liquid at different temperatures. A line from fitting the resonance width is overlaid.

The liquid temperature response for the other two beams was measured in a similar way. The centre frequency response from the other two beams are shown in figure 4.8.16 and the change in width is shown in figure 4.8.17. The 50 μm beam has the best agreement with the theory. The other two beams show promising shapes similar to what is expected but deviates further away than what the free parameters in equation 4.4.25 are able to accommodate. We found it best to provide the vacuum frequency for the shorter beams as the least squared minimisation found very poor and unrealistic parameters.

Table 5 shows a collection of parameters found by fitting the temperature curves. Due to the poor fitting some parameters are unrealistic, for example the intrinsic width Δf_i should never be negative, C should not go far above 2, and $\beta \approx 0$ would imply that the beam as zero volume.

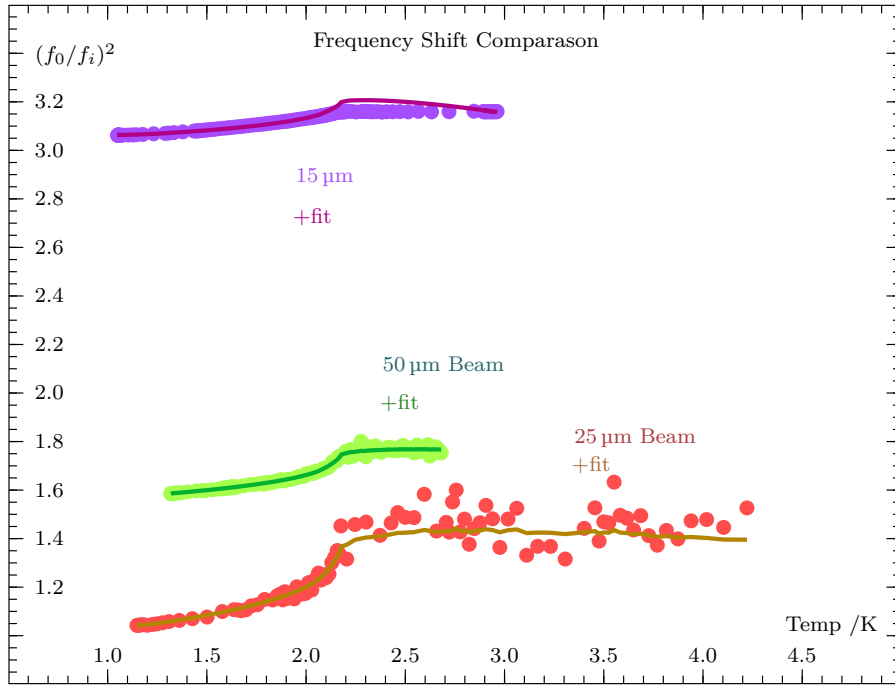


Figure 4.8.16: Comparing the normalised Resonant Frequency of the beam in liquid across beams of different lengths. The centre frequencies show exceptionally good agreement with the model.

Table 5: Summary of temperature dependence fits. Fitting parameters that are drastically far away from expected values are highlighted in red

l	f_0	applied power	β	B	C	Δf_i
μm	MHz	dBm				kHz
25	4.485	-90	0.00(1)	4.48(6)	9.25(2)	-47(5)
50	1.188	-90	1.02(1)	0.845(5)	1.67(2)	22.5(6)
15	8.513	-50	-0.05(5)	0.20(3)	2.52(7)	1.50(3)

Comparison to Tuning Forks and Vibrating Wire Resonators

To compare the nanomechanical beams to other mechanical oscillators, we use the normalised frequency shift of $(f_0/f_i)^2 - 1$. We compare the beams to a best-in-class tuning fork with a thickness of 25 μm , a sensitive 4.5 μm thick ‘uuu’ half loop vibrating wire resonator, and a typical goal-post wire resonator.

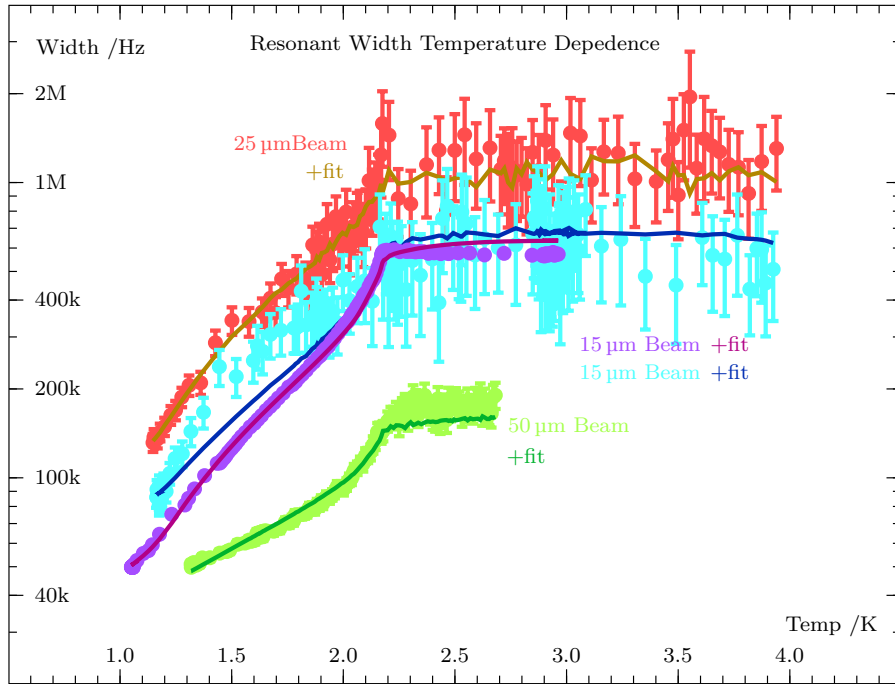


Figure 4.8.17: Comparing the change of width of resonance in liquid between beams of different lengths. Each data set is shown with a fit two equation 4.4.25. The width is notably not monotonic with beam length.

Figure 4.8.18 shows the comparison. This shows the NEMS is over an order of magnitude more sensitive with the normalised frequency shift, changing approximately 4.9% while the tuning fork over the range, 1.4 K to T_λ , and VWR changes 0.34% and .17% respectively.

Measuring in the Superconducting State

The aluminium construction of the beam is a normal conducting material in fields above 30 mT, and a temperature exceeding about 1 K. The actual critical field is dependent on the geometry of the aluminium, thin and narrow samples could have a lower critical field, the $B - T$ phase diagram of bulk aluminium can't be applied.

We are not able to lower the beam temperature enough to see superconductivity, but we can test the capability of the apparatus's signal/noise. We lower the applied field from the electromagnet to 4 mT.

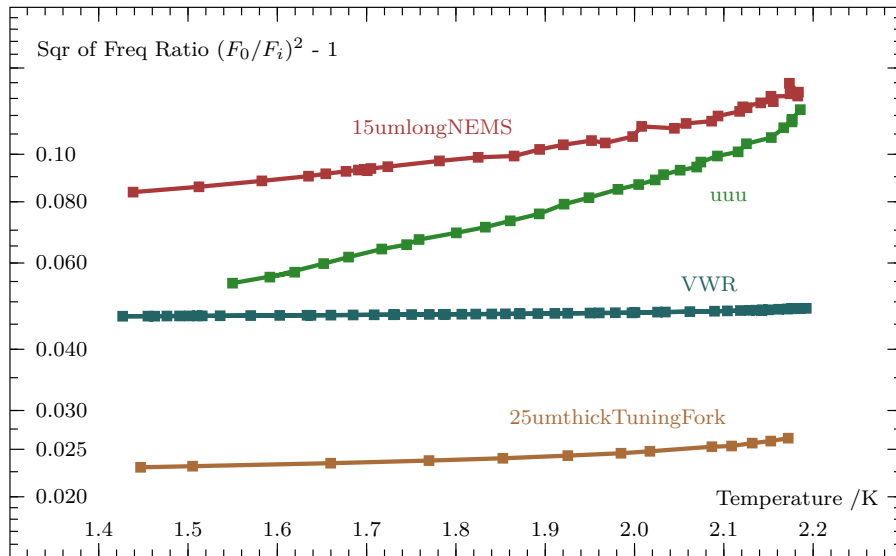


Figure 4.8.18: Comparing the sensitivity of devices while measuring superfluid helium-4. The NEMS beam from these measurements with a tuning fork [161]. A 127 μm diameter vibrating wire resonator in a 5 mm by 5 mm goalpost shape, and a very thin ‘uuu’ wire [162].

and used ten averages with high measuring power. The data shown in figure 4.8.19. This shows a signal to noise ratio of around 3.

However this is very promising as it would mean that if the sample were to be cooled below T_c then it could be used in a superconducting circuit there could be no ohmic dissipating at the beam, a characteristic that is crucial in ultra low temperature helium-3 measurements.

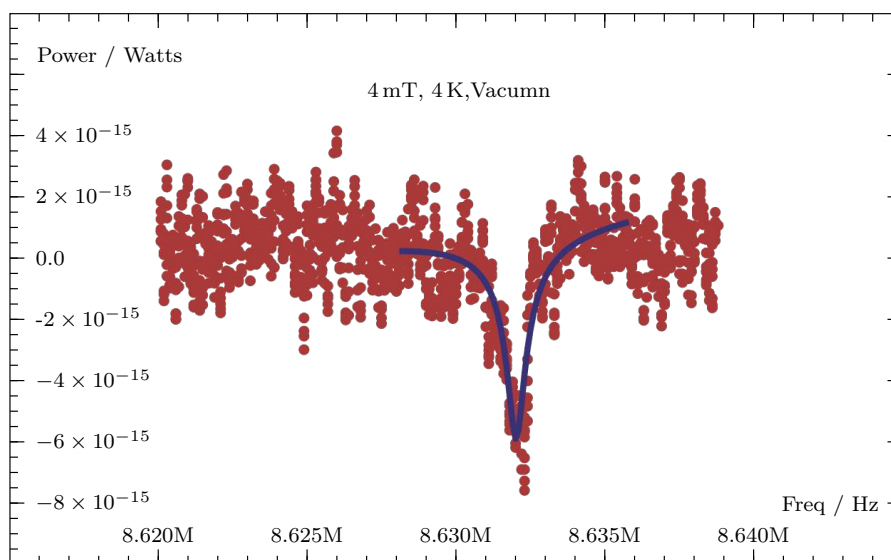


Figure 4.8.19: Measuring the beam in a field low enough to enable the aluminium to be superconducting.

DISCUSSION

The model used to describe the mass enhancement of the beam and the fluid damping both use the viscous penetration depth of the fluid around the device and the surface area to define a volume of attached fluid. The attached fluid volume is the protrusion of the beam's surface S out by a distance δ , as shown in figure 4.9.1. This approximation only works if the length scales of the beam profile are much larger than δ , as the error in volume estimation drops. This volume estimation error can be significant if δ becomes large.

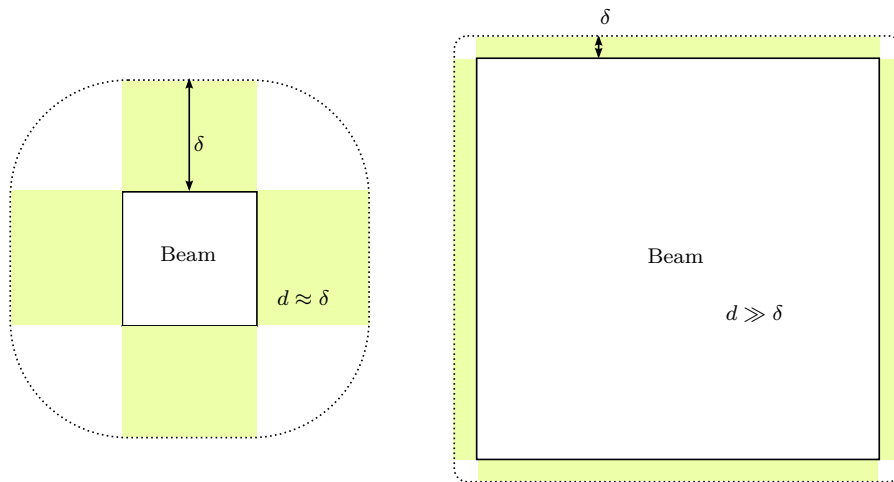


Figure 4.9.1: The viscous penetration depth, δ , into the liquid around the beam can become significant compared to the beam's diameter which drastically changes the error when calculating the volume of attached mass. If δ is small, shown on the right, then the volume is quite accurate. However if δ is large or comparable to size of the object d , then the modelled attached volume can be not representative of the volume of fluid that is attached.

Figure 4.9.2 shows the calculated liquid helium-4 viscous penetration depth for the frequencies of the 50 μm long beam using equation 4.4.24. Because the beams are operating where $\delta > d$ then the definition of the surface are S and the fitting constants C and B are now not well defined. The success of the model predicting the frequency change by using this is surprising as the assumptions are not valid. The success could be

that the power law scaling of S , being d^1 , is still true. Equation 4.4.23 could replace S with dl and have B now represent a different physical parameter for the attached mass.

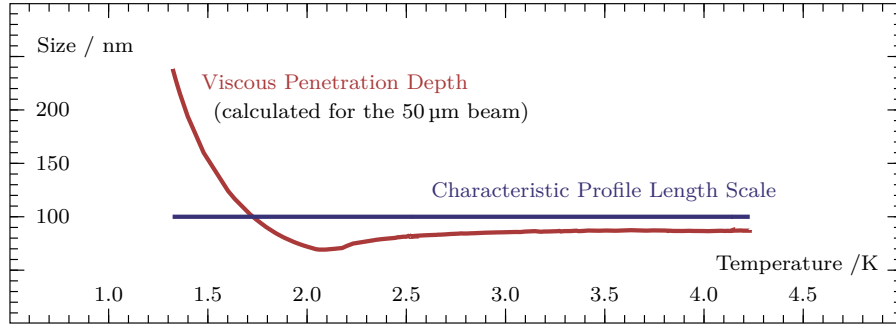


Figure 4.9.2: The calculated viscous penetration depth of the $50\ \mu\text{m}$ beam in liquid helium-4. The viscous penetration depth is a significant fraction of the thickness of the beam and is larger below $1.7\ \text{K}$.

Our analysis used the surface area of the beam calculated from a square profile. However the SEM images suggest that this is not true. A more accurate ‘egg’ shaped profile could be closer to the truth. The ripples in thickness down the length of the beam could catch and hold additional fluid that is not accounted for.

We can use existing data to attempt to measure the effective surface area. The surface area S is directly proportional to C and B , but not β , any error from a mis-calculated surface area would be absorbed into C and B . There is the possibility to allow S to be a free parameter. Each curve for Δf_1 and Δf_2 have S inseparable from other free parameters, we combine the curve to create the combined model of $[\Delta f_1, \Delta f_2]$ over the temperature range $[T, T]$. We fit both curves simultaneously and S is separable and can be measured by curve fitting. Table 6 compares the predicted S to a measured S . This suggests that the prediction using the square profile is a reasonable indicator for the short beams, but is not working well for the longest beams. This is still unable to explain why $C = 9$ for the $25\ \mu\text{m}$ beam in table 5.

Another cause for the poor width fitting could be the beam probing the partially clamped fluid between the beam and the substrate. The

Table 6: Measuring S using the combined model of frequency shift and width change. Changing S also changes all other fitting parameters, but they are omitted for brevity.

Length	Predicted $S / (1 \times 10^{-12} \text{m}^2)$	Measured $S / (1 \times 10^{-12} \text{m}^2)$
15 μm	6	6.6(6)
25 μm	10	11.4(3)
50 μm	20	12(5)

beam to substrate gap is a few micrometres, and could be reached with buckling seen on some of the SEM images. The beam needs to reach far enough to bring the beam within a few δ of the substrate surface. This buckling is random per-device and could mean that only individual samples could experience additional fluid-to-substrate clamping.

Even with the difficulty understanding the temperature dependent damping the beams could be used as a secondary thermometer by calibrating against a primary thermometer. The centre frequency has a large change over temperature. The precision is estimated by the standard deviation of the centre frequency provided during curve fitting and $\frac{d}{dT} f_i$ of the model's centre frequency in liquid evaluated using the measured parameters β and B . Even though we did not optimise measurements for maximum centre frequency precision, the 50 μm beam with our tests shows a thermometry precision of 20 mK between 1.2 K and T_λ .

The mass sensitivity of the beam is calculated from the precision of the centre frequency measurements. In liquid the beam is most sensitive at low temperatures when the resonance is sharpest. The mass sensitivity is $\Delta m \approx 2 \frac{m}{\omega} \Delta \omega$ and would have a coefficient of unity order to account for the effective mass from the total beam mass. The 50 μm beam at 1.2 K has a mass sensitivity of around 800 ag, while the smaller 15 μm long beam shows $\Delta m = 10$ ag. If the temperature of the system were to continue cooling and have the same trend of increasing Q , the

beam would have a mass sensitivity of 1×10^{-24} g at 10 mK. But is that unrealistic as the intrinsic resonator Q will become dominant. The mass sensitivity range around 1×10^{-24} g is very interesting for quantum fluids as the helium-4 mass is 6.64216×10^{-24} g, and individual quasi-particles in helium-3 have masses 1.4×10^{-24} g to 2.8×10^{-24} g depending on pressure [163], which suggests that the beams could measure a flux of quasi-particles with a number density of the order tens. There is not enough temporal resolution to see any individual quasi-particles as the time for a frequency sweep of the device is still very large.

The potential to use the beam in liquid prompts a comparison the the uses of other oscillators in liquid. The generation of superfluid turbulence is one such application. The turbulence is expected to be generated above a critical velocity

$$v_c \propto \sqrt{\kappa\omega}, \quad (4.9.1)$$

where $\kappa = 2\pi\hbar/m_4$ is the circulation quantum and ω is the oscillation frequency [133, 164]. This is a low estimation because of the required vortex nucleation problem. v_c is going to be very high just due to the high frequencies involved. And driving beams is to such speeds could be challenging. We may not be able to use NEMS as generators of turbulence, and so they will be dedicated only to detector applications.

FURTHER WORK

The existing devices should be used to test linear relationship between velocity and the magnetic field strength. The induced voltage from resonance which should scale as B^2 . Methods could be established to accurately measure the beam resistance. This will require modelling of signal reflection and transmission losses.

The beams could be used to observe the liquid temperature dependence on the device Q at low temperature below 1 K. A T^{-4}

dependency [51] would imply that the beam is entering the ballistic regime where damping from the excitation density decreases and the drag coefficient rapidly decreases.

To understand the effects of different length beams in liquid many more beams with length in the range 10 μm to 75 μm would need to be tested. There is some non-monotonic behaviour of width that could be exposed given more detailed range of beam lengths.

In very low temperature systems like the ballistic regime of helium-3 at around 200 μK which operate like a quantum vacuum. The additional damping from fluid effects is smaller and the change in Q is much less, the intrinsic beam quality factor may need to improve to provide the needed sensitivity. However the intrinsic width at these temperatures is unknown, and the effect of Q over the superconducting transition of aluminium is unknown. The low quality factor in normal aluminium is partially from grain boundaries in the aluminium and uneven deposition of aluminium. We would need a cleaner aluminium deposition method to be able to get the aluminium more pure and regular. We also know that the properties of the resonator can change drastically when becoming dirty from frozen nitrogen or oxygen that form on the beam. Having the devices exposed to an atmosphere of typical low-temperature laboratory air containing pump oils and dust is risking contamination. Improving the beam would involve enhanced clean-room fabrication techniques, and much more importantly cleaner handling techniques and methods when in a low temperature laboratory.

The beams could be attached with aluminium bonding to complete a superconducting circuit. This is critical to reduce heating for operating end of a nuclear demagnetisation stage.

Nanofabrication has the potential to construct a serial array of frequency separated tuned beams that enable simultaneous multiplexed measurements. There are fabrication challenges for the unknown

internal tension of the beam which can change the frequency of individual oscillators.

Nanomechanical capacitively driven beam arrays capable of multiplexed readout have been developed [165]. These use another design of NEMS: a capacitively coupled doubly clamped beam. This is not the only style of device, a capacitively driven T-shaped device could be used without a centre of mass motion. The benefit of capacitively driven beams is that they do not require a magnetic field, and can enable an post fabrication method of tuning of the resonant frequency.

Further analysis of the data could build a different model to describe the width response of the beam including the effect of acoustic losses. Some recent work by Aoust et al [166] has suggestions and presents a few models that we can try without needing to acquire any additional data. An additional loss mechanism at very low temperatures is the effect of normal-state electrons [167], this effect is comparably very small to fluid based damping but will become increasingly significant in helium-4 as this too is reduced.

CONCLUSIONS

Challenges and operational methods for using nanomechanical beams have been mostly overcome, they can be cryogenically cooled and measured in the experimental low temperature laboratory.

We measured the fluid properties of helium above and below the superfluid transition temperature. The response of the centre frequency shift due to the liquid fits very well to the established Blaauwgeers et al model [51] for all beams with a length between 15 μm and 50 μm . This is an incredible and surprising result that extends the experimentally validated range. The long, 50 μm beams work well with the hydrodynamic model, it yields physically plausible parameters for C , β , and b . These long beams could be used as sensors ‘as is’ without additional modifications to theory. The shorter and higher frequency beams have a larger deviation from the model and will require additional work to understand. The existing model suggests un-physical fitting parameters, particularly the C parameter which is impossibly large, around 9, implying an attached mass that is too large.

We measured the helium gas pressure dependence that showed $Q \propto P^{-0.4}$. This is close to the high pressure $Q \propto 1/\sqrt{P}$ model. A fitting of the quality factor to the kinetic gas equations showed good agreement with $C = 1.8(2)$, a value that is close to the value that is seen for damping in liquid.

The resonance quality factor in liquid helium at 4.2 K is of the order 10, and increases towards order 100 as the viscosity and temperature drop. The low quality factor and high resonant frequency creates a challenge to recover the complex induced voltage from resonance due to a large signal phase change in the frequency range of the resonance. This problem was solved successfully.

We analyse the harmonics of a beam and show that the resonance frequency and the harmonics scale closely with n and not like the clamped-clamped model of a fixed beam.

There is promising result that a signal has been acquired from beam operating in a low magnetic field that would enable the superconducting state of aluminium. The aluminium beams were not superconducting in our experiments and it is yet to be seen if these beams will become superconducting and at what temperature.

There is substantial sensitivity of the resonance response to enable nanomechanical beams to be used for probing superfluids. The extreme lightness of the narrow aluminium beams means the displaced fluid mass per unit length is a higher fraction of the beam's mass per unit length. The very small beam thickness means it has a high surface area to mass ratio that increases the sensitivity to the damping changes of the surrounding medium.

The beams sensitivity means that impurities of frozen gasses landing and freezing onto the beam cause significant changes in the frequency response, the creation of additional inconsistent resonance peaks and the shifting of the fundamental frequencies. Attempting to clean the beam by applying high measuring powers to melt off the dirt is a working method, but risks damaging out the beams. Problems with dirt and thermal annealing reduce the reproducibility of the devices.

CONCLUSIONS

This work showed different thermometry techniques: the CBT which measures electron temperatures in the millikelvin regime, and the NEMS beam that directly probes the surrounding environment for temperature dependent properties. These methods are developed to improve the understanding of low temperature systems and progress experimental physics techniques which are applicable to many other fields.

We have shown that a CBT can be sufficiently thermalised overcoming the weak electron-phonon coupling at low temperatures to measure the temperature of electrons in a nano-electronic device. In collaboration with the device's designers and fabricators of VTT and Aivon in Finland, we achieved an electron temperature below 3.7 mK by large on-chip thermalisation blocks, electronic filtering, dedicated sintering, and a custom experimental cell for immersion into the mixing chamber of a dilution refrigerator at 2.6 mK. Thermalisation time constant and thermalisation saturation measurements highlighted the importance of cooling the chip substrate and the electrical leads. The electron phonon thermalisation we measured showed a more beneficial $T^{2.7}$ saturation dependence, which is practically more useful than the expected T^5 dependence. We have shown that CBT can be used as practical thermometers, but also as a sensitive environmental noise sensor for preparing other experiments. This work paves the way by technique and demonstration that there are methods for designing experiments and measuring nanoelectronic devices at ever lower temperature approaching sub-millikelvin.

One smaller project undertaken developed a more efficient sampling pattern for peak like functions to improve the extraction of characteristic parameters, like the width or height. We focused on the Lorentz peak, which is used by the many resonating probes used in low temperature physics, but the results were also tested and are applicable to the Sinh function based peak of the CBT as well. We initially used simulated data to plot the location of information as it is distributed across the peak to gain insight into how different sampling densities would change the quality of parameter estimation. We tested the standard linear spaced sweep with different sweeping widths to discover an optimum sampling span of ± 3 times the full-width-at-half-maximum of the peak. This knowledge alone can provide a significant improvement over poorly chosen sweep parameter. To search for a more optimum sweep, one that uses a non-uniform sampling densities, we tested an equal-phase method which showed promising improvements over the linear spaced method. We then developed a new bespoke method for sampling by using the results of a genetic algorithm to solve the unconstrained optimisation problem. This new method was verified on ultra low temperature vibration wire resonators and showed a minimum improvement of 20%. The resilience to poorly initialised shows that the new method is better when the true peak centre lay within one FWHM of what was estimated. This new method could be used alongside existing methods to improve the quality of data acquired, reduce measurement time, or both without interfering with existing apparatus.

The final section described the results from a range of nanomechanical resonating beams fabricated by a colleague that have been developed for use as probes for liquid helium. The nanomechanical beams have lengths in the range between $15\ \mu\text{m}$ and $50\ \mu\text{m}$, with frequencies $1.5\ \text{MHz}$ - $8.6\ \text{MHz}$. These have a very high mass sensitivity due to the low linear mass density of the aluminium construction and a

narrow square profile of $100\text{ nm} \times 100\text{ nm}$. We overcame the challenges of using nanomechanical beams in a low temperature laboratory environment to measure the complex induced voltage resonance and recovered the physical properties of velocity and displacement of the beam. We achieved the first measurements of mechanical resonance of a nanomechanical beam in liquid helium and superfluid helium. This involved the construction of two versatile helium-4 probes and a cryogenic systems to measure the beam's resonance response in an environment of superfluid helium-4, in a variable pressure gas at 4 K, and in vacuum. The beam was simultaneously driven and measured using a vector network analyser, with the resulting data only requiring frequency dependency phase rotation to fully recover the induced voltage signal. We acquired measurements of the resonance while the beam was immersed in superfluid over a range of temperatures from 1.2 K to 4.2 K to demonstrate the beam's sensitivity to the fluid damping and viciously attached mass on the beam's surface. The change of resonance frequency and the change of quality factor agree with predictions based on the two fluid model for the largest, $50\text{ }\mu\text{m}$ long beam, and showed encouraging results for the shorter $15\text{ }\mu\text{m}$ and $25\text{ }\mu\text{m}$ beams. Measuring the beam in an environment of helium gas at differing pressures shows the beam as a sensitive pressure sensor, showing behaviour that can be described by a kinetic gas model. Both the liquid and gas environments for the beam appear to need additional dissipation methods, such as acoustic emission in order for the behaviour to be fully described. These NEMS devices are being developed to be used as sensors in helium-3 at ultra low temperatures to measure quasiparticles from decaying quantum turbulence with more sensitivity and a higher spacial resolution than existing tuning fork sensors.

Weather working on electronic systems at millikelvin temperatures, or probing helium as a quantum fluid with nanomechanical beams, this

thesis has demonstrated new thermometry techniques that explore the physics of low temperature devices to push towards newer and more advanced studies that are yet to come. The progresses made with low temperature technologies are part of a virtuous cycle to understanding low temperature physics.

A

APPENDIX

```

1 # *params contains the paramerters for the peak function
   #n is the number of points
3 #w is the smearing width
   def convolution(f,peakFunction,w,n,*params):
5     #sample accross the peak with a sinisoidal shape
       ws = w * np.cos( np.linspace(0,1,n) *np.pi) # each of
           the sample points make a width shift
7     r = np.zeros(len(f)) #make buffer the right size
       for wse in ws: #for each width shift element
9         r = r + peakFunction(f + wse,*params) # add each
           sample to the buffer
       return r / n # normalise for the mean average

```

Listing A.1: Peak Convolution Function

CODE LISTINGS

We include some example code to implement each of the measurement pattens.

The three functions listed here take four parameters:

- center: the best guess at the center frequency of the peak.
- width: the best guess at the width of the peak.
- widths: the number of widths to sweep out to. This gives the width of the measurement patten.
- points: the number of points to generate.

```

def mphaseSpacingV2(center,width,widths,points):
2   r = range(points)
   d_theta = 2.0/(points-1)
4   theta_max = 1.0/math.pi * math.atan(widths*2*math.sqrt
      (2))
   step = 0.01
6   last =0
   test = widths
8   for i in range(100):
       last = test
10      theta_max = min(theta_max,0.99999)
       #t = math.sin(math.pi * theta_max)/math.pi
12      t = theta_max
       t = t - math.sin(4*math.pi * t)/(4 * math.pi)
14      test = abs( widths - math.tan(t*math.pi / 2)/2 )
       if test < last:
16          step *= 1.2
       else:
18          theta_max -= step;
          step /= -2.0
20          theta_max += step

22      #generate the points
       theta_start = -1.0
24      for i in range(points):
          t = d_theta * i + theta_start
26          t = theta_max*(t + math.sin(math.pi * t)/math.pi)
          t = t - math.sin(4*math.pi *t) / (4*math.pi)
28          r[i] = math.tan(t * math.pi / 2) * width / 2.0 +
              center
   return np.array(r,dtype=np.float64)

```

Listing A.2: Generalised Improved Sampling Pattern

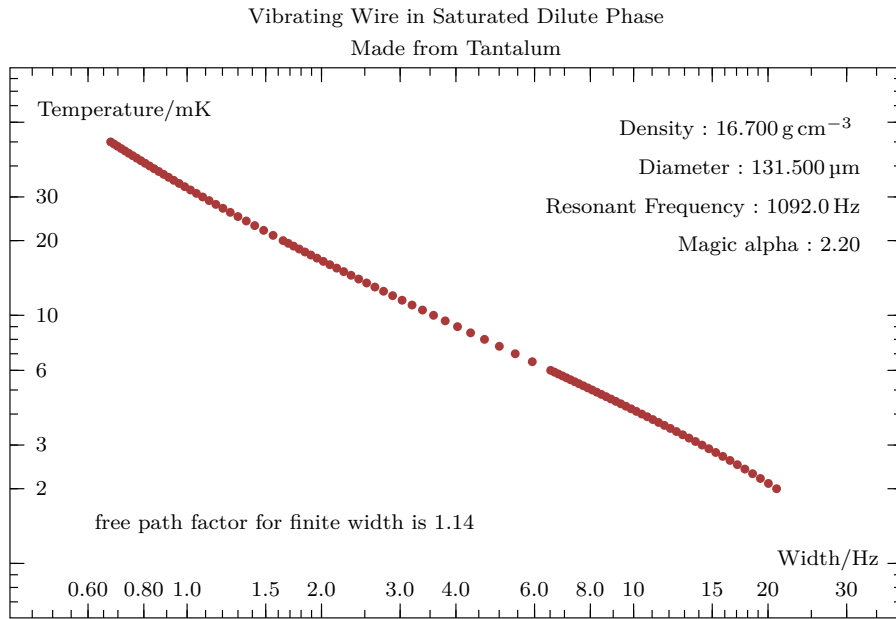


Figure A.0.1: The calibration curve of the Vibrating Wire Resonator thermometer in the mixing chamber. Generated from WinTwang [49]. This curve is specific to the wire used. The wire properties and the additional equation factors are shown on the graph.

```

1 def phaseSpacing(center, width, widths, points):
    r = range(points);
3     d_theta = 2.0/(points-1)
    theta_max = 2.0/3.1415 * math.atan(widths*2)
5     theta_start = -1
    for i in range(points):
7         t = theta_max*(d_theta * i + theta_start)

    r[i] = math.tan(t * 3.1415 / 2) * width / 2 +
        center
9     return np.array(r)

```

Listing A.3: Equal Phase Sampling Pattern

- Nanomechanical resonators

- Resist

Copolymer 6 % in Ethyl Lactate	2000 RRM	3 min @ 200°C
950 PMMA 2% in Anisole	7000 RPM	3 min @ 200°C

- Exposure

4 th lens	10 nA @ 50 kV	250 $\mu\text{C}/\mu^2$
2 nd aperture		1200 nC/ μ

- Development

(CH ₃) ₂ CHOH : H ₂ O	93 : 7	3 min
(CH ₃) ₂ CHOH	Rinse	30 s

- Plasma ashing

O ₂ (40 sccm) $P = 200$ mTorr	Mixing	3 min
O ₂ (40 sccm) $P = 200$ mTorr $\mathcal{P} = 50$ W	Ashing	30 s

- Deposition

Al	2 Å/s	1200 Å
----	-------	--------

- Lift-off

(CH ₃) ₂ CO		30 min
H ₂ O	Rinse	

- Silicon etching

O ₂ (4 sccm) SF ₆ (40 sccm) $P = 180$ mTorr	Mixing	5 min
O ₂ (4 sccm) SF ₆ (40 sccm) $P = 180$ mTorr $\mathcal{P} = 100$ W	Etching	3 min

Figure A.0.2: The process notes and recipe for the manufacture of NEMS in a clean room [168].

```

def linspace(center,width,widths,points):
2   r = range(points);
   df = widths*width*2.0/(points-1)
4   start = center - widths*width
   for i in range(points):
6       r[i] = start + i*df
   return np.array(r,dtype=np.float64)

```

Listing A.4: Linear Sampling Pattern

BIBLIOGRAPHY

- [1] J. R. Prance, D. I. Bradley, R. E. George, R. P. Haley, Yu A. Pashkin, M. Sarsby, J. Penttilä, L. Roschier, D. Gunnarsson, H. Heikkinen, and M. Prunnila. Nanoelectronic thermometers optimised for sub-10 millikelvin operation. *arxiv.org*, June 2015.
- [2] D. I. Bradley, R. E. George, D. Gunnarsson, R. P. Haley, H. Heikkinen, Yu A. Pashkin, J. Penttila, J. R. Prance, M. Prunnila, L. Roschier, and M. Sarsby. Nanoelectronic primary thermometry below 4mk. *Nature Publishing Group, a division of Macmillan Publishers Limited*, 7, 2016/01/27.
- [3] Richard Feynman. *The Feynman Lectures on Physics, Volume I*, volume 1. caltech.edu, 1964.
- [4] J. P. Pekola, K. P. Hirvi, J. P. Kauppinen, and M. A. Paalanen. Thermometry by arrays of tunnel junctions. *Phys. Rev. Lett.*, 73: 2903–2906, November 1994.
- [5] KP Hirvi, JP Kauppinen, MA Paalanen, and JP Pekola. Primary thermometry with nanoscale tunnel junctions. *Journal of low temperature physics*, 101(1-2):17–24, 1995.
- [6] DI Bradley, MR Follows, IE Miller, R Oswald, and M Ward. Simple design for dilution refrigerator with base temperature of 2.3 mk. *Cryogenics*, 34(6):549–550, 1994.
- [7] G Frossati. Obtaining ultralow temperatures by dilution of ^3He into ^4He . *Le Journal de Physique Colloques*, 39(C6):C6–1578, 1978.
- [8] BlueFors Cryogenics Oy Ltd. Bluefors cryogenics, July 2016. URL <http://www.bluefors.com/site/>.

- [9] Oxford Instruments plc. Dilution and helium3 refrigerators, July 2016. URL <http://www.oxford-instruments.com>.
- [10] ICEoxford Limited. Ice, July 2016. URL <http://www.iceoxford.com/Wet-Systems/Wet-Dilution-Refridgerators.htm>.
- [11] D. J. Cousins, S. N. Fisher, A. M. Guénault, R. P. Haley, I. E. Miller, G. R. Pickett, G. N. Plenderleith, P. Skyba, P. Y. A. Thibault, and M. G. Ward. An advanced dilution refrigerator designed for the new lancaster microkelvin facility. *Journal of Low Temperature Physics*, 114(5):547–570, March 1999.
- [12] AV Feshchenko, L Casparis, IM Khaymovich, D Maradan, O-P Saira, M Palma, M Meschke, JP Pekola, and DM Zumbühl. Tunnel-junction thermometry down to millikelvin temperatures. *Physical Review Applied*, 4(3):034001, 2015.
- [13] O. E. Dial, M. D. Shulman, S. P. Harvey, H. Bluhm, V. Umansky, and A. Yacoby. Charge noise spectroscopy using coherent exchange oscillations in a singlet-triplet qubit. *Phys. Rev. Lett.*, 110:146804, April 2013.
- [14] Hanhee Paik, D. I. Schuster, Lev S. Bishop, G. Kirchmair, G. Catelani, A. P. Sears, B. R. Johnson, M. J. Reagor, L. Frunzio, L. I. Glazman, S. M. Girvin, M. H. Devoret, and R. J. Schoelkopf. Observation of high coherence in josephson junction qubits measured in a three-dimensional circuit qed architecture. *Phys. Rev. Lett.*, 107:240501, December 2011.
- [15] JP Kauppinen, KT Loberg, AJ Manninen, JP Pekola, and RA Voutilainen. Coulomb blockade thermometer: Tests and instrumentation. *Review of scientific instruments*, 69(12):4166–4175, 1998.

- [16] S. Diner, D. Fargue, G. Lochak, and F. Selleri. *The Wave-Particle Dualism, A Tribute to Louis de Broglie on his 90th Birthday*, volume 3. Springer Netherlands, 1984.
- [17] BL Altshuler, PA Lee, and RA Webb. *Mesoscopic phenomena in solids*. Elsevier, 1991.
- [18] DV Averin and KK Likharev. Coulomb blockade of single-electron tunneling, and coherent oscillations in small tunnel junctions. *Journal of low temperature physics*, 62(3-4):345–373, 1986.
- [19] Francesco Giazotto, Tero T Heikkilä, Arttu Luukanen, Alexander M Savin, and Jukka P Pekola. Opportunities for mesoscopics in thermometry and refrigeration: Physics and applications. *Reviews of Modern Physics*, 78(1):217, 2006.
- [20] Sh Farhangfar, KP Hirvi, JP Kauppinen, JP Pekola, JJ Toppari, DV Averin, and AN Korotkov. One dimensional arrays and solitary tunnel junctions in the weak coulomb blockade regime: Cbt thermometry. *Journal of low temperature physics*, 108(1-2): 191–215, 1997.
- [21] M. J. Hagmann. Determination of barrier traversal time by modulation of the incident wave. *Applied Physics Letters*, 62(2):199–201, 1993.
- [22] Christoph Wasshuber. *About Single-Electron Devices and Circuits*. PhD thesis, Technischen Universität Wien (Technical University of Vienna - Faculty of Electrical Engineering), January 1997.
- [23] M. Meschke, J. P. Pekola, F. Gay, R. E. Rapp, and H. Godfrin. Electron thermalization in metallic islands probed by coulomb blockade thermometry. *Journal of Low Temperature Physics*, 134(5):1119–1143, March 2004.

- [24] KP Hirvi, JP Kauppinen, AN Korotkov, MA Paalanen, and JP Pekola. Arrays of normal metal tunnel junctions in weak coulomb blockade regime. *Applied physics letters*, 67(14):2096–2098, 1995.
- [25] M. Meschke, A.Kemppinen, and J. P. Pekola. Accurate coulomb blockade thermometry up to 60 kelvin. *Philosophical Transactions A*, 374(5):20150052, 2015.
- [26] M Meschke, A Kemppinen, and JP Pekola. Accurate coulomb blockade thermometry up to 60 kelvin. *arXiv preprint arXiv:1507.05462*, 2015.
- [27] S. J. Shin, J. J. Lee, H. J. Kang, J. B. Choi, S.-R. Eric Yang, Y. Takahashi, and D. G. Hasko. Room-temperature charge stability modulated by quantum effects in a nanoscale silicon island. *Nano Letters*, 11(4):1591–1597, 2011.
- [28] Tobias Bergsten, Tord Claeson, and Per Delsing. A fast, primary coulomb blockade thermometer. *Applied Physics Letters*, 78(9):1264–1266, 2001.
- [29] AivonOy. pycbt, February 2015. URL <https://github.com/AivonOy/pyCBT>.
- [30] M. Prunnila, M. Meschke, D. Gunnarsson, S. Enouz-Vedrenne, J. M. Kivioja, and J. P. Pekola. Ex situ tunnel junction process technique characterized by coulomb blockade thermometry. *Journal of Vacuum Science & Technology B*, 28(5):1026–1029, 2010.
- [31] JT Karvonen, LJ Taskinen, and IJ Maasilta. Influence of temperature gradients on tunnel junction thermometry below 1 k: Cooling and electron–phonon coupling. *Journal of Low Temperature Physics*, 146(1-2):213–226, 2007.

- [32] ML Roukes, MR Freeman, RS Germain, RC Richardson, and MB Ketchen. Hot electrons and energy transport in metals at millikelvin temperatures. *Physical review letters*, 55(4):422, 1985.
- [33] KL Viisanen and JP Pekola. Anomalous electronic heat capacity of copper nanowires at sub-kelvin temperatures. *arXiv preprint arXiv:1606.02985*, 2016.
- [34] P. M. Echternach, M. R. Thoman, C. M. Gould, and H. M. Bozler. Electron-phonon scattering rates in disordered metallic films below 1 K. *PhysRevB*, 46:10339–10344, October 1992.
- [35] AivonOy. pycbt. <https://github.com/AivonOy/pyCBT>, 2015. Python library for Coulomb Blockade Thermometer (CBT) data fitting.
- [36] Alan M Turing. On computable numbers, with an application to the entscheidungsproblem. *Proceedings of the London mathematical society*, 42(2):230–265, 1936.
- [37] D.E. Knuth. *The Art of Computer Programming: Third Edition*, volume 1. Addison Wesley Longman, May 1997. ISBN 0-201-89683-4.
- [38] Eric W. Weisstein. Least squares fitting–polynomial. From MathWorld–A Wolfram Web Resource., 2016. <http://mathworld.wolfram.com>.
- [39] Stephen M Goldfeld, Richard E Quandt, and Hale F Trotter. Maximization by quadratic hill-climbing. *Econometrica: Journal of the Econometric Society*, pages 541–551, 1966.
- [40] MA Black, HE Hall, and K Thompson. The viscosity of liquid helium 3. *Journal of Physics C: Solid State Physics*, 4(2):129, 1971.
- [41] TA Alvesalo, HK Collan, MT Lojonen, OV Lounasmaa, and MC Veuro. The viscosity and some related properties of liquid³He

- at the melting curve between 1 and 100 mk. *Journal of Low Temperature Physics*, 19(1-2):1–37, 1975.
- [42] JCH Zeegers, A de Waele, and HM Gijsman. Viscosity of saturated ^3He - ^4He mixture below 200 mk. *Journal of Low Temperature Physics;(United States)*, 84, 1991.
- [43] Elias Pentti, Juho Rysti, Anssi Salmela, Alexander Sebedash, and Juha Tuoriniemi. Studies on helium liquids by vibrating wires and quartz tuning forks. *Journal of Low Temperature Physics*, 165(3-4):132–165, 2011.
- [44] Griffith Andrew. Propagation of quantum turbulence in helium-4. Master’s thesis, Lancaster University, April 2012.
- [45] Emerson and Cuming. Stycast 1266 a/b, technical sheet. <http://www.capem.buffalo.edu/lab-manuals/stycast.pdf>, 1999.
- [46] Shaun Neil Fisher. *The Mechanical Properties of Superfluids ^3He -A and ^3He -B in the Ballistic Regime*. PhD thesis, University of Lancaster, Lancaster University, Lancaster, November 1991.
- [47] DI Bradley and R Oswald. Viscosity of the ^3He - ^4He dilute phase in the mixing chamber of a dilution refrigerator. *Journal of low temperature physics*, 80(1-2):89–97, 1990.
- [48] H. Højgaard Jensen, H. Smith, P. Wölfle, K. Nagai, and T. Maack Bisgaard. Boundary effects in fluid flow. application to quantum liquids. *Journal of Low Temperature Physics*, 41(5):473–519, 1980. ISSN 1573-7357.
- [49] D I Bradley. Win_Twang - Program to calculate VWR line widths in pure and dilute He-3. Lancaster Internal, January 2006. Version 1.4.1.
- [50] Inc. Lake Shore Cryotronics. Ruthenium oxide (roxTM). Online, 2016. <http://www.lakeshore>.

[com/products/cryogenic-temperature-sensors/
ruthenium-oxide-rox-rtlds/models/pages/Overview.aspx](http://www.cmr-direct.com/products/cryogenic-temperature-sensors/ruthenium-oxide-rox-rtlds/models/pages/Overview.aspx).

- [51] R Blaauwgeers, M Blazkova, M Človečko, VB Eltsov, R De Graaf, J Hosio, M Krusius, D Schmoranzer, Wilfried Schoepe, L Skrbek, et al. Quartz tuning fork: thermometer, pressure-and viscometer for helium liquids. *Journal of low temperature physics*, 146(5-6): 537–562, 2007.
- [52] F. Pobell. *Matter and methods at low temperatures*. Springer textbook. Springer-Verlag, 1992. ISBN 9780387537511.
- [53] CMR-Direct. Ge varnish - for cryogenic heatsinking. <http://www.cmr-direct.com/en/ge-varnish>, 2016.
- [54] S. W vanSciver. *Helium Cryogenics*. Springer, 1986.
- [55] Eric T Swartz and Robert O Pohl. Thermal boundary resistance. *Reviews of modern physics*, 61(3):605, 1989.
- [56] APJ Voncken, D Riese, LP Roobol, R König, and F Pobell. Thermal boundary resistance between liquid helium and silver sinter at low temperatures. *Journal of low temperature physics*, 105(1-2):93–112, 1996.
- [57] H Franco, J Bossy, and H Godfrin. Properties of sintered silver powders and their application in heat exchangers at millikelvin temperatures. *Cryogenics*, 24(9):477–483, 1984.
- [58] Stephen Brunauer, Paul Hugh Emmett, and Edward Teller. Adsorption of gases in multimolecular layers. *Journal of the American chemical society*, 60(2):309–319, 1938.
- [59] S.J. Gregg and K.S.W. Sing. *Adsorption, surface area, and porosity*. Academic Press, 1991. ISBN 9780123009562.
- [60] DJ Cousins, SN Fisher, AM Guénault, GR Pickett, EN Smith, and RP Turner. T- 3 temperature dependence and a length scale

- for the thermal boundary resistance between a saturated dilute ^3He - ^4He solution and sintered silver. *Physical review letters*, 73 (19):2583, 1994.
- [61] DJ Cousins, AM Guénault, GR Pickett, P Thibault, RP Turner, EN Smith, C Bäuerle, Yu M Bunkov, SN Fisher, and H Godfrin. A geometry dependent thermal resistance between a saturated dilute ^3He - ^4He solution and sintered silver powder. *Journal of low temperature physics*, 101(1-2):259–264, 1995.
- [62] L Roschier, D Gunnarsson, M Meschke, A Savin, J S Penttilä, and M Prunnila. Effect of on-chip filter on coulomb blockade thermometer. *Journal of Physics: Conference Series*, 400(5):052029, 2012.
- [63] Emerson and Cuming Microwave Products (Randolph, MA). Eccosorb. Commercial Product, July 2016. Emerson & Cuming Microwave Products, a unit of Laird Technologies.
- [64] DF Santavicca and DE Prober. Impedance-matched low-pass stripline filters. *Measurement Science and Technology*, 19(8):087001, 2008.
- [65] Christian P Scheller, Sarah Heizmann, Kristine Bedner, Dominic Giss, Matthias Meschke, Dominik M Zumbühl, Jeremy D Zimmerman, and Arthur C Gossard. Silver-epoxy microwave filters and thermalizers for millikelvin experiments. *Applied Physics Letters*, 104(21):211106, 2014.
- [66] J. Blatt. *Thermoelectric Power of Metals*. Springer Science & Business Media, 2002.
- [67] Goodfellow Cambridge Ltd. Tantalum wire - 0.125mm ta005120. <http://www.goodfellow.com>, 1946-Present. Diameter : 0.125mm, Purity : 99.9%, Temper : Annealed.

- [68] J Inoue and M Shimizu. Electronic structure and magnetic properties of γ Fe₁₄B. *Journal of Physics F: Metal Physics*, 16(8):1051, 1986.
- [69] PM Echternach, MR Thoman, CM Gould, and HM Bozler. Electron-phonon scattering rates in disordered metallic films below 1 K. *Physical Review B*, 46(16):10339, 1992.
- [70] J Pollanen, H Choi, JP Davis, BT Rolfs, and WP Halperin. Low temperature thermal resistance for a new design of silver sinter heat exchanger. In *Journal of Physics: Conference Series*, volume 150, page 012037. IOP Publishing, 2009.
- [71] jonasalmeida. jmat.fminsearch. Online - <https://github.com/jonasalmeida/fminsearch> Commit 45fcdcf, January 2014.
- [72] Jeffrey C Lagarias, James A Reeds, Margaret H Wright, and Paul E Wright. Convergence properties of the nelder-meade simplex method in low dimensions. *SIAM Journal on optimization*, 9(1):112–147, 1998.
- [73] Eric Jones, Travis Oliphant, Pearu Peterson, et al. SciPy: Open source scientific tools for Python. <http://www.scipy.org/>, 2001–. [Online; accessed 2016-01-13].
- [74] Jorge J Moré. The levenberg-marquardt algorithm: implementation and theory. In *Numerical analysis*, pages 105–116. Springer, 1978.
- [75] Kenneth De Jong. Adaptive system design: a genetic approach. *IEEE Transactions on Systems, Man, and Cybernetics*, 10(9):566–574, 1980.
- [76] Scott Kirkpatrick, C Daniel Gelatt, Mario P Vecchi, et al. Optimization by simulated annealing. *science*, 220(4598):671–680, 1983.

- [77] RW Eglese. Simulated annealing: a tool for operational research. *European journal of operational research*, 46(3):271–281, 1990.
- [78] John Grefenstette, Rajeev Gopal, Brian Rosmaita, and Dirk Van Gucht. Genetic algorithms for the traveling salesman problem. In *Proceedings of the first International Conference on Genetic Algorithms and their Applications*, pages 160–168. Lawrence Erlbaum, New Jersey (160-168), 1985.
- [79] David E Goldberg and Manohar P Samtani. Engineering optimization via genetic algorithm. In *Electronic computation*, pages 471–482. ASCE, 1986.
- [80] Lawrence Davis. *Handbook of genetic algorithms*. Van Nostrand Reinhold Company, 1991.
- [81] D Goldberg. A note on boltzmann tournament selection for genetic algorithms and population-oriented simulated annealing. tcga 90003. *Engineering Mechanics, Univ. Alabama*, 1990.
- [82] Andreas Kraus, Artur Erbe, and Robert H Blick. Nanomechanical vibrating wire resonator for phonon spectroscopy in liquid helium. *Nanotechnology*, 11(3):165, 2000.
- [83] AW Baggaley, Viktor Tsepelin, CF Barenghi, SN Fisher, GR Pickett, YA Sergeev, and Nugzar Suramlishvili. Visualizing pure quantum turbulence in superfluid he-3: Andreev reflection and its spectral properties. *Physical review letters*, 115(1):015302, 2015.
- [84] DC Carless, HE Hall, and JR Hook. Vibrating wire measurements in liquid ^3He II. The superfluid B phase. *Journal of low temperature physics*, 50(5-6):605–633, 1983.
- [85] AM Guénault, V Keith, CJ Kennedy, SG Mussett, and GR Pickett. The mechanical behavior of a vibrating wire in

- superfluid $^3\text{He-B}$ in the ballistic limit. *Journal of low temperature physics*, 62(5-6):511–523, 1986.
- [86] D. I. Bradley, S. N. Fisher, A. Ganshin, A.M. Guénault, R. P. Haley, M. J. Jackson, G. R. Pickett, and V. Tsepelin. The Onset of Vortex Production by a Vibrating Wire in Superfluid He-3-B. *Journal of Low Temperature Physics*, 171(5-6):582–588, July 2013.
- [87] Ian Bradley, Shaun Fisher, A.M. Guénault, Richard Haley, George Pickett, David Potts, and Viktor Tsepelin. Direct measurement of the energy dissipated by quantum turbulence. *Nature Physics*, 7(6):473–476, July 2011.
- [88] D. Ian Bradley, D. O. Clubb, Shaun N. Fisher, A.M. Guénault, Richard P. Haley, C. J. Matthews, George R. Pickett, Viktor Tsepelin, and K. Zaki. Decay of pure quantum turbulence in superfluid He-3-B. *Physical Review Letters*, 96(3):035301, January 2006.
- [89] D. Ian Bradley, Shaun N. Fisher, A.M. Guénault, Richard P. Haley, Samantha O’Sullivan, George R. Pickett, and Viktor Tsepelin. Fluctuations and correlations of pure quantum turbulence in superfluid He-3-B. *Physical Review Letters*, 101(6):065302, August 2008.
- [90] Jan Jäger, Berthold Schuderer, and Wilfried Schoepe. Turbulent and laminar drag of superfluid helium on an oscillating microsphere. *Physical review letters*, 74(4):566, 1995.
- [91] DI Bradley, SN Fisher, A Ganshin, AM Guénault, RP Haley, MJ Jackson, GR Pickett, and V Tsepelin. The onset of vortex production by a vibrating wire in superfluid $^3\text{He-B}$. *Journal of Low Temperature Physics*, 171(5-6):582–588, 2013.

- [92] D Ian Bradley, DO Clubb, Shaun N Fisher, AM Guénault, Richard P Haley, CJ Matthews, George R Pickett, Viktor Tsepelin, and K Zaki. Emission of Discrete Vortex Rings by a Vibrating Grid In Superfluid He-3-B: A Precursor to Quantum Turbulence. *Physical review letters*, 95(3):035302, 2005.
- [93] D. O. Clubb, O. V. L. Buu, R. M. Bowley, R. Nyman, and J. R. Owers-Bradley. Quartz tuning fork viscometers for helium liquids. *Journal of Low Temperature Physics*, 136(1):1–13, 2004.
- [94] D. I. Bradley, M. Človečko, S. N. Fisher, D. Garg, E. Guise, R. P. Haley, O. Kolosov, G. R. Pickett, V. Tsepelin, D. Schmoranzer, and L. Skrbek. Crossover from hydrodynamic to acoustic drag on quartz tuning forks in normal and superfluid ^4He . *Phys. Rev. B*, 85:014501, January 2012.
- [95] Marcel Človečko, Emil Gažo, Martin Kupka, Maroš Skyba, and Peter Skyba. High quality tuning forks in superfluid ^3He -B below $200 \mu\text{k}$. *Journal of Low Temperature Physics*, 162(5-6):669–677, 2011.
- [96] P Günther, U Ch Fischer, and K Dransfeld. Scanning near-field acoustic microscopy. *Applied Physics B*, 48(1):89–92, 1989.
- [97] Andrew Woods. *Visualisation of quantum turbulence in superfluid ^3He -B using a novel 2D quasiparticle detector*. PhD thesis, Lancaster University, 2015.
- [98] S. L. Ahlstrom, D. I. Bradley, S. N. Fisher, A. M. Guénault, E. A. Guise, R. P. Haley, S. Holt, O. Kolosov, P. V. E. McClintock, G. R. Pickett, M. Poole, R. Schanen, V. Tsepelin, and A. J. Woods. A quasiparticle detector for imaging quantum turbulence in superfluid ^3He -B. *Journal of Low Temperature Physics*, 175(5): 725–738, 2014.

- [99] R.P. Feynman, R.B. Leighton, and M.L. Sands. *The Feynman Lectures on Physics: Mainly mechanics, radiation, and heat*, volume 1 of *Basic Books*. Basic Books, 2011. ISBN 9780465024933.
- [100] M. Defoort, S. Dufresnes, S. L. Ahlstrom, D. I. Bradley, R. P. Haley, A. M. Guénault, E. A. Guise, G. R. Pickett, M. Poole, A. J. Woods, V. Tsepelin, S. N. Fisher, H. Godfrin, and E. Collin. Probing bogoliubov quasiparticles in superfluid ^3He with a ‘vibrating-wire like’ mems device. *Journal of Low Temperature Physics*, 183(3):284–291, May 2016.
- [101] M Gonzalez, WG Jiang, P Zheng, CS Barquist, HB Chan, and Y Lee. Temperature Dependence of Viscosity in Normal Fluid ^3He Below 800mK Determined by a Micro-electro-mechanical Oscillator. *arXiv preprint arXiv:1604.08554*, 2016.
- [102] M Gonzalez, P Zheng, E Garcell, Y Lee, and Ho Bun Chan. Comb-drive micro-electro-mechanical systems oscillators for low temperature experiments. *Review of Scientific Instruments*, 84(2):025003, 2013.
- [103] Eddy Collin, J Kofler, J-S Heron, Olivier Bourgeois, Yu M Bunkov, and Henri Godfrin. Novel “vibrating wire like” mems and mems structures for low temperature physics. *Journal of Low Temperature Physics*, 158(3-4):678–684, 2010.
- [104] Eddy Collin, Thomas Moutonet, J-S Heron, Olivier Bourgeois, Yu M Bunkov, and Henri Godfrin. A tunable hybrid electro-magnetomotive mems device for low temperature physics. *Journal of Low Temperature Physics*, 162(5-6):653–660, 2011.
- [105] M. Defoort, S. Dufresnes, S. L. Ahlstrom, D. I. Bradley, R. P. Haley, A. M. Guénault, E. A. Guise, G. R. Pickett, M. Poole, A. J. Woods, V. Tsepelin, S. N. Fisher, H. Godfrin, and E. Collin.

- Probing Bogoliubov Quasiparticles in Superfluid He with a ‘Vibrating-Wire Like’ MEMS Device. *JOURNAL OF LOW TEMPERATURE PHYSICS*, 183(3-4):284–291, May 2016.
- [106] Chih-Ming Ho and Yu-Chong Tai. Micro-electro-mechanical-systems (mems) and fluid flows. *Annual Review of Fluid Mechanics*, 30(1):579–612, 1998.
- [107] AN Cleland and ML Roukes. Fabrication of high frequency nanometer scale mechanical resonators from bulk si crystals. *Applied Physics Letters*, 69(18):2653–2655, 1996.
- [108] Eloi Marigó, Marc Sansa, Francesc Pérez-Murano, Arantxa Uranga, and Núria Barniol. Top-down cmos-nems polysilicon nanowire with piezoresistive transduction. *Sensors*, 15(7):17036–17047, 2015.
- [109] Harold G Craighead. Nanoelectromechanical systems. *Science*, 290(5496):1532–1535, 2000.
- [110] Anja Boisen, Søren Dohn, Stephan Sylvest Keller, Silvan Schmid, and Maria Tenje. Cantilever-like micromechanical sensors. *Reports on Progress in Physics*, 74(3):036101, 2011.
- [111] Severin Waldis, Frederic Zamkotsian, Pierre-Andre Clerc, Wilfried Noell, Michael Zickar, and Nico de de Rooij. Arrays of high tilt-angle micromirrors for multiobject spectroscopy. *IEEE Journal of Selected Topics in Quantum Electronics*, 13(2):168–176, 2007.
- [112] Vural Kara, Y-I Sohn, Haig Atikian, Victor Yakhot, Marko Lončar, and Kamil L Ekinci. Nanofluidics of single-crystal diamond nanomechanical resonators. *Nano letters*, 15(12):8070–8076, 2015.
- [113] X Rojas and JP Davis. Superfluid nanomechanical resonator for quantum nanofluidics. *Physical Review B*, 91(2):024503, 2015.

- [114] YT Yang, Carlo Callegari, XL Feng, KL Ekinici, and ML Roukes. Zeptogram-scale nanomechanical mass sensing. *Nano letters*, 6(4):583–586, 2006.
- [115] I Kozinsky, HW Ch Postma, I Bargatin, and ML Roukes. Tuning nonlinearity, dynamic range, and frequency of nanomechanical resonators. *Applied Physics Letters*, 88(25):253101, 2006.
- [116] HW Ch Postma, I Kozinsky, A Husain, and ML Roukes. Dynamic range of nanotube-and nanowire-based electromechanical systems. *Applied Physics Letters*, 86(22):223105, 2005.
- [117] HJR Westra, M Poot, HSJ Van Der Zant, and WJ Venstra. Nonlinear modal interactions in clamped-clamped mechanical resonators. *Physical review letters*, 105(11):117205, 2010.
- [118] Dustin W Carr, Stephane Evoy, Lidija Sekaric, Harold G Craighead, and Jeevak M Parpia. Measurement of mechanical resonance and losses in nanometer scale silicon wires. *Applied Physics Letters*, 75(7):920–922, 1999.
- [119] P Mohanty, DA Harrington, KL Ekinici, YT Yang, MJ Murphy, and ML Roukes. Intrinsic dissipation in high-frequency micromechanical resonators. *Physical Review B*, 66(8):085416, 2002.
- [120] Sergey Kafanov. *Noise Properties of the Single-Electron Transistor*. PhD thesis, Chalmers University of Technology - Department of Microtechnology and Nanoscience, SE-412 96 Göteborg, Sweden, 2008.
- [121] Yakov Greenberg, Yurii Aleksandrovich Pashkin, and Evgeni Il'ichev. Nanomechanical resonators. *Physics-Uspeski*, 55(4):382–407, 2012.
- [122] John F. Cochran and D. E. Mapother. Superconducting transition in aluminum. *Phys. Rev.*, 111:132–142, July 1958.

- [123] Maciek Zgirski, Karri-Pekka Riikonen, Vladimir Touboltsev, and Konstantin Arutyunov. Size dependent breakdown of superconductivity in ultranarrow nanowires. *Nano letters*, 5(6): 1029–1033, 2005.
- [124] AN Cleland and ML Roukes. External control of dissipation in a nanometer-scale radiofrequency mechanical resonator. *Sensors and Actuators A: Physical*, 72(3):256–261, 1999.
- [125] AH Nayfeh and DT Mook. Nonlinear oscillations, physics and applied mathematics: A wiley-interscience series of texts, monographs & tracts, 1979.
- [126] Ron Lifshitz and MC Cross. Nonlinear dynamics of nanomechanical and micromechanical resonators. *Review of nonlinear dynamics and complexity*, 1:1–52, 2008.
- [127] C.M. Harris. *Shock and vibration handbook*. McGraw Hill reference books. McGraw-Hill Ryerson, Limited, 2002. ISBN 0-07-137081-1.
- [128] Van S and Steven W. *Helium Cryogenics*. International Cryogenics Monograph Series. Springer Science & Business Media - Springer New York, 2012.
- [129] CA Swenson. Recommended values for the thermal expansivity of silicon from 0 to 1000 k. *Journal of physical and chemical reference data*, 12(2):179–182, 1983.
- [130] Tom Irvine. Natural frequencies for common systems. Modal Analysis and Controls Laboratory of the University of Massachusetts Lowell, Unknown Publication Date.
- [131] J. Emsley. *Nature's Building Blocks: An A-Z Guide to the Elements*. Oxford University Press, 2001. p. 178. ISBN 0-19-850340-7.

- [132] R.C.Weast. *The Handbook of Chemistry and Physics*. CRC Press, Cleveland, 1976.
- [133] A. M. Guénault. *Basic Superfluids*. Master's Series in Physics and Astronomy. CRC Press, first edition, November 2002. ISBN-10: 0748408924.
- [134] A.M. Guénault. *Statistical Physics*. Student Physics Series. Springer Netherlands, 2007. ISBN 9781402059742.
- [135] P.V.E. McClintock, D. J. Meredith, and J. K. Wigmore. *Matter at Low Temperatures*. Blackie Academic & Professional, 1984.
- [136] Lev Davidovich Landau. On the theory of phase transitions. i. *Zh. Eksp. Teor. Fiz.*, 11:19, 1937.
- [137] Russell J Donnelly. The discovery of superfluidity. *Physics Today*, 48(7):30–38, 1995.
- [138] JF Allen and AD Misener. Flow of liquid helium II. *Nature*, 141 (3558):75, 1938.
- [139] K.Mendelssohn. *The Quest for Absolute Zero*. Taylor and Francis, London, second edition, 1977.
- [140] Bureau International des Poids et Mesures. *The International Temperature Scale of 1990 (ITS-90)*. www.its-90.com, 1990. Table 3.
- [141] R. J. Donnelly. *Quantised Vortices in Helium II*. Cambridge University Press, Cambridge, 1991.
- [142] J. Wilks. *The Properties of Liquid and Solid Helium*. Clarendon Press, Oxford, 1967.
- [143] W. F. Vinen. Quantum turbulence: Achievements and challenges. *Journal of Low Temperature Physics*, 161:419–444, 2010.

- [144] Richard P Feynman. Chapter II - Application of Quantum Mechanics to Liquid Helium. *Progress in low temperature physics*, 1:17–53, 1955.
- [145] Russell J Donnelly and Carlo F Barenghi. The observed properties of liquid helium at the saturated vapor pressure. *Journal of physical and chemical reference data*, 27(6):1217–1274, 1998.
- [146] DI Bradley, M Človečko, SN Fisher, D Garg, E Guise, RP Haley, O Kolosov, GR Pickett, V Tsepelin, D Schmoranzer, et al. Crossover from hydrodynamic to acoustic drag on quartz tuning forks in normal and superfluid ^4He . *Physical Review B*, 85(1):014501, 2012.
- [147] RP Kanwal. Vibrations of an elliptic cylinder and a flat plate in a viscous fluid. *ZAMM-Journal of Applied Mathematics and Mechanics/Zeitschrift für Angewandte Mathematik und Mechanik*, 35(1-2):17–22, 1955.
- [148] Minhang Bao. *Analysis and design principles of MEMS devices*. Elsevier, 2005.
- [149] JD Zook, DW Burns, H Guckel, JJ Sniegowski, RL Engelstad, and Z Feng. Characteristics of polysilicon resonant microbeams. *Sensors and Actuators A: Physical*, 35(1):51–59, 1992.
- [150] John E Sader, James WM Chon, and Paul Mulvaney. Calibration of rectangular atomic force microscope cantilevers. *Review of Scientific Instruments*, 70(10):3967–3969, 1999.
- [151] David Michael Rowe. *Thermoelectrics handbook: macro to nano*. CRC press, 2005.
- [152] K. Kurokawa. Power waves and the scattering matrix. *IEEE Transactions on Microwave Theory and Techniques*, 13(2):194–202, March 1965.

- [153] Oerlikon Leybold Vacuum. *Fundamentals of Vacuum Technology*. Oerlikon Group, June 2007.
- [154] Glenn Elert. The physics hypertextbook - latent heat. <http://physics.info/heat-latent/>, 1998-2016.
- [155] Jerome G Hust and Alan B Lankford. Thermal conductivity of aluminum, copper, iron, and tungsten for temperatures from 1 k to the melting point. Technical report, National Bureau of Standards, Boulder, CO (USA). Chemical Engineering Science Div., 1984.
- [156] Adam L Woodcraft. Recommended values for the thermal conductivity of aluminium of different purities in the cryogenic to room temperature range, and a comparison with copper. *Cryogenics*, 45(9):626–636, 2005.
- [157] AF Clark and JG Hust. The lorenz ratio as a tool for predicting the thermal conductivity of metals and alloys. *ntrs.nasa.gov*, 1971.
- [158] Norman H. March William Jones. *Theoretical Solid State Physics*. Courier Dover Publications, 2dn edition, 1985.
- [159] Inna Kozinsky. *Nonlinear nanoelectromechanical systems*. PhD thesis, California Institute of Technology, 2007.
- [160] Thomas Faust, Johannes Rieger, Maximilian J Seitner, Jörg Peter Kotthaus, and Eva Maria Weig. Coherent control of a classical nanomechanical two-level system. *Nature Physics*, 9(8):485–488, 2013.
- [161] David Ian Bradley, Richard Peter Haley, Sergey Kafanov, MT Noble, George Richard Pickett, Viktor Tsepelin, Jakub Vonka, and Tom Wilcox. Probing liquid ^4He with quartz tuning forks using a novel multifrequency lock-in technique. *Journal of Low Temperature Physics*, 184(5-6):1080–1091, 2016.

- [162] Mark Theodore Noble. Behavior of oscillatory wires in liquid helium-4 at 4.2 k and 1.5 k. Master's thesis, Lancaster University, April 2015.
- [163] Roland Dobbs. *Helium Three*. Number 108 in International series of monographs on physics. Oxford University Press on Demand, 2000.
- [164] R Hänninen and Wilfried Schoepe. Universal critical velocity for the onset of turbulence of oscillatory superfluid flow. *Journal of low temperature physics*, 153(5-6):189–196, 2008.
- [165] Patrick A Truitt, Jared B Hertzberg, CC Huang, Kamil L Ekinci, and Keith C Schwab. Efficient and sensitive capacitive readout of nanomechanical resonator arrays. *Nano letters*, 7(1):120–126, 2007.
- [166] Guillaume Aoust, Raphaël Levy, Béatrice Bourgeteau, and Olivier Le Traon. Acoustic damping on flexural mechanical resonators. *Sensors and Actuators A: Physical*, 238:158 – 166, 2016.
- [167] KJ Lulla, Martial Defoort, Christophe Blanc, Olivier Bourgeois, and Eddy Collin. Evidence for the role of normal-state electrons in nanoelectromechanical damping mechanisms at very low temperatures. *Physical review letters*, 110(17):177206, 2013.
- [168] Sergey Kafanov. Process, nanomechanical resonators. Clean Room Notes, April 2016.
- [169] André Miede. classicthesis. <http://code.google.com/p/classicthesis/>, 2015.
- [170] Matthew Sarsby. MJS Plot. http://generalsarsby.github.io/mjs_plot/, 2016. A javascript library for highly interactive graphs for analysis and data exploration.

- [171] Inkscape. Inkscape. <http://inkscape.org>, 2016.
- [172] MathWorks. MATLAB R2011a. <http://uk.mathworks.com/products/matlab>, 2011.
- [173] Fernando Pérez and Brian E. Granger. IPython: a system for interactive scientific computing. *Computing in Science and Engineering*, 9(3):21–29, May 2007.
- [174] Project Jupyter. Jupyter Notebook. <http://jupyter.org/>, 2016.
- [175] National Instruments. LabVIEW System Design Software. <http://www.ni.com/labview/>, 2016.



THE UNIVERSITY OF LANCASTER

COLOPHON

This document was typeset using a modified version of the typographical look-and-feel `classicthesis` [169].

The graphs and plots were made using a custom written MJS-Plot [170] as written by the author. The sketches and diagrams were made with Inkscape [171]. Data processing was initially done in Matlab [172], later work was completed in Python/iPython [173] using the Jupyter Notebook environment [174].

Much of the data acquisition was done with LabVIEW [175], with later work using Matlab.